

**Cranfield University**

**Sameer M BARGIR**

**Nanoscale Investigations of Surface Phenomena in the Water Treatment  
Industry using the Atomic Force Microscope**

**Centre for Water Science  
Microsystems and Nanotechnology Centre**

**PhD**

**Cranfield University**

School of Applied Sciences  
Centre for Water Science  
Microsystems and Nanotechnology Centre

PhD Thesis

Academic Year 2006 - 2007

Sameer M BARGIR

Nanoscale Investigations of Surface Phenomena in the Water Treatment Industry using  
the Atomic Force Microscope

SUPERVISORS:

Dr Steve Dunn  
Dr Bruce Jefferson  
September 2007

*This thesis is submitted in fulfilment of the requirements for the degree of Doctor of  
Philosophy*

©Cranfield University 2008. All rights reserved. No part of this publication may be  
reproduced without written consent of the copyright owner

## ABSTRACT

Understanding the interaction between surfaces at the intermolecular level in ambient conditions is not only a fundamental science, but is of increasing value to water treatment systems. Here the uses of the atomic force microscopy (AFM) modified with particles of interest are assessed, and compared to bench-scale experimental techniques. In the first part of this study, the results from force measurements performed with calcite-modified probes in synthetic hard water (SHW) on selected substrates showed there was no correlation with macroscale scaling rate experiments. However, unmodified tips showed some correlation with non-metal substrates, where carbon coatings (Dymon-iC and Graphit-iC) were least adhesive. Although unmodified tips were unlikely to represent one of the surfaces of interest in water treatment systems, the findings suggest they can be used to screen materials with  $R_a < 50$  nm. Contact angle measurements complemented force data, indicating the origin of repulsive forces on carbon coatings was due to hydrophilic repulsion because carbon and calcite were highly basic. Enhanced adhesion was caused by hydrophobic attraction and the presence of acidic surface groups. In the 2<sup>nd</sup> part of this study, force measurements were performed on natural organic matter (NOM) polyanions such as humic acid fraction (HAF), fulvic acid fraction (FAF) and hydrophilic acid (HPIA) using modified and unmodified tips. The results showed in symmetric NOM-NOM interactions with modified tips, HPIA-HPIA dominated both adhesion and detachment lengths, while FAF-FAF and HAF-HAF gave similar adhesion profiles. It is thought these intermolecular interactions can be transferred to floc size data, where HPIA flocs were bigger than FAF flocs. In non-symmetric systems adhesion between FAF-NOM was indiscriminate, compared to HAF and HPIA polyanions, indicating FAF polyanions were most likely to control coagulation performance during NOM removal.

## **ACKNOWLEDGMENTS**

I would like to thank my supervisors Dr Steve Dunn and Dr Bruce Jefferson for their assistance and support throughout the project. I would also like to thank Dr Rob Boyd for his assistance particularly during the 2<sup>nd</sup> half of my project. I also express my thanks to Christine Kimpton, Maxime Mergen, Dr Emma Goslan, Dr Peter Jarvis, Dr Spyros Ranil and Aurelien Moreaux for their help during the different parts of my studies. My thanks also go to the office and lab colleagues of building 39.

I would finally like to thank my family including my mum, dad, brother and sisters as well as my friends for their abundant support throughout the project.



## CONTENTS

<b>Table of Contents</b>	<b>v</b>
<b>List of Figures</b>	<b>x</b>
<b>List of Tables</b>	<b>xiv</b>
<b>List of Equations</b>	<b>xvii</b>
<b>Common Symbols</b>	<b>xix</b>
<b>Glossary of Terms</b>	<b>xxi</b>
<b>Chapter 1 Introduction .....</b>	<b>1</b>
1.1 Background and information.....	1
1.2 Motivation for work .....	1
1.3 Scope of study .....	2
1.4 Thesis plan.....	2
<b>Chapter 2 Literature Review.....</b>	<b>4</b>
2.1 The Atomic Force Microscope (AFM) .....	4
2.1.1 Basic Operating Principles .....	4
2.1.2 Imaging mode.....	5
2.1.3 Force-Displacement Mode .....	6
2.1.4 Uses of the AFM .....	7
2.1.5 Cantilever calibration .....	13
2.1.6 AFM contact mechanics.....	16
2.1.7 Affect of surface roughness.....	17
2.1.8 Use of modified tips .....	19
2.1.9 Methods of tip modification.....	20
2.1.10 Applications of tip modification .....	22
2.2 Application of the AFM to Water Treatment Systems .....	25
2.2.1 Scaling Systems.....	25
2.2.1.1 Theory of scale formation .....	25
2.2.1.2 Theory of surface charge.....	28
2.2.1.3 Application of the AFM to Scaling.....	29
2.2.2 Natural Organic Matter .....	31

2.2.2.1	Application of the AFM to NOM Characterization .....	33
2.2.2.1.1	Imaging Mode .....	33
2.2.2.1.2	Force-Displacement Mode .....	38
2.2.3	Biological Systems .....	42
2.2.3.1	Introduction .....	42
2.2.3.2	Applications of the AFM to biofouling and bacterial adhesion .....	42
<b>Chapter 3</b>	<b>Materials and Methods .....</b>	<b>45</b>
3.1	Chemicals, Solutions and Sample Preparation .....	45
3.1.1	Solid specimens .....	45
3.1.2	Summary of the water treatment works .....	47
3.1.3	Resin Preparation .....	48
3.1.4	Fractionation Procedure .....	49
3.1.5	NOM Fraction Immobilization .....	49
3.2	AFM tip modification .....	49
3.2.1	Tip modification in calcite chapter of work .....	50
3.2.1.1	Calcite-Attached (CA) Tips .....	50
3.2.1.2	Calcite Grown (CG) Tips .....	50
3.2.1.3	Calcite-Orientated (CO) Tips .....	51
3.2.2	Tip modification in NOM chapter of work .....	51
3.2.2.1	PLL-modified tips .....	51
3.2.2.2	Glycine-coated tips .....	51
3.2.2.3	NOM-Modified Tips .....	52
3.2.2.4	Resin Probes .....	52
3.2.2.5	NOM-Coated Resin Probes .....	52
3.3	Instrumentation .....	52
3.3.1	Contact Angle Apparatus .....	52
3.3.2	Scanning probe microscope .....	53
3.3.3	Cantilevers .....	54
3.3.4	Scanning Electron Microscope .....	54
3.3.5	pH meter .....	55
3.4	Analytical Techniques .....	55

3.4.1	Contact angle measurements and surface free energy calculation.....	55
3.4.2	AFM imaging.....	57
3.4.3	Force measurements.....	58
3.5	Laboratory Experiments.....	59
3.5.1	Calcite Adhesion Experiments.....	59
3.5.1.1	Effect of substrate material on adhesion .....	59
3.5.1.2	Effect of molar concentration on adhesion .....	59
3.5.1.3	Effect of solution pH on adhesion.....	59
3.5.1.4	Effect of calcite crystal orientation on adhesion .....	60
3.5.1.5	Effect of calcite surface defects on adhesion .....	60
3.5.1.6	Rapid scaling tests.....	60
3.5.2	NOM Experiments .....	60
<b>Chapter 4</b>	<b>Results and Discussion part 1 - Calcite Adhesion .....</b>	<b>63</b>
4.1	Substrate topography characterization .....	63
4.2	Contact angle measurements and surface free energy calculation.....	69
4.2.1	Calculation of $\gamma^{LW}$ (apolar) surface free energies .....	71
4.2.2	Calculation of $\gamma^+$ and $\gamma^-$ (polar) components using the graphical plot method.....	72
4.2.2.1	Use of liquid triplets.....	73
4.2.2.2	Use of multiple liquids.....	76
4.2.2.3	Comparison of the triplet average and sextet methods .....	77
4.2.3	Theoretical calculation of adhesion using roughness model.....	80
4.3	AFM force measurements .....	85
4.3.1	Adhesion force measurements in SHW .....	85
4.3.2	Adhesion force measurements in varying electrolyte concentration .....	90
4.3.3	Adhesion force measurements at different pH.....	95
4.3.4	Affect of calcite crystal roughness on adhesion.....	96
4.3.4.1	Use of unmodified tips .....	96
4.3.4.2	Use of modified tips .....	98
4.3.5	The effect of substrate surface properties/tip modification on adhesion .....	101

4.3.6	Link between theoretical and measured adhesion forces with scaling rate experiments .....	103
<b>Chapter 5 Results and Discussion part 2 - Surface Characterization of NOM.</b>		<b>109</b>
5.1	Introduction .....	109
5.2	Contact angle measurements .....	110
5.2.1	NOM surface free energy measurements .....	112
5.3	AFM force measurements .....	116
5.3.1	Silica probe versus NOM surface.....	116
5.3.1.1	Attractive forces .....	118
5.3.1.2	Adhesion forces.....	120
5.3.1.3	Pull-off length versus adhesion force.....	122
5.3.2	Silica/PLL probe versus NOM surface .....	127
5.3.2.1	Attractive forces .....	128
5.3.2.2	Adhesion forces.....	128
5.3.2.3	Pull-off length versus adhesion force.....	131
5.3.3	Silica/PLL/NOM probes versus NOM surface .....	134
5.3.3.1	Attractive forces .....	135
5.3.3.2	Adhesion forces.....	135
5.3.3.3	Pull-off length versus adhesion force.....	138
5.3.4	Silica/PLL/Glycine probes versus NOM surface.....	140
5.3.5	XAD4/XAD8/MIEX® probes versus NOM surface .....	142
5.3.6	Resin/NOM probes versus NOM surface.....	145
5.3.7	Interpretation of detachment signatures with AFM tips.....	147
5.3.8	Interpretation of detachment signatures in NOM-NOM systems .....	149
5.3.9	Comparison of tip-modification methods-NOM-coated tips vs. NOM-coated resins .....	151
5.3.10	Potential application of detachment signatures to NOM removal performance.....	151
5.3.10.1	Linking symmetric NOM interactions with floc properties.....	152
<b>Chapter 6 Overview Discussion .....</b>		<b>155</b>
6.1	Application of unmodified tips to water treatment systems.....	155

6.2	Application of modified tips to water treatment .....	157
<b>Chapter 7</b>	<b>Conclusions .....</b>	<b>160</b>
<b>Chapter 8</b>	<b>Future Work.....</b>	<b>164</b>
<b>Chapter 9</b>	<b>References .....</b>	<b>165</b>
<b>Chapter 10</b>	<b>Appendices .....</b>	<b>179</b>

# LIST OF FIGURES

## Chapter 2 Literature Review

Figure 2.1	Schematic of an AFM showing the main components of the AFM; the probe, piezoscanner, detection system and feedback mechanism.....	4
Figure 2.2	Schematic diagram of an ideal force-displacement curve showing the behaviour of the cantilever and its deflection during sections of the approach and retract cycle.....	6
Figure 2.3	Combination of vdW and EDL forces can be explained by DLVO theory, where A indicates the secondary minimum (Israelachvili, 1992).....	8
Figure 2.4	Force curve examples and subsequent force laws used to interpret them. Forces detected are (a) vdW, (b) adhesion, (c) electrostatic, (d) capillary, (e) brush, (f) polymer extension, (g) elastic and (h) binding forces. Modified from Heinz and Hoh, (1999). ....	10
Figure 2.5	(a) Deformation of an elastic sphere on a rigid surface during equilibrium following Hertz and JKR theory; (b) Elastic adhering about to separate spontaneously from adhesive contact during pull-off; and (c) Applicability of DMT model showing forces acting outside contact area. Where $a_{JKR}$ and $a_{HERTZ}$ are the contact radius following Hertz and JKR theories. Modified from Israelachvili (1992).....	16
Figure 2.6	Schematic illustration of the geometric model used by Rabinovich <i>et al.</i> , (2000) to calculate theoretical adhesion force (Permission obtained from Elsevier Press).....	18
Figure 2.7	Heterogeneous nucleation showing the three interfacial phases (Israelachvili, 1992). ....	26

## Chapter 3 Materials and Methods

Figure 3.1.	Digital images of the three monitors (a), the AFM stack locked into the stage (b) and the stage sitting on the hydraulic bench (c). ....	53
Figure 3.2.	Digital image of fluid cell (middle, 12 mm diameter) with protective skirt (left) and dry cantilever holder (right).....	54
Figure 3.3.	Digital photograph taken of water on a solid substrate, using Image Pro Plus® The Proven Solution™ software. ....	56

## Chapter 4 Results and Discussion part 1 - Calcite adhesion

Figure 4.1.	2D AFM topographic images of all substrates performed in DI water using contact mode imaging. ....	64
Figure 4.2.	3D AFM topographic images of group I and II materials performed in DI water using contact mode. Z-range of inset images are 1000 nm for comparative purposes unless stated otherwise. ....	67
Figure 4.3.	Measured contact angles of all materials using a total of six probe liquids. Contact angles are shown in order of their angle with B.....	70

Figure 4.4.	Linear plot to determine the Lewis acid and basic components of Dymon-iC (♦), Graphit-iC (□) and ‘used copper’ (Δ) with SD values. $(\gamma^-/\gamma^+)^{1/2}$ values of probe liquids are shown above the plot. ....	72
Figure 4.5.	Calculated $\gamma^+$ , (top) and $\gamma^-$ (bottom) SFE components of materials using the graphical plot method (McCafferty, 2002), obtained from four sets of triplets. *Used Copper gave $\gamma^+$ of $9.09 \pm 4.57 \text{ mJ.m}^{-2}$ for BWG triplet. (Cop = Copper; MFs = MF steel; RFs = RF steel, SBs = SB steel, K.C. = kettle coating, Dym = Dymon-iC). ....	74
Figure 4.6.	The calculated $\gamma^+$ (top) and $\gamma^-$ (below) values obtained using 3, 4, 5 and 6 liquids from the GP method. ....	77
Figure 4.7.	Comparison of the $\gamma^+$ and $\gamma^-$ components of selected group I and group II materials using the sextet and triplet methods (in $\text{mJ.m}^{-2}$ ). ....	78
Figure 4.8.	SEM images of unmodified (top) and modified (bottom) probes used during force measurements performed in SHW. ....	85
Figure 4.9.	Frequency distribution of force measurements on selected substrates using the UM (top) and CG (below) probes in SHW. ....	87
Figure 4.10.	Frequency distribution plots of all six probes on MF steel in varying electrolyte concentration and (below) showing approach (a) and retract (b) cycles using the CG1 probe at three different $\text{CaCO}_3$ concentrations. ....	92
Figure 4.11.	Schematic showing how the addition of a salt compresses the double layer (from (left to right), permitting closer contact on approach. ....	93
Figure 4.12.	Histogram showing the distribution of pull-off forces on (a) Dymon-iC and (b) MF steel. ....	95
Figure 4.13.	AFM deflection images of optically pure calcite {104} showing (a) flat calcite ( $50 \mu\text{m}^2$ ), (b) calcite with moderate surface roughness ( $15 \mu\text{m}^2$ ) and (c) calcite with single large defect ( $5 \mu\text{m}^2$ ). Numbers on images represent locations of force plots. ....	97
Figure 4.14.	Frequency distribution graph of force measurements on three calcite {104} surfaces with variations in surface defects using an unmodified tip. ....	97
Figure 4.15.	Scatter plot showing the distribution of adhesion forces at all 10 locations of the three calcite surfaces. ....	98
Figure 4.16.	Optical images of calcite probes with different levels of roughness (a-f) (6 probes consist of 2 rough, 2 intermediate and 2 flat calcite surfaces). Scale bar $30 \mu\text{m}$ . ....	99
Figure 4.17.	Column chart showing the pull-off (adh.) and attractive (att.) forces between modified tips with calcite faces and MF steel, Dymon-iC and mica substrates in SHW using six calcite probes with different surface roughness. Inset image shows the average adhesion from the two flat crystals because forces were too small. ....	100
Figure 4.18.	Column chart showing the measured attractive and adhesive forces selected group I and II materials using the rough-1 probe. ....	100
Figure 4.19.	Scatter plots of scaling rate vs. work of adhesion with all the materials using the triplet (left) and sextet (right) method. ....	104
Figure 4.20.	Schematic showing the affect of modified and unmodified tips on surfaces with different $R_a$ values relative to contact area. ....	107

## Chapter 5      **Results and Discussion part 2 - Surface characterization of immobilized NOM**

Figure 5.1.	Contact angle values of probe liquids on HAF, FAF and HPIA and glass and PLL control surfaces.....	110
Figure 5.2.	$\gamma^{LW}$ values of HAF, FAF and HPIA polyanions obtained from five water samples.....	112
Figure 5.3	Histograms showing the $\gamma^-$ surface free energy values (in $\text{mJ.m}^{-2}$ ) for the five NOM sources and PLL/glass controls. ....	113
Figure 5.4.	Histograms showing the $\gamma^+$ SFE values (in $\text{mJ.m}^{-2}$ ) for the five sources of HAF, FAF, HPIA and PLL/glass controls. ....	114
Figure 5.5	Force vs. separation approach and retraction cycles of a silica tip on HAF, HPIA, FAF polyanions and PLL.....	117
Figure 5.6	Schematic of three different configurations of polymer-tip interaction during force measurements on NOM (a) and PLL (b).....	118
Figure 5.7	Histogram showing the distribution plot of attractive forces with a silica tip (U1) on (a) HAF, (b) FAF and (c) HPIA from all five samples. ....	119
Figure 5.8	Histogram showing the distributions of adhesion peaks with probe U1 on HAF (a), FAF (b) and HPIA (c) from all five samples. ....	121
Figure 5.9	Scatter plot of pull-off length vs. pull-off force for (a) silica tip 1 and (b) silica tip 2 on NOM surfaces and PLL control. ....	123
Figure 5.10.	Column chart showing the distribution of forces at different locations of HPIA polyanions with both unmodified tips (U1 and U2). ....	126
Figure 5.11	Force vs. separation approach and retraction cycles using one PLL-coated tip on HAF, FAF, HPIA polyanions and PLL control. ....	127
Figure 5.12	Histogram showing the distribution plot of attractive forces with a PLL coated tip on HAF (a), FAF (b) and HPIA (c) from all five samples. ....	129
Figure 5.13	Histogram showing the distribution plot of peak adhesion forces with a PLL coated probe on HAF, FAF and HPIA from all five samples.....	130
Figure 5.14	Scatter plots of pull-off length vs. pull-off force using PLL-coated tips (a) and (b) on NOM surfaces and PLL control.....	132
Figure 5.15	Histogram showing the distribution plot of attractive forces with NOM-coated tips on HAF (a), FAF (b) and HPIA (c).....	136
Figure 5.16	Histogram showing distribution plots of adhesion forces with NOM-coated tips on HAF (a), FAF (b) and HPIA (c).....	137
Figure 5.17	Scatter plot of pull-off length vs. pull-off force of NOM-coated tips (columns) on NOM surfaces (rows) from Penwhirn reservoir. ....	139
Figure 5.18	Scatter plot of force vs. pull-off length for glycine-coated (left) and PLL (right) tips on polyanions from Penwhirn reservoir.....	141
Figure 5.19	Optical microscope images of AFM tips modified with XAD4, XAD8 and MIEX® resins showing side (top) and birds-eye views (bottom). Each image was a montage produced from images taken at different focal lengths. Software used to generate image was Auto-Montage (Synoptics Ltd, version 3.02.005). ....	142
Figure 5.20.	Scatter plot of force vs. pull-off length for three resin-attached probes (column) on three NOM polyanions (rows).....	144



Figure 5.21	Scatter plot of force vs. pull-off length for NOM-coated resin probes (2 x FAF, 2 x HAF and 1 x HPIA). .....	146
Figure 5.22.	Comparison of high MW (left) and low MW NOM polyanions showing increased contact area and interaction (highlighted) is prevalent with the high MW polyanions from Widdop and Gorple reservoirs. Diagram not to scale. ....	148
Figure 5.23	Schematic of pull-off interaction between HPIA-HPIA (left) and HAF-HAF/FAF-FAF systems showing longer lengths for HPIA than hydrophobics. Balls (right) indicate micellar structure of hydrophobic polyanions. Micelles are for illustrative purposes only.....	149
Figure 5.24	Scatter plots showing force vs. pull-off length of symmetric NOM systems. ....	152

# LIST OF TABLES

## Chapter 2 Literature Review

Table 2.1	Examples of some fundamental intra- and inter-molecular forces that occur between molecules or colloidal particles.....	7
Table 2.2	Summary of uses of the AFM to measure intermolecular forces using modified and unmodified tips. ....	12
Table 2.3	Summary of resonance and static loading methods used for measuring the spring constant (modified from Gibson <i>et al.</i> , (1996)). ....	13
Table 2.4	Summary of tip modification techniques used to perform force measurements. ....	21
Table 2.5	List of subject areas utilizing the AFM for force measurements, the systems used, linkage procedure, forces detected and information gained from the measurements. ....	23
Table 2.6	Summary of force measurements performed with modified and unmodified AFM tips with on inorganic surfaces.....	30
Table 2.7	Structural units found experimentally in humic acid from several sources. Modified from Mao <i>et al.</i> , (2001). ....	32
Table 2.8	Summary of NOM sources that were imaged using the AFM in tapping mode. ....	36
Table 2.9	Summary of force measurements performed with modified and unmodified AFM tips in NOM solution or using NOM-modified tips and their application.....	39

## Chapter 3 Materials and Methods

Table 3.1	A summary of solutions and various probe liquids used throughout the investigation. All the specified liquids except probe liquids for contact angle measurements were used during force measurements.....	46
Table 3.2.	Description of materials used for experiments (supplied by Model Products Ltd, Bedford, UK). Coatings were prepared by Teercoatings® on stainless steel substrates. Solid phase elemental analysis of MF steel and SB steel was performed using ESEM-EDX.....	47
Table 3.3.	A summary of experiments performed using the NOM (HAF, FAF and HPIA) fractions. All numbers in each box indicate the number of AFM tips used to perform the force measurements. W = water; HA/FA/HP indicate HAF, FAF and HPIA, respectively. PL indicates poly-L-lysine. ....	61

## Chapter 4 Results and Discussion part 1 - Calcite Adhesion

Table 4.1.	List of surface roughness values (Ra) of materials from lowest to highest and % surface area difference. R <sub>a</sub> values calculated from an average of five images of 25 x 25 µm.....	68
Table 4.2.	Surface free energies and their components (in mJm <sup>-2</sup> ) of commonly used probe liquids (Van Oss, 2003).....	69

Table 4.3.	Summary of $\gamma^{LW}$ surface free energy components of group I and group II materials. ....	71
Table 4.4.	Comparison of condition numbers of four triplets (McCafferty, 2002; Della Volpe and Siboni, 2000). ....	73
Table 4.5.	Calculated acid-base ( $\gamma^{AB}$ ) SFE values obtained from the average of four triplets. ....	75
Table 4.6.	Summary of advantages and disadvantages of using the triplet average and sextet methods for calculating material SFE values. ....	80
Table 4.7.	SFE values of calcite calculated from contact angle measurements on the calcite {104} face using B-W-E-F probe liquids, using the triplet average and four-liquid graphical method. Measured values are compared to literature. TLW = thin layer wicking. ....	81
Table 4.8.	List of Hamaker constants used in Equation 2.11 to predict the adhesion force based on the roughness model (Rabinovich <i>et al.</i> , 2000). ....	82
Table 4.9.	Summary of theoretical adhesion force between the AFM tip or calcite-coated tip and material substrates, calculated using equation 2.11. and comparing the percentage deviation with JKR/DMT theories. Calculations were based on liquid surface tension parameters obtained from Van Oss <i>et al.</i> , (1986). ....	83
Table 4.10.	Average pull-off forces of UM, CG and CA probes on all materials in SHW. ....	86
Table 4.11.	The affect of concentration on Debye length. Also shown is the pH of the solutions that were used. ....	91
Table 4.12.	Summary of trends observed for each material from modified (calcite-attached (CA) and calcite-grown (CG) and unmodified (UM) tips when electrolyte concentration was increased from 0.0005M to 0.001M. ....	91
Table 4.13.	Summary of Dymon-iC, Graphit-iC and MF steel (as reference) material rankings based on adhesion force using modified tips. Low = material in bottom 3 of all materials; Medium = material in middle 3 of materials; High = material in top 3 of materials. ....	103
Table 4.14.	Material scaling rates (in $\text{g CaCO}_3 \cdot \text{m}^{-2} \cdot \text{h}^{-1}$ ) after classification in group I and II materials. ....	104
Table 4.15:	Comparison of scaling rate (numbered from 1-12 low-high) and AFM/contact angle measurements based on material $R_a$ values. ....	106
<b>Chapter 5</b>	<b>Results and Discussion part 2 - Surface Characterization of immobilized NOM</b>	
Table 5.1	Summary of AFM force measurements performed using both modified and unmodified tips, and the motivation for performing such experiments ....	116
Table 5.2	Summary of pull-off lengths and adhesion forces on NOM sources with silica tips. ....	125
Table 5.3.	Summary of average pull-off lengths and peak adhesion forces on all four sources using PLL tips. ....	134

Table .5.4.	A summary comparing dominant polyanions using silica and PLL-coated tips. ....	147
Table 5.5.	Summary of parameters used to compare to AFM pull-off forces and pull-off lengths.....	152

# LIST OF EQUATIONS

## Chapter 2 Literature Review

$F = -kd$	Equation 2.1 .....	7
$k = \frac{Et^3w}{4l^3}$	Equation 2.2 .....	13
$k = (2\pi)^2 \frac{M}{(1/v_1^2) - (1/v_0^2)}$	Equation 2.3 .....	14
$k = 0.1906 p_f b L Q \Gamma_i(\omega_f) \omega_f^2$	Equation 2.4 .....	14
$k = k_m \left( \frac{L - \Delta L}{L} \right)^3$	Equation 2.5 .....	15
$M_t = M_m \left( \frac{L - \Delta L}{L} \right)^3$	Equation 2.6 .....	15
$k = \frac{8\pi R^3 \rho g}{3\Omega X}$	Equation 2.7 .....	15
$F = 1.5\pi R W_{132}$	Equation 2.8 .....	16
$F = 2\pi R W_{132}$	Equation 2.9 .....	17
$\mu = \frac{2.06}{z_0} \sqrt{\frac{R W_{132}^2}{\pi K^2}}$	Equation 2.10 .....	17
$F = \frac{AR}{6H_0^2} \left[ \frac{1}{1 + \frac{58R(rms_2)}{\lambda_2^2}} + \frac{1}{\left( 1 + \frac{58R(rms_1)}{\lambda_1^2} \right) \left( 1 + \frac{1.82rms_2}{H_0} \right)^2} \right]$	Equation 2.11 .....	18
$F = \frac{3\pi W R_1 r_2}{2(r_2 + R_1)} + \frac{(AR_t / 6H_0^2)}{\left( 1 + \frac{58rms_1}{\lambda_1^2} \right) \left( 1 + \frac{1.82rms_2}{H_0} \right)^2}$	Equation 2.12 .....	18
$\Delta G = 4\pi^2 \gamma_{13} - \frac{4}{3} \pi^3 \Delta G_V$	Equation 2.13 .....	26
$\Delta G_{crit} = \frac{4}{3} \pi^2 \gamma_{13}$	Equation 2.14 .....	26
$\Delta G'_{crit} = \Phi \Delta G_{crit}$	Equation 2.15 .....	26
$\Phi = \frac{(2 + \cos \theta)(1 - \cos \theta)^2}{4}$	Equation 2.16 .....	26
$\gamma_{13} \cos \theta = \gamma_{23} - \gamma_{12}$	Equation 2.17 .....	27

$$J^{het} = A' \exp\left(-\frac{\Delta G_{crit}}{k_B T}\right) \quad \text{Equation 2.18 ..... 27}$$

$$m_d = A' \exp\left[-\Phi \frac{16\pi}{3} \frac{\gamma_{13}^3 v^2}{k_B^3 T^3 \ln^2(c/c_s)}\right]. \quad \text{Equation 2.19 ..... 27}$$



### Chapter 3 Materials and Methods

$$\gamma_s^{LW} = \gamma_l \frac{(1 + \cos \theta)^2}{4} \quad \text{Equation 3.1 ..... 56}$$

$$\begin{bmatrix} (\gamma_{L1}^{LW})^{1/2} (\gamma_{L1}^-)^{1/2} (\gamma_{L1}^+)^{1/2} \\ (\gamma_{L2}^{LW})^{1/2} (\gamma_{L2}^-)^{1/2} (\gamma_{L2}^+)^{1/2} \\ (\gamma_{L3}^{LW})^{1/2} (\gamma_{L3}^-)^{1/2} (\gamma_{L3}^+)^{1/2} \end{bmatrix} \begin{bmatrix} (\gamma_s^{LW})^{1/2} \\ (\gamma_s^+)^{1/2} \\ (\gamma_s^-)^{1/2} \end{bmatrix} = 1/2 \begin{bmatrix} \gamma_{L1} (1 + \cos \theta_1) \\ \gamma_{L2} (1 + \cos \theta_2) \\ \gamma_{L3} (1 + \cos \theta_3) \end{bmatrix} \quad \text{Equation 3.2 ..... 56}$$

$$W_{sl} = \left( \gamma_l^{LW} + 2\sqrt{\gamma_l^+ \gamma_l^-} \right) (1 + \cos \theta) = 2 \left( \sqrt{\gamma_s^{LW} \gamma_l^{LW}} + \sqrt{\gamma_s^+ \gamma_l^-} + \sqrt{\gamma_s^- \gamma_l^+} \right) \dots\dots\dots \quad \text{Equation 3.3 ..... 57}$$

$$W_{132} = W_{12} + W_{33} - W_{13} - W_{23} \quad \text{Equation 3.4 ..... 57}$$

$$W_{132} = 2 \left[ \begin{aligned} & \sqrt{\gamma_1^{LW} \gamma_3^{LW}} + \sqrt{\gamma_2^{LW} \gamma_3^{LW}} - \sqrt{\gamma_1^{LW} \gamma_2^{LW}} - \gamma_3^{LW} \\ & + \sqrt{\gamma_3^+} \left( \sqrt{\gamma_1^-} + \sqrt{\gamma_2^-} - \sqrt{\gamma_3^-} \right) + \sqrt{\gamma_3^-} \left( \sqrt{\gamma_1^+} + \sqrt{\gamma_2^+} - \sqrt{\gamma_3^+} \right) \\ & - \sqrt{\gamma_1^+ \gamma_2^-} - \sqrt{\gamma_1^- \gamma_2^+} \end{aligned} \right] \quad \text{Equation 3.5 ..... 57}$$

## COMMON SYMBOLS

$\Delta G$	Gibbs free energy
$A$	Hamaker constant (J)
$A'$	Pre-exponential factor
$c$	Concentration
$D$	Distance between two surfaces (m)
$E$	Young's modulus ( $\text{N m}^{-2}$ )
$F$	Force (N)
$H_0$	Distance of closest approach of surfaces
$K$	Reduced Young's modulus
$k$	Spring constant ( $\text{N m}^{-1}$ )
$k_B$	Boltzmann's constant
$M$	Particle mass
$m_d$	Mass deposition ratio
$\rho_f$	Density of fluid
$Q$	Quality factor
$R$	Probe radius (m)
$t$	Cantilever thickness
$W$	Work of adhesion ( $\text{J.m}^{-2}$ )
$X$	Difference in cantilever deflection between rotated and non-rotated measurements
$z_0$	Equilibrium size of atoms in contact
$\gamma^-$	Electron-donating surface free energy
$\gamma$	Total surface free energy
$\gamma^+$	Electron-accepting surface free energy
$\gamma^{AB}$	Acid-base surface free energy
$\Gamma_i$	Imaginary component of the hydrodynamic function
$\gamma^{LW}$	Lifshitz-van der Waals surface free energy
$\theta$	Contact angle
$\lambda$	Wavelength
$\nu_0$	Resonant frequency of unmodified cantilever

$\nu_1$	Resonant frequency of modified cantilever
$\Omega$	Deflection calibration
$\omega_f$	Fundamental mode resonant frequency



## GLOSSARY OF TERMS

AFM	Atomic force microscopy
BSA	Bovine serum albumin
CA	Calcite-attached probe
CG	Calcite-grown probe
CML	Carboxylate-modified latex
CVD	Chemical vapour deposition
DBP	Disinfection by-products
DLC	Diamond-like-carbon
DLVO	Derjaguin B.V, Landau L. D, Verwey E. J. W and Overbeek J. T. theory of colloidal stability
DMSO	Dimethylsulfoxide
DMT	Derjaguin, Muller and Toporov theory
DOC	Dissolved organic carbon
DOPA	Dihydroxy-L-alanine
EDL	Electrical double layer
EDTA	Ethylenediaminetetraacetic acid
EPS	Extracellular polymer substance
ESEM	Environmental scanning electron microscope
EW	Electron-withdrawing
FAF	Fulvic acid fraction
F-D	Force displacement plot/curve
HAA	Haloacetic acids
HAF	Humic acid fraction
HB	Hydrophobic
HL	Hydrophilic
HPIA	Hydrophilic acid
HPINA	Hydrophilic non-acids
HPLC	High performance liquid chromatography
HPOA	Hydrophobic fractions

IEP	Isoelectric point
JKR	Johnson, Kendall and Robert theory
LPS	Lipopolysaccharide
LWAB	Lifshitz-van der Waals acid base theory
MIEX®	Magnetic Ion Exchange Resin ®
NOM	Natural organic matter
OTS	Octadecyltrichlorosilane
PAHA	Purified Aldrich Humic Acid
PBS	Phosphate buffered saline
PE-CVD	Plasma-enhanced chemical vapour deposition
PEI	Polyethyleneimine
PLL	Poly-L-lysine
PMMA	Polymethylmethacrylate
PTFE	Polytetrafluoroethylene
PZT	Lead Zirconate Titanate
R <sub>a</sub>	Roughness average (nm)
<i>rms</i>	Root mean square
RO	Reverse osmosis
SAM	Self-assembled monolayer
SDS	Sodium dodecyl sulphate
SEM	Scanning electron microscopy
SFE	Surface free energy
SHA	Suwannee River Humic Acid
SHW	Synthetic hard water
SPM	Scanning probe microscopy
SRNOM	Suwannee River NOM
THM	Trihalomethanes
TM-AFM	Tapping-mode AFM
UM	Unmodified AFM tip
vdW	van der Waals
UF	Ultrafiltration

WTW	Water treatment works
XAD	Ion-exchange resin

## Chapter 1

## Introduction

### 1.1 Background and information

Ever since the atomic force microscope (AFM) was invented by Binnig, Quate and Gerber in 1985 for which they received a Nobel prize the following year, it has become a highly versatile tool that can be used as a surface profiler (imaging mode) and for measuring ultra-small forces (Leite and Herrmann, 2005). The AFM has been applied to a number of natural and engineered surfaces which may be electrically conducting or insulating with application to water treatment (Considine *et al.*, 2002), biofouling (Wang *et al.*, 2004), drug delivery systems (Beach *et al.*, 2002), membrane cleaning (Bowen *et al.*, 2000), mineral flotation (Fa *et al.*, 2003) and many more. This is because standard AFM tips can be modified to widen the spectrum of materials under investigation, effectively making the study more relevant. As a result, modified tips are routinely used as a screening tool in applications such as membrane cleaning and colloidal systems (Bowen *et al.*, 2000; Adler *et al.*, 2001).

### 1.2 Motivation for work

The field of water treatment has recently come under challenges to develop novel methods of characterizing materials with optimal performance without using bench-scale apparatus that is not always feasible or practical. By modifying AFM tips, *in situ* operation conditions can be tailored at the sub-micron level. For instance, to determine a potential link between the macroscale scaling rate experiments at bench scale (performed by MacAdam, 2004) and their nanoscale interaction, force measurements were performed with modified and unmodified AFM tips. The AFM may also provide a platform for studying the interaction of fractionated Natural Organic Matter (NOM) polyanions, by quantifying detachment forces between organic polymers at the intermolecular level. To assess the interaction between NOM polyanions it was decided to modify AFM tips with NOM and other compounds such as poly-L-lysine (PLL) and glycine.

### 1.3 Scope of study

The focus was on using AFM tip modification techniques to measure interaction forces between calcite and a series of solid substrates in water, as well as measuring the forces between NOM from different geographical sources. For clarity the thesis is divided into three major parts:

1. Identifying a potential link between adhesion force and macroscale scaling rate experiments.
2. Analysis of AFM interaction forces from fractionated organic matter.
3. Overall benefits/drawbacks of AFM tip modification in water treatment systems.

### 1.4 Thesis plan

A literature review was carried out (Chapter 2) to determine what information could be gained from modifying AFM tips, problems of modification (and not modifying), and particular applications of tip modification to water treatment. In chapter 4 a total of thirteen materials were grouped into high energy (metals) and low energy (non-metals) surfaces, and were also characterized into their surface free energies using contact angle measurements. Contact angle techniques and the AFM were compared and a potential link to the macroscale bench-level experiments was scrutinized.

In the second part of the study, the AFM was used as a proof-of-concept study to explore detachment profiles of a series of NOM polyanions from four different sources (Albert water treatment works, Penwhirn water reservoir, Widdop and Lower Gorple reservoir) (Chapter 5). Detachment profiles will provide chemical signatures of polyanions, which might be related to their intramolecular and intermolecular interaction within flocs, their reactivity with disinfectants or simply their origin. The information gained may in future be used for developing innovative NOM removal strategies. AFM tips were modified with poly-L-lysine (Chapter 5, section 5.3.2), isolated NOM fractions (Chapter 5, section 5.3.3), glycine (Chapter 5, section 5.3.4), adsorbent resins (Chapter 5, section 5.3.5) and NOM-coated adsorbent resins (Chapter 5, section 5.3.6). Due to the polymeric nature of NOM polyanions, their reactivity was investigated by measuring polyanion pull-off length versus adhesion force. This required the use of a MATLAB program written by

Rob Boyd to measure fraction pull-off length vs. adhesion force. The analysis and findings from these experiments are also discussed in Chapter 5. In an attempt to discuss the application of AFM tip modification (Part 3) Chapter 6 gives an overview discussion of the above work. The conclusions drawn are provided in Chapter 7.

In an attempt to answer the final part of the project scope, the findings from this investigation showed AFM tip modification can be a simple and effective procedure but the analysis of force data can be highly complicated when (a) contact area is unknown, (b) robustness of the modified tip is in question and (c) the anchoring particle is a highly complex organic molecule. However, the benefits associated with tip modification tend to outweigh the above drawbacks, and this was apparent from using NOM-modified probes, where adhesion forces correlated with macroscale floc size experiments.

## Chapter 2

## Literature Review

### 2.1 The Atomic Force Microscope (AFM)

#### 2.1.1 Basic Operating Principles

The four main hardware components that are common in all AFM systems are the cantilever consisting of the probe tip, a piezoelectric scanner, a detection mechanism and feedback electronics including the AFM software (Figure 2.1). The terms cantilever, probe and tip are used interchangeably by many AFM users but all are, in fact, very different. The ‘tip’ is the only potential ‘atomic’ part that directly interacts with the sample, which is mounted to and supported by the ‘cantilever’, that is sometimes visible to the naked eye. Both these parts constitute a unified ‘probe’. The piezoscanner is usually a cylindrical tube containing a piezoelectric material that expands and contracts in a defined way when an electric field is applied across the material, known as the piezoelectric effect (Colton *et al.*, 2001).

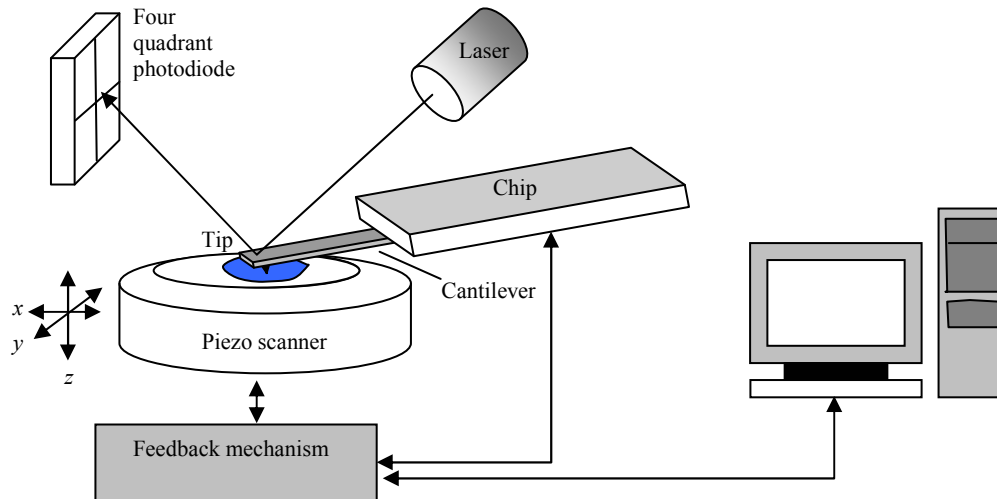


**Figure 2.1** Schematic of an AFM showing the main components of the AFM; the probe, piezoscanner, detection system and feedback mechanism.

Piezoelectric materials used in AFM systems are usually ceramics based on lead, zirconium and titanium oxides (PZT) due to their strong piezoelectric effect. PZT belong to this family of perovskites. Most AFM systems use the transverse piezoelectric effect, where the applied electric field  $E$  is perpendicular to the direction of

expansion/contraction. Piezo translators based on the transverse piezoelectric effect have a wide range of sensitivities. For large sample scanners the piezo tube itself has separate electrodes for X, Y and Z that are driven by separate circuits to scan precisely in the x-y plane in a raster pattern and also in the z direction.

The detection mechanism is based on an optical lever technique, where an optical beam is focussed on the cantilever and reflected onto a position-sensitive photodiode detector (Figure. 2.1). As the cantilever experiences a force, it bends and displacement of the beam on the photodiode is proportional to the applied force. The final critical element to AFM systems is the feedback system, which is designed to keep the tip-sample interaction constant.

### **2.1.2 Imaging mode**

To generate an image, the tip is brought in close proximity to the sample and then raster scanned, causing the cantilever to deflect due to changes in surface topography or surface forces. There are several imaging modes of which two are most widely used; contact mode and tapping mode. The forces acting on the tip and sample vary depending on the operating mode and imaging conditions.

In contact mode AFM the tip is essentially dragged across the sample and constant cantilever deflection is maintained by a feedback loop that moves the scanner vertically at each lateral data point to produce the topographic image (Shi and Zhao, 2004). High contact stresses make this mode suitable for rigid materials such as crystals and other inorganic materials, while imaging in water overcomes the adverse capillary forces due to adsorbed moisture. During tapping mode, the cantilever is oscillated at its resonant frequency and amplitude of 20 to 200 nm. The feedback system is set to detect any change on oscillation amplitude or phase caused by momentary contact with the surface during each oscillation cycle. The advantage of tapping mode is that it operates at lower compressive forces than during contact mode, and it eliminates lateral and shear forces that may damage soft samples (Henderson, 1994).



### 2.1.3 Force-Displacement Mode

During force-displacement (F-D) mode the AFM is used as a force-sensing device, lowering the tip toward the surface and then retracting the tip to detect interaction forces. A schematic of the corresponding force distance curve generated from a single cycle is shown in Figure 2.2 (not drawn to scale).

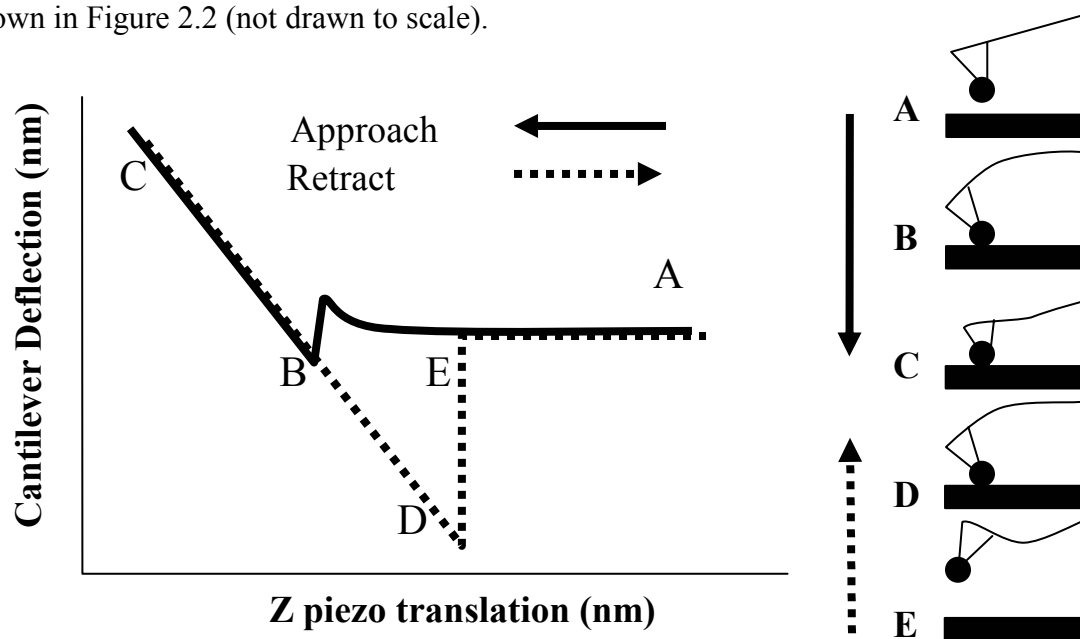


**Figure 2.2** Schematic diagram of an ideal force-displacement curve showing the behaviour of the cantilever and its deflection during sections of the approach and retract cycle.

The force distance curve shows the vertical cantilever deflection vs. lever sample displacement. The displacement is effectively measured between the sample and the firmly held back end of the cantilever. A useful way to consider the force profile is the simple ‘ball on a weak spring model’, which is shown on the right of Figure 2.2 (Heinz and Hoh, 1999). During the approach cycle the tip is lowered (A) and prior to contact there is an initial repulsion due to hydration forces in liquids followed by a sudden attraction to the surface (point B), thus signifying a negative (attractive) force. This force may be of van der Waals (vdW), electrostatic or other origin. Jump-to events result when the gradient of attractive forces exceeds the cantilever spring constant and any electrostatic repulsive forces that arise when water molecules are squeezed out (Senden and Ducker, 1994). As the piezoscaner continues to expand the cantilever bends upwards (region B-C) and Born hard-sphere repulsion dominates as the tip is drawn into the sample producing the diagonal line, known as the constant compliance region. The

displacement direction is then reversed at a time chosen by the user (region C). Upon retraction (i.e. moving right in plot), the force becomes negative and the cantilever continues to move with the surface as adhesion maintains contact until the spring constant exceeds maximum adhesion (or ‘pull-off’) force. As it reaches the lowest point in the force curve, the tip loses contact and the cycle is complete (D-E). Notice that the distances and forces are not drawn to scale. The resulting adhesion force (N) is calculated using *Hooke’s law*:

$$F = -kd \quad \text{Equation 2.1}$$

Where  $k$  is the cantilever spring constant ( $\text{N/m}^{-1}$ ) and  $d$  is the cantilever deflection (in m). Methods of calculating the spring constant are shown in section 2.1.5.

#### 2.1.4 Uses of the AFM

The AFM is primarily used to study interaction forces. Therefore, a basic understanding of forces acquired between the tip and sample is essential for effective force data analysis. The major forces that come into play between the tip and the sample are summarised in Table 2.1.

**Table 2.1** Examples of some fundamental intra- and inter-molecular forces that occur between molecules or colloidal particles.

Type of force		Energy (kJ/mol)	Range (nm)	Estimated force (nN)	Reference
Molecular	Intramolecular (ionic or covalent)	200-800	0.1-0.2	1-15 (single bond)	Beyer & Clausen-Schaumann (2005)
	H-bonding	10-40	0.5 to 3	1-10	Israelachvili, (1992)
	Dipoles	~100s	0.5 to 3	10-20	-
Colloidal	Electrostatic	10 to 100	10s to 100s	-	Drelich <i>et al.</i> , (2004)
	van der Waals	1 to 5	5 to 10	10-20	Goodman and Garcia, (1991)
	Solvation/Hydration	1 to 10	< 5	-	Drelich <i>et al.</i> , (2004)
	Hydrophobic	-8.4 to -11.3	10s to 100s	-	Butt <i>et al.</i> , (2005)
	Capillary	-	10s to 1000s	100	Finot <i>et al.</i> , (2001)

The covalent or ionic bonds are by far the strongest, ranging around  $500 \text{ kJ.mol}^{-1}$  for the Au-Au bond. This is compared to  $1\text{-}15 \text{ kJ mol}^{-1}$ , for the vdW ‘bond’. Goodman and Garcia (1991) used the AFM to measure vdW forces in the region of 10 to 20 nN. The

relatively weak vdW forces are quantum mechanical in nature, non-localized and present in both neutral and charged molecules. Attractive vdW forces are electrostatic, arising from the dipole field of an atom or molecule which is induced by the neighbouring atom or molecule that essentially becomes polarised due to this field (Israelachvili, 1992). For this reason they are the longest range non-covalent force (Van Oss, 2003).

When a surface is immersed in liquid, electrical double-layer (EDL) forces arise due to electrostatic forces, which may be attractive or repulsive. Because water has a high dielectric constant surfaces become charged due to ionization or dissociation of surface groups, or by adsorption of ions (Israelachvili, 1992). Surface charge is balanced by dissolved counterions which are attracted back to the surface by the ensuing electric field. EDL forces decay exponentially with distance as a function of the diffuse ionic double layer. Therefore, changes in electrolyte concentration and pH can have a significant effect on interaction forces (attractive and adhesion) (Freitas *et al.*, 2001).

Total interaction ( $V_{TOT}$ ) of attractive vdW and repulsive EDL forces is described by DLVO (Derjaguin and Landau, Verwey and Overbeek) theory (Filip *et al.*, 2005). The combined action of these two forces is shown schematically in Figure 2.3 using the assumption repulsive potentials are positive and attractive potentials are negative.

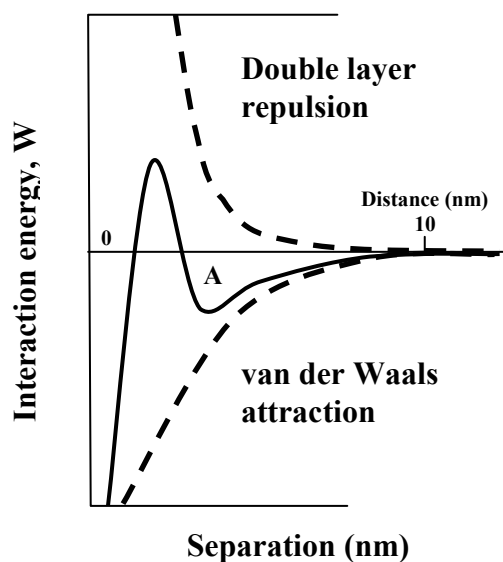


**Figure 2.3** Combination of vdW and EDL forces can be explained by DLVO theory, where A indicates the secondary minimum (Israelachvili, 1992).

There is a possibility of a ‘secondary minimum’ at high electrolyte concentration, where a weaker and potentially reversible adhesion occurs between particles (Figure 2.3). Freitas *et al.*, (2001) performed force measurements with glass particles in varying electrolyte concentration. They showed good agreement in hydrophilic systems with DLVO theory at relatively large separation.

When interacting particles or surfaces are within a few nanometres non-DLVO forces come into play that are much stronger than DLVO forces. In hydrophilic systems hydrogen bonds occur both intermolecularly and intramolecularly, and at 10-40 kJ.mol<sup>-1</sup> are much stronger than the average vdW ‘bond’ (Israelachvili, 1992). There has been extensive research using the AFM to measure H-bonds between numerous functional groups (Vezenov *et al.*, 2005).

Figure 2.4 shows a selection of forces measured with the AFM and the force laws used to interpret them. For instance attractive and retractive cycles during the vdW interaction are shown in Figure 2.4a, b. Although capillary forces dominate in air they are eliminated in liquid and vacuum environments (Figure 2.4d). Figure 2.4f shows elongated pull-off events during polymer-pulling and steric interactions (non-DLVO forces). Abrupt jumps during the retraction cycle indicate unwinding or detachment of sections of the polymer. For example, this was observed by Sander *et al.*, (2004) with adsorbed Suwannee humic acid (SHA, a highly complex organic molecule) on alumina surfaces at pH~6. Bowen and Doneva, (2000) performed colloidal force measurements with solid substrates and found non-DLVO forces were dominant when double layer effects were present.

Extended DLVO theory considers hydrophobic/hydrophilic interactions (described by Van Oss (2003) as acid-base forces) as well as osmotic forces that have been known to play an important role in polar media. Hydrophobic forces develop because water around hydrophobic surfaces is structured, and strong attraction can be measured (Nalaskowski *et al.*, 2003). Brant *et al.*, (2006) performed force measurements on membrane surfaces and found extended DLVO theory agreed with force measurements in hydrophilic

systems. The authors also found both DLVO and extended DLVO predictions agreed with hydrophobic force measurements.

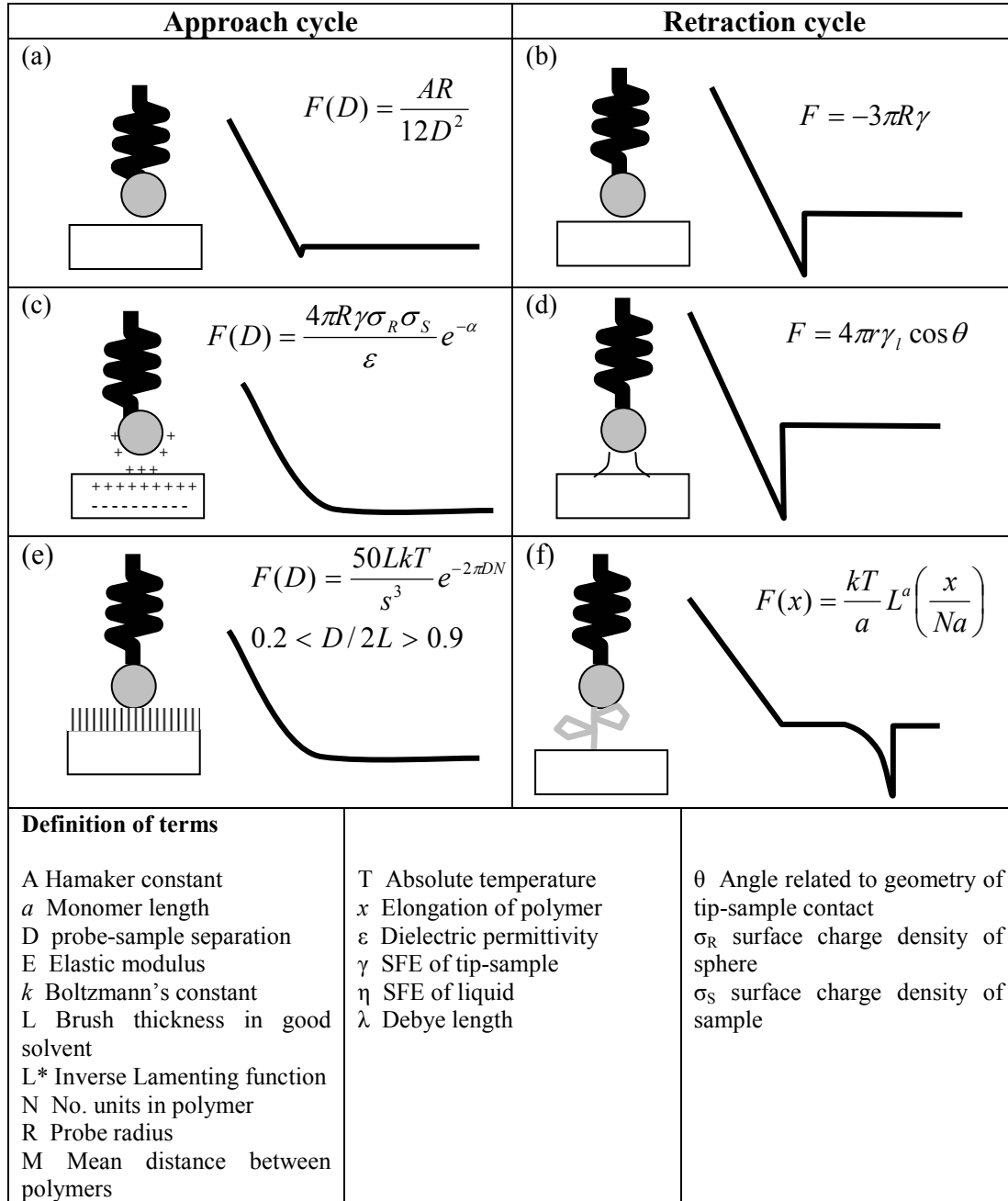


**Figure 2.4** Force curve examples and subsequent force laws used to interpret them. Forces detected are (a) vdW, (b) adhesion, (c) electrostatic, (d) capillary, (e) brush, (f) polymer extension, (g) elastic and (h) binding forces. Modified from Heinz and Hoh, (1999).

Table 2.2 gives a summary of force measurements performed with modified and unmodified tips to measure forces given in Table 2.1. Methods of tip modification are described in section 2.1.6. A more extensive analysis of force measurements in aqueous solution is given by Butt *et al.*, (1995), Van Oss (2003) and Liu *et al.*, (2005).

Table 2.2 Summary of uses of the AFM to measure intermolecular forces using modified and unmodified tips.

Type of force	Range (nm)	Bond/Tip information	Application	Information gained	Reference
Intramolecular (ionic or covalent)	< 1	A biotinylated cell physically glued to Si <sub>3</sub> N <sub>4</sub> tip	Adhesion mechanism of Cell-cell adhesion, Cellular motility Single molecule force spectroscopy	Results suggest that N-cadherin and E-cadherin molecules form homophilic bonds between juxtaposed cells that have significantly different kinetic and micromechanical properties.	Panorchan <i>et al.</i> , (2006)
H-bonding	0.5 to 3	-COOH/NH <sub>2</sub> /CH <sub>3</sub> /Unmodified tip	Signal transduction; Membrane assembly; Protein chemistry	Forces between COOH, CH <sub>3</sub> and OH groups found to be chemically specific	Vezenov <i>et al.</i> , (2005)
Dipoles Ion-dipole	0.5 to 3	COO-Ca <sup>2+</sup> tip and CH <sub>3</sub> /OH/ CONHCH <sub>3</sub> surface	Pharmaceuticals	Interaction was strong between COOCa-OH due to ion-dipole interaction Adhesion in order CH <sub>3</sub> <CONHCH <sub>3</sub> <OH	Morales-Cruz <i>et al.</i> , (2005)
Electrostatic	10s to 100s	Si-Si in presence and absence of copper	Colloidal stabilization in natural and engineered systems	Used to explain aggregation, deposition and transport of colloidal particles under unfavourable chemical conditions	Taboada-Serrano <i>et al.</i> , (2005).
van der Waals	1 to 10	Diamond-Diamond	Nanomechanical properties	Strong attractive van der Waals forces due to nitrogen atmosphere.	Burnham and Colton, (1989)
Hydrophobic	10s to 100s	Polyethylene and SiO <sub>2</sub> in water	Cleanup of contaminated soil	Hydrophobicity of silica causes increase in adhesion force between polyethylene and SiO <sub>2</sub>	Nalaskowski <i>et al.</i> , (2003)

### 2.1.5 Cantilever calibration

The ability to experimentally determine the spring constant of AFM, cantilevers is of fundamental importance in force-sensitive applications. For rectangular cantilevers, the spring constant (in  $\text{N m}^{-1}$ ) can be calculated simply from the material properties of an end-loaded cantilever :

$$k = \frac{Et^3w}{4l^3} \quad \text{Equation 2.2}$$

Where  $E$  is the Young's modulus,  $t$  is the thickness,  $l$  is the length and  $w$  is the width of the cantilever (Cleveland *et al.*, 1993). However, accurate determination of  $t$  which is considerably smaller than the width and length for which  $k$  is dependent to the third power, is extremely difficult. Furthermore, the Young's modulus compositional consistencies may be grossly inaccurate for silicon nitride tips ranging from  $\text{Si}_3\text{N}_4$  to  $\text{Si}_{15}\text{N}_4$ . For the above reasons, spring constants are measured manually, and several methods are available and listed in Table 2.3.

**Table 2.3** Summary of resonance and static loading methods used for measuring the spring constant (modified from Gibson *et al.*, (1996)).

	Resonance methods			Static loading methods		
	Cleveland <i>et al.</i> , (1993)	Hutter and Bechhoefer, (1993)	Sader <i>et al.</i> , (1999)	Senden and Ducker, (1994)	Butt <i>et al.</i> , (1993)	Li <i>et al.</i> , (1993)
	A	B	C	D	E	F
Principles	Force vs. load	Shape of resonance curve vs. thermal noise spectrum	Relates cantilever dimensions, resonance frequency and quality factor	Deflection vs. load $\mu\text{m}$ spheres	Deflection vs. load pendulum	Deflection vs. load glass fibres
Claimed accuracy	~10%	10-20%	~10-15%	~15%	30-40%	15-20%
Userfriendliness	Poor	Good	Good	Poor	Poor	Poor
Complications	Sphere placement/ Glue affects $k$	Temperature variations low $k$ only	None	System calibration Sphere placement	Combined deflection of system	Needs $k$ of standard loading point
Potential destructiveness	High	Low	Low	High	Medium	Low

The methods given in Table 2.3 claim accuracies ranging from 10-40% but some are typically more user-friendly than others. Generally, the resonance methods such as that



given by Hutter and Bechhoefer (1993) (B in Table 2,3) give better accuracies than the static loading methods, are also less destructive and require less equipment. Furthermore, the static loading methods place high demands on the dexterity and experience of the user.

Of the resonance methods, Cleveland *et al.*, (1993) (hereafter referred to as the Cleveland method) gives one of the best accuracies for beam-shaped cantilevers (~10%) (Table 2.3). This method is based on a decrease in the resonant frequency of the modified cantilever as the mass on the beam is increased, thus decreasing the spring constant;

$$k = (2\pi)^2 \frac{M}{(1/v_1^2) - (1/v_0^2)} \quad \text{Equation 2.3}$$

Where  $v_0$  and  $v_1$  are the resonant frequencies of the unmodified and modified cantilevers and  $M$  is the particle mass. However, the problem with this technique is the sphere placement and quantity/placement of adhesive could have a significant affect on the resonant frequency. Nonetheless, it is routinely used in the majority of AFM studies (McNamee *et al.*, 2004)

Sader *et al.*, (1999) proposed the use of an unloaded resonance technique, which entailed measurement of the unloaded resonance frequency, the quality factor of the fundamental mode of vibration and the plan view dimension. The spring constant is given by:

$$k = 0.1906 p_f b L Q \Gamma_i(\omega_f) \omega_f^2 \quad \text{Equation 2.4}$$

Where  $p_f$  is the density of the fluid (given as 1.18 kg/m<sup>3</sup> for air),  $b$  and  $L$  is the width and length of the cantilever, respectively,  $Q$  is the quality factor,  $\Gamma_i$  is the imaginary component of the hydrodynamic function and  $\omega_f$  the fundamental mode resonant frequency.  $\Gamma_i$  is dependent on the Reynolds number  $Re = p_f(2\pi v) \omega_f^2/4\eta$ , where  $\eta$  is the viscosity of the surrounding medium. Unlike the Cleveland method this technique eliminates the need to measure the mass of a particle. Furthermore, good accuracies were claimed by the author for cantilevers with an aspect ratio ( $L/b$ ) of 3.3 to 13.7, which were used in the present study. When 100-200  $\mu\text{m}$  cantilevers were tested by Sader *et al.*, (1999) and compared to the Cleveland method, there was a ~1% variation.

More recently, Green *et al.*, (2004) applied a correction to the *Cleveland* method due to difficulties in placing the particle at the end of a tip-less cantilever. The modification took account of the distance the particle is placed away ( $\Delta L$ ) from the tip:

$$k = k_m \left( \frac{L - \Delta L}{L} \right)^3 \quad \text{Equation 2.5}$$

Where  $k_m$  is the measured spring constant. The effect of the mass on the resonant frequency would therefore be:

$$M_t = M_m \left( \frac{L - \Delta L}{L} \right)^3 \quad \text{Equation 2.6}$$

Where  $M_t$  is the mass of the test mass and  $M_m$  is the measured test mass.

Using a static loading method Senden and Ducker (1994) measured the static deflection of a cantilever under the force of a known end mass. Deflection was measured after attaching tungsten beads and again after turning the cantilever upside down to give the spring constant:

$$k = \frac{8\pi R^3 \rho g}{3\Omega X} \quad \text{Equation 2.7}$$

Where  $\Omega$  is the deflection calibration,  $g$  is the acceleration due to gravity,  $\rho$  is the density,  $R$  is the radius of the spheres and  $X$  is the difference in cantilever deflection between the rotated and non-rotated measurements. This method has been reported as being very poor due to the increased risk of breaking the cantilever when turning the cantilever upside down after adding a test mass (Gibson *et al.*, 1996).

When Gibson *et al.*, (2005) compared Sader and Cleveland methods for rectangular cantilevers up to 203  $\mu\text{m}$  in length both produced near identical spring constants. As a result, it was decided to use the Cleveland method as this only required measuring the resonant frequency of the unloaded and loaded cantilever, and not the cantilever dimensions, which can vary between cantilevers from the same batch.

### 2.1.6 AFM contact mechanics

In order to describe fundamental adhesion forces quantitatively, some approximating models are used. The interaction between an AFM tip and surface are based on the Hertzian theory (developed in 1881) of contact mechanics (Shi and Zhao, 2004). Currently, two theoretical models are used to describe contact between a sphere and flat surface; Johnson, Kendall and Robert (1971) theory (JKR) and Derjaguin, Muller and Toporov theory (DMT) (1975). The JKR approach is confined to forces inside the contact area, and is based on the expression:

$$F = 1.5\pi RW_{132} \quad \text{Equation 2.8}$$

where  $W_{132}$  is the work of adhesion (in  $\text{J}\cdot\text{m}^{-2}$ ). Calculation of the  $W_{132}$  is described in section 3.4.1. The JKR model is applied to adhesion between a large elastic sphere and surface, and as a result the theory behaves hysteretically because during unloading a ‘neck’ links the tip and sample (Figure 2.5b) (Cappella and Dietler, 1999).

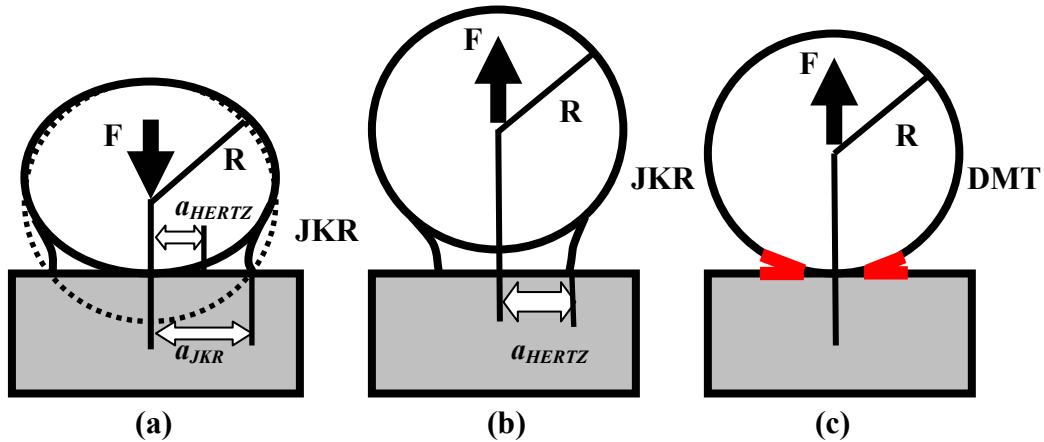


**Figure 2.5** (a) Deformation of an elastic sphere on a rigid surface during equilibrium following Hertz and JKR theory; (b) Elastic adhering about to separate spontaneously from adhesive contact during pull-off; and (c) Applicability of DMT model showing forces acting outside contact area. Where  $a_{JKR}$  and  $a_{HERTZ}$  are the contact radius following Hertz and JKR theories. Modified from Israelachvili (1992).

In contrast, the DMT model regards long-range contact forces acting along the contact area perimeter (highlighted in Figure 2.5c), which is appropriate for rigid solids of small radii (Drelich *et al.*, 2004). The effect is an additional probe-sample attraction that prevents elastic repulsive forces (unlike JKR theory), and predicts a slightly higher force:

$$F = 2\pi RW_{132} \quad \text{Equation 2.9}$$

Unfortunately, it still remains unclear which model to apply, although Maugis (1992) analysed both models and suggested a transition between the two models can be applied using the dimensionless parameter  $\mu$ ,

$$\mu = \frac{2.06}{z_0} \sqrt{\frac{RW_{132}^2}{\pi K^2}} \quad \text{Equation 2.10}$$

Where  $K$  is the reduced Young's modulus and  $z_0$  is the equilibrium size of the atoms at contact. The significance of  $\mu$  has been interpreted as the ratio of elastic deformation resulting from adhesion to the effective range of surface forces (Shi and Zhao, 2004). When  $\mu \geq 5$ , JKR theory is used, otherwise DMT theory is applied if  $\mu \leq 0.1$  (Drelich *et al.*, 2004). In light of the Maugis-Dugdale theory (1992), discrepancies on the appropriate selection of contact theories still remain (Jacquot and Takadom, 2001; Leite and Herrmann, 2005), and in the next section it will be shown how surface roughness can further complicate calculation of theoretical adhesion forces.

### 2.1.7 Affect of surface roughness

Real surfaces are rough which can limit the practical application of JKR and DMT models. In a study by Heim *et al.*, (2002), it was determined that force measurements were much lower than expected from JKR and DMT theories. It was not until imaging that surface roughness was found to play a key role. In another study Leite and Herrmann, (2005) measured 13% variation in force measurements taken on a single location of atomically smooth mica. In another study by Hodges *et al.*, (2002) they found asperities as small as 1 to 2 nm affected adhesion. All these studies show surface roughness effects could not be ignored.

The first systematic study for surface roughness effects on adhesion between elastic bodies was conducted by Fuller and Tabor in 1976 (Leite and Herrmann, 2005; Tabor, 1977). The study found asperity height distribution was a major factor during adhesion between rough surfaces. Based on asperity height distribution, Rabinovich *et al.*, (2000a,b) modelled surface roughness by incorporating the mean peak to peak distance

between neighbouring asperities and the root mean square (rms) roughness of the substrate (Figure 2.6). The model describes two sets of asperities having a large or short wavelength ( $\lambda_1$  and  $\lambda_2$ , respectively), each exhibiting a different level of surface roughness. Accordingly, larger wavelengths consist of large asperities ( $r_1$ ) while the shorter wavelengths consist of smaller asperities.

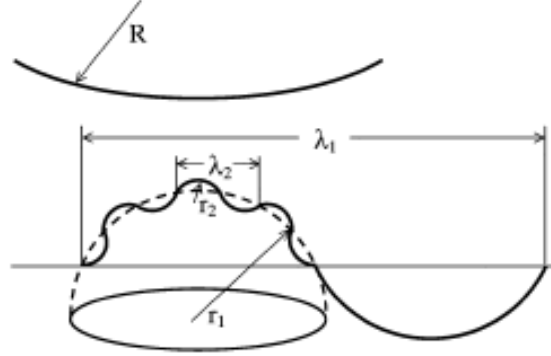


**Figure 2.6** Schematic illustration of the geometric model used by Rabinovich *et al.*, (2000) to calculate theoretical adhesion force (Permission obtained from Elsevier Press).

The two asperity scales are characterized by having  $rms_1$  and  $rms_2$  values, and can both be determined experimentally from roughness profiles. Rabinovich *et al.*, (2000a,b) applied two approaches for modelling the adhesion force, the vdW approach (equation 2.11) and the surface energy approach (equation 2.12).

$$F = \frac{AR}{6H_0^2} \left[ \frac{1}{1 + \frac{58R(rms_2)}{\lambda_2^2}} + \frac{1}{\left(1 + \frac{58R(rms_1)}{\lambda_1^2}\right) \left(1 + \frac{1.82rms_2}{H_0}\right)^2} \right] \quad \text{Equation 2.11}$$

$$F = \frac{3\pi WR_1 r_2}{2(r_2 + R_1)} + \frac{(AR_t / 6H_0^2)}{\left(1 + \frac{58rms_1}{\lambda_1^2}\right) \left(1 + \frac{1.82rms_2}{H_0}\right)^2} \quad \text{Equation 2.12}$$

Where  $R_t$  is probe tip radius, and  $r_2$  and  $r_1$  are the radii small and large asperities, respectively, having a long-range roughness,  $\lambda_1$ .  $H_0$  and  $A$  is the distance of closest approach and Hamaker constant, respectively. The vdW approach was used by Beach *et al.*, (2002) using irregular shaped pharmaceutical particles of beclamethasone propionate exhibiting high levels of microroughness. The authors found the model predicted accurate

adhesion forces between the silanized glass particle on a flat surface but underestimated adhesion with peptide and polystyrene particles by an order of magnitude. The anomaly was attributed to the deformation of the peptide material and polystyrene particles, and their poor representation by the Rabinovich model.

Drelich *et al.*, (2004) applied the Rabinovich model to measure the interaction between silanized glass probes in contact with polypropylene substrates with random roughness levels. The results gave an average theoretical work of adhesion of  $\sim 50 \text{ mJm}^{-2}$  with the surface energy approach (Equation 2.12), compared to the experimental value of  $55 \text{ mJm}^{-2}$ . This agreed well with the roughness model. This study and that by Beach *et al.*, (2002) indicate the roughness model may not be suitable for surfaces having a complex geometry in the microscale.

From an industrial point of view, utilizing smooth particles that are free from surface asperities are impractical. However, to reduce surface roughness effects between rigid bodies, the probe must be larger than asperities on the probe and surface. For this reason probes modified with rigid microparticles reduce surface roughness effects compared to unmodified tips. Otherwise, force measurements should be analysed using a suitable theoretical model, and to date the Rabinovich (2000) roughness model appears to be the most appropriate for application to rigid particles.

### **2.1.8 Use of modified tips**

Conventional cantilevers are only manufactured from  $\text{SiO}_2$  or  $\text{Si}_3\text{N}_4$ , therefore AFM tips must be modified to widen the spectrum of materials to be studied. In addition, tip modification overcomes some of the problems associated with unmodified tips as modified tips often use well-defined spherical particles (1-100  $\mu\text{m}$ ). As a result, they can also be modelled using existing contact mechanics theories (Kappl and Butt, 2002). The first probe modification technique was applied by Ducker *et al.*, (1991) and became known as the colloidal probe technique, which was the benchmark for driving new applications towards force microscopy.

### 2.1.9 Methods of tip modification

There are several ways of modifying AFM tips of which two were used in this study. In the first method a two-part epoxy resin is used to attach silica microparticles, crystals or particles coated with the material of interest (Liu *et al.*, 2005). Commonly used resins are Epicote 1004®, Loctite® glass bond or Araldite®. Once the resin is transferred to the cantilever, the microparticle is attached to the resin with a micromanipulator. This technique was used most often in the present study, and a summary of this technique and its applications is given in Table 2.4. The other linkage procedure is the physical adsorption method, where an adhesion promoter such as poly-L-lysine (positively-charged) is used to adsorb the particle of interest, which must convey a negative charge for successive functionalisation. Other techniques such as self-assembled monolayers (SAM's) and mechanical fixation were not used in this study (Table 2.4).

Table 2.4 Summary of tip modification techniques used to perform force measurements.

Tip modification method	Linkage procedure/equipment required	Advantages	Disadvantages	Substances linked to tip/cantilever	Reference
<b>Epoxy</b>	Two part epoxy resin such as Epon R 1004f (Shell Chemicals Co.) and micromanipulator/ No special conditions	Simple and fast No pre-treatment required Good for large particles, both spherical and non-spherical. Can be used in tandem with physical adsorption.	Epoxy can affect spring constant. Effectiveness depends on dexterity of user.	Colloids, crystals, Coated colloids	Sander <i>et al.</i> , (2004); Liu <i>et al.</i> , (2005); Dunn <i>et al.</i> , (2004); Finot <i>et al.</i> , (2001)
<b>Physical adsorption</b>	Adsorbents like poly-L-lysine, Poly(ethyleneimine) required. Micromanipulator. Glutaraldehyde (optional) to strengthen bond.	Simple preparation Suitable for biopolymers Less destructive than epoxy method. Can be used in tandem with epoxy	Bonding procedure not as strong as epoxy or SAM's Adsorbent can affect properties of bacteria/biomolecules Particle could detach during force measurements.	Polymers such as PEG, Biopolymers Cells BSA Proteins	Tanaka <i>et al.</i> , (1994); Wang <i>et al.</i> , (2004); Ong <i>et al.</i> , (1999); Lower <i>et al.</i> , (2000); Pasche <i>et al.</i> , (2005)
<b>SAM's/covalent bond</b>	Chrome/nickel and gold or gold-coated probes Incubation of probes in SAMs solution such as 16-mercaptohexadecanol overnight SAMs probe immersed in desired solution for immobilization	Covalent bond is stronger than adsorption method. Polymers are stably attached to tip for up to 40,000 force curves. Suitable for single bond force microscopy	Special coating procedure required Long procedure Limited to particle size	Functional groups ranging from OH, COOH, CH <sub>3</sub> , NH <sub>2</sub> . Biopolymers such as BSA, living and dead cells	Vezenov <i>et al.</i> , (2005); Wang <i>et al.</i> , (2004); Friedsam <i>et al.</i> , (2004).
<b>Mechanical fixation</b>	AFM tip scanned over particle of interest to mechanically trap them onto tip	No sample preparation required	Poor reproducibility Contact area not defined Only suitable for soft elastic samples such as dead cells or biopolymers Procedure can contaminate cantilever Highly damaging to substance	Humic acid Dead cells Soft biopolymers	Plaschke <i>et al.</i> , (2000); Vadiello-Rodriguez <i>et al.</i> , (2005)



**2.1.10 Applications of tip modification**

A summary of the subject areas, the interactions studied, linkage procedure, forces measured and the information gained from the force measurements is shown in Table 2.5. A majority of the subject areas use epoxy as the linkage procedure because the colloidal probe is more applicable to these fields.

**Table 2.5** List of subject areas utilizing the AFM for force measurements, the systems used, linkage procedure, forces detected and information gained from the measurements.

Application	Particle of interest/ tip radius	Linkage procedure	Forces measured	Information gained	Reference
<b>Water treatment</b>	Glass beads adhesion to oocysts 2µm (bead size)	Epoxy	Double layer repulsion Van der Waals Steric repulsion	Repulsive forces always exist between surfaces in a range of conditions. Addition of DOC compressed hairy layer. Reduction in decay length accompanied by reduction in adhesion	Considine <i>et al.</i> , (2002)
<b>Bacterial infection and biofouling of implanted materials</b>	Bovine serum albumin (BSA) Not given	SAMs	Receptor-ligand base pairs Van der Waals Electrostatic Hydrophobic Steric forces	Greatest pull-off observed with BSA and OH group. Smaller pull-off forces with CH <sub>3</sub> , COOH and NH <sub>2</sub> Hydrophobic interactions play no role in BSA adhesion.	Wang <i>et al.</i> , (2004)
<b>Biosensors and implants</b>	PEG-Nb <sub>2</sub> O <sub>5</sub> surfaces 4-5µm	Adsorption	Electrostatic Steric	Highlights importance of ionic- strength-dependent minimum PEG layer thickness for screening electrostatic interactions of charged surfaces.	Pasche <i>et al.</i> , (2005)
<b>Composites/ Microelectronic s</b>	Silica-Teflon	Epoxy	Electrostatic Van der Waals	Range and strength of attractive interactions are reduced by the addition of KOH.	Drechsler <i>et al.</i> , (2004)
<b>Colloidal stability Coatings</b>	Glass-Glass	Epoxy	Non-DLVO forces Steric forces	Van der Waals attraction originating from a thin gel layer the addition stability and coagulation behaviour of silica.	Adler <i>et al.</i> , (2001)
<b>Drug delivery systems</b>	Beclomethasone propionate and rough polymers 10µm (nominal diameter)	Epoxy	Van der Waals	Surface roughness was dominant factor in measured pull-off forces. Irregular particles made contact at more than one point. Contact area critical for effective drug delivery	Beach <i>et al.</i> , (2002).

<b>Membrane cleaning</b>	Silica-AFC99 membrane interaction in NaCl solutions 4.2µm	Epoxy	Electrical double layer	Adhesion at membrane peak using silica colloid probe was much smaller than membrane valleys by up to a factor of 20. Double layer repulsion was reduced at peaks compared to valleys. Colloid probe imaging also made locations of peaks and valleys possible. Adhesion at peaks and valleys decrease with decreasing salt concentration.	Bowen and Doneva, (2000)
<b>Tablet manufacturer</b>	Salbutamol-Highly orientated pyrolytic graphite	Epoxy (Loctite)	Van der Waals	A lower force per unit area was observed for the SEDS™ materials, and this was possibly due to the surface free energy. AFM was effective for distinguishing between particles from different manufacturing techniques.	Hooton <i>et al.</i> , (2003)
<b>Flotation</b>	Silica particles and air bubble	Epoxy	Van der Waals Hydrophobic force	Hydroxylation of silica particles increased adhesion force to liquid bubbles. Hydrophilic particles were not adhesive or attractive to air bubble.	Fielden <i>et al.</i> , (1996)
	Calcium diolate sphere - calcite/fluorite surfaces. 14µm	Epoxy	Electrostatic	Fluorite found to demonstrate excellent flotation behaviour, as demonstrated by stronger adhesion forces by a factor of 50 compared to calcite.	Fa <i>et al.</i> , (2003)
<b>Marine Biofouling</b>	Silica spheres and <i>Mytilus edulis</i> foot protein	Epoxy	Electrostatic Steric repulsion	Ionic concentration of environment within mussel byssus may be tailored to achieve maximum adhesion and minimum curing time.	Frank and Belfort, (2002)

## **2.2 Application of the AFM to Water Treatment Systems**

### **2.2.1 Scaling Systems**

The accumulation of scale deposits is an extensive problem in domestic and industrial plants that include shower heads, kettles, water cooling systems and processing equipment. Scale acts as an insulator on heat transfer surfaces and reduces the heat transfer coefficient and the product's life expectancy. For instance, a 2 mm layer of scale can reduce heat transfer efficiency by up to 47% (Cosslett, 2001). Calcium carbonate ( $\text{CaCO}_3$ ) is the common scale-forming mineral of which calcite is the primary stable polymorph that is deposited as the initial conditioning layer (MacAdam, 2005). Extensive research has shown scaling to be a two-stage process, with the first period identified as the 'induction period' and the second period known as the 'fouling period' (Karabelas, 2002).

#### **2.2.1.1 Theory of scale formation**

During the induction period a small amount of scale (in inorganic particulate fouling) accumulates on the surface without significantly affecting material performance. Although the quantity of scale formed is small, it is enough to condition the surface and enable a thin layer of scale to form. It is this conditioned layer which is succeeded by the 'fouling period', an overall decrease in the performance of the system. The induction period, while often neglected, offers much potential for mitigating fouling and is the focus of this section.

The formation of a conditioning layer during the induction period is a balance between the deposition and removal of material at the interface between the solid and liquid (Förster and Bohnet, 1999). The deposition process is classically viewed as a heterogeneous nucleation process, where foreign bodies or impurities act as nucleation sites. The energetics of heterogeneous nucleation is described as a modification of homogeneous nucleation to account for the different interfaces and precipitation processes (Stefanescu, 1990). The energetics of cluster formation in homogeneous nucleation is expressed in terms of a surface and volume contribution:

$$\Delta G = 4\pi r^2 \gamma_{13} - \frac{4}{3} \pi r^3 \Delta G_v \quad \text{Equation 2.13}$$

Where  $\Delta G$  is the net free energy change,  $r^2$  is the radius of the nuclei squared,  $\gamma_{13}$  is the interfacial tension between the solid (subscript 1) and liquid (subscript 2),  $r^3$  is the volume of the nuclei and  $\Delta G_v$  is the free energy of transformation per unit volume. Differences in the dependency on radius of the nuclei provide an activation barrier for nucleation,  $\Delta G_{crit}$  that corresponds to a minimum stable nucleus size,  $r_{crit}$ , as given by:

$$\Delta G_{crit} = \frac{4}{3} \pi r_{crit}^2 \gamma_{13} \quad \text{Equation 2.14}$$

During heterogeneous nucleation foreign bodies such as walls or impurities act to promote crystallization by lowering  $\Delta G_{crit}$ , such that:

$$\Delta G'_{crit} = \Phi \Delta G_{crit} \quad \text{Equation 2.15}$$

Where the correction (or shape) factor ( $\Phi$ ), ranges from zero to unity depending on the affinity of the nucleus to the surface. Volmer (Förster and Bohnet, 1999) shows:

$$\Phi = \frac{(2 + \cos \theta)(1 - \cos \theta)^2}{4} \quad \text{Equation 2.16}$$

Where  $\theta$  is the contact angle between the crystalline deposit and the surface. This angle corresponds to the wetting angle in liquid/solid/vapour systems, and is given special attention. Assuming the nucleus takes the form of a hemispherical cap, the nuclei will grow depending on the substrate surface properties, and the points of contact between the three interfacial phases (Figure 2.7).

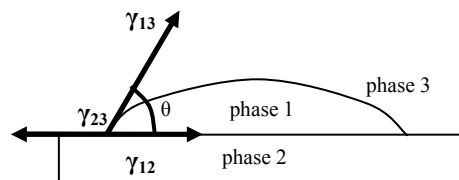


**Figure 2.7** Heterogeneous nucleation showing the three interfacial phases (Israelachvili, 1992).

Where each of the subscripts in the three interfacial phases ( $\gamma_{12}$ ,  $\gamma_{13}$  and  $\gamma_{23}$ ) is designated: phase 1 is the adhesive (or foulant), phase 2 is the surface and phase 3 is the liquid. Since the  $\gamma_{23}$  free energy interface can be determined from contact angle measurements, resolving the forces in the horizontal direction in Figure 2.7 we get:

$$\gamma_{13} \cos \theta = \gamma_{23} - \gamma_{12} \quad \text{Equation 2.17}$$

Also known as Young's equation, where  $\theta$  is the contact angle between a probe liquid with known surface tension and a solid surface. The methodology used to calculate the surface free energy of the interfacial ( $\gamma_{xy}$ ) and solid ( $\gamma_2$ ) phases is given in section 3.4.1. The relationship between the critical number of nuclei formed per unit time and volume (rate of nucleation) can be written based on the Arrhenius equation: (Förster and Bohnet, 1999):

$$J^{het} = A' \exp\left(-\frac{\Delta G_{crit}}{k_B T}\right) \quad \text{Equation 2.18}$$

Where  $A'$  is the pre-exponential factor and  $k_B$  is the Boltzmann constant. The rate of nucleation is proportional to the mass deposition ratio ( $m_d$ ) during the induction period:

$$m_d = A' \exp\left[-\Phi \frac{16\pi}{3} \frac{\gamma_{13}^3 v^2}{k_B^3 T^3 \ln^2(c/c_s)}\right]. \quad \text{Equation 2.19}$$

With  $v$  the molecular volume,  $c$  and  $c_s$  is the concentration of precipitating material at the bulk and surface, respectively. The above equation provides a link between the mass deposition rate  $m_d$  and the correction (or shape) factor  $\Phi$ . Therefore, by using Young's equation (Eq. 2.17), this shows variation of the interfacial free energy provides one method of modifying  $m_d$ . As the interfacial free energy ( $\gamma_{12}$ ) is directly influenced by the surface free energy of the heat transfer surface ( $\gamma_2$ ), modifying the surface provides an alternative route for prolonging the induction period during fouling (Hasson *et al.*, 2003; Förster *et al.*, 1999 and Yang *et al.*, 2002).

Numerous research efforts that have focussed on the effect of surface roughness (Keysar *et al.*, 1994; Muller-Steinhagen, 2000; Doyle *et al.*, 2002; MacAdam, 2005) and substrate surface free energy (Förster *et al.*, 1999; Hasson *et al.*, 2003) on fouling. Many attempts

have also been made to produce low adhesive surfaces, which include coatings such as Teflon (PTFE), ceramics and diamond-like carbons (DLC). However, such coatings have low thermal conductivities so they must be thin enough to permit heat transfer but thick enough to withstand the mechanical stresses of heat transfer.

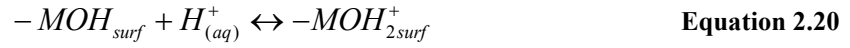
In a recent study by Zhao *et al.*, (2005b), the surface free energy of fluorinated DLC coatings were compared and linked to  $\text{CaSO}_4$  deposition rate. The authors found  $\text{CaSO}_4$  deposition was lowest when  $\gamma^{\text{LW}}$  (dispersive component) surface free energy of fluorinated DLC was reduced to  $29 \text{ mJ.m}^{-2}$ . In addition, the authors found high deposition rates on untreated stainless steel heater at  $2.9 \text{ g/cm}^3$  compared to  $1.1 \text{ g/cm}^3$  for fluorinated DLC coatings.

Bornhorst *et al.*, (1999) found DLC-sputtered surfaces were less likely to foul (using  $\text{CaSO}_4$ ), and scale deposits were thinner and easier to remove than untreated stainless steel. More importantly, the heat transfer coefficient remained unaffected with DLC. In an attempt to link the surface free energy with the low adhesion of  $\text{CaSO}_4$  to DLC, the authors estimated the high contact angle with water was responsible for low  $\text{CaSO}_4$  deposition rate.

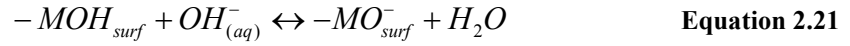
### 2.2.1.2 Theory of surface charge

Among the three non-covalent forces acting in aqueous media, Lifshitz-van der Waals, Lewis acid-base (or electron-acceptor/electron donor) and electrical double layer force, the acid-base forces are by far the dominant ones (Van Oss, 2003). Therefore, understanding the acid-base properties of oxide covered metals is paramount because these forces have been shown to represent 90% of all non-covalent interactions in water (Grasso *et al.*, 2002). Oxide-covered metals (where M is any metal) immersed in water terminate in an outermost layer of hydroxyl groups (M-OH), and they will remain undissociated as long as the pH of the solution is the same as the isoelectric point (IEP) of the metal oxide (Barthes-Labrousse, 2002). This is where the surface carries no net electrical charge, with equal numbers of  $\text{H}^+$  or  $\text{OH}^-$  or other charged anion/cation

adsorbed on the surface. If the pH is less than the isoelectric point, the surface will carry a positive surface charge,



If the pH is more than the IEP, the surface will acquire a negative charge,



or



In the above example,  $-MOH_2^{+}$  is the electron acceptor, while  $-MO^{-}$  is the electron donor. Hence, the hydroxylated oxide layer can become a Lewis acid or base depending on the pH of the medium. McCafferty (2001) determined the IEP of several metal oxides by measuring the contact angles at the hexadecane/aqueous solution interface as a function of the pH of the aqueous phase. The author found the IEP of several metal oxides including  $SiO_2$ ,  $Al_2O_3$ ,  $ZnO$  and  $Cr_2O_3$  was 2, 9.2, 10 and 5.2, respectively. McCafferty (2001) observed the adhesion force (pull-off) of a basic polymer (poly(methyl methacrylate) (PMMA) was strongest on acidic oxide films, with the acidic polymer (pressure-sensitive adhesive) more adhesive (peel force) to basic oxide films. These findings indicate Lewis acid-base forces dominate adhesive forces in an aqueous environment.

### 2.2.1.3 Application of the AFM to Scaling

The use of the AFM in force-displacement mode with modified and unmodified tips with application to scaling mitigation has been seldom performed. However, in the first study of its kind, Finot *et al.*, (1999), gypsum ( $CaSO_4 \cdot 6H_2O$ ) crystal adhesion was performed using the AFM in air. With their well-defined shape, different crystal faces of gypsum were orientated and mounted on an AFM cantilever. Adhesion between different crystal faces showed there was a strong preference of the (-101) crystal face for the other crystal faces due to the negatively-charged surface (Finot *et al.*, 1999). Although the motivation of the study was not directly linked to gypsum scaling, the possibility of studying crystal



adhesion with a common scale-forming mineral (e.g. calcite) using the AFM is of fundamental interest. In the same year, Dunn *et al.*, (2004) used the AFM to measure forces with an unmodified tip and several substrates in DI water. When adhesion forces were plotted against scaling rate a preliminary trend between adhesion force and struvite ( $\text{MgNH}_4\text{PO}_4 \cdot 6\text{H}_2\text{O}$ ) scaling rate was observed, indicating surfaces with greater struvite scaling rates produced stronger adhesive forces. These findings were also confirmed using a modified struvite probe on PTFE and PMMA, in agreement with bench-scale experiments. Although the cantilever was not calibrated, deflection data showed the higher scaling material of PTFE produced stronger deflection.

A summary of these experiments are listed in Table 2.6.

**Table 2.6** Summary of force measurements performed with modified and unmodified AFM tips with on inorganic surfaces.

Application		Forces detected	Tip modification method + calibration	Tip interaction and conditions	Information gained	Reference
Force-displacement mode	Scaling	Electrostatic vdW	Epoxy resin (modified tip not calibrated)	$\text{SiO}_2$ -metals/polymers Struvite-Polymers in DI water and ionic solution	PTFE and stainless steel were more adhesive to $\text{SiO}_2$ tip. PTFE also adhesive to struvite	Dunn <i>et al.</i> , (2004)
	Crystal adhesion during plaster hardening (non-scaling)	Electrostatic Capillary vdW	Epoxy resin	$\text{SiO}_2$ -gypsum gypsum-gypsum in relative humidity ranging from 10-35% Faces (010), (120) and (101) tested.	Three forces on crystal faces distinguished. Face (101) was electrostatically more adhesive than others.	Finot <i>et al.</i> , (1999)
	Geochemical properties of calcite	vdW Electrostatic	Unmodified	$\text{SiO}_2$ -calcite	Adhesion as strongest at above and below isoelectric point of calcite	Churchill <i>et al.</i> , (2004)

### 2.2.2 Natural Organic Matter

Natural organic matter (NOM) is a ubiquitous mixture of organic material in natural waters that has a profound effect on many hydrobiogeochemical processes (Zbytniewski and Buszewski, 2005). NOM is microbially (autochthonous) or terrestrially derived (allochthonous, from animals, plants and soil matter), and is the commonest organic pollutant in source waters. NOM-rich waters are costly to treat because of increased demand for coagulants, activated carbon, disinfectants, and increased frequency of membrane cleaning. Structurally, NOM is poorly defined because its chemistry is dictated by the chemical conditions of the source water. And although harmless in its native form, NOM reacts with chlorine to produce potentially carcinogenic disinfection by-products (DBPs) such as chloroform, bromoform and dibromochloromethane (Panyapinyopol *et al.*, 2005).

NOM removal by coagulation using trivalent ions such as  $\text{Fe}^{3+}$  and  $\text{Al}^{3+}$  are well established at water treatment works (WTW) (Goslan, 2003). Several mechanisms govern coagulation such as (a) charge neutralisation, (b) charge complexation/precipitation and (c) adsorption onto OH species (Murray, 2005). Coagulation of NOM is strongly influenced by interparticle forces that depend on coagulant concentration, promoting the formation of strong aggregates (or flocs) that are resistant to breakage giving greater settling rates that are subsequently easier to remove. However, recently there has been an increase in fragile flocs that break into smaller flocs with poor removal rates, which was found to be due to a characteristic change in NOM chemistry. For instance, when NOM was fractionated by commercial ion-exchange (XAD) resins into hydrophobic and hydrophilic parts, it was found increasing levels of the highly charged fulvic acid fraction (FAF) exerted the most influence on shrinking raw water flocs (Sharp *et al.*, 2006).

Hydrophobic components of NOM consist of humic acid (HA) and fulvic acid (FA) fractions while hydrophilic acid (HPIA) and hydrophilic non-acids (HPINA) comprise the major hydrophilic components. Hydrophobic acids account for approximately 50% of the dissolved organic carbon (DOC) (Owen *et al.*, 1995), although their chemical

character varies with source. Following fractionation, fractions can be analysed using a range of analytical techniques, ranging from pyrolysis mass spectrometry (Mertig *et al.*, 1999), ultrafiltration (Mertig *et al.*, 1999), solid-state  $^{13}\text{C}$  NMR (Mao *et al.*, 2001) (Zbytniewski and Buszewski, 2005), fluorescence spectroscopy (Klapper *et al.*, 2002) differential scanning potentiometry (Campitelli *et al.*, 2006), atomic force microscopy (Guan *et al.*, 2006; Liu *et al.*, 2000) and classical chemical and spectroscopic techniques. Reported molecular weights vary from 500-100 000 Da (Thurman, 1985), and the size may vary from several nm to several  $\mu\text{m}$  depending on solution pH, concentration and ionic strength (Guan *et al.*, 2006).

Although the molecular structures of humic acids remain unknown, the functional groups and chemical composition are becoming increasingly well characterized (Christy and Egeberg, 2000). One of the main properties of humic acids is its large buffering capacity at a wide pH range, due to the presence of acidic functional groups. There is general consensus that the carboxylic acid functionality dominates the humic acid structure, followed by phenolic-OH and enolic groups, giving HA overall a negative charge (Campitelli *et al.*, 2006). Imides and amines are also present to some extent. Additional functionalities include aromatic C-H, aliphatic C-H and alicyclic C-H, quinines and tetrahydrofurans (Table 2.7) amongst the main three (Mao *et al.*, 2001).

**Table 2.7** Structural units found experimentally in humic acid from several sources. Modified from Mao *et al.*, (2001).

Brief description of chemical groups identified
Phenols, quinines, aliphatic links; many OH groups
2 aromatic rings, 1 tetrahydro-furan ring, $\text{CH}_3$ on side groups
4 mainly aromatic blocks
Aromatic rings linked by long alkyl chains; $\text{COOH}$ and $\text{OH}$
Di- or tri-hydroxyphenol rings bridged by $\text{O}$ , $(\text{CH}_2)_n$ $\text{NH}$ , $\text{N}$
Aliphatic and aromatic rings with nucleus and peripheral parts
Linked aromatic, phenolic, or quinonic rings

Adsorption kinetics of purified Aldrich humic acid (PAHA) (a reference standard representative of humic acid) on hydrophilic and hydrophobic surfaces using reflectometry have shown that carboxylic acid and phenolic groups are exposed to the outside of HA molecules (Avena and Koopal, 1999). They found that at hydrophobic

sites, attachment took place through hydrophobic attachment, which required HA molecules to rearrange themselves in order to expose the hydrophobic groups. As pH was increased, the charge on PAHA increased without affecting the hydrophobic polystyrene surface. Attachment rates of PAHA to hydrophilic surfaces (Fe and Al oxides) were fast due to the presence of surface hydroxyl groups (Avena and Koopal, 1999).

### **2.2.2.1 Application of the AFM to NOM Characterization**

#### **2.2.2.1.1 Imaging Mode**

Although other in-situ techniques such as imaging X-ray (synchrotron) microscopy are providing detailed images of NOM (Namjesnik-Dejanovic and Maurice, 2001), AFM currently provides the highest resolution for adsorbed structures. Indeed, X-ray (synchrotron) microscopy and AFM are complementary, and show that surface NOM conformations are often similar to conformations in solution. However, the AFM allows visualization of NOM colloids during aggregation, adsorption or other morphological changes affected by the interaction of ions. More recently, the AFM was used to characterize the surface topography and sorption kinetics of different NOM components, particularly hydrophobic humic and fulvic acids (Maurice and Namjesnik-Dejanovic, 1999).

The AFM was the first technique to show how NOM adsorbs in the form of globular aggregates on mineral surfaces, and not as monolayers (Maurice and Namjesnik-Dejanovic, 1999). Furthermore, changes in pH, ionic concentration and NOM concentration during AFM imaging indicated the NOM conformation could be modified to produce spherical, ring-shaped and linear structures that were sensitive to the solution chemistry (Namjesnik-Dejanovic and Maurice, 2001). This was because humic acid comprised of mainly carboxylic and phenolic acid groups that were naturally oxidized, giving the surface a negative charge (Avena and Koopal, 1999). The addition of monovalent and divalent ions to the solution results in the formation of coordination complexes between acidic groups of humic substances (Jada *et al.*, 2006).

Several authors have also used the AFM to measure the dimensions of immobilised NOM fractions in aqueous solution, which are listed in Table 2.8. Imaging of humic and fulvic acid fractions has only been performed due to the lack of research of low molecular weight of hydrophilic acid (HPIA and HPINA) fractions. Although hydrophilic fractions can be removed to some extent, their role in environment is yet to be learned. Tapping mode AFM (TM-AFM) was recently used by Balnois *et al.*, (1999) who obtained HA from Suwannee river (a standard humic acid solution) and measured heights ranging from 0.5-2 nm at different ionic strengths. Guan *et al.*, (2006) also performed TM-AFM on PAHA, and found the size of humic substances increased with decreasing pH. They also found the length and diameter of humic aggregates decreased considerably between pH 5 and 6, which was partly due to the intermolecular charge effect between HA molecules. Several studies have substantiated these findings. For instance, Alvarez-Puebla *et al.*, (2004) reported size variation from 50-300 nm of gray humic acid when the pH was reduced from 9 to 1.5 (Mertig *et al.*, 1999).

Some of the more fascinating structures were observed by Namjesnik-Dejanovic and Maurice (2001) at relatively high NOM concentration using soil fulvic acid (FA) (approaching 100 mg C/L) at pH 5, in CaCl<sub>2</sub> on mica. Under these conditions, the authors observed sorbed fulvic acid had formed ring-shaped aggregates with diameters on the scale of tens of nanometres. This structure may be caused by the hydrophilic ends of a single molecule/linear aggregate coming together to lower the energetics of this unfavourable configuration (Israelachvili, 1992). Rigid globular structures are favoured at low pH, although the linear structure appears less favoured. Spheres, aggregated branches and perforated sheets were also observed at high concentration (Maurice and Namjesnik-Dejanovic, 1999). Some of the chain-like and sheet-like features observed by Maurice and Namjesnik-Dejanovic (1999) were consistent with the complex nature of the hydrophobic core and hydrophilic terminal (Droppo, 2005).

The majority of TM-AFM images of humic substances were performed on mica due to their preference for mineral adsorption through OH complexation (Feng *et al.*, 2005). As a result conformations and aggregates of humics/fulvics given in Table 2.8 may

potentially be influenced by mineral surface properties. Furthermore, questions remain over the affect of imaging artefacts. Consequently, immobilization of NOM fractions on different substrates will invariably have an effect on NOM conformation, which may not reflect their configuration in bulk water. As the fulvic acid fraction is poorly removed during coagulation, studies on different fulvic acid sources will provide an indication of why some FA fractions are removed more easily than others. In addition, this can be compared to the humic acid fraction which exhibits a very high removal rate.

Table 2.8 Summary of NOM sources that were imaged using the AFM in tapping mode.

Reference	NOM source	Imaging conditions	Adsorbed NOM shape	Mean x-y (nm, STD)	Mean height (nm,STD)	Substrate
(Namjesnik-Dejanovic and Maurice, 2001)]	Stream FA	pH 3 0.1 M LiCl, 25 mgC/L	Spheres	3.4±1.0	0.6±0.2	mica
	FA	pH 3, 0.001 M CaCl <sub>2</sub> , 20-100 mgC/L	Spheres	12.2±3.3	0.6±0.2	
		pH 5, 0.1M CaCl <sub>2</sub> , < 100 mgC/L	Ring-shaped aggregates	49±10	1.3±0.7	
		pH 6, 0.03M CaCl <sub>2</sub> , 75 mgC/L	Oblate -spherical aggregates	78±13	3.5±1.7	
		pH 8, 0.001M CaCl <sub>2</sub> , 100 mgC/L	Linear aggregates	53±21 (width)	3.9±1.4	
	Muck FA	pH 11 adjusted with NaOH, no additional electrolytes, 50 mgC/L	Fine-linear features	6.4±1.9 width	1.5±0.6	mica
	Ground water NOM	pH 4, no electrolyte added (naturally high Fe and Al***), 27 mgC/L	Globular or toroidal aggregates	300-1000	-	Hematite
Mertig <i>et al.</i> , (1999)	Spin-coated peat HA	pH 4.2-11.3, 0.02 mg/ml Height reduced with increasing pH	Globular appearance	1.5-3.5	1.5-3.77	Mica
Balnois <i>et al.</i> , (1999)	Suwannee river peat HA	pH > 5, 500mM NaCl, 10 mg/L pH	Globular aggregates	-	0.5-2	Mica
Wilkinson <i>et al.</i> , (1999)	Laurentian soil FA Natural HA	pH <2 2.7 g C L-1	Spherical	<2 Possibly due to flattening	-	Mica
Liu <i>et al.</i> , (2000)	Purified Aldrich HA molecular layers	pH 6.5, 0.001M NaNO <sub>3</sub> , 10 mgC/L	Cylindrical configuration	-	4.2-5.7 3.1-3.7	Mica

<b>Plaschke <i>et al.</i>, (2000)</b>	Purified HA (Aldrich)	pH 7, in presence of 0.1-0.00005M Eu (III), 80-200 mg/L <sup>-1</sup>	Large agglomerates	300	4-20	Mica
	Natural HA	0.00005M Eu (III)	Fibrous structures	0-17		
	Aldrich HA	0.00005M Eu (III)	Fibrous structure	0-3		
<b>Keller <i>et al.</i>, (2003)</b>	Peat-derived HA	Ambient conditions	Amorphous clumps	-	-	Mica
<b>Guan <i>et al.</i>, (2006)</b>	HA From Aldrich	pH at 6, 7 and 8, 5 mg/L <sup>-1</sup>	Globular aggregates Number of HA aggregates increased with decreasing pH.	50-200 nm	-	Silicon



### 2.2.2.1.2 Force-Displacement Mode

The study of NOM using force microscopy falls into two categories, (a) where NOM (or a model compound) is immobilized on the tip and/or surface and (b) where force measurements are performed in NOM-rich waters that are relevant to the process. Most AFM studies have focussed on the former because NOM fouling is a major problem in reverse osmosis (RO) and ultrafiltration (UF) membranes. Table 2.9 gives a summary of force measurements performed with modified and unmodified tips in process relevant environments that are related to NOM aggregation phenomena. The majority of probe modification techniques use epoxy glue to attach the colloid/coated colloid to the cantilever. In all cases, polymer pulling events/adhesion on NOM or with NOM-coated tips were identified with changes in solution chemistry in the same way the NOM conformation was modified during AFM imaging. For instance, Sander *et al.*, (2004) detected polymer pulling events between alumina surfaces with adsorbed Suwannee river humic acid (SHA). When force measurements were performed in  $\text{CaCl}_2$  solution, bridging events were observed with adsorbed SHA, and pull-off forces were stronger than in the presence of NaCl. These findings linked well with humic acid removal during coagulation, and were also consistent with the Schulze-Hardy rule of high valency counterions reducing double layer repulsion.

In a study by Plaschke *et al.*, (2000), force measurements were performed with humic acid-coated AFM tips on mica in the presence and absence of europium electrolyte (Eu(III)). Tips were prepared using the mechanical fixation method, by dragging the tip onto adsorbed humic acid. Their results gave pull-off forces of  $5.4 \pm 0.5$  nN and  $0.7 \pm 0.2$  nN in the presence and absence of Eu(III), indicating bridging phenomena between humic acid and mica. A common feature of force measurements with NOM-coated tips and/or in NOM solutions is their ability to form multiple binding sites largely due to the large molecular size and humics negative surface charge. To represent humic acid carboxylate-modified latex (CML) particles were used as a surrogate by Lee *et al.*, (2006) because model organic compounds mainly comprised of carboxylic functional groups.

**Table 2.9** Summary of force measurements performed with modified and unmodified AFM tips in NOM solution or using NOM-modified tips and their application.

Modified tips					
Application	Forces detected	Tip modification method and radius ( $\mu\text{m}$ )	Tip interaction, solution conditions, NOM source	Information gained and potential drawbacks	Reference
Colloidal aggregation Water treatment	Electrostatic (20-100nm) van der Waals Steric repulsion	Epoxy	Alumina-SiO <sub>2</sub> Fe <sub>2</sub> O <sub>3</sub> - SiO <sub>2</sub> in different ionic and pH conditions. Suwannee River humic acid	SHA very strongly adsorbed to Fe <sub>2</sub> O <sub>3</sub> and Alumina. Van der Waals attraction more dominant for alumina particle than iron oxide. Shrinkage of humic acid layer with increase in ionic strength	Sander <i>et al.</i> , (2004)
Colloidal stabilization by NOM Water treatment	Electrostatic repulsion Steric Van der Waals	Epoxy	Fe <sub>2</sub> O <sub>3</sub> -Fe <sub>2</sub> O <sub>3</sub> in NaCl at pH 3.8-9.2. NOM-NOM in NaCl at pH 3.8-9.2.	NOM adhesive at pH 3.8 than 7 or 9 due to presence of COOH groups. NOM-NOM bridging effects and pull-off events observed over 2-7nm. Strong stabilizing effect of NOM on Fe <sub>2</sub> O <sub>3</sub> particles due to electrostatic and steric forces	Mosley <i>et al.</i> , (2003)
Cleaning of nanofiltration membranes	Electrostatic	Epoxy, unknown	COO <sup>-</sup> (carboxylate particle)-membrane surface	Carboxylate-modified latex particle as surrogate for humic acid. Ca <sup>2+</sup> enhanced NOM fouling through cationic bridging. Efficient cleaning achieved when Ca <sup>2+</sup> was removed	Li and Elimelech (2004)
Aggregation of humic acid for influencing mobilization of metal ions	Electrostatic Ion-dipole	Adsorption, 30nm	Humic acid-Mica in presence and absence of Eu(III) ions	Adhesion forces stronger in Eu(III) solution than electrolyte solution. Bridging effects observed directly with humic acid. Adhesion greater with humic acid tip than unmodified tip.	Plaschke <i>et al.</i> , (2000)

					However, no pull-off sequential events observed. Poor tip geometry.	
	<b>Fouling reduction in water treatment systems</b>	Electrostatic	Epoxy	COO <sup>-</sup> (carboxylate particle)-membrane surface in different ionic strength, pH, divalent ion concentration, organic foulant strength	Adhesion strong on fouled membranes in the presence of Ca <sup>2+</sup> . Foulant-foulant adhesion interaction linked to fouling.	Lee and Elimelech, (2006)
<b>Unmodified tips</b>	<b>Transport of colloidal particles Water treatment systems</b>	Electrostatic van der Waals	Unmodified Si <sub>3</sub> N <sub>4</sub>	Si <sub>3</sub> N <sub>4</sub> -SiO <sub>2</sub> in presence and absence of copper ions, under varying pH (4.5-5.5) and ionic strength (NaCl).	Local charge differences on surface resulted in changes in magnitude and direction of surface forces. Force images showed charge reversal occurring at pH 5.5. Colloidal particles will experience charged regions differently, and depend on the relative size of the particle and charged region.	Taboada-Serrano <i>et al.</i> , (2005)

The authors were particularly interested in foulant-foulant interactions because their molecular interaction governed fouling layer thickness and compactness. The CML particle was attached to the AFM tip to represent the foulant, while alginate and Suwannee River NOM (SRNOM) were used as model organic foulants. Foulant-foulant interactions were performed in the presence and absence of  $\text{Ca}^{2+}$ ,  $\text{Mg}^{2+}$  and at various pH. They found fouling rate and adhesion forces were stronger at low pH, high ionic concentration and in the presence of  $\text{Ca}^{2+}$ , which confirmed intermolecular bridging between model foulants. They also found intermolecular adhesion force (and fouling) was stronger with alginate than SRNOM, that was attributed to the larger alginate molecular network which was dominated by hydrophilic organic macromolecules rather than a hydrophobic core. These findings gave a strong correlation between fouling rate, determined from flux-decline curves, and adhesion force giving  $R^2$  values of 0.972 and 0.933 for runs in NaCl and  $\text{CaCl}_2$ , respectively. The results strongly support the suggestion AFM adhesion forces with modified tips can be used as an indicator of fouling potential.

In a similar example Li and Elimelech (2004) performed force measurements with CML-modified AFM tips and fouled/clean nanofiltration (NF) membranes in various solutions where SHA was used as the foulant. The authors found excellent correlation between measured adhesion force and membrane cleaning, and confirmed  $\text{Ca}^{2+}$  enhanced NOM fouling which was reversed by the removal of  $\text{Ca}^{2+}$ . Furthermore, force measurements were performed in the presence of different chemical cleaning agents such as EDTA (ethylenediamine tetraacetate), SDS (sodium dodecyl sulphate) and NaOH, which strongly correlated with bench-scale fouling/chemical cleaning experiments. As  $\text{Ca}^{2+}$  is present during the filtration process, EDTA was able to form a stronger complex with  $\text{Ca}^{2+}$  than SHA, thus making it easier to remove humic acid from fouled membranes by rinsing. These findings and other numerous studies linking intermolecular adhesion force to NOM fouling, membrane cleaning and general water treatment systems have demonstrated the use of modified tips as an excellent screening tool that not only complements existing bench-scale experiments, but also allows for more targeted remedial techniques.

### 2.2.3 Biological Systems

#### 2.2.3.1 Introduction

This final section of the literature review looks at the field of biofouling, the unwanted accumulation of microorganisms, plants, algae and animals on submerged surfaces. It will focus on studies where the AFM has been used to understand foulant-surface and foulant-foulant interactions, as well as the development of novel coatings in fouling prevention. Numerous studies have shown the first stage of biofouling is the adsorption of a conditioning film deposited from dissolved organic material or plasma proteins (albumin) from serum. Within hours bacteria colonise the film by secreting sticky extracellular polymeric substances (EPS), which increases drag in marine systems while causing bacterial infection in humans (Callow and Callow, 2002). The outer membrane of Gram-negative bacteria is mainly comprised of phospholipids, proteins and polysaccharides, where lipopolysaccharides (LPS) form the major component that gives bacteria their structural integrity and negative surface charge, which can vary between different strains (Burks *et al.*, 2003). Because the EPS and LPS both play an integral role in biological fouling, the AFM has been used to investigate both of these surfaces.

#### 2.2.3.2 Applications of the AFM to biofouling and bacterial adhesion

Although modified tips increase the range of materials to be studied, force measurements with unmodified tips still provides information that is of fundamental and practical importance, not least because of its known geometry and chemistry. For instance Callow and Callow, (2000) performed force measurements in filter-sterilized seawater with silicon nitride tips on the adhesive pad of the green algal spore *Enteromorpha Linza*. The spores secrete an adhesive (a glycoprotein) that gives firm anchorage to the substratum, which are commonly found on ships' hulls causing algal biofouling. During force measurements force curves gave characteristic saw-toothed curves with multiple pull-off events that were typical of multiple binding regions of glycoproteins. Interestingly, freshly-released adhesive from spores gave mean forces of  $173 \pm 1.7$  mN and within minute's adhesion was reduced by 65% due to the curing process. From existing force data, it was also found the compressibility of the adhesive was reduced with time giving a 10-fold increase in Young's modulus.

AFM tips have also been modified with marine adhesives such as the hydrophilic *Mytilus edulis* foot protein (Mefp-1 ~ 130 000 Da), because of its adverse effect on marine biofouling which are also important for developing synthetic adhesives in solutions (Frank and Belfort, 2002). Mefp-1 is one of four proteins that is part of the Eastern blue mussel, a good model for understanding marine fouling because it comprises of 3,4-dihydroxyphenyl-L-alanine (DOPA) residues which are ubiquitous among invertebrates. Mefp1 was adsorbed onto silica-modified cantilevers and force measurements were performed on silica substrates in different ionic solutions. In solutions containing  $\text{MgCl}_2$ ,  $\text{CaCl}_2$  and  $\text{Na}_2\text{SO}_4$  multiple pull-off events were common, which are typical for biological systems due to metal complexation. Interestingly, multiple events were not observed in  $\text{FeCl}_3$  although adhesion was much stronger possibly due to the oxidation of DOPA to *o*-quinones and then cross-linking to Lys residues present on Mefp-1, These results showed the ionic composition of the environment inside the mussel foot could be tailored by the mussel to achieve maximum adhesion, and provides further information for developing synthetic adhesives.

Since bacteria can adhere to a host of surfaces, bacterial infection is a major problem in health and biomedical applications. *Escherichia coli* is frequently at the forefront of many AFM studies because of its omnipresence in the environment and living systems. Ong *et al.*, (1999) performed force measurements using polyethyleneimine (PEI)-coated AFM tips modified with *E. coli* D21f2 (mutant form) and D21 strains in Tris buffer on mica, glass, polystyrene and Teflon. The authors found adhesion of D21f2 (hydrophobic strain) to Teflon was stronger due to the hydrophobic effect. The hydrophilic strain (D21) was more adhesive to hydrophilic surfaces of mica and glass, although it was most adhesive to hydrophobic octadecyltrichlorosilane-treated (OTS) glass. The authors found this was due to different lipopolysaccharide (LPS) lengths, thus affecting cell surface charge and hydrophobicity. These findings showed hydrophobic interactions played the dominant role, while vdW and electrostatic interactions were less important. As LPS was found to play an important role in bacterial adhesion, additional AFM studies on *E. coli* followed comparing the adhesion of different LPS chain lengths with unmodified tips (Burks *et al.*, 2003)

AFM tips have also been coated with bovine serum albumin (BSA), the most abundant protein in blood plasma that has been extensively studied (Xu and Logan, 2006). Albumin adheres unfavourably to implanted biomaterials causing adverse reactions such as blood clots and fibrous capsules (Wang *et al.*, 2004). The authors used the SAM's technique for preparing CH<sub>3</sub> and OH terminated SAM's before covalently immobilizing BSA. Force measurements were performed in 10 nM phosphate buffered saline (PBS) buffer at room temperature on BSA, anti-BSA and different terminal groups. The authors found adhesion was strongest to hydrophilic OH-terminated surfaces and anti-BSA, which did not correlate with previous observations. More importantly, adhesion was weakest to dextran-coated surface, which was most hydrophilic although repulsive steric effects were also likely to have played a role. At the time of this study the development of non-adhesive coatings for biomaterial surfaces using the AFM was in its infancy, but it emphasizes the importance of tip modification in AFM studies. Other studies have focussed on the affect of residence time of protein/dextran adhesion on biomaterials using the colloidal probe (Xu and Logan, 2006).

In the field of water treatment modified tips were used to perform force measurements on the oocyst *Cryptosporidium parvum*, a major contaminant of drinking water and also an enteric pathogen (Considine *et al.*, 2002). *Cryptosporidium parvum* is a protozoal parasite that is ubiquitous in the environment with worldwide distribution and is frequently the cause of many disease outbreaks. Silicate glass beads were used to modify tips because sand bed filtration is one of the main barriers that offer protection. Force measurements were performed at different pH in solutions of KNO<sub>3</sub>, Ca(NO<sub>3</sub>)<sub>2</sub> and DOC. Pull-off forces gave polymer pulling events reaching 250 nm in KNO<sub>3</sub> that are characteristic of an extended hairy protein layer. It was found on addition of Ca<sup>2+</sup> and DOC there was increased coulombic screening that compressed the protein layer on the oocyst surface, thus reducing the adhesion force. This study showed how changing the ionic concentration was effective in reducing adhesion between the oocyst and glass beads.

## Chapter 3

## Materials and Methods

### 3.1 Chemicals, Solutions and Sample Preparation

All solutions were obtained from Fisher Scientific and Aldrich Chemicals, UK, of analytical grade. The solutions used are summarised in Table 3.1. Synthetic hard water (SHW) was prepared by mixing solutions of analytical grade 0.1M  $\text{CaCl}_2$  with 0.1M  $\text{NaHCO}_3$  (Supplied by Aldrich Chemicals, UK) to achieve the same hardness as a sample of hard water obtained from a test site near Attleborough (Norfolk, UK) which exhibited a hardness of 310 mg/L of  $\text{CaCO}_3$ .

#### 3.1.1 Solid specimens

The thirteen specimens used in the calcite section of this study (see 3.5.1) were in the form of 12 mm pipe sections, and were either coated or uncoated with the coating specified by the supplier (Teercoatings®). All materials were placed into one of two groups, group I which comprised of high energy metals, and group II, which were predominantly non-metallic (Table 3,2). Aluminium was in group II because it was not a transition metal, unlike the other metals in group I. A full description of the materials used and their preparation is listed in Table 3.2.

The purpose of the materials used in the calcite section was to link surface properties (including surface topography, SFE and adhesion force) to their rate of  $\text{CaCO}_3$  scaling (see section 3.5.2.6), where all the materials required extensive surface characterization. This was why some surfaces were polished (MF steel), abraded (SB and RF steel), corroded (used copper pipe specimen) or prepared with variations in coating thickness (gold coatings) or simply in their coating technique (Dymon-iC and Graphit-iC). Dymon-iC and Graphit-iC carbon-based coatings were used because they exhibit a high slide wear resistance and low friction in dry conditions, and have shown to reduce scale formation at the bench-level (MacAdam, 2005). TiN is a hard, dense, wear resistant coating, and is applied mainly for tooling applications.



**Table 3.1** A summary of solutions and various probe liquids used throughout the investigation. All the specified liquids except probe liquids for contact angle measurements were used during force measurements.

Calcite Experiments	Synthetic $\text{CaCO}_3$ solutions	Natural hard water ( $\text{CaCO}_3$ )	Ultrapure water (18 M $\Omega$ )	Synthetic $\text{CaCl}_2$ solution	Other solutions or liquids
Effect of substrate material	Yes	Yes	Yes		
Effect of molar concentration	0.001M, 0.0005M, 0.0008M				
Effect of solution pH on adhesion	pH 7, 8, 9 and 10				
Effect of calcite orientation	SHW (pH 7.4 – 7.6)		Yes		
Effect of calcite surface defects	Yes				
Natural Organic Matter experiments			Yes	Yes	Raw water from four sources Poly-L-lysine Glycine
Contact angle probe liquids			Yes		1-Bromonaphthalene (B) Diiodomethane (DI) Ethylene Glycol (EG) Formamide (F) Glycerol (G) Dimethylsulfoxide (D)

The base materials of stainless steel 306a, aluminium and copper are frequently used for the manufacture of heaters and boilers, which were essentially used to be compared to the different coating specimens. The ‘used’ copper specimen was effectively analyzed so its surface properties can be compared to its unused counterpart.

**Table 3.2.** Description of materials used for experiments (supplied by Model Products Ltd, Bedford, UK). Coatings were prepared by Teercoatings® on stainless steel substrates. Solid phase elemental analysis of MF steel and SB steel was performed using ESEM-EDX.

Group I Material	Description	Group II Material	Description
Mirror-finish stainless steel Model 306a (referred to as MF steel hereafter)	Polished to a mirror finish. Fe (61%), Cr (17%), C (11%), O (10%), Ni (9%) and Mn, Mo and Si (<2%).	Dymon- <i>iC</i> <sup>TM</sup> (referred to as Dymon- <i>iC</i> hereafter)	Hydrogenated, amorphous carbon coating (a-C:H) produced by closed-field unbalanced magnetron sputter ion plating (CFUBMSIP) with 2 µm thickness.
Sandblasted stainless steel Model 306a (referred to as SB steel hereafter)	Sand or other abrasive blown against substrate. C (44%), Fe (24%), O (17%), Cr (7%), Ni (3%), Al (3%) and Mn, Mo and Si (<2%).	Graphit- <i>iC</i> <sup>TM</sup> (referred to as Graphit- <i>iC</i> hereafter)	Hydrogen-free, amorphous, carbon-chromium coating (a-C) produced by CFUBMSIP with 2.5 µm thickness.
Roughened stainless steel (referred to as RF steel hereafter)	Abraded with sandpaper. Model 306a.	TiN	Titanium nitride coating with 3 µm thickness.
Gold (0.1 mm)	0.1 mm thick coating of gold.	PTFE	Poly(tetrafluoroethylene coating of unknown thickness.
Gold (0.3 mm)	0.3 mm thick coating of gold.	Kettle element coating (referred to as ‘K. coating’)	Unspecified coating of unknown thickness
Copper	Unused copper pipe.	Aluminium	Model 608226
‘Used’ copper	Used copper pipe that is discoloured due to corrosion.		

### 3.1.2 Summary of the water treatment works

Raw water samples were provided by several students, which were collected from four different water treatment works (WTW) at various time intervals. Raw water from two WTW (Giddop and Lower Gorple reservoirs, Pennine Moorlands, UK) was fractionated into NOM components (described in section 3.1.3 and 3.1.4). The fractionated NOM components (HAF, FAF and HPIA fractions) of three other samples were provided by Mr Mergen (Penwhirn reservoir, Stranraer, Dumfries and Galloway and Albert reservoir

waters, Halifax, Yorkshire, UK) and Dr Goslan (Albert reservoir, 2001) from Cranfield University.

Albert water treatment works is fed by an upland peat catchment system. This includes a 3 stage treatment plant processing a flow of 33,000-55,000 m<sup>3</sup> d<sup>-1</sup> on the western side of Halifax (Yorkshire, UK), which has drained through a peat catchment system before reaching the plant's reservoir. Widdop Reservoir was built for Halifax Corporation in 1878, processes 2,877,618 m<sup>3</sup> d<sup>-1</sup> (or 633 million gallons), and along with Lower Gorple feed the Albert reservoir that is 10 miles southeast. Lower Gorple is one of two reservoirs situated on Black Moor and set in the midst of the Pennine moorland, with a capacity of 1,033,851 m<sup>3</sup> d<sup>-1</sup> (272 million gallons). Widdop and Gorple reservoir water sources will also be referred to as 'feeders' in this report. Penwhirn WTW is a 4 stage treatment plant that processes 13,000-14,000 m<sup>3</sup> d<sup>-1</sup>. It was established in 1955 and covers the Stranraer area (Dumfries & Galloway, UK) treating upland peat water. The organics from Gorple and Albert raw waters were extracted and fractionated using XAD8/XAD4 resin chromatography, adapted by a method from Malcolm and McCarthy (1992) (Goslan, 2003) (See section 3.1.3 and 3.1.4).

### 3.1.3 Resin Preparation

XAD-4 and XAD-8 Amberlite resins were prepared using the same procedure. XAD4 and XAD8 resins are porous, non-polar, highly cross linked styrene divinylbenzene copolymer beads used for the adsorption of NOM fractions during fractionation (Aiken *et al.*, 1979). The XAD4 beads were used to isolate HPIA, while XAD8 are used to isolate HAF and FAF. The resin (200ml) was inserted into a round-bottomed flask (750ml) containing methanol (450ml), followed by the addition of 5-6 anti-bumping granules. The flask was connected to a reflux condenser and refluxed for 24 hrs. The resin was then packed into a fractionation column to produce a single bed volume of resin (~75 ml). The resin was rinsed with de-ionized water (15 MΩ) until the DOC level was <2mg/L using a Watson Marlow pump (Model 505Da, UK). This normally required rinsing with DI water (400ml). The column was then rinsed with 1M NaOH (2.5 bed volumes), followed by the equivalent volume of 0.1M HCl acid to remove impurities.

### 3.1.4 Fractionation Procedure

Raw inlet water (2L) from Lower Gorple and Widdop water reservoirs was passed through 0.45 $\mu$ m filter paper (Whatman plc., Maidstone, Kent, UK), acidified to pH 2 with HCl acid, and then passed through the XAD8 column followed by XAD-4. The effluent from the XAD-4 column contained the HPINA fraction. When columns were saturated with hydrophobic and HPIA organics on XAD-8 and XAD-4 resins, respectively, 0.1M NaOH (~100ml) was passed through each column until all the colour was washed off the resins. The eluate from the XAD-4 column was the HPIA fraction. The hydrophobics produced from XAD-8 was acidified to pH 1, allowed to settle for 24 hrs, and then centrifuged. The ensuing supernatant (FAF) was decanted, and the resulting residue (HAF) was dissolved in a minimum volume of 0.1M NaOH. The fractions produced at the end of the procedure were HAF, FAF, HPIA and HPINA isolates.

### 3.1.5 NOM Fraction Immobilization

Fractions were immobilized onto a glass slide suitable for performing contact angle and force measurements using the following procedure. NOM-coated slides were prepared by cleaning fresh glass slides in an ethanol bath. Poly-L-lysine (PLL, Supplied by Sigma Aldrich, UK) was then used as an adhesion promoter. A 1:10 dilute solution of PLL was prepared using distilled water and the clean glass slide was immersed into the PLL solution for 5 min. They were then placed into an oven at 60°C for 1 hour. PLL-coated slides were rinsed with ultrapure water (18M $\Omega$ ) and allowed to dry at room temperature. Slides were inserted into a Petri dish containing each of the NOM fractions for 2 hrs, washed with ultrapure water then allowed to dry at room temperature before use.

## 3.2 AFM tip modification

AFM cantilevers were used on the Dimension 3000 (SPM) system equipped with a NanoScope IIIa controller (Veeco instruments, Santa Barbara, California, USA). All AFM cantilevers were obtained from Nanosensors (Wetzlar, Germany). The cantilevers used to perform force measurements were model numbers PPP-CONT-50/20.

### **3.2.1 Tip modification in calcite chapter of work**

Three types of calcite modified probes were prepared, calcite-grown tips, calcite-attached (CA) tips and calcite-orientated tips.

#### **3.2.1.1 Calcite-Attached (CA) Tips**

The AFM cantilever (Nanosensors (Wetzlar, Germany) spring constant ranging from  $0.07\text{--}0.4\text{ N/m}^{-1}$ ), was first cleaned with  $0.1\text{ M HCl}$  acid for 10 minutes. With the aid of an optical microscope the terminal of a clean cantilever was lowered into an epoxy adhesive (ZAP, Pacer technology, California, USA) with tweezers for several seconds, after which it was removed. A freshly pulled glass probe was inserted into the micromanipulator and used to collect a calcite crystal that was prepared earlier and then lowered onto the adhesive on the cantilever. The crystal was positioned for about 10-15 seconds to allow the adhesive to cure.

#### **3.2.1.2 Calcite Grown (CG) Tips**

$0.1\text{ M Na}_2\text{CO}_3$  was added to  $0.1\text{ M CaCl}_2$  solution to induce  $\text{CaCO}_3$  precipitation. A quarter of the cantilever was introduced into the supersaturated solution and left in solution for 5 minutes, after which the cantilever was analyzed for crystal growth either on or near the apex. One calcite crystal was then moved in juxtaposition to the tip while excess calcite was removed using a freshly pulled glass probe prepared using a PC-10 glass puller (Narishige Co. Ltd, Tokyo, Japan) with the aid of an MMO-202ND Three-axis Hanging Joystick Oil Hydraulic micromanipulator (Saitama, Japan) equipped with an optical microscope. The cantilever was then re-inserted into the supersaturated droplet for a further 20 min. and analysed under the microscope. Excess calcite was removed from the back of the cantilever by using a droplet of  $\text{HCl}$  acid ( $0.1\text{M}$ ). The cantilever was allowed to make contact with the droplet with the calcite crystal inserted into the droplet. The surface tension of the  $\text{HCl}$  solution was allowed to bend the cantilever without contacting the modified side of the cantilever. The cantilever was held in position for 1 min. after which the cantilever was withdrawn and then analyzed. The process was repeated until all crystals were removed from the back side of the cantilever.

### **3.2.1.3 Calcite-Orientated (CO) Tips**

Several fresh glass probes were prepared using a PC-10 glass puller (Narishige Co. Ltd, Tokyo, Japan). Epoxy adhesive (Araldite ®) was collected on a glass probe and transferred to the tip/cantilever surface. A calcite crystal (as prepared in section 3.2.1.3) was collected with a second glass probe attached to the micromanipulator. The glass probe was first inserted into the NaHCO<sub>3</sub> solution to moisten the end of the probe and promote capillary adhesion to the calcite crystal. The probe was gently lowered onto a suitable calcite crystal, and the probe tip was carefully manoeuvred until the crystal adhered to the probe through capillary forces. The crystal was then lowered onto the adhesive of the AFM probe. Calcite-oriented tips were prepared by moving the crystal on the adhesive until the face, corner or edge of the crystal was facing up.

## **3.2.2 Tip modification in NOM chapter of work**

AFM tips were modified with poly-L-lysine (PLL), glycine and fractionated NOM polyanions. Three types of NOM modified probes were prepared. They were NOM-modified tips, where the fractions were adsorbed on unmodified tips, resin-modified tips, where XAD-4, XAD-8 and MIEX® was attached to an AFM tip with an adhesive and NOM-coated resin probes, where the resins were coated in NOM prior to attaching to the cantilever.

### **3.2.2.1 PLL-modified tips**

A 1:10 solution of PLL was prepared using distilled water and the AFM tip was inserted into the solution for 5 minutes by inserting the cantilever portion only into the a droplet of PLL solution. The chip was then transferred to the oven for 60 min, at 60°C.

### **3.2.2.2 Glycine-coated tips**

PLL-coated tips prepared in 3.2.2.1 were coated in glycine as follows. The glycine solution was prepared by dissolving 2 g of analytical grade glycine (Fisher Scientific, UK) in water (10 ml). A droplet of the solution was then placed onto a petri dish and freshly-prepared PLL-coated tips were inserted into the solution for 1 hr. The tip was then removed and rinsed in ultrapure water and stored before use.

### 3.2.2.3 NOM-Modified Tips

NOM-modified probes were prepared as follows. PLL-coated tips were inserted into a Petri dish containing the desired NOM fraction (1:10 dilution was required for HAF due to reduced quantities of this fraction) for 2 hrs. The cantilever was then rinsed with ultrapure water (18 M $\Omega$ ) two times before leaving to dry for 2 hours and ready for force measurements.

### 3.2.2.4 Resin Probes

AFM tips modified with XAD4, XAD8 and MIEX® resins. MIEX® is a re-usable magnetic ion exchange polymer used to remove primarily low MW dissolved organic carbon (DOC) (Zhang *et al.*, 2006), used as a pre-treatment method (Singer and Bilky, 2002; Boyer and Singer, 2006). Using an optical microscope the terminal of a fresh silicon cantilever was lowered into an epoxy adhesive (ZAP, Pacer technology, California, USA) with tweezers for several seconds, after which it was removed. A freshly pulled glass probe was inserted into the micromanipulator and used to collect a single resin from a clean glass slide and then lowered onto the adhesive on the cantilever. The resin was positioned for about 10-15 seconds to allow the adhesive to cure.

### 3.2.2.5 NOM-Coated Resin Probes

The same procedure used to attach the resins to the tip was used. The resin-attached probe was then inserted into the desired NOM solution for 30 minutes. Care was taken not to coat the cantilever in NOM so only the resin was inserted into the NOM droplet with the aid of an optical microscope.

## 3.3 Instrumentation

### 3.3.1 Contact Angle Apparatus

Contact angles (CA) of probe liquids were performed using a Jai-CV-M90 Interlaced CCD camera connected to a personal computer. The samples were first cleaned after immersing a lens cleaner in methanol and gently wiping the surface of the substrate. The samples were then fixed to a plastic base with sellotape about 30 cm from the camera, and a 5 ml syringe was held about 10mm above the sample with the aid of a clamp.

### 3.3.2 Scanning probe microscope

The scanning probe microscope (also called AFM) used to perform all probe measurements was the Dimension 3000 system equipped with a NanoScope IIIa controller (Veeco instruments, Santa Barbara, California, USA), operated in both air and liquid environments. The controller was connected to a PC, equipped with NanoScope IIIa software (version 4.42r4). The set-up included two monitors, one for controlling the real-time control panel and a second for observing the output signal. A third monitor was independently connected to a camera, inserted into the X-Y stage, for observing the position of the laser and cantilever relative to the sample. The X-Y stage was placed on a hydraulically-controlled bench to eliminate external vibration. The complete set-up of the equipment is show in Figure 3.1.

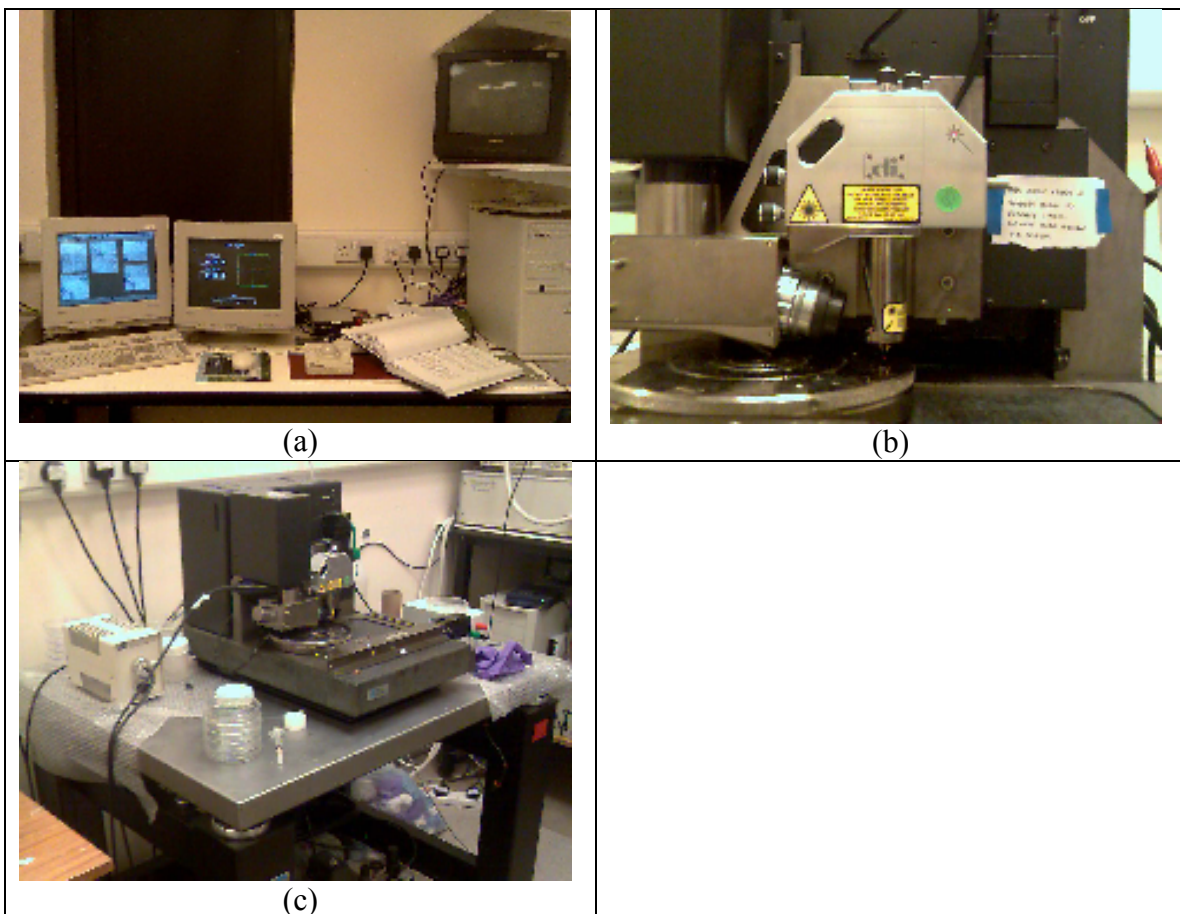


**Figure 3.1.** Digital images of the three monitors (a), the AFM stack locked into the stage (b) and the stage sitting on the hydraulic bench (c).



The AFM stack (or SPM head) is slotted into the computer-controlled X-Y stage. The stack (Figure 3.1, model number: DMLS) comprises of laser and photodetector adjustment screws for aligning the laser and photodetector, respectively, to the back of the cantilever. At the bottom of the SPM stack, four pins are present for inserting the cantilever holders. Two types of cantilever holders were used. One for operating in air, and the other in fluid, which are shown in Figure 3.2.

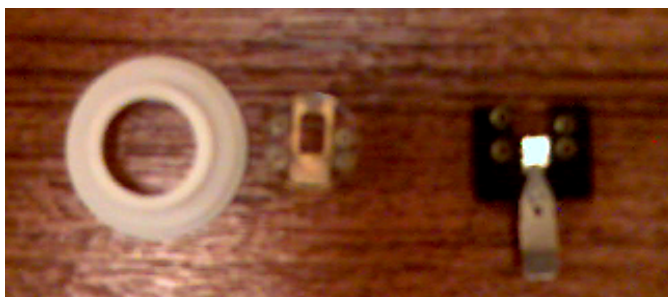


**Figure 3.2.** Digital image of fluid cell (middle, 12 mm diameter) with protective skirt (left) and dry cantilever holder (right).

### 3.3.3 Cantilevers

All AFM cantilevers were obtained from Nanosensors (Wetzlar, Germany). The cantilevers used for specific modes of operation were as follows:

Imaging in air: PPP-NCL-50/20 (tapping mode); PPP-CONT-50/20 (contact mode).

Imaging/F-D mode PPP-CONT-50/20 (contact mode)

in fluid

### 3.3.4 Scanning Electron Microscope

Images of AFM tips modified with calcite and beads were performed using the Philips EL30 Environmental Scanning Electron Microscope (ESEM), and performed in water vapour mode prior to analysis. All AFM probes were fixed onto a stud before imaging.

### 3.3.5 pH meter

The pH was measured using the Jenway pH meter with a Merck Gelplas General Purpose pH probe. The meter was calibrated using pH 4 and pH 7 buffer solutions prior to pH measurements.

## 3.4 Analytical Techniques

### 3.4.1 Contact angle measurements and surface free energy calculation

All solid-state samples were cleaned after immersing a lens cleaner in methanol and gently wiping the surface of the substrate. The thirteen substrates used in the calcite chapter of the study were in the form of 12 mm pipe sections with a length of 80 mm, so measurements could be performed on the original uncut specimens (See section 3.5.1 for detailed description of materials). In the NOM chapter, immobilized polyanions (see 3.1.5) were rinsed in ultrapure water before performing contact angles. Samples were then fixed to a plastic base with sellotape about 30 cm from the camera. All of the probe liquids were HPLC grade (>99.5% purity). Probe liquids were diiodomethane, 1-bromonaphthalene ethylene glycol, formamide, glycerol, dimethylsulfoxide (Fisher Scientific, UK) and ultrapure water (purified using a Barnstead Nanopure II water purification system). The probe liquid was collected into a 5 ml syringe and held in position about 10 mm above the sample with the aid of a clamp. Miniscule droplets of the probe liquid were dispensed from the syringe onto the substrate. A new syringe was used for each probe liquid to prevent contamination. An image of the contact angles was taken several seconds after dispensing the liquid. A total of 8 drops (about 5  $\mu$ l) of each probe liquid was dispensed, each side of symmetrical sessile drops giving a total of 16 contact angle measurements. Digital images were taken using Image Pro Plus® The Proven Solution™ software once the contact angle stabilized. Measurements were performed using the same software (Figure 3.3), and after completing each set of probe liquid measurements.

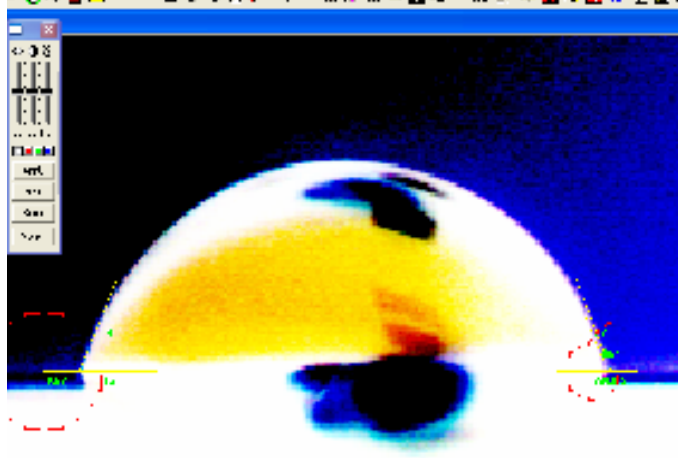


**Figure 3.3.** Digital photograph taken of water on a solid substrate, using Image Pro Plus® The Proven Solution™ software.

Having measured the contact angles, the graphical plot (McCafferty, 2002) and matrix methods (Van Oss, 2002) were used to calculate the surface free energy (SFE) components. The  $\gamma^{LW}$  (dispersive component) was calculated using equation 3.1:

$$\gamma_s^{LW} = \gamma_l \frac{(1 + \cos \theta)^2}{4} \quad \text{Equation 3.1}$$

The polar,  $\gamma_s^-$  and  $\gamma_s^+$  components were calculated using the McCafferty (2002) linear plot method. SFE parameters were based on a linear plot of

$$\frac{(1 + \cos \theta) \gamma_L - (\gamma_s^{LW} \gamma_L^{LW})^{1/2}}{(\gamma_L^+)^{1/2}} \text{ against } \left( \frac{\gamma_L^-}{\gamma_L^+} \right)^{1/2} \text{ to obtain the acid base parameters } \gamma_s^+ \text{ and } \gamma_s^-.$$

The linear plot produces a straight line, where  $(\gamma_s^+)^{1/2}$  is given by the slope and  $(\gamma_s^-)^{1/2}$  is the intercept.

The matrix method comprises solutions of equation 3.1 written as a set of three simultaneous equations and expressed in matrix form (Van Oss, 2002):

$$\begin{bmatrix} (\gamma_{L1}^{LW})^{1/2} (\gamma_{L1}^-)^{1/2} (\gamma_{L1}^+)^{1/2} \\ (\gamma_{L2}^{LW})^{1/2} (\gamma_{L2}^-)^{1/2} (\gamma_{L2}^+)^{1/2} \\ (\gamma_{L3}^{LW})^{1/2} (\gamma_{L3}^-)^{1/2} (\gamma_{L3}^+)^{1/2} \end{bmatrix} \begin{bmatrix} (\gamma_s^{LW})^{1/2} \\ (\gamma_s^+)^{1/2} \\ (\gamma_s^-)^{1/2} \end{bmatrix} = 1/2 \begin{bmatrix} \gamma_{L1} (1 + \cos \theta_1) \\ \gamma_{L2} (1 + \cos \theta_2) \\ \gamma_{L3} (1 + \cos \theta_3) \end{bmatrix}$$

**Equation 3.2**

Where numerical subscripts ( $L1$ ,  $L2$ ,  $L3$ ) represent the wetting liquid. Equation 3.2 may also be written as  $Ax = b$ , where  $A$  is the matrix containing the surface tension parameters.

By using the Young-Dupre equation (equation 3.1), the idea that the surface free energy is the sum of the Lifshitz-van der Waals and Lewis AB (LWAB) contributions, and the Good-Girifalco combining rule for interfaces, van Oss, Chaudhury, and Good (Good *et al.*, 1992) obtained equation 3.3:

$$W_{sl} = \left( \gamma_l^{LW} + 2\sqrt{\gamma_l^+ \gamma_l^-} \right) (1 + \cos \theta) = 2 \left( \sqrt{\gamma_s^{LW} \gamma_l^{LW}} + \sqrt{\gamma_s^+ \gamma_l^-} + \sqrt{\gamma_s^- \gamma_l^+} \right) \quad \text{Equation 3.3}$$

Where  $W_{sl}$  is the work of adhesion for the solid (s) and liquid (l) phases,  $\theta$  is the liquid contact angle, and  $\gamma^+$ ,  $\gamma^-$  and  $\gamma^{LW}$  are the electron-accepting, electron-donating and LW surface tension values for the liquid (l) or solid (s), respectively. Equation 3.3 is also known as the VCG equation. To calculate the work of adhesion between the foulant and substrate in a medium that is analogous to the energy required to detach a foulant (1) from a surface (2) in liquid (3), the various works of adhesion must be resolved (Israelachvili, 1992):

$$W_{132} = W_{12} + W_{33} - W_{13} - W_{23} \quad \text{Equation 3.4}$$

Alternately, the work of adhesion ( $W_{132}$ ) may also be calculated from the following expression (Van Oss, 2002):

$$W_{132} = 2 \left[ \begin{aligned} & \sqrt{\gamma_1^{LW} \gamma_3^{LW}} + \sqrt{\gamma_2^{LW} \gamma_3^{LW}} - \sqrt{\gamma_1^{LW} \gamma_2^{LW}} - \gamma_3^{LW} \\ & + \sqrt{\gamma_3^+} \left( \sqrt{\gamma_1^-} + \sqrt{\gamma_2^-} - \sqrt{\gamma_3^-} \right) + \sqrt{\gamma_3^-} \left( \sqrt{\gamma_1^+} + \sqrt{\gamma_2^+} - \sqrt{\gamma_3^+} \right) \\ & - \sqrt{\gamma_1^+ \gamma_2^-} - \sqrt{\gamma_1^- \gamma_2^+} \end{aligned} \right] \quad \text{Equation 3.5}$$

Where  $W_{132}$  is also related to the adhesion force using equation 2.8 (section 2.1.6).

### 3.4.2 AFM imaging

In the calcite section of the experiments, substrate samples were imaged in water and electrolyte solutions using the fluid cell at a room temperature of 22°C. Substrates were first cleaned by dousing a lens cleaner in ethanol and gently wiping the surface prior to

mounting the sample on the stage. Imaging was performed in contact mode prior to changing to force-distance mode.

### 3.4.3 Force measurements

All force measurements were performed in a liquid environment using the fluid cell, to eliminate the capillary forces and amplify the van der Waals and double layer forces. The liquids included ultrapure water, de-ionized water and electrolytic solutions. Before commencing force measurements, a drop of the liquid was placed onto the fluid cell after mounting the cantilever into the holder. A droplet was also applied to the sample. The cantilever was then allowed to stabilize in the fluid environment for several minutes until stable force curves were generated. Adjustments were made to the real-time control panels including the setpoint, scan rate, ramp size, x-y offsets and data centre to generate good force curves. Each force curve was comprised of a row of maximum 250 data points acquired during vertical movements of approach and retraction of the cantilever. For all sets of force curves, a total of 10 random locations were sampled, and 10 force curves were performed on each data point to produce 100 force curves in total per sample.

Cantilever calibration was required for force measurements only using two methods. In most cases, springs constants were provided by the manufacturer while modified tips were calibrated using the resonance techniques only. In the literature review Cleveland *et al.*, (1993) gave accuracies to within 10%. The Cleveland method required measuring the resonant frequency of the cantilever using the sweep controls on the AFM before and after modifying the tip/cantilever, and also measuring the particle diameter and calculating its mass. However, resin-modified (XAD4/XAD8/MIEX®) probes were calibrated using the thermal noise method (See method B in Table 3.2) due to difficulties with the Cleveland method. For instance, calibration of XAD8 resin probes using the Cleveland method gave spring constants 100-fold greater than unmodified tips, which was significantly greater than the 15-30% uncertainty given in the literature (Ohler, 2007). After calculating the spring constant, the measured force was determined using Hooke's law. To convert the raw deflection data (Appendix A) to force data more efficiently, a MATLAB® programme was created by Rob Boyd and is given in Appendix B.

## **3.5 Laboratory Experiments**

### **3.5.1 Calcite Adhesion Experiments**

A series of experiments were conducted to measure the adhesion force of unmodified and modified AFM tips on the substrates given in section 3.1.1. These experiments were performed to compare different surface chemistries (3.5.1.1), different solution chemistries (3.5.1.2 and 3.5.1.3) and the effect of the calcite crystal itself (3.5.1.4 and 3.5.1.5).

#### **3.5.1.1 Effect of substrate material on adhesion**

During this experiment two techniques of characterization were performed, contact angle and force measurements. Contact angle measurements were performed on all the substrates using the technique described in section 3.4.1. Force measurements were performed using the fluid cell on each substrate using two unmodified AFM tips on random points for each of the samples in ultrapure and synthetic hard waters. This was repeated using two types of modified tips. They were calcite-grown (CG) (See 3.2.1.2) and calcite-attached (CA) (See 3.2.1.1) tips.

#### **3.5.1.2 Effect of molar concentration on adhesion**

Force measurements (See section 3.4.3) were performed using the fluid cell on all substrates in three different molar solutions of  $\text{CaCO}_3$ , and they were 0.001M, 0.0008M and 0.0005M. The experiments were performed in the following order, 0.0005M, 0.0008M then 0.001M. Each probe was used for all the substrates before changing solution and tip. The CA and CG modified probes produced earlier (section 3.2.1.1, 3.2.1.2) were used for this series of experiments and compared to each other.

#### **3.5.1.3 Effect of solution pH on adhesion**

The CA and CG tips were used to perform force measurements (section 3.4.3) using the fluid cell in 0.001M  $\text{CaCO}_3$  solutions at pH 7, 8, 9 and 10. The solutions were prepared by adding drops of 0.1M NaOH to the 0.001M  $\text{CaCO}_3$  solution until the desired pH was obtained. Three different probe types were compared, calcite-grown, calcite-attached and unmodified tips.

#### **3.5.1.4 Effect of calcite crystal orientation on adhesion**

Force measurements were performed using a total of six calcite-orientated probes using the fluid cell on Mica, mirror-finish stainless steel and Dymon-iC. All measurements were performed in synthetic hard water.

#### **3.5.1.5 Effect of calcite surface defects on adhesion**

Calcite probes were produced using the same procedure shown in section 3.2.1.3. Six calcite probes with three levels of surface defects were prepared and tested on Mica, mirror-finish stainless steel and Dymon-iC. Force measurements were performed at room temperature in synthetic hard water using the fluid cell.

#### **3.5.1.6 Rapid scaling tests**

This experimental test was conducted by Jitka MacAdam (MacAdam, 2005) on the twelve specimens listed in Table 3.2. The experimental rig was constructed by Model Products Ltd., and comprised of a plastic tank, a submerged heating element (one of the twelve specimens given in Table 3.2) with a removable sleeve, a magnetic stirrer and a temperature control unit. Synthetic  $\text{CaCO}_3$  solutions were used, by preparing  $\text{CaCl}_2 \cdot \text{H}_2\text{O}$  and  $\text{NaHCO}_3$  with a hardness ( $\text{CaCO}_3$ ) ranging from 100 to 300  $\text{mg} \cdot \text{L}^{-1}$ . The test solution was heated to either 42°C or 70°C for 45 minutes to complete 1 cycle. The test solution was then replaced and the heating element allowed to cool for 15 minutes in the new solution. The solution was magnetically stirred throughout the experiment, and after five or ten cycles (depending on temperature for all specimens), the sleeve was removed from the heater. The adsorbed  $\text{CaCO}_3$  was dissolved in 0.1% HCl and the calcium content analyzed using an Inductively Coupled Plasma Atomic Emission Spectrophotometer (ICP-AES).

### **3.5.2 NOM Experiments**

NOM-modified glass substrates with the aid of an adhesion promoter were prepared using the same procedure described in section 3.2.2.3. A table summarizing the NOM experiments performed on immobilized NOM fractions using NOM-modified probes, resin-modified probes and NOM-coated resin probes are given in Table 3.2. All force measurements were performed in ultrapure water.

**Table 3.3.** A summary of experiments performed using the NOM (HAF, FAF and HPIA) fractions. All numbers in each box indicate the number of AFM tips used to perform the force measurements. W = water; HA/FA/HP indicate HAF, FAF and HPIA, respectively. PL indicates poly-L-lysine.

Experimental Procedure	NOM FRACTION SOURCE/YEAR/SEASON						Other substrates
	Albert R 2001	Albert R 2006	Penwhim 2005	Lower Gorple 2006	Widdop 2006		Glycine (NH <sub>2</sub> )
XPS analysis	Done	Done	Done	Done	Done		-
Contact angles (4L) – (B, W, EG, F)	Done	Done	Done	Done	Done		-
<b>FORCE MEASUREMENTS – NOM probes</b>							
NOM-coated probes.			2x HAF (W)				
In water:			2x FAF (W)				
UM tips (no.)			2x HPIA (W)				
In water:	<b>2x</b>	<b>2x</b>	2x	2x	2x		2x
<b>MODEL PROBES (2 hydrophilic and 2 hydrophobic)</b>							
PLL tip (NH <sub>3</sub> <sup>+</sup> ):							
In water:	<b>2x</b>	<b>2x</b>	2x	2x	2x		2x
Glycine (NH <sub>2</sub> ) tips:							
In water:		2x					2x
<b>RESIN PROBES</b>							
XAD4:							
In water:	<b>2x</b>	<b>2x</b>	2x HA/FA/HP				
XAD8:							
In water:			3x HA/FA/HP				



MIEX®:								
In water:								
<b>NOM-COATED COLLOID PROBES (Penwhirn 2005 source only on probe)</b>								
HAF-XAD8								
In water:								
FAF-XAD8								
In water:								
HPiA-XAD4								
In water:								

## **Chapter 4                      Results and Discussion part 1 - Calcite Adhesion**

### **4.1 Substrate topography characterization**

Surface topography of all the materials was assessed using AFM in imaging mode. Figure 4.1 shows 2D AFM topographical images of all materials and their respective Z range values, determined using the AFM software. The 2D images showed 0.1 mm gold, 0.3 mm gold and MF steel were predominantly uniform, with a few abrasion marks with widths ranging from 0.1 to 50  $\mu\text{m}$  due to handling. MF steel was polished by the manufacturer, giving a typically homogeneous finish that was absent of any surface asperities. Both 2D images of the rough steel samples were illuminated using the AFM software due to the very poor contrast of their respective height images (see Appendix C for their height images). RF steel displays long cavities, with trenches up to several hundred nm deep that were continuous along the pipe. The trenches also varied in width from 0.1 to 2-3  $\mu\text{m}$ . In contrast SB steel gave a non-random roughness profile, and because the Z-range was 1000 nm, the asperities were much larger than the cavities on RF steel. This was because SB steel was prepared by a process termed ‘sandblasting’, a process in which compressed air (or an abrasive) is blown against the substrate to produce a highly roughened finish. In contrast RF steel was prepared by mechanically abrading with an abrasive (not known), by the manufacturer (Model Products Ltd).

Of the group II materials, Graphit-iC, Dymon-iC and TiN had grainy microstructures that were typical of coatings produced by conventional chemical vapour deposition (CVD) (Perry, 2000). The grains on Dymon-iC were smaller, uniform and ranged from 0.1-0.2  $\mu\text{m}$ , while those on TiN and Graphit-iC range from 0.2 to 0.5  $\mu\text{m}$ . Dymon-iC is produced in a plasma enhanced CVD process using a hydrocarbon gas precursor, with a greater proportion of  $\text{sp}^3$  than  $\text{sp}^2$  bonds (Field *et al.*, 2004). It is thought the dense amorphous grains are due to the formation of a lubricious graphite-like transfer layer formed during sliding between the counterpart and the coating (Field *et al.*, 2004).

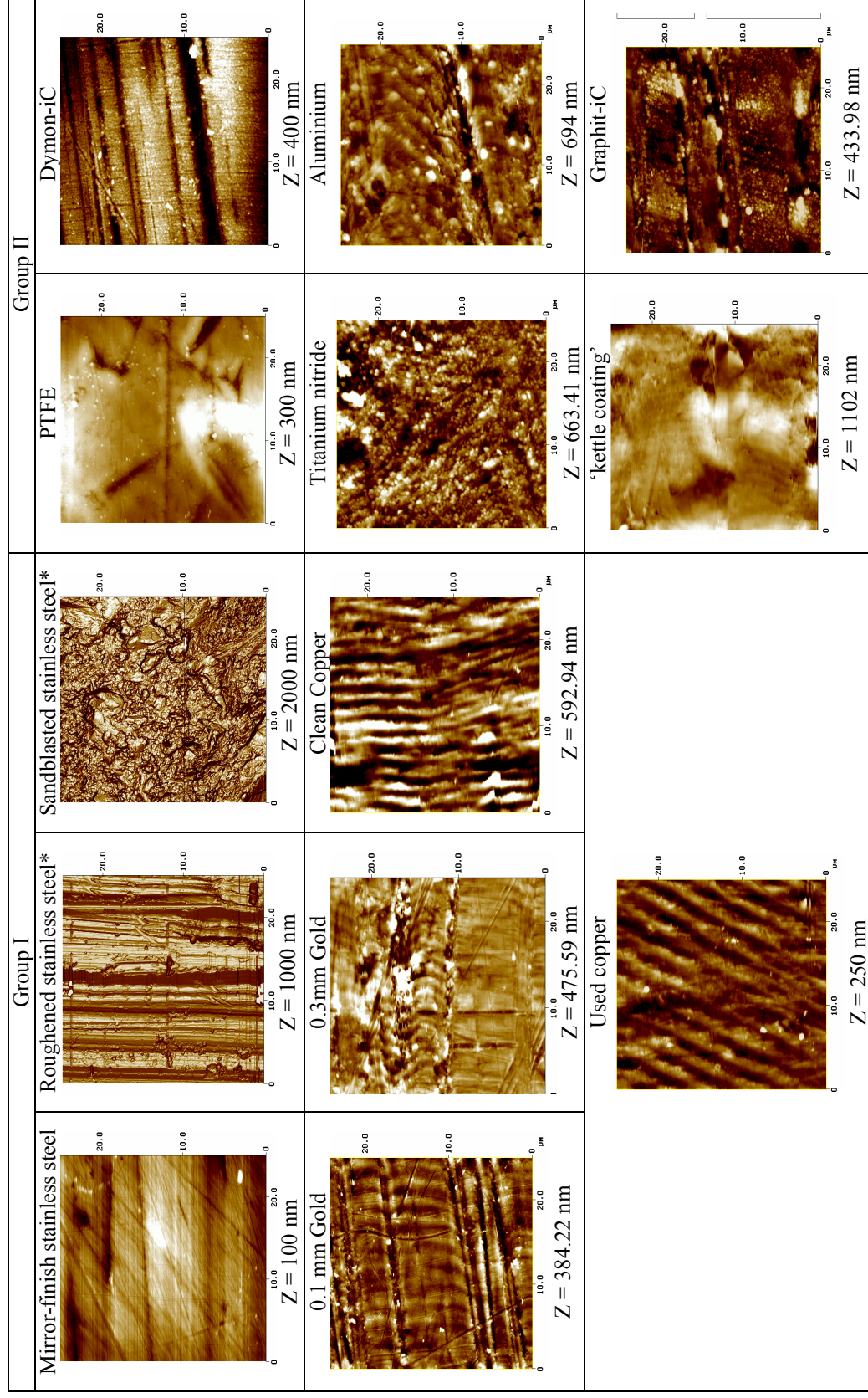


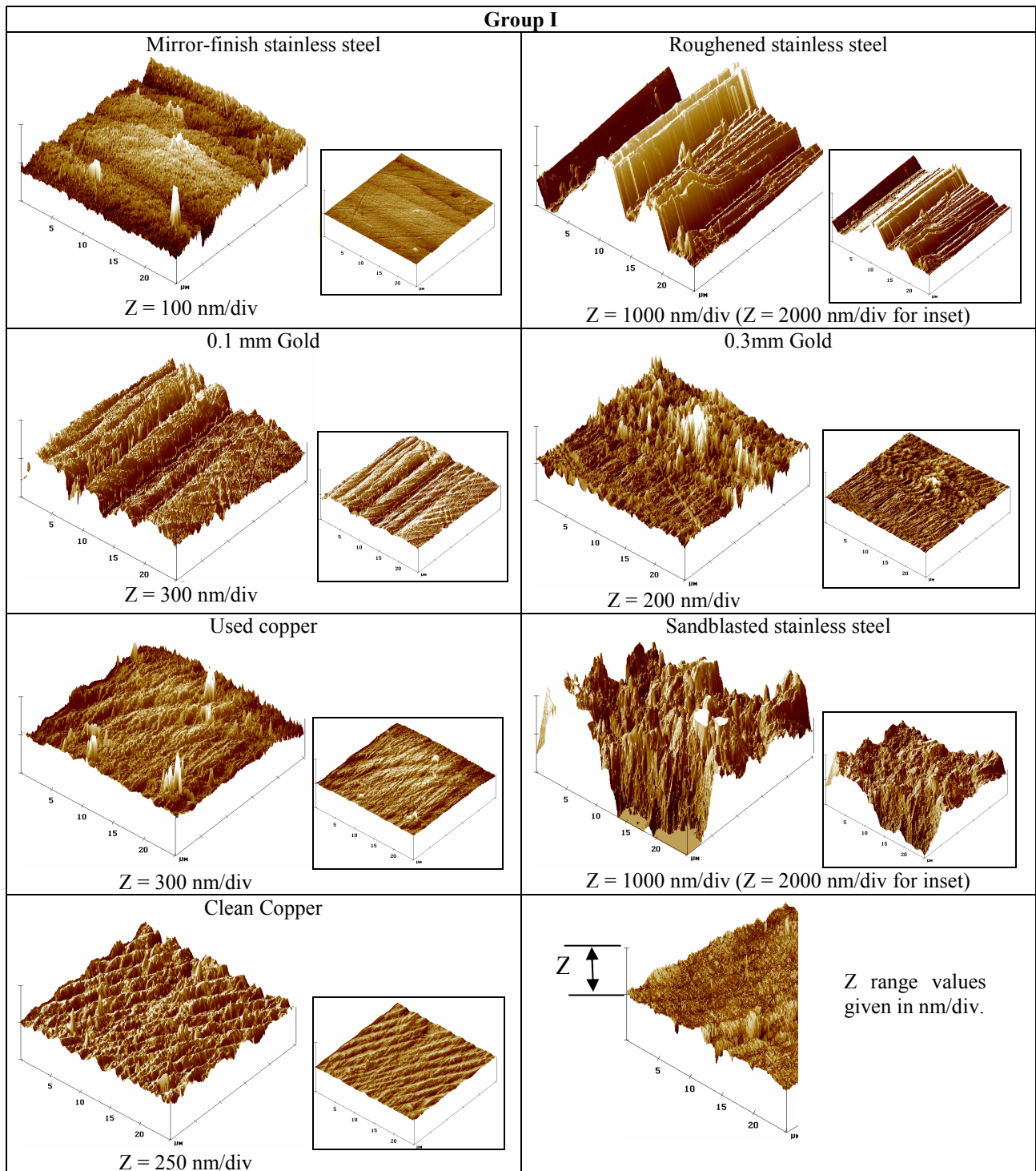
**Figure 4.1.** 2D AFM topographic images of all substrates performed in DI water using contact mode imaging.

\* Image produced using a combination of height and illumination to show greater clarity. See Appendix C for the non-illuminated image.

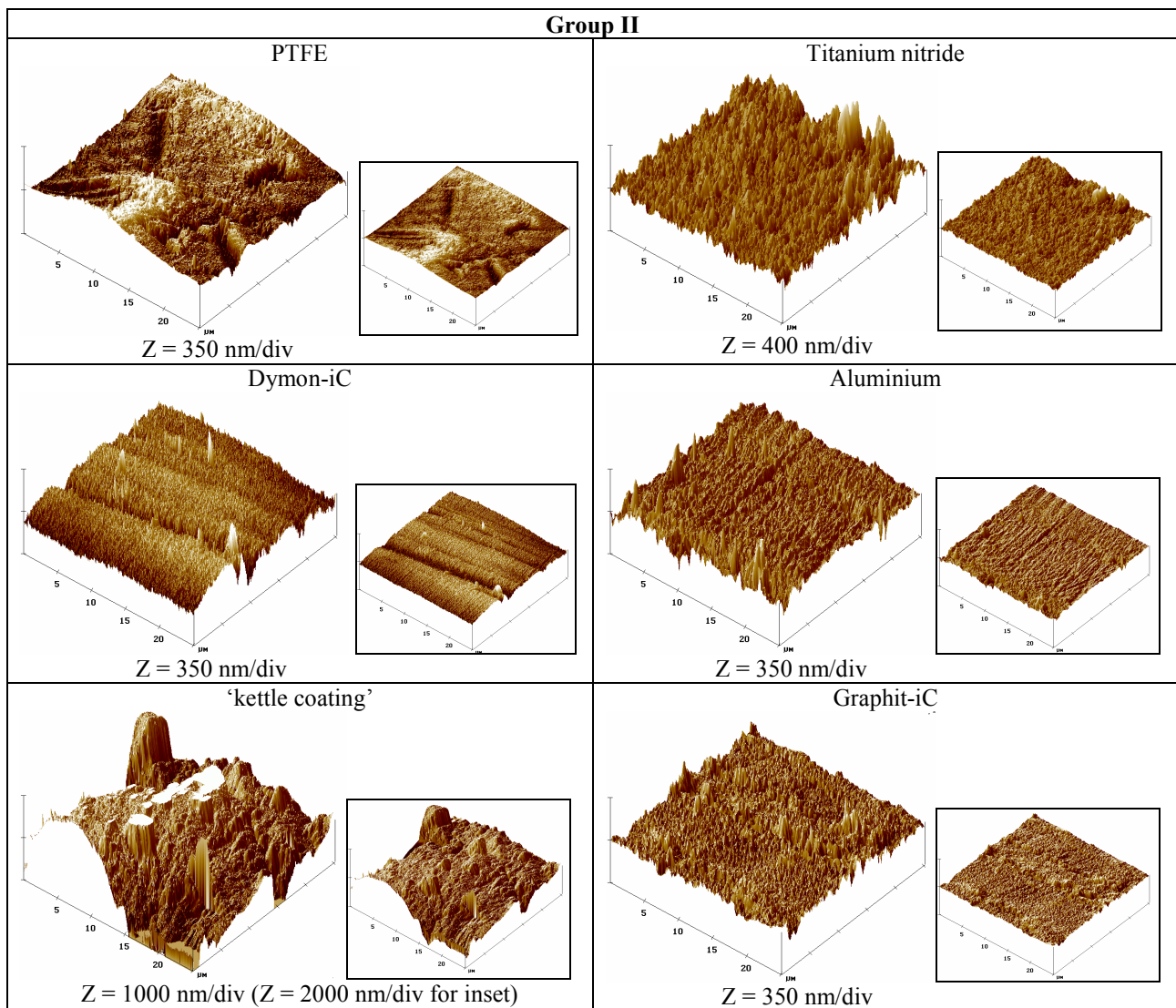
The Graphit-iC coating appears more heterogeneous although the coating itself was thicker. Aluminium, ‘kettle coating’, clean copper and used copper presented a coarse surface finish with larger asperity heights ranging from 0.1 to 0.5  $\mu\text{m}$ . A more detailed description of the materials will be provided with their 3-D images.

Figure 4.2 shows 3D-AFM images of all substrate materials, with close-up images giving more detailed information while inset images ( $Z = 1000 \text{ nm/div}$  unless stated otherwise) permit better comparison between surface. From group I MF steel was most uniform, with extremely shallow trenches. Trenches were more visible on the gold-0.1 sample, although they were not typical of the coatings itself. The large asperity peaks of the gold-0.1 also comprised of a certain degree of microroughness. Both copper samples gave a wavy-like surface structure, although the unused sample gave reduced height values of asperity peaks. RF steel gave a carved appearance on a much grander scale with much greater asperity peak heights, as displayed on both 3D images. However, SB steel gave a grainy appearance with much larger asperities compared to all the other surfaces, which also appeared more random relative to RF steel. The Z ranges for both these images were increased compared to the rest of the group materials due to the tall asperity heights.

In group II, ‘k. coating’ gave asperities that were similar to SB steel, along with a large distribution of asperities up to several  $\mu\text{m}$  in width and 2  $\mu\text{m}$  in height. PTFE exhibited a number of cavities ( $\sim\mu\text{m}$  deep) possibly caused by a combination of sample handling and the inherent roughness of the base material. In contrast, the grainy microstructures on Dymon-iC were much smaller and denser than Graphit-iC, and were highly uniform even at 300 nm. Furthermore, cavities on Dymon-iC were visible and up to 200 nm deep. Aluminium and TiN gave a similar distribution of surface asperities,







**Figure 4.2.** 3D AFM topographic images of group I and II materials performed in DI water using contact mode. Z-range of inset images is 1000 nm for comparative purposes unless stated otherwise.

Table 4.1 gives measured average roughness ( $R_a$ ) values of all materials obtained from five images of each surface, and the difference in surface area compared to the nominal area of an atomically flat surface.  $R_a$  is the average roughness of profile height deviations (peaks and valleys) from the mean line.  $R_a$  was also selected because it was least affected by much larger asperities present on SB steel, RF steel and 'k. coating'.

**Table 4.1.** List of surface roughness values ( $R_a$ ) of materials from lowest to highest and % surface area difference.  $R_a$  values calculated from an average of five images of 25 x 25  $\mu\text{m}$ .

Material	Group	Measured $R_a$ values (nm)	Surface area difference (%)
Gold-0.1mm	I	$8.74 \pm 2.56$	$0.50 \pm 0.71$
MF steel	I	$10.48 \pm 12.24$	$0.33 \pm 0.58$
PTFE	II	$12.67 \pm 3.75$	$0.50 \pm 0.71$
Gold-0.3mm	I	$13.64 \pm 3.18$	$0.72 \pm 0.57$
Copper	I	$15.36 \pm 6.28$	$0.63 \pm 0.31$
Graphit-iC	II	$18.53 \pm 0.03$	$2.45 \pm 0.45$
Dymon-iC	II	$27.54 \pm 33.96$	$2.57 \pm 1.92$
TiN	II	$30.66 \pm 0.54$	$3.89 \pm 1.19$
Aluminium	II	$32.13 \pm 15.51$	$2.69 \pm 0.81$
'K. coating'	II	$75.10 \pm 25.63$	$8.27 \pm 5.13$
RF steel	I	$167.42 \pm 83.08$	$14.13 \pm 2.91$
SB steel	I	$225.41 \pm 104.89$	$27.66 \pm 19.47$
Copper-used	I	$278.20 \pm 68.61$	$26.73 \pm 6.77$

Generally, group I materials gave a greater range of  $R_a$  values from 8.74 to 278.20 nm, while group II materials were less dispersed in the 16 to 97 nm range. Literature  $R_a$  values of stainless steels indicate they can be produced with a wide range of  $R_a$  values depending on their application (Santos *et al.*, 2004). It can be seen that RF steel, 'k. coating', SB steel and used copper gave high  $R_a$  values. This was because the latter two materials were covered by abrasion marks with peak height and widths ranging up to several  $\mu\text{m}$ . The high  $R_a$  values were also reflected in their additional surface area, with SB steel giving almost an additional 50% when the standard deviation is also considered.

From group II 'k. coating' produced the highest  $R_a$  value of  $75.10 \pm 25.63$  nm, which was indicative of its 3D image. This coating was designed with a certain degree of roughness by the manufacturer to enhance bubble formation and reduce material scaling. Measured  $R_a$  values of Graphit-iC ( $18.53 \pm 0.03$  nm) and Dymon-iC ( $27.54 \pm 33.96$  nm) made them not too dissimilar to MF steel, although the presence of trenches on Dymon-iC was the cause of its greater  $R_a$  value. The measured  $R_a$  of TiN was 30.66 nm, which was similar to aluminium, and the AFM images indicated they exhibited an almost identical surface finish.

## 4.2 Contact angle measurements and surface free energy calculation

Static contact angles ( $\theta$ ) were measured instead of advancing and receding contact angles because droplet volume was limited due to the curvature of the 12 mm pipe samples. Table 4.2 shows surface free energies of the six probe liquids used in the present study.

**Table 4.2.** Surface free energies and their components (in  $\text{mJm}^{-2}$ ) of commonly used probe liquids (Van Oss, 2003).

Liquid	$\gamma^L$	$\gamma^{LW}$	$\gamma^-$	$\gamma^+$
1-bromonaphthalene (B)	44.4	44.4	0	0
Water (W)	72.8	21.8	25.5	25.5
Glycerol (G)	64	34	57.4	3.92
Ethylene glycol (EG)	48	29	47	1.92
Formamide (F)	58	39	39.6	2.28
Dimethylsulfoxide (D)	44	36	30	0.5

Figure 4.3 shows the mean contact angles of six probe liquids with different polarities on all materials. All materials gave low average contact angle values with 1-bromonaphthalene due to its low surface tension ( $\gamma^L = 44.4 \text{ mJ.m}^{-2}$ ) caused by its apolar properties that are dominated by vdW forces only. Contact angles ranged from 12 to 25° and 19 to 44° for groups I and II respectively. Group I materials were wetted by the apolar 1-Br due to their high surface free energies (Israelachvili, 1992). ‘K. coating’, PTFE and aluminium produced were less wetted than their metal and carbon-based counterparts.

Water produced the largest average contact angle of  $68.62 \pm 8.44^\circ$  due to the high surface tension ( $\gamma^L = 72.8 \text{ mJ.m}^{-2}$ ). Generally, hydrophobic materials were ‘k. coating’, PTFE, copper, and other materials seen on the right of each group ( $\theta > 65^\circ$ ). Copper contact angle was similar to that obtained by Zhao *et al.*, (2005) of  $80.9^\circ$ . Graphit-iC and Dymon-iC gave contact angles of  $50.67 \pm 4.84^\circ$  and  $59.30 \pm 5.45^\circ$ , respectively, and were relatively hydrophilic ( $\theta < 65^\circ$ ) when compared to other materials. In agreement with Ostrovskaya *et al.*, (2003) using hydrogenated carbon coatings, the hydrogenated Dymon-iC coating was less hydrophilic than non-hydrogenated Graphit-iC. Smaller contact angles were observed with D than E, G and F.



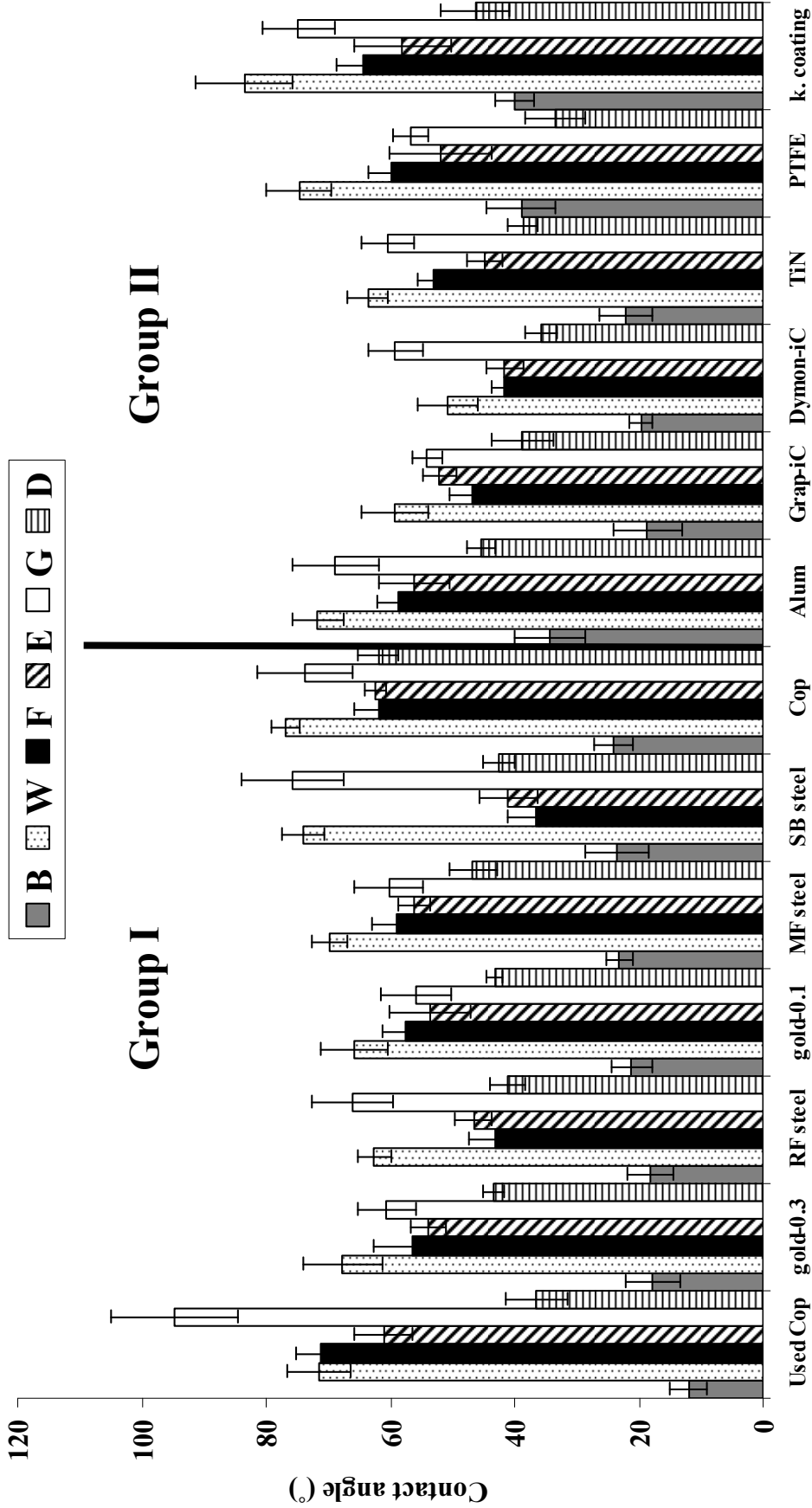


Figure 4.3. Measured contact angles of all materials using a total of six probe liquids. Contact angles are shown in order of their angle with B.

For dimethylsulfoxide (D) the  $\gamma^-/\gamma^+$  ratio is high, and is a potent hydrogen acceptor that forms hydrogen bonds with water that was present as a thin film on each substrate (Gordeliy *et al.*, 1998). Thus larger contact angles with D indicate greater electron-donating behaviour on increasingly hydrophobic surfaces due to the absence of water. This was apparent for clean Cu and 'k. coating'. Contact angles with F did not show as much variation between the two groups. However, SB steel and RF steel were wetted by F, with contact angles of  $36.79^\circ$  and  $43.15^\circ$ , respectively. Similar contact angles for F and EG probe liquids were obtained due to their similar acid-base components (Van Oss, 2002).

#### 4.2.1 Calculation of $\gamma^{LW}$ (apolar) surface free energies

The  $\gamma^{LW}$  component was calculated using Equation 3.1. Table 4.3 shows  $\gamma^{LW}$  components of group I and II materials using 1-bromonaphthalene.

**Table 4.3.** Summary of  $\gamma^{LW}$  surface free energy components of group I and group II materials.

Group I	$\gamma^{LW}$ (mJ.m <sup>-2</sup> )	Group II	$\gamma^{LW}$ (mJ.m <sup>-2</sup> )
Copper	$40.56 \pm 0.87$	'K coating'	$34.56 \pm 1.40$
MF steel	$40.88 \pm 0.62$	PTFE	$34.96 \pm 2.42$
SB steel	$40.67 \pm 1.51$	Aluminium	$36.91 \pm 2.21$
RS steel	$42.13 \pm 0.88$	TiN	$41.09 \pm 1.34$
Gold-0.3	$42.19 \pm 1.14$	Graphit-iC	$41.94 \pm 1.36$
Gold-0.1	$41.39 \pm 0.87$	Dymon-iC	$41.82 \pm 0.45$
Used Copper	$43.38 \pm 0.45$		

All samples gave similar  $\gamma^{LW}$  values except PTFE ( $34.96 \text{ mJ.m}^{-2}$ ) and kettle coating ( $34.55 \text{ mJ.m}^{-2}$ ) and aluminium ( $36.90 \text{ mJ.m}^{-2}$ ), which were markedly smaller. Low  $\gamma^{LW}$  of aluminium was similar to that obtained by Holysz (2000) of  $37.4 \pm 0.2 \text{ mJ.m}^{-2}$  using aluminium sheets, due to the presence of an oxide ( $\text{Al}_2\text{O}_3$ ) layer. Unlike the rest of the metals, aluminium is a d-block element which has reduced electron density, thus giving lower  $\gamma^{LW}$  values than neighbouring metals. Low  $\gamma^{LW}$  values for PTFE was due to its reduced Hamaker constant ( $3.8 \times 10^{-20} \text{ J}$ ), caused by a reduced density of fluorocarbons at the terminals. All other materials produced  $\gamma^{LW}$  values ranging from 40 to  $43 \text{ mJ.m}^{-2}$ , of which group I metals were similar to the literature (Radelczuk *et al.*, 2002; Förster and Bohnet, 2000), indicating the  $\gamma^{LW}$  values were accurate. High  $\gamma^{LW}$  values were typical for metal substrates due to strong vdW forces between tightly bound transition metal atoms, with Hamaker constant values ranging from  $30\text{-}50 \times 10^{-20} \text{ J}$  (Israelachvili, 1992). TiN,

Graphit-iC and Dymon-iC gave  $\gamma^{LW}$  values of 41.09, 41.94 and 41.82 mJ.m<sup>-2</sup>, respectively. These values were much greater than the three non-PE-CVD materials. Jacquot and Takadoum, (2001) showed markedly lower  $\gamma^{LW}$  values for TiN and Graphit-iC of  $33.2 \pm 0.4$  and  $37.3 \pm 0.4$  mJ.m<sup>-2</sup>, respectively. This was attributed to larger contact angles with B, possibly caused by an increase in hydrogen content of their tested samples.

#### 4.2.2 Calculation of $\gamma^+$ and $\gamma^-$ (polar) components using the graphical plot method

The graphical plot method is based on an x-y plot of equation 3.1a against 3.1b using a minimum of two polar liquids, where one liquid must be water (Van Oss, 2003). Figure 4.4 shows the affect of each liquid of five on the slope ( $\gamma^+$ ) and intercepts ( $\gamma^-$ ) for Dymon-iC, Graphit-iC and ‘used copper’, where the least squares method was applied to obtain the trend line. As water must be one of the polar liquids, each of the remaining liquids will have a significant effect on the polar components.

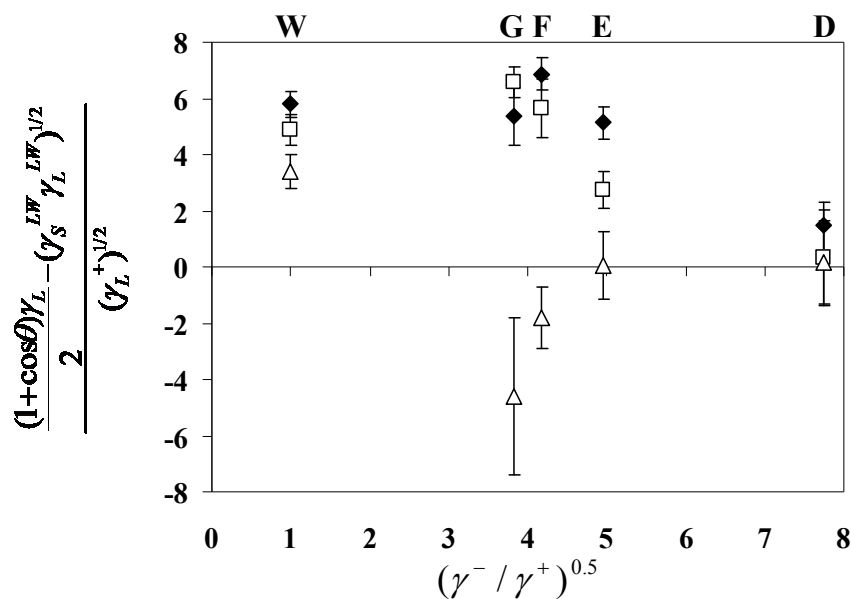


**Figure 4.4.** Linear plot to determine the Lewis acid and basic components of Dymon-iC (♦), Graphit-iC (□) and ‘used copper’ (Δ) with SD values. Locations of  $(\gamma^-/\gamma^+)^{1/2}$  values for probe liquids are highlighted above the plot.

It was clearly observed the gradient used to measure  $\gamma^+$  for ‘used copper’ was significantly affected by the non-aqueous polar liquids of G and F, when compared to the position of D in the plot. This was in contrast to the amorphous carbon coatings, which gave similar values for G, F and E relative to W. As a result, depending on the strength of

the interaction between a surface and the probe liquid, polar components will vary according to the number and type of probe liquids used. The plot also shows several liquids could be used, although there is a minimum of two liquids.

#### 4.2.2.1 Use of liquid triplets

The SFE values were calculated from four sets of liquid triplets (i.e. four sets of polar liquid pairs used in the graphical plot shown in Figure 4.4). Selection of appropriate triplets was based on their condition numbers ( $C_n$ ).  $C_n = \|A\|_1 \cdot \|A^{-1}\|_1$ , where  $\|A\|_1 = \max_j \sum_i |A_{i,j}|$ : Where A is the matrix containing the various surface tension parameters (also see Eq. 3.2), A high  $C_n$  means a strong sensitivity to solutions (Della Volpe and Siboni, 2000).  $C_n$  values are based on appropriate selection of a liquid triplet having an apolar (liquid 1), polar (liquid 2) and non-aqueous polar (liquid 3) properties based on their assigned  $\gamma^{LW}$ ,  $\gamma^+$  and  $\gamma^-$  values by Van Oss and Good (1986). The triplets used and their respective condition numbers are given in Table 4.4. Problems arise when ‘ill-conditioned’ triplets are used, which occurs with triplets having  $C_n$  values above 10. Based on  $C_n$  values below 10, Table 4.4 gives four acceptable triplets where the B-W-E triplet should give the least number of data errors.

**Table 4.4.** Comparison of condition numbers of four triplets (McCafferty, 2002; Della Volpe and Siboni, 2000).

Liquid triplet	Condition number ( $C_n$ )
B-W-E	6.11
B-W-G	6.13
B-W-D	6.83
B-W-F	7.35
Average	6.61

Figure 4.5 shows calculated Lewis acid-base surface energy components using the GP method from four triplets. High  $\gamma^-$  values were routine for the Lewis acid-base technique, where surface tension values assigned to the non-aqueous polar probe liquids (E, F, G and D) by Van Oss and colleagues (1986) have higher  $\gamma^-$  values. Large error bars were typical for the  $\gamma^+$  component because non-aqueous polar liquids were predominantly basic while water had equal values for  $\gamma^+$  and  $\gamma^-$ . Group I materials generally exhibited

greater  $\gamma^+$  values than group II for all triplets. This was because from group I the transition metals were hydroxylated and therefore amphoteric in character.

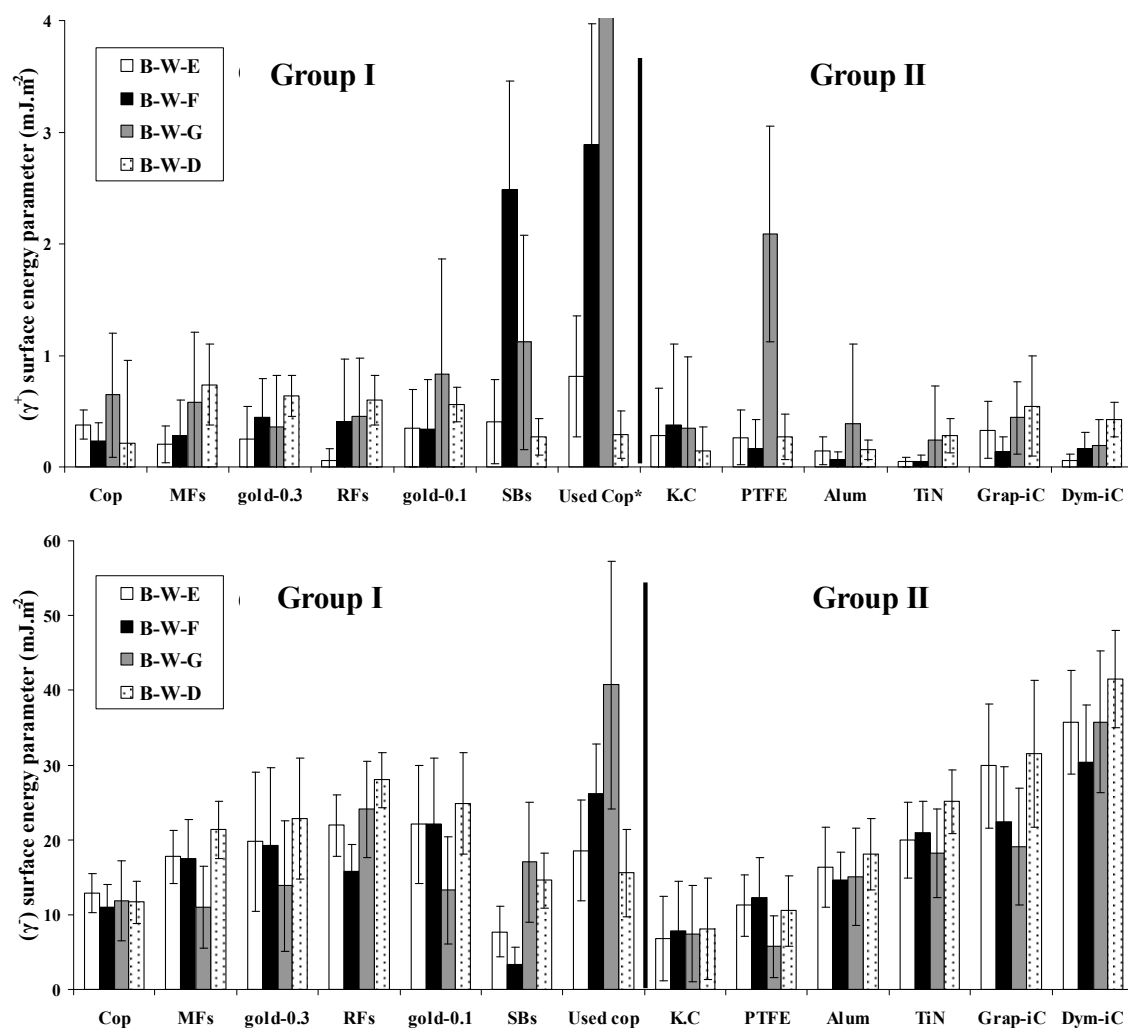


**Figure 4.5.** Calculated  $\gamma^+$ , (top) and  $\gamma^-$  (bottom) SFE components of materials using the graphical plot method (McCafferty, 2002), obtained from four sets of triplets. \*Used Copper gave  $\gamma^+$  of  $9.09 \pm 4.57$  mJ.m<sup>-2</sup> for BWG triplet. (Cop = Copper; MFs = MF steel; RFs = RF steel, SBs = SB steel, K.C. = kettle coating, Dym = Dymon-iC).

Glycerol from the B-W-G triplet significantly increased the  $\gamma^+$  component for 'used copper', PTFE and SB steel to an extent, compared to the other triplets. Formamide (from B-W-F) increased  $\gamma^+$  for used copper and SB steel more than the other surfaces. This was interesting because both surfaces gave high  $R_a$  values (Table 3), indicating surface asperities composed of polar groups. However the B-W-D triplet substantially reduced their  $\gamma^+$  component, which was unexpected because dimethylsulfoxide was also a highly basic probe liquid, Considering the contrast in  $\gamma^+$  and  $\gamma^-$  values given by the triplets on SB

steel and used copper, this may also be attributed to their highly roughened finish, which may be more sensitive to the surface tension of the liquid than their acid-base effects. Bearing in mind the corroded copper sample had previously been used during scaling experiments (MacAdam, 2005), the surface chemistry was expected to be much different to its unused counterpart. Discolouration of the corroded copper sample will also indicate the presence of  $\text{Cu}(\text{OH})$ ,  $\text{CuCO}_3$  and  $\text{Cu}(\text{I})$  oxides that are sensitive to the polar liquids, thus contributing to deviations in the  $\gamma^+$  and  $\gamma^-$  components. The high hygroscopicity of dimethylsulfoxide also provides greater interaction with polar groups via hydrogen bonding. Surface asperities on SB steel are also likely to adsorb organic contaminants from the atmosphere. For instance, carbon-based groups on SB steel may behave as electron acceptors, thus increasing the  $\gamma^+$  component from  $0.45 \text{ mJ.m}^{-2}$  for unmodified MF steel to  $1.09 \text{ mJ.m}^{-2}$ . Apart from SB steel and ‘used copper’ both  $\gamma^+$  and  $\gamma^-$  values from the rest of the samples gave similar values for all sets of triplets. Clean copper was least basic having average  $\gamma^-$  value of  $11.81 \pm 2.27 \text{ mJ.m}^{-2}$  compared to its used counterpart of  $25.21 \pm 5.88 \text{ mJ.m}^{-2}$ . The two gold surfaces gave expectedly similar average  $\gamma^-$  and  $\gamma^+$  values ranging from  $0.14$  to  $0.52 \text{ mJ.m}^{-2}$  and  $18.89$  to  $20.52 \text{ mJ.m}^{-2}$ , respectively. This was because the only variation in their preparation was coating thickness, and the contact angle measurement is a predominantly surface-sensitive technique. In group II ‘k. coating’ was least basic followed by PTFE.

Table 4.5 gives calculated acid-base ( $\gamma^{\text{AB}}$ ) values from the four triplets. Used copper and gold gave high values for the combined acid-base component.

**Table 4.5. Calculated acid-base ( $\gamma^{\text{AB}}$ ) SFE values obtained from the average of four triplets.**

<b>Group I</b>	<b><math>\gamma^{\text{AB}} (\text{mJ.m}^{-2})</math></b>	<b>Group I</b>	<b><math>\gamma^{\text{AB}} (\text{mJ.m}^{-2})</math></b>
<b>MF steel</b>	5.26	<b>K. coating</b>	2.98
<b>SB steel</b>	5.50	<b>Aluminium</b>	3.34
<b>RF steel</b>	5.56	<b>TiN</b>	3.35
<b>Gold-0.3mm</b>	5.57	<b>PTFE</b>	4.20
<b>Gold-0.1mm</b>	6.31	<b>Dymon-iC</b>	5.34
<b>Clean copper</b>	7.18	<b>Graphit-iC</b>	6.07
<b>Used copper</b>	16.89		

Of the non-metals, Graphit-iC, PTFE and Dymon-iC gave high acid-base component values, but these values were highly dependent on their basic surface free energy

component (Figure 4.5). When calculated SFE values were compared to the literature, there was good consistency for most materials except copper. However, it should be emphasized there have been few attempts to use multiple triplets. So the actual SFE values were dependent on the triplets as well as the approach used such as the geometric-mean, harmonic mean or Lewis acid-base method, which was used in this study (van Oss, 2002). Observation of the total SFE values did not provide any additional information regarding specific interactions at the liquid-surface interface so this data was omitted.

#### 4.2.2.2 Use of multiple liquids

Figure 4.6 shows SFE values of selected group I and II materials with two to five liquids used in the graphical plot. For most materials (group I and II) there was no observable pattern on the affect of liquid number on the  $\gamma^+$  component. However, dimethylsulfoxide caused a significant increase in  $\gamma^+$  for selected materials, with a more consistent increase in the  $\gamma^-$  component. This was largely because of the low surface tension of dimethylsulfoxide, where all the solid substrates gave lower contact angles with this liquid than any other non-aqueous probe liquid. Although all surfaces were sensitive to the surface tension of dimethylsulfoxide, the group I materials were more sensitive to its polar groups. And while the  $\gamma^-/\gamma^+$  ratio of 7.75 for dimethylsulfoxide assigned by Van Oss and Good (1986) appeared to be high, more recent acid-base components given by Della Volpe and Siboni (2000) gave a much greater  $\gamma^-/\gamma^+$  ratio of 143.02. This caused the locations of the remaining non-aqueous polar liquids to be bunched together, effectively making dimethylsulfoxide disproportionately dominate the slope and the  $\gamma^+$  component. Therefore, one could only use acid-base components given by Della Volpe and Siboni (2000) in the absence of dimethylsulfoxide as a probe liquid. For the purpose of this study, it was thought the strong monopolarity of dimethylsulfoxide was necessary for calculating the  $\gamma^+$  surface tension component, and as a result the surface tension components given by Della Volpe and Siboni (2000) were not used for the remainder of this investigation.

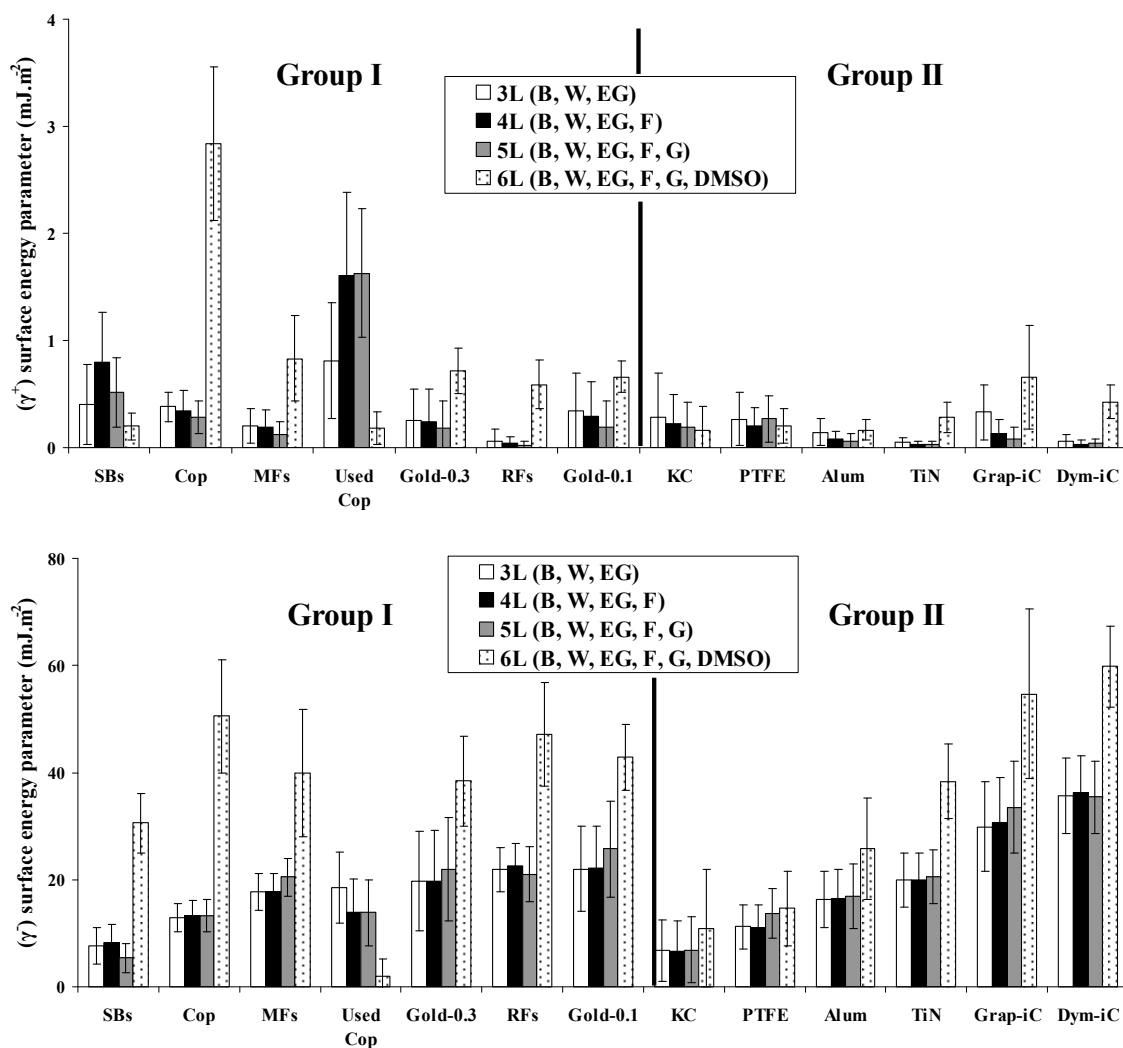


Figure 4.6. The calculated  $\gamma^+$  (top) and  $\gamma^-$  (below) values obtained using 3, 4, 5 and 6 liquids from the GP method.

#### 4.2.2.3 Comparison of the triplet average and sextet methods

Figure 4.7 shows direct comparisons of  $\gamma^-$  and  $\gamma^+$  values obtained from the triplet and sextet methods for selected materials. It was apparent that calculated  $\gamma^-$  and  $\gamma^+$  values were reduced and increased, respectively, using the triplet average method for most materials. Some differences, such as the  $\gamma^+$  values for used copper and SB steel were significant, while others such as 'k. coating' were not. Changes in the  $\gamma^-$  values for MF steel and Graphit-iC were also significant. Because of these, it was apparent that one of the methods either underestimated or overestimated the acidic and/or basic components of substrates.



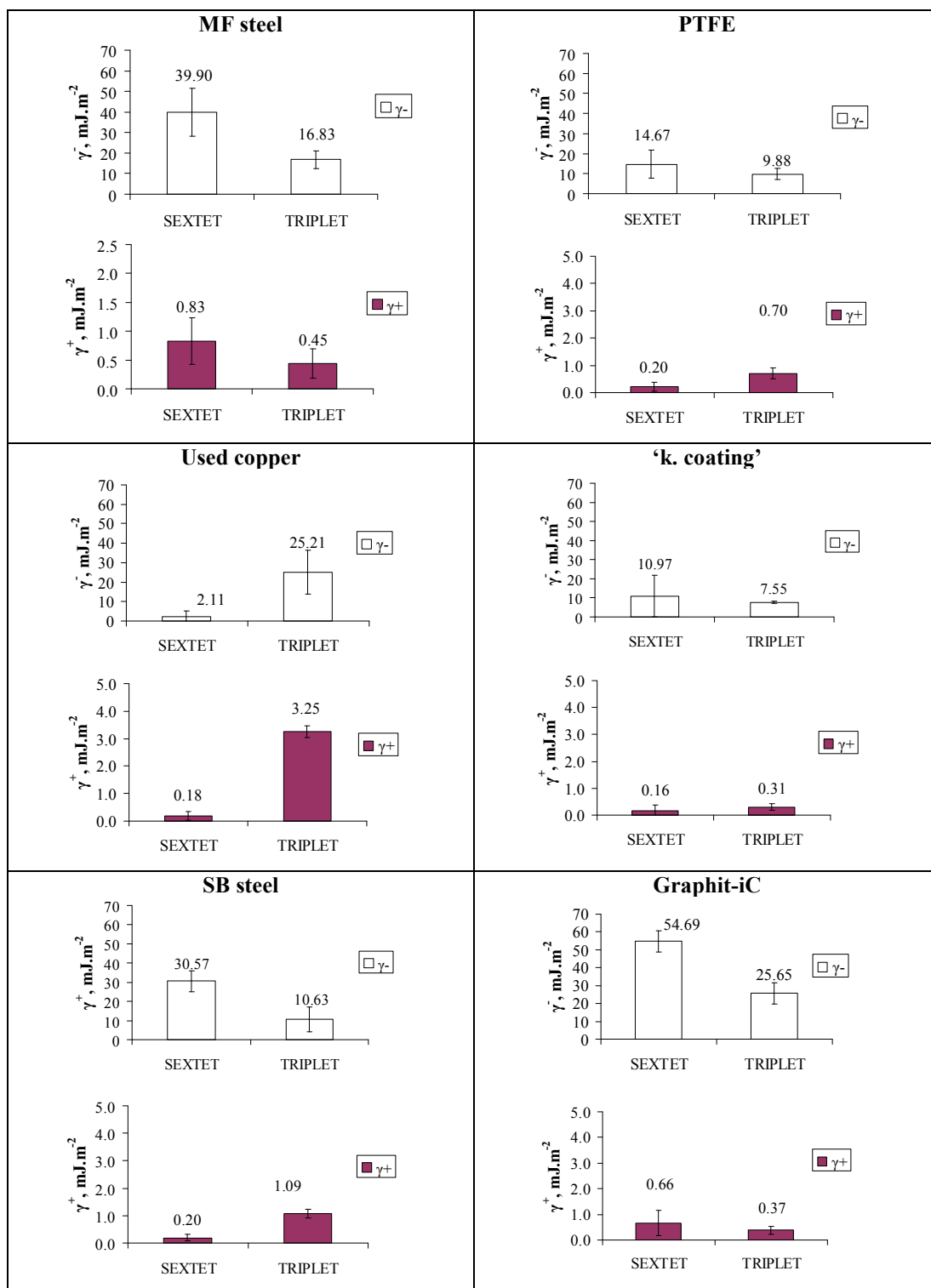


Figure 4.7. Comparison of the  $\gamma^+$  and  $\gamma^-$  components of selected group I and group II materials using the sextet and triplet methods (in mJ.m<sup>-2</sup>).

It was found the main advantage of the triplet average method was that not a single liquid dominated both acidic and basic components. This was imperative because the rationale behind triplet selection was to reduce the sensitivity of probe liquids on material acid-base components. Furthermore, the triplet average method gave identical acid/base values to the matrix method, which has been the routine methodology used in most SFE calculations. In addition, B-W-E, B-W-F and B-W-G triplets gave very large error values for the  $\gamma^+$  component, which frequently exceeded mean  $\gamma^+$  values. However, the B-W-D triplet gave lower error values for  $\gamma^+$ , thus stabilizing them. As a result, D (non-aqueous polar liquid) should be included in a triplet without significant contribution to the deviations calculated from other triplets. D also appears to be a critical liquid due its unique aprotic property (absence of H), which was most sensitive to hydrated surfaces. As F, E, G and W form hydrogen bonds internally, dimethylsulfoxide ( $\text{CH}_3\text{-S(O)-CH}_3$ ) can only undergo H-bonding to host surfaces. Thus acidic sites may be more sensitive to D than the other polar liquids, as confirmed by the high  $\gamma^-/\gamma^+$  ratio of 143.02 given by Della Volpe and Siboni (2000). Finally, the triplet average method gave more robust sets of  $\gamma^-$  data because both polar liquids (W and E, F, G or D) gave an equal contribution to the plot.

The main advantage of using multiple liquids (3 or more in plot) was the contribution of each liquid on the slope and intercept was graphically observed (McCafferty, 2002). However, D appeared to have an adverse effect on the  $\gamma^-$  component for most materials. When four/five liquids (4L/5L) were used (excluding D) in the graphical plot, the  $\gamma^-$  component did appear robust enough because there was no significant change in basicity of the materials. With the absence of D the 4L/5L sets gave low  $\gamma^+$  values for most group I materials, which did not seem to reflect their actual acidic (cationic) character. For instance, the stainless steels and clean copper were expected to have more acidic sites by virtue of the amphoteric character of  $\text{Fe}_2\text{O}_3$ ,  $\text{Cr}_2\text{O}_3$  and  $\text{CuO}$ . When D was used as the sixth liquid it correctly increased the ‘relative’  $\gamma^+$  values of these materials but also their  $\gamma^-$  component. The use of dimethylsulfoxide in the plot gave a reduction in  $\gamma^-$  for the used copper sample with little effect on unused copper. This may have been caused by greater quantities of  $\text{Cu(OH)}_2$  on used copper, which formed hydrogen bonds with

dimethylsulfoxide. In fact, unused copper and used copper gave opposing acid-base character from the two different methods, possibly due to differences in oxidation. A summary of the advantages/disadvantages of each method are given in Table 4.6.

**Table 4.6. Summary of advantages and disadvantages of using the triplet average and sextet methods for calculating material SFE values.**

Method	Advantages	Disadvantages
<b>Sextet (or multiple liquids)</b>	<ul style="list-style-type: none"> <li>• Dominance of single liquid (e.g. D) can be observed.</li> <li>• More than three liquids can be displayed in plot.</li> <li>• Error values are smaller in absence of D.</li> <li>• Other liquids can be used instead of D.</li> </ul>	<ul style="list-style-type: none"> <li>• SFE were dominated by D, without any increase in <math>\gamma^+</math> values.</li> <li>• Errors in <math>\gamma^+</math> and <math>\gamma^-</math> values were amplified with D.</li> <li>• D found to be critical for SFE calculation.</li> <li>• Data cannot be compared to matrix method.</li> </ul>
<b>Triplet average</b>	<ul style="list-style-type: none"> <li>• No single liquid dominance of <math>\gamma^+</math> and <math>\gamma^-</math> values.</li> <li>• D had no adverse effect on <math>\gamma^+</math> and <math>\gamma^-</math> values.</li> <li>• Use of D increased relative acidity of mineral oxide surfaces.</li> <li>• Average values are no different to matrix method.</li> <li>• Both polar liquids dominate plot, giving more robust linear regression.</li> </ul>	<ul style="list-style-type: none"> <li>• Error values over 100% were obtained due to changes in gradient for certain triplets. This can be resolved by using D in another triplet.</li> </ul>

It was found the selection of either method (triplet/sextet or multiple liquids) hinged on whether D would be used in the calculation. As explained earlier, dimethylsulfoxide was found to play a pivotal role for determining acidic behaviour of amphoteric surfaces. Therefore, these findings suggest the triplet average method was most appropriate because dimethylsulfoxide was sensitive to acidic (cationic) sites, while also reducing the error values. The findings also suggest previous attempts in the literature to calculate the SFE components of amphoteric surfaces such as mineral oxides may have underestimated the contribution of  $\gamma^+$  to its acid-base ( $\gamma^{AB}$ ) character. It must be highlighted that these findings were based on the Van Oss and Good liquid SFE components (Table 4.2).

#### 4.2.3 Theoretical calculation of adhesion using roughness model

The work of adhesion ( $W_{132}$ ,  $\text{mJ.m}^{-2}$ ) provides a theoretical estimation of the energy required to separate two surfaces (subscript 1 and 2) from contact in a medium (subscript

3). Having calculated SFE for all base materials, the SFE of calcite was calculated using B-W-E and B-W-E-F liquid sets. These are given at the top two rows of Table 4.7, and are compared to selected literature values. High  $\gamma^-$  values originate from the presence of electron donor sites, particularly oxygen groups due to  $\text{CO}_3^{2-}$ . In such cases cationic sites ( $\text{Ca}^{2+}$ ) were either fewer in numbers or positioned beneath the surface monolayer of carbonate groups. Furthermore, the van Oss method (1986) inherently shows all organic materials as monopolar, so even though the surface was highly basic, this may have been overestimated by the technique used. So, based on the measured and literature SFE values, calcite was considered to be a basic foulant (adhesive).

**Table 4.7.** SFE values of calcite calculated from contact angle measurements on the calcite {104} face using B-W-E-F probe liquids, using the triplet average and four-liquid graphical method. Measured values are compared to literature. TLW = thin layer wicking.

Method	$\gamma^{\text{LW}}$ (mJ.m <sup>-2</sup> )	$\gamma^+$ (mJ.m <sup>-2</sup> )	$\gamma^-$ (mJ.m <sup>-2</sup> )	Reference
Contact angle (B-W-E)	43.83	0.07	29.55	Measured
Contact angle (B-W-E-F)	43.83	0.05	30.54	Measured
Contact angle (optically pure calcite)	40.20	1.30	54.40	Wu <i>et al.</i> , (1996)
TLW (grounded calcite)	29.10	0.50	31.60	Wu <i>et al.</i> , (1996)
TLW (grounded calcite)	48.00	0	79.00	Holysz and Chibowski, (1994)

The table shows Wu *et al.*, (1996) also performed contact angle measurements on optically clear calcite crystals, but used advancing contact angle measurements. Consequently, they calculated greater  $\gamma^{\text{LW}}$  values due to the greater advancing contact angles measured on calcite. This was because advancing contact angles measure the energy of cohesion vs. energy of adhesion between the solid and liquid. They also calculated higher  $\gamma^+$  and  $\gamma^-$  components because their calcite crystal was almost wetted by formamide and water. This was possibly due to reduced air exposure time of the crystal face between cleavage and contact angle measurements of only several seconds. In the present study, several minutes had elapsed before contact angles were performed on the surface, which would have resulted in the formation of a water film. Interestingly, Wu *et al.*, (1996) calculated different  $\gamma^{\text{LW}}$  values on ground calcite using thin layer wicking

(TLW) method due a change in surface properties. Thin-layer wicking is performed by measuring the rate of capillary rise of the probe liquid through a bed or layer of packed particles. Using this method acid-base values were similar possibly due to greater exposure of the ground calcite to water vapour. Ground calcite may also exhibit greater  $\gamma^+$  and  $\gamma^-$  components than the calcite face due to increased surface area.

Of the other TLW methods used in literature, Holysz and Chibowski, (1994) gave greater  $\gamma^-$  values on ground calcite with the B-W-F triplet. The precise preparation method was not given, but it was likely that calcite was left at room temperature for several hours before wicking was performed. This may have resulted in greater penetration depth of the probe liquids, resulting in higher  $\gamma^-$  values.

Theoretical adhesion force was calculated using the Rabinovich roughness model (equation 2.11) (Rabinovich *et al.*, 2000a, 2000b). Tip radius was ~20 nm and Hamaker constants of the substrates, silicon and calcite are given in Table 4.8.

**Table 4.8.** List of Hamaker constants used in Equation 2.11 to predict the adhesion force based on the roughness model (Rabinovich *et al.*, 2000).

Group I Material	Hamaker constant ( $\times 10^{-19}$ J)	Reference	Group II Material	Hamaker constant ( $\times 10^{-19}$ J)	Reference
RF steel	3.25	Israelachvili (1992)	Dymon-iC	2.38	Turq <i>et al.</i> , (2005)
Gold-0.1	3.25	Israelachvili (1992)	Graphit-iC	2.38	Turq <i>et al.</i> , (2005)
MF-steel	3.25	Israelachvili (1992)	Al	1.40	Israelachvili (1992)
Gold-0.3	3.25	Israelachvili (1992)	TiN	2.65	Rabinovich <i>et al.</i> , (2000)
SB steel	3.25	Israelachvili (1992)	PTFE	0.38	Israelachvili (1992)
Copper-new	3.25	Israelachvili (1992)	K coating	0.38	Israelachvili (1992)
Copper-used	3.25	Israelachvili (1992)	Calcite	0.22	Cavalier and Larche, (2002)
			Silicon	2.65	Rabinovich <i>et al.</i> , (2000)

Using the AFM software each of the parameters;  $rms_1$ ,  $rms_2$ ,  $\lambda_1$  and  $\lambda_2$  were measured at ten locations after cross-sectioning the image of each surface. Mean values of  $W_{132}$  were used in the calculation. Table 4.9 gives calculated theoretical adhesion forces (F) using the Rabinovich roughness model with calcite and silicon adhesives based on the triplet average and sextet methods.

Negative values indicate repulsive interactions between two materials of similar acid-base behaviour, which are indicative of the LWAB approach. Theoretical forces ranged from -2.54 to 0.75 nN and -1.06 to 1.23 nN to silicon using sextet and triplet methods, respectively. This was because the used  $\gamma^-/\gamma^+$  ratio of calcite was 406 mJ.m<sup>-2</sup>, which was four times greater than 85 mJ.m<sup>-2</sup> for silicon. Thus in water, hydrophilic repulsion dominates because a net repulsion results between hydrophilic surfaces (Mantel *et al.*, 1995 and van Oss, 2003).

Group I materials gave theoretical forces ranging from -1.69 to 2.70 nN and -0.19 to 0.81 nN for the silicon sextet and triplet methods, respectively. This was essentially due to their high  $\gamma^-$  value and low  $\gamma^+$  values.

**Table 4.9.** Summary of theoretical adhesion force between the AFM tip or calcite-coated tip and material substrates, calculated using equation 2.11. and comparing the percentage deviation with JKR/DMT theories. Calculations were based on liquid surface tension parameters obtained from Van Oss *et al.*, (1986).

GROUP I	Theoretical adhesion force (nN)				Adhesion reduction (%) relative to ..	
	Silicon-triplet	Calcite-triplet	Silicon-sextet	Calcite-sextet	JKR Theory	DMT Theory
<b>RF steel</b>	-0.19±0.02	0.64±0.12	-1.69±0.31	-1.04±0.19	28.88 (8)	5.17
<b>Gold-0.1</b>	0.02±0.00	0.92±0.02	-1.63±0.03	-0.90±0.02	26.02 (2)	1.36
<b>MF-steel</b>	0.31±0.01	1.26±0.01	-1.42±0.01	-0.67±0.01	25.70 (1)	1.49
<b>Gold-0.3</b>	0.18±0.01	1.13±0.02	-1.32±0.02	-0.56±0.01	26.81 (6)	2.37
<b>Copper</b>	0.80±0.17	1.84±0.49	-1.91±0.43	-1.37±0.70	26.45 (4)	1.88
<b>SB steel</b>	0.81±0.02	1.12±0.01	0.98±0.01	1.58±0.01	37.95 (13)	17.27
<b>Used copper</b>	-0.09±0.00	0.61±0.01	2.70±0.02	3.95±0.04	26.32 (3)	1.77
<b>GROUP II</b>						
<b>Dymon-iC</b>	-1.06±0.18	-0.56±0.01	-2.54±0.10	-2.09±0.09	30.90 (10)	7.80
<b>Graphit-iC</b>	-0.39±0.01	0.44±0.02	-2.23±0.06	-1.56±0.04	34.10 (12)	12.12
<b>Alumin</b>	0.23±0.01	1.20±0.05	-0.59±0.02	0.30±0.01	26.80 (5)	2.40
<b>TiN</b>	-0.14±0.00	0.80±0.02	-1.40±0.04	-0.60±0.02	29.10 (9)	5.44
<b>PTFE</b>	0.96±0.04	1.97±0.03	0.40±0.01	1.37±0.02	27.75 (7)	3.79
<b>K coating</b>	1.23±0.05	1.86±0.34	0.75±0.14	1.56±0.29	32.54 (11)	10.05

Theoretical adhesion to calcite and silicon was strongest on SB steel and both copper substrates, which were the most hydrophobic of group I ( $\theta > 65^\circ$ ). From group II PTFE and 'k. coating' exhibited stronger theoretical adhesion with calcite and silicon, both of which were also classed as hydrophobic. In light of these findings the general pattern to emerge was hydrophilic surfaces were less theoretically adhesive and roughness did not

appear to play a significant role. This was because the magnitude of roughness-induced adhesion for Graphit-iC/Dymon-iC, and PTFE/‘K.coating’ material pairs was similar.

Generally, all materials showed theoretical adhesion using the roughness model was at least 25% smaller than JKR theory. The drop in adhesion force relative to the DMT model ranged from 1.49 to 17.27%. Considering the range of  $R_a$  values exhibited by all materials, differences between JKR theory and the roughness model was relatively small. The biggest drop in adhesion from group I was observed for SB steel, while MF steel gave the least variation compared to the contact theories. This was because for small asperity size, SB steel gave  $r^2$  values greater than tip radii (20 nm), with MF steel giving values an order of magnitude smaller. SB steel and RF steel also gave high  $R_a$  values, which validated the data. When the reduction in adhesion from the roughness model was paired with material roughness ( $R_a$ ) there was no correlation between roughness and theoretical adhesion. Therefore, it was found the roughness model did not accurately characterize the mid-range to highly rough substrates. This was reflected by the relatively small deviations in theoretical adhesion between mid-high  $R_a$  materials and their low  $R_a$  counterparts.

### 4.3 AFM force measurements

Force measurements were conducted in three different solution chemistries, synthetic hard water (SHW) (section 4.3.1), different ( $\text{CaCO}_3$ ) molar concentration (section 4.3.2) and at different pH (4.3.3) using both modified (with calcite) and unmodified ( $\text{SiO}_2$ ) probes. Finally, force measurements were conducted in SHW using modified probes with variation in the calcite surface roughness and crystal orientation (4.3.4). Finally, a discussion linking measured adhesion force to material substrate is given (4.3.5)

#### 4.3.1 Adhesion force measurements in SHW

Figure 4.8 shows ESEM images of three types of AFM tips that were used, unmodified (UM), calcite-grown (CG) and calcite-attached (CA) tips.

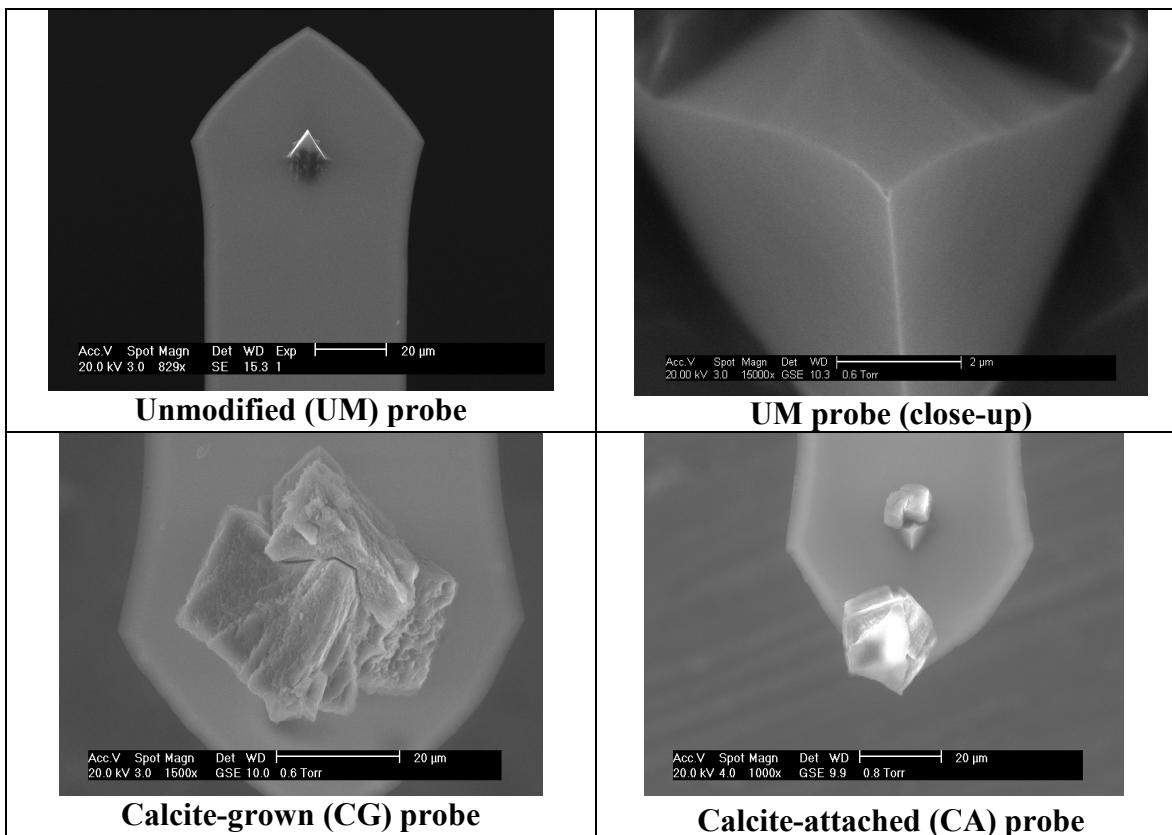


**Figure 4.8.** SEM images of unmodified (top) and modified (bottom) probes used during force measurements performed in SHW.

The unmodified tip has a radius of curvature of about 20 nm. Contact area of each tip was estimated to be  $10 \text{ nm}^2$ ,  $5 \text{ } \mu\text{m}^2$  and  $2 \text{ } \mu\text{m}^2$  for the UM, CG and CA probes. Contact area for the modified tips was estimated using the ESEM software by measuring the distance



from one end of the crystal to the other (Figure 4.8). The respective force measurements performed on the group I and II materials using each of the above probes are given in Table 4.10. One of each probe was used for all materials to ensure consistency. Generally, measured adhesive forces were lower for unmodified tips due to reduced contact area.

**Table 4.10. Average pull-off forces of UM, CG and CA probes on all materials in SHW.**

	Measured average pull-off force (nN)						
GROUP I	UM tip	CG tip	CA tip	GROUP II	UM tip	CG tip	CA tip
RF steel	1.41±0.67	2.62±1.11	2.61±1.11	Dymon-iC	0.52±0.47	0.26±0.16	3.05±1.21
Gold-0.1	2.53±1.07	7.41±3.65	3.70±1.31	Graphit-iC	0.66±0.54	3.07±1.76	0.71±0.47
MF steel	5.63±2.65	1.77±0.64	6.38±1.08	Alum	0.83±0.50	3.83±2.62	5.43±1.87
Gold-0.3	1.19±0.40	4.32±1.51	3.62±1.25	TiN	1.16±1.06	0.88±0.54	3.55±1.85
SB steel	5.43±3.63	0.36±0.40	0.87±0.55	PTFE	1.57±0.66	0.65±0.21	1.27±1.05
Copper**	4.40±1.53	-	-	Kettle coating	2.34±1.16	3.80±2.17	5.91±3.02
Used Copper*	0.55±0.67	-	-				
Average	3.02±2.11	3.29±1.30	3.43±2.00	Average	1.18±0.68	2.08±1.07	3.32±2.11

\*\* CG and CA tips had broken prior force measurements.

\* Force data was of poor quality for CG and CA tips.

Stainless steels were most adhesive from group I with less variation in forces measured on group II materials. Dymon-iC at  $0.52 \pm 0.47$  nN was least adhesive followed by Graphit-iC. 'K. coating' was most adhesive with a force of  $2.34 \pm 1.16$  nN. When compared to group I materials, TiN, PTFE and 'k. coating' produced forces of 1.16, 1.57 and 2.34 nN, respectively. Frequency distribution plots of group I and II materials with the unmodified tip are shown in Figure 4.9. Low adhesion forces on Graphit-iC and Dymon-iC correlated with low theoretical adhesion forces (Section 4.2.3), which was in agreement with Lewis acid-base theory, where both surfaces were hydrophilic (Van Oss *et al.*, 1986). Acid-base theory states the interaction energy between two hydrophobic (HB-HB) is stronger than a hydrophobic-hydrophilic (HB-HL), which in turn is stronger than two hydrophilic surfaces (HL-HL) in water. To confirm these findings, Kvasnica *et al.*, (2006) also measured reduced adhesion forces on DLC films (unknown thickness) of 76.48 nN using an SiO<sub>2</sub> tip compared to 445 nN for Ti-containing nanocrystalline carbon film performed in air.

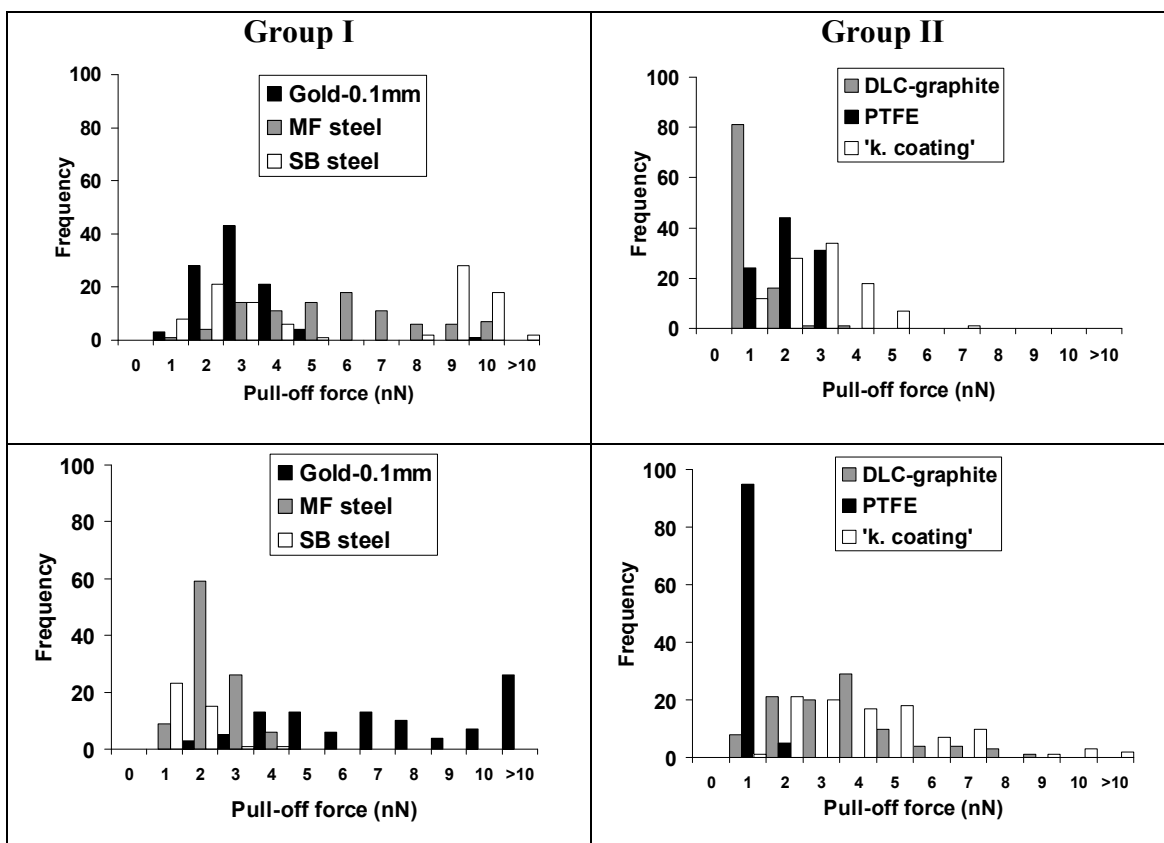


Figure 4.9. Frequency distribution of force measurements on selected substrates using the UM (top) and CG (below) probes in SHW.

Lifshitz-van der Waals ( $\gamma^{LW}$ ) values of amorphous carbon-based coatings and stainless steels were similar so this was not the driving force behind low adhesion. Acid-base forces could explain this disparity. In water both amorphous carbon coatings were likely passivated, and competition for H-bonds between negatively charged  $\text{SiOH}^-$  (silanol) and oxidised surface groups (C-OH and C(O)OH) (with unknown surface charge) may have increased their hydrophilic behaviour ( $\theta < 65^\circ$ ). This hypothesis is in agreement with the wetting behaviour of diamond films that are naturally oxidised (Ostrovskaya, 2002). Ostrovskaya (2002) found oxidation increased wetting of diamond-like films while hydrogenation reduced wetting by forming strong C-H bonds. However, increased oxidation is associated with increased adhesion, as is common with stainless steels. In the case of the amorphous carbon coatings this appears to be due to undissociated OH groups as a result of carbon's high electronegativity. Molecular density of C-OH groups was also high due to the short C-C bond length ( $\sim 154$  pm), which may have enhanced wetting (McMurray, 1995). Although  $\gamma^{LW}$  forces were high for the carbon coatings, their high

basicity ( $\gamma^-$ ) may have been caused by a greater ratio of undissociated C-OH to dissociated C-OH groups, which were available for H-bonding, giving them their hydrophilic character. From group I, adhesion to MF steel, gold-0.1mm and unused copper with unmodified tips was enhanced, possibly due to increased electrostatic forces due to ion-ion interactions. Acid-base forces were found to increase adhesion due to ionizable surface groups, in the case of MF steel this was  $\text{Fe}_x\text{O}_y$  and  $\text{Cr}_x\text{O}_y$  surface layers. This was because OH groups of metal oxides are amphoteric in character so the rate at which OH dissociates or protons get added depends on the charge and radius of the metal ion. This may have made surfaces more hydrophobic as their contact angles were  $\geq 65^\circ$  (Mantel *et al.*, 1995), thus increasing adhesion due to hydrophobic-hydrophilic (HL-HB) attraction. Li and Logan (2004) also observed Co/Fe/Cr/O-coated surfaces were hydrophobic ( $\theta = 62 \pm 4^\circ$ ) and more adhesive to Gram-negative bacteria. To further substantiate these findings the most hydrophobic metal with low  $R_a$  was unused copper ( $\theta > 70^\circ$ ), which also gave strong adhesion. Acid-base forces were also highest on used copper ( $16.89 \text{ mJ.m}^{-2}$ ), primarily due to a high density of acidic sites (Figure 4.6). Therefore, the main difference between MF steel/copper/gold and amorphous carbon coatings materials appeared to be hydrophilicity, which provides the first evidence for their low adhesion.

Both PTFE and 'k. coating' were relatively hydrophobic ( $\theta > 70^\circ$ ) compared to the amorphous carbon coatings. Furthermore, 'k. coating' gave low acid-base forces ( $2.98 \text{ mJ.m}^{-2}$ ) compared to Dymon-iC ( $5.34 \text{ mJ.m}^{-2}$ ) and Graphit-iC ( $6.07 \text{ mJ.m}^{-2}$ ). The absence of acidic or basic sites on these materials may partly explain strong adhesion to the  $\text{SiOH}^-$  tip was due to hydrophobic-hydrophilic (HL-HB) attraction. PTFE has also shown to retain charge very well, so forces on a previously contacted area will be larger than a new surface. As electrostatic forces are longer ranged, they will invariably lead to stronger adhesion than short range acid-base forces. Furthermore, with the moderate to high surface roughness of PTFE and 'k. coating', adhesion was enhanced on both materials.

Observation of the acidity of MF steel and other group I metals showed they gave average  $\gamma^+$  values ranging from 0.5 to  $1 \text{ mJ.m}^{-2}$ . This was relatively high compared to 0.2

to  $0.5 \text{ mJ.m}^{-2}$  for the amorphous carbon coatings. This difference in acidity may be significant. It was assumed MF steel comprised of a mixture of amphoteric  $\text{Fe}_x\text{O}_y$  and  $\text{Cr}_x\text{O}_y$  groups with IEP values ranging from 6-10 (McGuire *et al.*, 2006) and 5-6 (McCafferty, 2002), respectively. The SHW solution had a pH of  $\sim 7.5$ , so MF steel had near neutral surface charge during force measurements, although contact angle data showed the surface had a level of acidity greater than other group I materials. Used and unused copper also gave a much higher ratio of acidic to basic sites than the other substrates. As silicon was highly basic (IEP  $\sim 2$ ), it was deduced adhesion to MF steel and copper was driven by electrostatic forces in addition to hydrophobic forces. For SB steel adhesion was further enhanced by increased surface area. For example, the tip was small enough to slip into valleys to give either a snug or loose fit, which depended on the valley's width. It was considered for SB steel the ratio of tip:valley interacting systems was greater than tip:peak interactions, thus giving stronger adhesion.

The calcite grown (CG) probe generally produced a greater range of forces. This ranged from 0.1 to 10 nN on group I materials, with strong adhesion to gold-0.1mm in particular. MF steel and RF steel were slightly more adhesive peaking at 2 and 3 nN respectively. Of the group II materials, Dymon-iC was least and aluminium was most adhesive, peaking at 0.1 and 3 nN. For aluminium and 'k. coating' maximum adhesion reached 10.5 nN and 13 nN, respectively. For calcite-attached (CA) tips, MF steel, SB steel and RF steel were most adhesive. Both gold coatings gave smaller forces, peaking at 0.1-1 nN. For group II 'k. coating' was again the most adhesive, peaking at 5 nN followed by aluminium (peak 3 nN). Remaining group II materials gave peaks at around 1 and 2 nN, for which Graphit-iC was least adhesive.

The mechanism of adhesion with calcite probes may also be explained by substrate hydrophilicity but this does not clarify disparities between the two calcite probes. As calcite in solution is comprised of a mixture of several ionic species,  $\text{Ca}^{2+}$ ,  $\text{CO}_3^{2-}$  and  $\text{HCO}_3^-$  in the presence of potential determining ions, the calcite-substrate speciation interface was unpredictable. At pH 7.8 in which experiments were performed, calcite exhibits a positive surface charge because research has shown precipitated calcite has an

IEP of 9.5 (Churchill *et al.*, 2004). Of the metal oxides, Giesbers *et al.*, (2002) measured an IEP of  $\sim 4.5$  for gold. The gold substrates were also the most adhesive to both calcite probes, but gave low adhesivity to the  $\text{SiOH}^-$  tip. However, the chemistry of the oxide layer on gold, if present, was unclear. Interestingly, gold surfaces also gave high  $\gamma^{\text{AB}}$  values, so adhesion was possibly driven by acid-base interaction forces that are shorter ranged than hydrophilic-hydrophobic forces. SFE calculations showed gold exhibited just as much Lewis acidity as MF steel, but was slightly more basic, which resulted in increased amphoteric behaviour and stronger adhesion. The complex chemistry of MF steel and its potentially variable surface charge makes it difficult to clarify its position on its adhesion ranking with calcite. Charge reversal may have increased or decreased adhesion based on the relative ratios of Fe/Cr oxides at specific regions. Nevertheless, electrostatic forces were also critical to calcite-based adhesion to flat metal oxides. On a rough substrate reduced contact area may also result, due to tip-on-peak interactions. Contact area at each sampling point will also vary giving a greater range of forces. Consequently, SB steel gave lower forces compared to MF and RF steels, which may have been caused by calcite interacting with asperity peaks due to the large crystal size. This was in contrast to the unmodified tip which exhibited greater interaction with valleys of smaller size, thus increasing contact area.

#### **4.3.2 Adhesion force measurements in varying electrolyte concentration**

This section aims to assess the impact of electrolyte concentration on adhesion so absolute adhesion forces are not presented. All materials were tested in varying  $\text{CaCO}_3$  concentrations using modified and unmodified tips. The pH at which the measurements were performed ranged from 7.24 and 8.24, giving calcite a slight positive charge and unmodified tips a negative charge (McCafferty, 2002) (Table 4.11). The range and strength of electrostatic interactions were determined by the surface potential and Debye length. Debye lengths of the divalent electrolyte used in this study are given in Table 4.11. Debye length was shown to increase exponentially with decrease in ionic concentration.

**Table 4.11.** The affect of concentration on Debye length. Also shown is the pH of the solutions that were used.

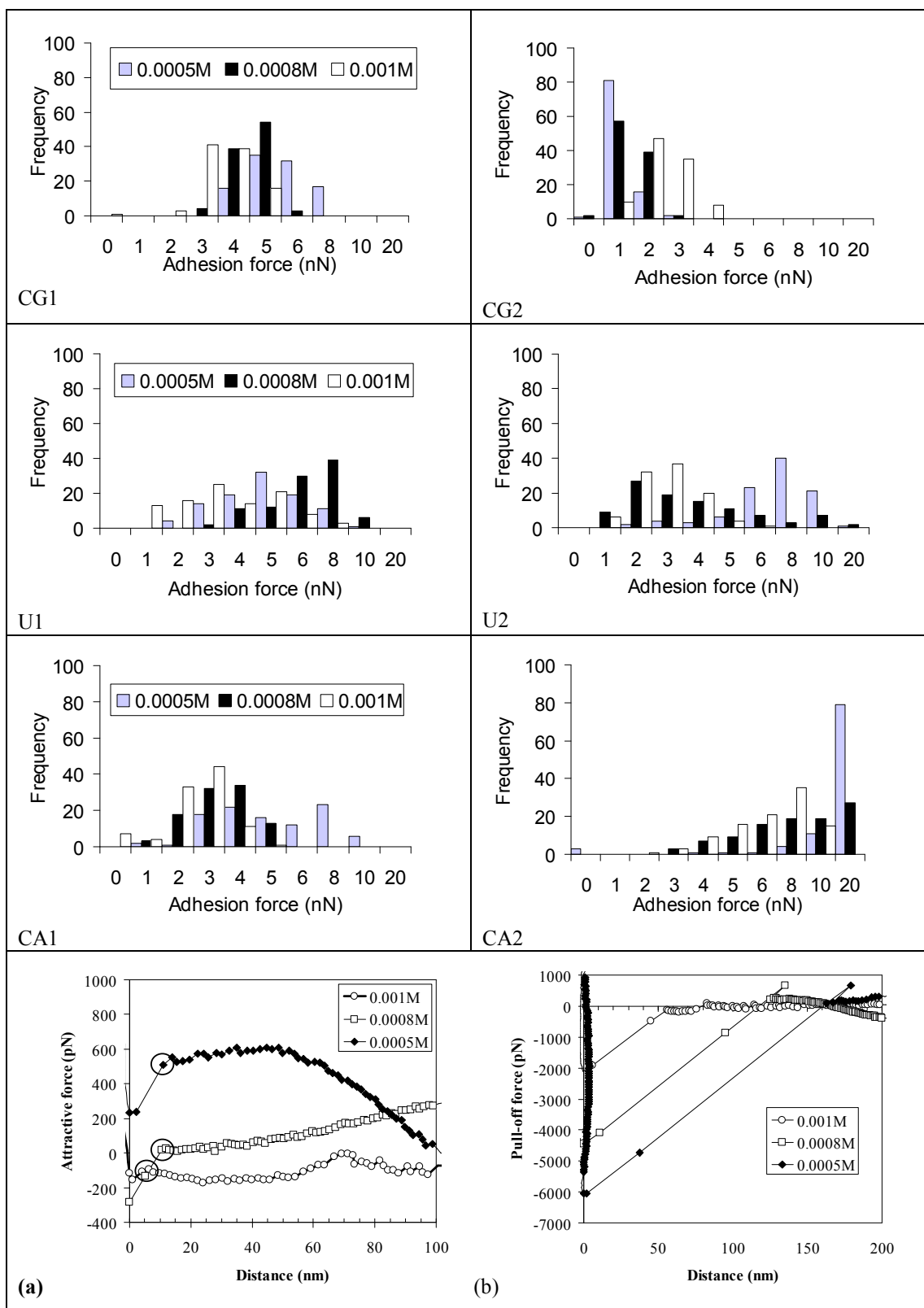
Concentration	Debye length (nm)	pH
SHW	2.67	7.8
0.001M	4.81	8.24
0.0008M	5.37	7.47
0.0005M	6.80	7.24

Table 4.12 lists trends observed for each material during adhesion when electrolyte concentration was increased from  $5 \times 10^{-4} \text{M}$  to 0.001M. Data showed most materials gave a reduction in adhesion with increased electrolyte concentration, although this was restricted to some materials using certain AFM tips. MF steel was most significant because four of six probes gave this trend, possibly as a result of its low  $R_a$  and high SFE. One logical explanation was that in reducing the Debye length (Table 4.11), the electrical double layer was compressed, allowing greater surface intimacy.

**Table 4.12.** Summary of trends observed for each material from modified (calcite-attached (CA) and calcite-grown (CG) and unmodified (UM) tips when electrolyte concentration was increased from 0.0005M to 0.001M.

Material	Increase in adhesion force	Decrease in adhesion force
R steel		CG1/UM1
Cu-unused		CG1
Cu-used		
Gold-0.3	CA1	
Gold-0.1	CG2	UM2
MF steel		CG1/CA1/CA2/UM2
SB steel		CG2/UM1
Graphit-iC		
Dymon-iC	CA2	UM1
Aluminium		CA1
TiN		CG1/CA2/UM1
PTFE		CG1/UM1/UM2
K coating	CG2	

As MF steel and tip were negatively charged, both surfaces may have adsorbed  $\text{Ca}^{2+}$  with increasing electrolyte concentration, resulting in repulsive electrostatic interaction and reduced adhesion. Three of four calcite-modified tips (CG1, CA1 and CA2) also showed this trend, the results of which are given in Figure 4.10.



**Figure 4.10.** Frequency distribution plots of all six probes on MF steel in varying electrolyte concentration and (below) showing approach (a) and retract (b) cycles using the CG1 probe at three different  $\text{CaCO}_3$  concentrations.

The positively-charged calcite (IEP  $\sim 9.5$ ), was expected to adsorb  $\text{CO}_3^{2-}$  ions and strongly adhere to  $\text{Ca}^{2+}$  adsorbed on MF steel. In contrast, there was a reduction in adhesion with increasing  $\text{CaCO}_3$  concentration, which may be attributed to a neutral calcite surface with equivalent  $\text{Ca}^{2+}$  and  $\text{CO}_3^{2-}$  ions. Three approach and retract cycles using the CG1 tip on MF steel are shown in Figure 4.10(a,b). At low ionic strength (0.0005M), repulsive forces were observed on approach cycles due to double layer repulsion (Figure 4.10a), which was compressed at higher electrolyte strength (Figure 4.10b). The approach cycles also showed the jump-to distance (circled in Figure 4.10a) for the low ionic strength solution was about 10 nm, compared to 4-6 nm for the 0.001M solution. A schematic showing the effect of charged groups on the double layer during approach cycles is given in Figure 4.11.

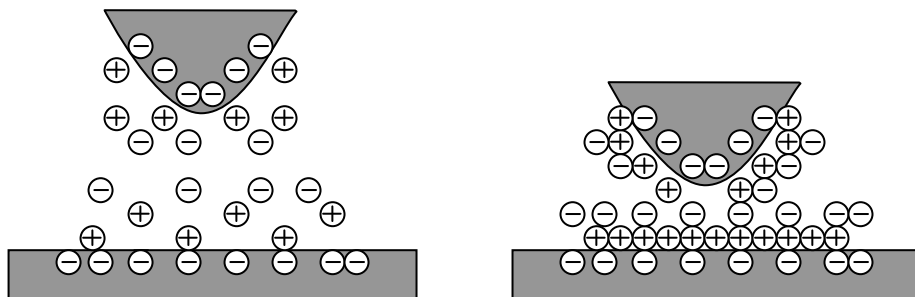


**Figure 4.11.** Schematic showing how the addition of a salt compresses the double layer (from left to right), permitting closer contact on approach.

At 0.001M vdW attraction dominated. However, these events were not consistent in all locations possibly due to fluctuations in contact area and also the complex topography of the calcite crystal used for different probes. This behaviour was also demonstrated by Weidenhammer and Jacobasch (1996), using PEEK (poly-(ether ether ketone)) polymer substrates. They found with increasing ionic strength of KCl and KOH solutions up to 0.0005M, adhesion with  $\text{SiOH}^-$  tips was reduced until no interaction (attractive or adhesive) was observed.

Several materials gave no trend with increasing ionic concentration, such as both copper substrates, Graphit-iC, Dymon-iC, 'k. coating' and both gold substrates. A logical explanation can be given for used copper, SB steel and 'k. coating' because these materials exhibited high  $R_a$  values, which were much greater than the Debye lengths.



This was because surface asperities will cause the Debye length to fluctuate, while also increasing the surface area for which charged groups will adsorb. However, Graphit-iC and Dymon-iC had slightly higher  $R_a$  values to MF steel, so their adhesion was expected to be less ambiguous.

Both Graphit-iC and Dymon-iC were highly polar coatings that were predominantly basic, and were expected to have a preference for  $\text{Ca}^{2+}$  ions. This was due to the presence of C-OH and C(O)OH groups on Dymon-iC and surface C-H groups on Graphit-iC. However, with increasing ionic concentration there was no increase in  $\text{Ca}^{2+}$  adsorption to either surface, possibly due to the presence of uncharged C-OH ( $\text{sp}^3$ ) and C(O)OH ( $\text{sp}^2$ ) groups. An additional explanation may be that at 0.001M the pH increased to 8.24, which may have affected the surface chemistry of the diamond-like films. Ostrovskaya *et al.*, (2002) observed that at  $\text{pH} > 7$  amorphous carbon films may corrode due to their increased wetting. However, the precise mechanism of the potential adverse effects on the amorphous carbon coatings was not known and any significant increase or decrease in adhesion with ionic concentration was not observed. Therefore, the behaviour of both diamond films remained ambiguous and further research was required.

Both gold substrates also showed adhesion was ambiguous with unmodified and modified tips because roughness effects were anticipated to have a negligible effect on interaction forces. As both gold substrates and the  $\text{SiOH}^-$  tip were negatively charged, repulsion was expected due to adsorption of  $\text{Ca}^{2+}$ . Although adhesion was lower at 0.001M and larger at 0.0005M, there was no mid-range adhesion at 0.0008M. This may have been caused by reduced sensitivity of the gold layer to bulk electrolyte concentration possibly caused by changes in surface potential during the adhesive interaction. Although acid-base values of gold were high, their high surface free energy may have increased surface wettability and caused the double layer to be less structured relative to that of MF steel.

It appears adsorbed ions did affect adhesion systematically but this was restricted to MF steel, due its low  $R_a$  low wettability and negatively-charged surface, which may have

caused greater coverage of cations. Gold substrates did not show this trend due to their greater wetting. Other substrates showed no affect of electrolyte concentration on adhesion due to their high  $R_a$  and stronger mechanical effects, which caused anions/cations to adsorb on peaks/valleys at insufficient quantities to have any discernible double layer interaction. As a result, there is a need to repeat these experiments on atomically flat surfaces of the same chemistry to explain their precise interaction mechanism.

### 4.3.3 Adhesion force measurements at different pH

The affect of solution pH on adhesion force was tested on selected materials. MF steel, Dymon-iC, TiN and SB steel were tested only using modified and unmodified tips at pH 8, 9 and 10. The materials were selected based on their different surface chemistries and surface topographies. Figure 4.12 shows representative force plots on Dymon-iC at pH 8, 9 and 10, as well as pull-off forces on MF steel, Dymon-iC, TiN and SB steel.

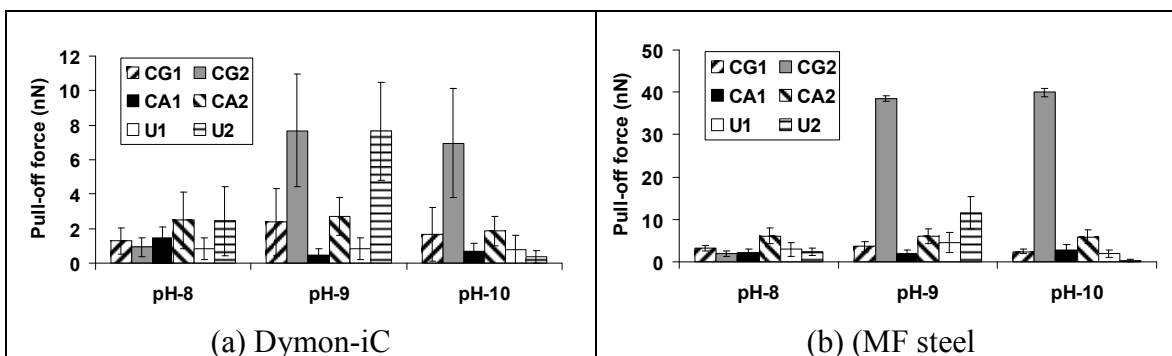


**Figure 4.12.** Histogram showing the distribution of pull-off forces on (a) Dymon-iC and (b) MF steel.

At the three pH values, no distinct pattern emerged for all substrates using calcite tips. However, at pH 9 and 10, CG probes appeared to show an increase in adhesion for Dymon-iC and MF steel materials. In the case of MF steel, this may have been caused by surface coverage of  $\text{Ca}^{2+}$  at pH 9 and 10. The surface charge of calcite was approaching neutral ( $\sim 9.5$ ), and at pH 9 and 10 calcite may have exhibited similar surface potentials. This may have caused adhesion to peak at pH 9 and 10, as calcite comprised of equivalent  $\text{Ca}^{2+}$  and  $\text{CO}_3^{2-}$  groups while MF steel remained negatively charged. This may also explain why adhesion at pH 9 and 10 also peaked for Dymon-iC.

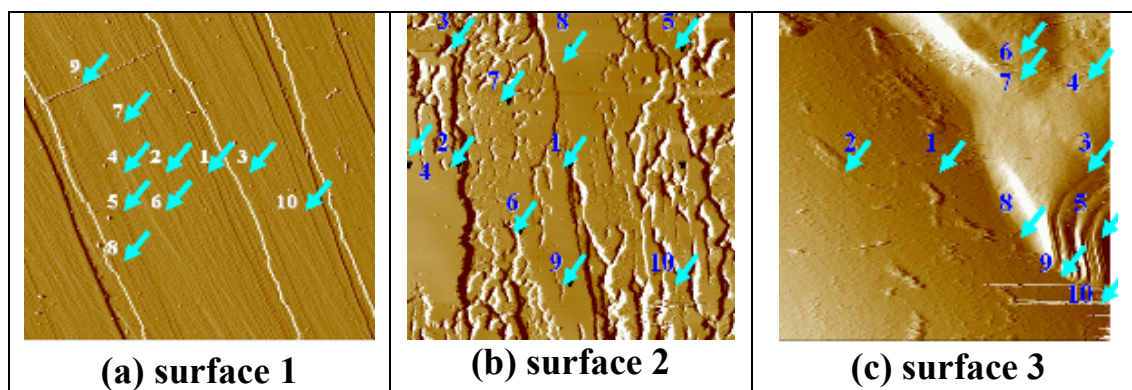
With the negatively-charged silica tip, adhesion was stronger at pH 9 to all substrates except SB steel. The cause of this behaviour was uncertain because MF steel and TiN also carried a negative charge. Adhesion was expected to decrease with increasing pH because the surface charge difference between tip and substrate was expected to drop. As a result long-range repulsion was expected due to adsorption of  $\text{Ca}^{2+}$  on both surfaces. Even though adhesion dropped at pH 10, the cause of adhesion peaking at pH 9 was uncertain. Experiments were performed in the order pH 8, 9 then 10, so measurements were performed systematically. Although the risk of cross-contamination was small, erosion of the silica tip during force measurements may have increased contact area and inadvertently caused adhesion to increase after performing force measurements at pH 8. Alternatively, the difference in solution pH was too small to cause any significant change to the surface charge of calcite using modified tips. The surface charge of the unmodified tip remained highly negative from pH 8 to 10, so any differences in adhesion was likely to be caused by differences in contact area than actual surface charge effects.

#### **4.3.4 Affect of calcite crystal roughness on adhesion**

This section aims to assess the impact of calcite surface roughness on adhesion. In section 4.3.1 calcite-modified tips did not adhere to SB steel in the expected trend and there was considerable variation between calcite-modified probes on MF steel. Furthermore, by varying surface topography this may recreate mechanical effects of adhesion on rough substrates. The experiment involved force measurements with unmodified tips on calcite surfaces with varying degrees of surface roughness, and with the use of calcite-modified probes having various degrees of roughness.

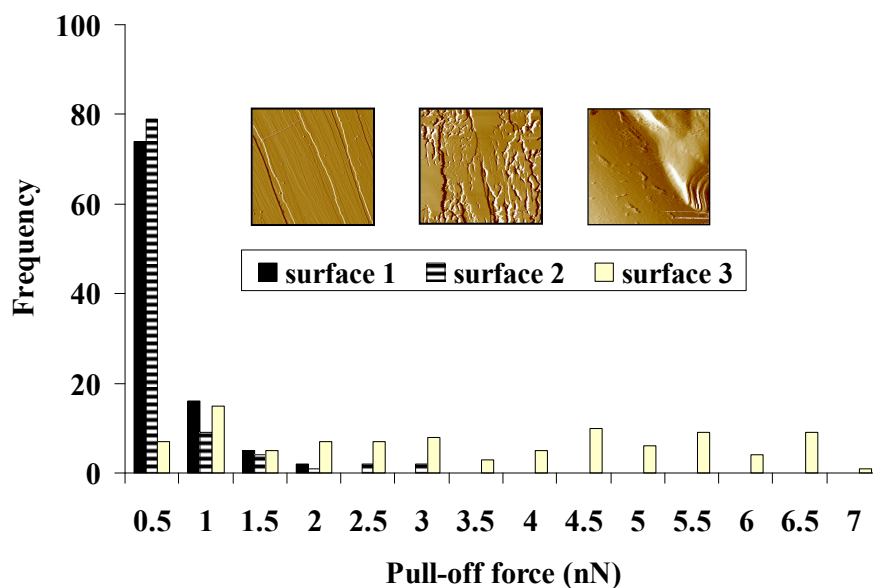
##### **4.3.4.1 Use of unmodified tips**

Figure 4.13 shows AFM deflection images of atomically flat and rough calcite surfaces (Manchester minerals), and estimated locations where force plots were performed. Scan areas were 50 x 50  $\mu\text{m}$ , 15 x 15  $\mu\text{m}$  and 5 x 5  $\mu\text{m}$  for surface 1, surface 2 and surface 3, respectively. A small scan area was selected for surface 3 after zooming in to a site defect which comprised of an etch pit. Surface 2 (Figure 4-13b) was dominated by trench-like etch pits that were inter-connected and ranged from 10 to 500 nm.



**Figure 4.13.** AFM deflection images of optically pure calcite {104} showing (a) flat calcite ( $50 \mu\text{m}^2$ ), (b) calcite with moderate surface roughness ( $15 \mu\text{m}^2$ ) and (c) calcite with single large defect ( $5 \mu\text{m}^2$ ). Numbers on images represent locations of force plots.

$R_a$  values indicated surface 3 was significantly rougher than the other two. Figure 4.14 shows force measurements performed on the three calcite surfaces. Pull-off forces on surfaces 1 and 2 were statistically the same, while surface 3 gave a greater distribution of forces.



**Figure 4.14.** Frequency distribution graph of force measurements on three calcite {104} surfaces with variations in surface defects using an unmodified tip.

Reverting back to the AFM images of surfaces 1 and 2, the presence of microcavities on surface 2 did not reflect on pull-off forces, which may have caused little, if any, effect on the contact area. Figure 4.15 shows measured pull-off forces at each location for each

surface. As expected, there was considerable variation on surface 3 amongst regions and at the same location.

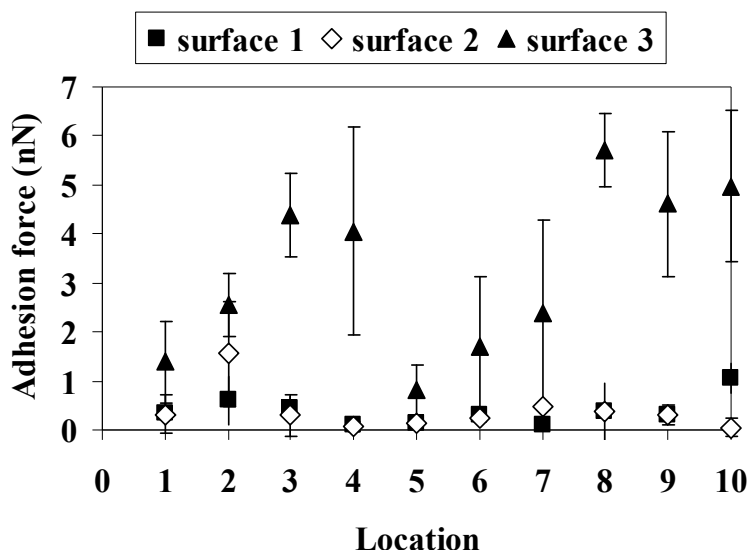
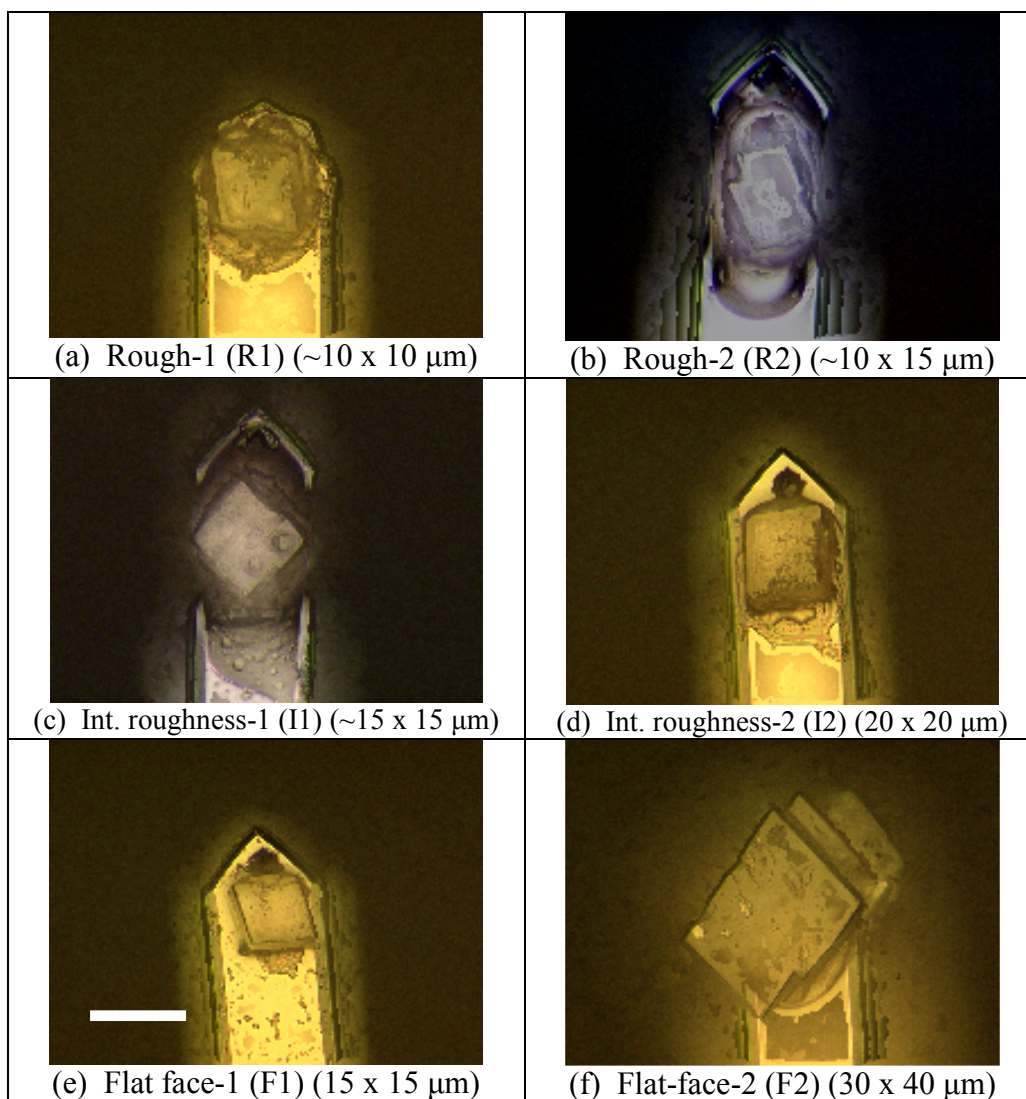


**Figure 4.15.** Scatter plot showing the distribution of adhesion forces at all 10 locations of the three calcite surfaces.

Surface topography and possibly chemical heterogeneity was the main cause of the large distribution of forces on surface 3, and not surface charge. However, the likelihood of surface asperities to attract contaminants from the substrate as well as  $\text{Ca}^{2+}$  and  $\text{CO}_3^{2-}$  ions from solution disproportionately could not be eliminated. On the other hand surface 1 had an intact crystallographic {104} face that exhibited neutral charge character due to the presence of coplanar  $\text{Ca}^{2+}$  and  $\text{CO}_3^{2-}$  groups. Although surface 2 did exhibit a certain level of roughness as presented by the presence of microcavities such as elongated etch pits, they were insufficient to cause any increase in surface area during force cycles. Furthermore, pull-off forces were subject to the required tip-defect interaction, which was not always possible.

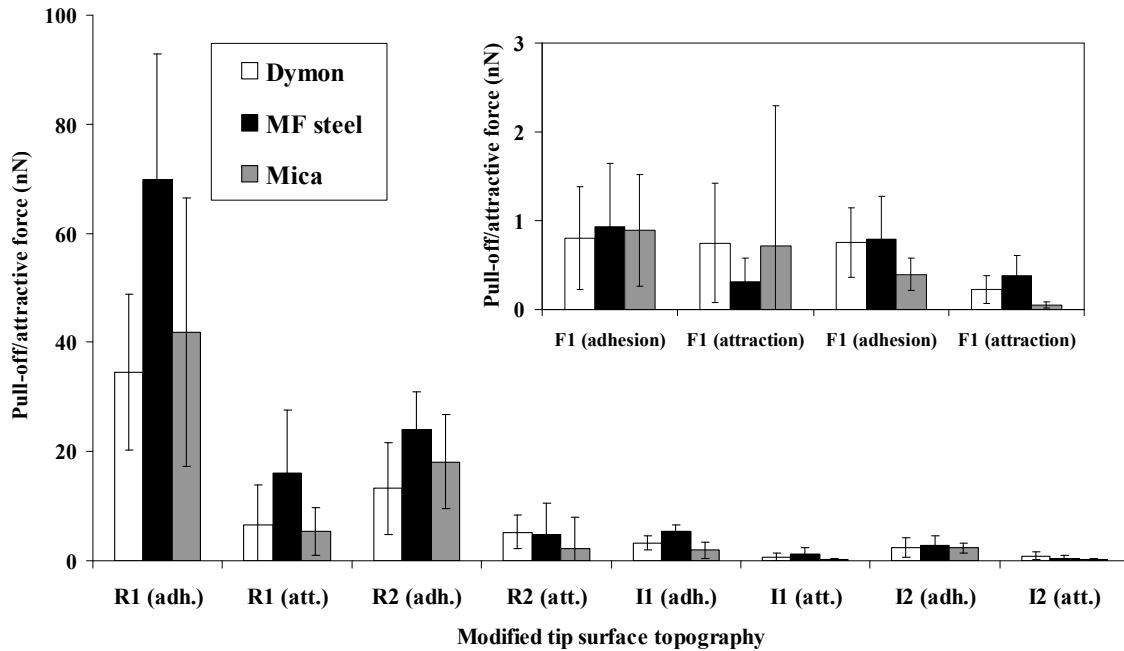
#### 4.3.4.2 Use of modified tips

Six probes were labelled rough-1, rough-2, intermediate-1, intermediate-2, flat-face-1 and flat-face-2 and shown in Figure 4.16(a-f).



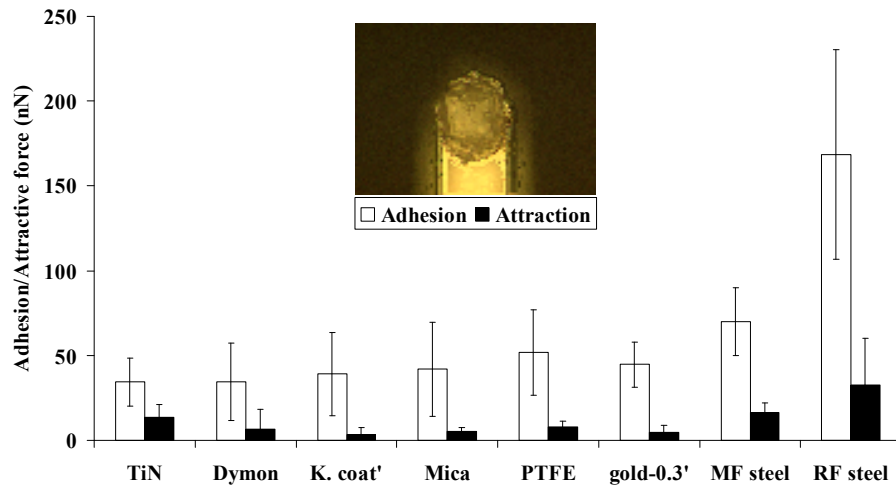
**Figure 4.16.** Optical images of calcite probes with different levels of roughness (a-f) (6 probes consist of 2 rough, 2 intermediate and 2 flat calcite surfaces). Scale bar 30  $\mu\text{m}$ .

Figure 4.17 shows attractive/adhesive force data performed on Dymon-iC, MF steel and Mica substrates using the six probes. The order of adhesion and attractive forces between the different calcite probes was as follows: Rough calcite probes > Intermediate > Flat. Compensating for contact area adhesion was  $0.081 \text{ nN}/\mu\text{m}^2$ ,  $0.026 \text{ nN}/\mu\text{m}^2$  and  $0.003 \text{ nN}/\mu\text{m}^2$  for rough, intermediate and flat calcite probes, respectively.



**Figure 4.17.** Column chart showing the pull-off (adh.) and attractive (att.) forces between modified tips with calcite faces and MF steel, Dymon-iC and mica substrates in SHW using six calcite probes with different surface roughness. Inset image shows the average adhesion from the two flat crystals because forces were too small.

Figure 4.18 shows measured adhesive/attractive forces on materials using the rough-1 probe. Adhesion was enhanced on RF steel, with an average force of  $168.51 \pm 61.67$  nN. Surface roughness of the calcite crystal on the rough-1 probe was difficult to quantify, although the preference for RF steel was clearly due to the interlocking (or topographical) interaction between the peaks and valleys of asperities during contact.



**Figure 4.18.** Column chart showing the measured attractive and adhesive forces selected group I and II materials using the rough-1 probe.

#### 4.3.5 The effect of substrate surface properties/tip modification on adhesion

The results presented here consistently showed adhesion between an unmodified or modified tip and the substrates could not be ranked in a single order. This was because a number of contributing factors affect the total adhesive interaction: contact area, acid-base forces, electrostatic forces, hydrophilicity/hydrophobicity, solution chemistry and surface heterogeneity, all of which played a role of varying importance.

Contact area was a key factor in determining the force of adhesion between two surfaces. It was anticipated that the unmodified tip would provide a more robust set of force data due to its small contact area and greater ability to enter microgrooves of the rough substrates and sub-micron asperities of more uniform substrates. In these types of experiments, contact area will vary for materials with increasing roughness, but not in a linear fashion because of the randomness of tip-on-asperity contacts.

For materials with an  $R_a < 35$  nm surface chemistry was critical to substrate adhesion. In the case of diamond-like materials, it was deduced that hydration forces were key to preventing adhesion in synthetic hard water due to undissociated C-OH groups. Hydrophilic groups (due to high  $\gamma$  values) were found to reduce acid-base forces, while adhesion forces in different molar concentrations were also lowest on amorphous carbon coatings. The same force can also explain adhesion of silica tips to hydrophobic PTFE, due to uncharged C-F bonds. The low total acid-base SFE of PTFE indicate increased adhesion was due to hydrophilic-hydrophobic (HP-HB) attraction. However, force measurements in increasing electrolyte concentration showed adhesion decreased with increasing ionic concentration for some probes. It was not known whether this was due to adsorption of anions/cations on PTFE or the tip or both. Kokkoli and Zukoski (2000) found the interaction between a hydrophilic charged surface (-COOH) and a hydrophobic uncharged surface (-CH<sub>3</sub>) in NaCl was purely repulsive. Contrastingly, Freitas *et al.*, (2001) observed that interactions between a hydrophobic glass slide (-CH<sub>3</sub>) and a hydrophilic glass bead in KCl solutions were purely attractive, and stronger than the HL-HL system. As acid-base forces were virtually non-existent on the PTFE surface, it was deduced that adhesion was based on the adsorption of ions from solution, thus reducing



double layer repulsion. Even in the absence of electrolyte, PTFE was expected to strongly adhere to  $\text{SiOH}^-$  due to a net attraction (Freitas *et al.*, 2001). The presence of acidic sites on PTFE as well as copper, due to the high  $\gamma^+:\gamma^-$  ratio, also appears to enhance adhesion because calcite was a basic adhesive according to measured and literature SFE values. For the remaining materials with  $R_a > 35$  nm, adhesion was dependent on a complex interplay of contact area, hydrophilicity, electrostatic forces and heterogeneity, for which contact area was the main driving force.

With calcite-modified tips contact area was increased relative to unmodified tips but it was difficult to quantify with certainty due to the inherent difficulty of not knowing the number and areas of contact regions. At the start of the study two tip preparation methods were used, calcite-grown and calcite-attached in synthetic hard water. Both methods gave reasonably good material ranking of adhesion but large deviations. This problem was exacerbated on SB steel, used copper, RF steel, 'k. coating' and PTFE. Furthermore, with the attachment of calcite crystals with varying degrees of surface roughness, the order of adhesion was modified with relative ease, and contact area could indeed be altered to a certain degree. This showed tip modification with calcite crystals was applicable to surfaces with  $R_a$  not exceeding 30 nm, and beyond this calcite probes should be prepared with a single contacting point. For example this may be achieved by growing several layers of calcite on an unmodified tip or a bead/sphere, and then attaching the calcite-coated bead to the tip.

When modified probes were used on amorphous carbon coatings lower forces were not always measured. To emphasize this, a summary of the performance of Graphit-iC and Dymon-iC with modified tips in comparison to MF steel is given in Table 4.13. The majority of calcite probes used in the different liquids showed that Dymon-iC and Graphit-iC were the least adhesive substrates. The mechanism of this behaviour has been explained before with  $\text{SiOH}^-$  tips. However, calcite probes that did adhere to Dymon-iC and Graphit-iC may not have reflected the physicochemical properties of these surfaces. For instance, this may have been caused by the complex calcite-water interface which

experienced degradation or even contamination during force measurements (Churchill *et al.*, 2004).

**Table 4.13.** Summary of Dymon-iC, Graphit-iC and MF steel (as reference) material rankings based on adhesion force using modified tips. Low = material in bottom 3 of all materials; Medium = material in middle 3 of materials; High = material in top 3 of materials.

Variation in solution/calcite probe	Adhesion ranking		
	Dymon-iC	Graphit-iC	MF steel (reference)
SHW CA CG	High Low	Low High	High Medium
Different solutions $\text{CaCO}_3$ CG CA	Low Medium	Low Medium	Low/Medium High
Different pH conditions CG CA	Low/Medium Low	Low/Medium Low	High High
Rough calcite probes	Low	Low	High
Flat calcite probes	Low	Low	High
Oriented calcite probes	Low	Low	High

It was well known that silica tips experience wear during force measurements, and it was possible calcite probes may have eroded, although it was difficult to confirm this from SEM images. Alternately, the extent of oxidation on the two carbon-based films was not consistent; therefore it was possible that pockets of hydrophobic regions (such as C-H) were present on the coatings which increased their adhesion to calcite due to HB-HL interaction.

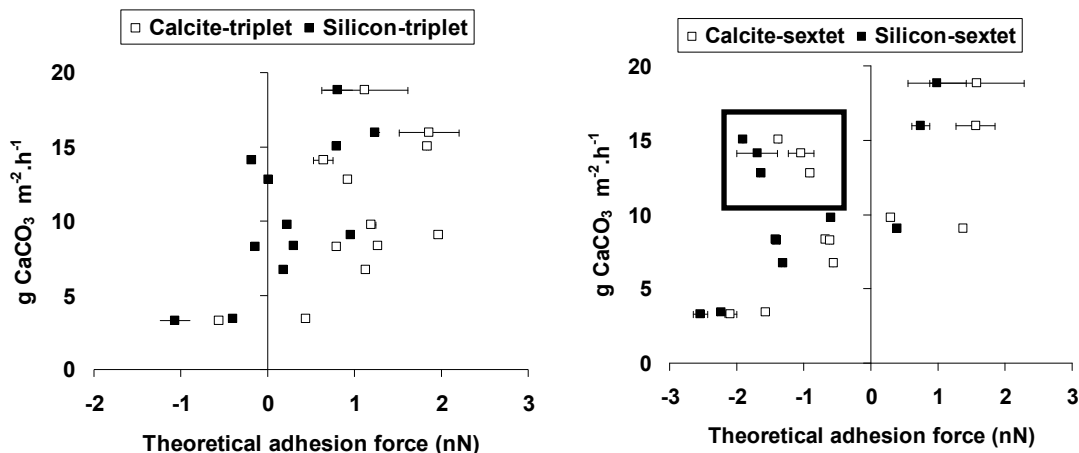
#### 4.3.6 Link between theoretical and measured adhesion forces with scaling rate experiments

In the final section of this chapter, it was hypothesized that material surface free energy and/or adhesion force measurements may be linked to their scaling rate using a rapid scaling methodology performed by Jitka MacAdam (2005). Scaling rate experiments were performed on twelve of the thirteen specimens using the procedure given in section 3.5.1.6. The results are given in Table 4.14 and are presented as g  $\text{CaCO}_3$  formed per  $\text{m}^2$  per hour, at a temperature of  $72^\circ\text{C}$ . A detailed discussion of the rate of  $\text{CaCO}_3$  scaling is given by MacAdam (2005), so it will not be given here.

**Table 4.14.** Material scaling rates (in  $\text{g CaCO}_3 \cdot \text{m}^{-2} \cdot \text{h}^{-1}$ ) after classification in group I and II materials.

Group I	Scaling rate ( $\text{g CaCO}_3 \cdot \text{m}^{-2} \cdot \text{h}^{-1}$ )	Group II	Scaling rate ( $\text{g CaCO}_3 \cdot \text{m}^{-2} \cdot \text{h}^{-1}$ )
Gold-0.3mm	6.73	Dymon-iC	3.28
MF steel	8.33	Graphit-iC	3.42
Gold-0.1mm	12.78	TiN	8.26
RF steel	14.1	PTFE	9.04
Copper-unused	15.05	Aluminium	9.78
SB steel	18.81	'K. coating'	15.97

Because surface properties are known to affect the rate of calcium carbonate scaling (Keysar *et al.*, 1994), it would be reasonable to assume the rapid scaling experiments performed by MacAdam (2005) comprise of both the induction and fouling periods. Furthermore, it would also be reasonable to assume the greater the material scaling rate, the shorter the induction and fouling periods. Figure 4.19 shows theoretical force (where the Rabinovich roughness model was applied) vs. scaling rate for all materials in a single plot. It was found the scaling experiment and contact angle measurements gave reasonably good similarities between low and some high scaling rate materials but not RF steel, gold-0.1mm and copper (highlighted in Figure 4.19). For instance, these materials gave high scaling rates but theoretical estimates with the Lewis acid-base (LWAB) approach indicated the materials as weakly adhesive.

**Figure 4.19.** Scatter plots of scaling rate vs. work of adhesion with all the materials using the triplet (left) and sextet (right) method.

When these three materials were removed from the plot, a better correlation between theoretical force and scaling rate was observed (not shown). If roughness had affected

material placement then SB steel and 'k. coating' should also have been affected. It was also reasonable to assume no direct correlation between the two techniques was obtainable due to fundamental differences between the two techniques. For instance, in scaling rate experiments the quantity of  $\text{CaCO}_3$  deposited on the surface was taken after all the cycles were complete. So once a layer of calcite had covered the material, the material exerted little, if any, effect on additional scale deposits forming on the base layer of scale. Furthermore, Bornhorst (1999) observed  $\text{CaSO}_4$  deposits obtained on a diamond-like carbon surface were easier to remove than on untreated stainless steel heaters during fouling experiments, This indicates that while inorganic deposits will form on carbon coated surfaces (amorphous and diamond-like), the strength of adhesion between the deposit and the coating will be much less. In addition, from the scaling rate data shown in Figure 4.19, it is impossible to know how easy or difficult it was to remove the  $\text{CaCO}_3$  deposits. Consequently, it would have been more applicable to relate the rate of scale formation up until a monolayer of scale (predominantly calcite) covers the surface, with contact angle measurements.

An interesting observation in the above plot was the link between theoretical adhesion and scaling rate was much stronger for materials that gave scaling rates up to  $10 \text{ g CaCO}_3 \text{ m}^{-2} \text{ h}^{-1}$ . This can be seen with triplet and sextet methods, where all these materials gave  $R_a$  values below 35 nm. With increasing  $R_a$  the ability to screen surfaces using the contact angle technique became problematic, since isolating a segment of these surfaces at the micron-scale was not representative of their behaviour at the bench level, where scaling rate experiments are performed. Therefore, it was apparent the complex interplay of surface roughness and material heterogeneity, which present domains of different surface chemistry were responsible for discrepancies between theory and reality. These surfaces were likely to have domains where a single droplet can wet grooves as well as sit on peaks of the surface, thus affecting the apparent contact angle (He *et al.*, 2004). Because the three-phase contact line on a rough substrate was expected to drift on the x-y plane at different rates until an optimal angle was obtained, it was difficult to observe when this point was reached. However, the majority of these materials gave greater mean contact angles than materials with low  $R_a$ , so droplets were more likely to sit on peaks, making

them less hydrophilic. As SB steel and 'k. coating' were most hydrophobic (most of the drop sitting on surface peaks), this was why both these materials appeared to fit in the trend linking theoretical force with scaling rate seen in the top right of the plots shown in Figure 4.19. Therefore, a more precise indicator of scaling rate of a material may be provided simply by its water contact angle, although surfaces with high  $R_a$  values will certainly obscure any trend.

When force measurements with modified and unmodified tips were also plotted against scaling rate no trend was observed. This was because the contact area was much smaller (at the nanometre for unmodified tips) than contact angles, so the best way to explain this behaviour was by grouping materials into metallic/non metallic surfaces with their  $R_a$  values (Table 4.15).

**Table 4.15:** Comparison of scaling rate (numbered from 1-12 low-high) and AFM/contact angle measurements based on material  $R_a$  values.

	<b>Low <math>R_a</math></b>	<b>Mid <math>R_a</math></b>	<b>High <math>R_a</math></b>
<b>Non-metallic</b>	Dymon-iC (1) Graphit-iC (2) PTFE (6)	'K. coating' (11)	
<b>Metallic</b>	Gold-0.1mm (8) Gold-0.3mm (3) MF steel (5) Unused copper (10)	TiN (4) Al (7)	RF steel (9) SB steel (12) Used copper (not tested)
<b>Scaling rate correlation with AFM</b>	Excellent	Good	Poor
<b>Scaling rate correlation with contact angles</b>	Excellent	Good	Good

For low  $R_a$  materials, force measurements with unmodified and modified tips gave excellent correlation of metallic and non-metallic substrates, where adhesion was consistently stronger on metallic than non-metal substrates. For instance, silica and calcite tips were weakly adhesive to amorphous carbon coatings and strongly to gold-0.1mm/MF steel. Generally, these substrates gave reproducible forces by virtue of their uniform topography and surface chemistry, and the forces that came into play have already been discussed. For mid to high  $R_a$  substrates, it was no surprise three of the most scaling substrates (According to data given in Table 4.14) was in this category. When

force measurements were performed on mid to high  $R_a$  materials, it was also apparent adhesion ranking fluctuated, as demonstrated with modified and unmodified tips in particular. Similar to issues affecting the contact angle method, force measurements on these materials depended on recurring tip-on-valley interactions to give stronger adhesion, but calcite probes gave greater tip-on-peak interactions due to the large crystal size. It appears experiments with unmodified tips on medium to high  $R_a$  materials represent the extreme limit of very low available surface area, which is fundamentally different to the experimental conditions of scaling rate. This is precisely why AFM images are performed with unmodified tips and not modified tips, because the ultrasmall tip is able to enter the smallest of microgrooves and show this as an asperity on the image. The contact scenarios is shown in Figure 4.20.

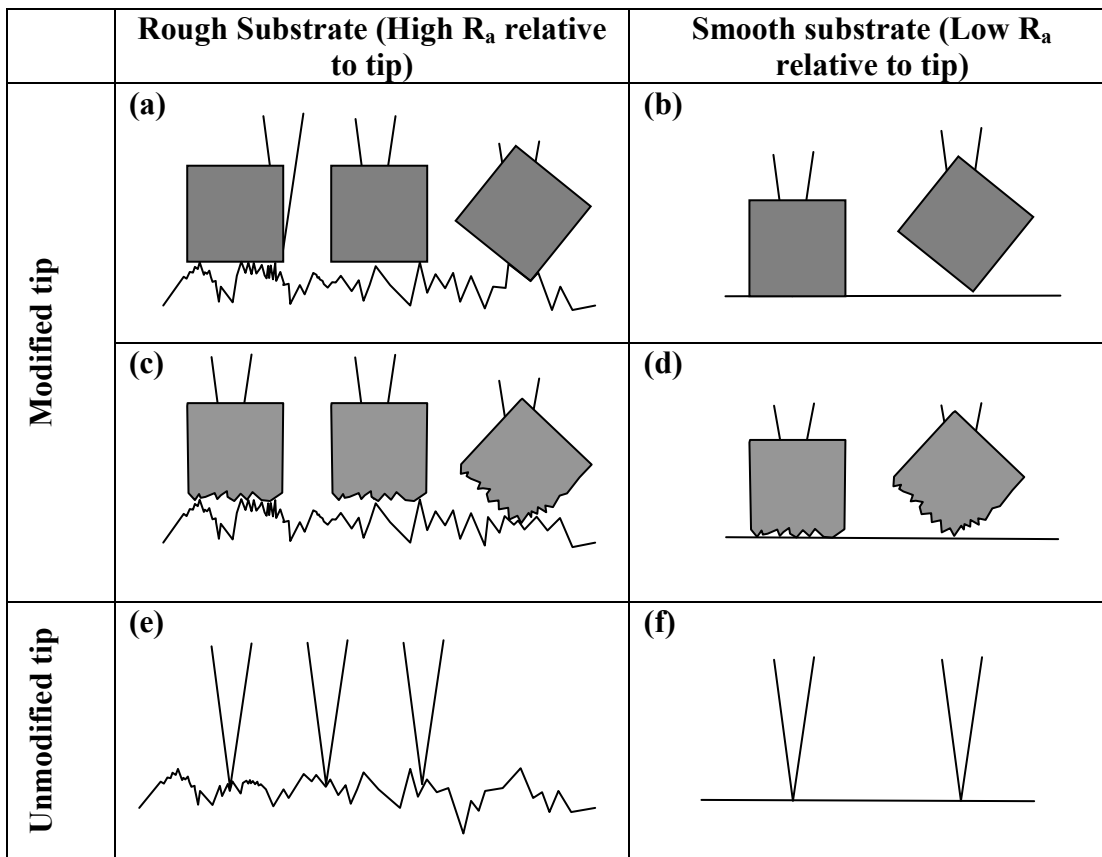


**Figure 4.20.** Schematic showing the affect of modified and unmodified tips on surfaces with different  $R_a$  values relative to contact area.

When mid to high  $R_a$  materials are combined with modified tips with non-planar surface profiles, contact area fluctuated (Figure 4.20c). With unmodified tips contact area was

somewhat more reproducible, but as shown in Figure 4.20e, subtle changes in contact area could still have a dramatic impact on adhesion. The ideal situation for reducing the affect of contact area was to use substrates with low  $R_a$  relative to the tip (Figure 4.20f) or use modified tips with a uniform surface profile (Figure 4.20b), like spherical particles.

Other causes of ambiguity was scaling rate experiments were performed at the elevated temperature of 72°C whilst force measurements were performed at room temperature, so materials may have responded differently to these conditions. For instance, at 42°C MF steel exhibited a similar scaling rate to RF steel, but at 72°C it scaled only half as much (MacAdam, 2005). With all other parameters remaining the same, temperature appears to promote scaling rate on rough substrates, possibly by enhancing precipitation in asperities at the solid liquid interface. For high  $R_a$  materials, it can be deduced their increased surface area promotes greater lateral calcite growth with stronger mechanical fixation to valleys during scaling experiments (Keysar *et al.*, 1994).

There was an attempt to recreate these mechanical effects with the use of rough calcite probes, which enhanced adhesion to RF steel. In contrast, low  $R_a$  materials promoted few mechanical effects and greater surface force effects, which were more applicable to AFM studies. Consequently, it may be more appropriate to perform scaling rate experiments until a monolayer of calcite precipitates on the substrate. It would then be possible to learn the size and topography of calcite crystals precipitated in valleys of rough substrates, and then attach crystals to the tip. They may also be compared to crystals precipitated on low  $R_a$  materials. But due to the difficulties in observing this behaviour it may easier to perform time-dependent experiments. On the other hand, a mathematical approach could be used, where the surface profile of a given substrate is determined with existing AFM imaging and incorporated into a mathematical model based on the Rabinovich roughness model.

## **Chapter 5                      Results and Discussion part 2 - Surface Characterization of NOM**

### **5.1 Introduction**

Natural organic matter is defined as an intricate mixture of organic material present in natural waters. It adversely affects many parts of water treatment, including the performance of unitary processes (such as adsorption, coagulation and oxidation) and the application of disinfectants (Krasner *et al.*, 1989). As a result, process optimization with respect to NOM removal has gained a lot more attention (Sharp *et al.*, 2004; Qin *et al.*, 2006 and Sharp *et al.*, 2006). One of the NOM fractions, humic acid fraction (HAF), has been a known precursor for disinfection by-product (DBP) formation (Singer, 1999). A more recent study by Kanokkantapong *et al.*, (2006) confirmed hydrophobic fractions were more reactive with chlorinated disinfectants than hydrophilic acids (HPIA). However, of increasing concern is the formation of halogen-based by-products from NOM, of which trihalomethanes (THM's) and haloacetic acids (HAAs) are suspected human carcinogens (Black *et al.*, 1996).

The coagulation process is an integral operation to reduce NOM levels in surface waters and coagulants most commonly used are iron and aluminium salts. However, removal efficiency is variable, depending on the physical and chemical characteristics of the water and the operating conditions. In one study Sharp *et al.*, (2006) found NOM's fractional make-up can significantly impact coagulation performance. The authors found the fulvic acid fraction (FAF) most resembled bulk water operational characteristics in relation to certain floc properties, but was less readily removed using existing coagulation techniques. They also found elevated FAF levels control raw water floc size leading to poor removal. As hydrophobic FAF is one of the main precursors for DBP formation, it is essential FAF's general reactivity and poor removal efficiency must be addressed at a more fundamental level. Therefore, understanding the mechanism of intermolecular interactions amongst fractions in situ is an integral part of the present study. The AFM is an important tool for investigating detachment profiles of polymeric materials, of which



NOM fractions, and particularly humic components, are classically viewed as negatively-charged, branched polyanions (Christl *et al.*, 2000). In this proof-of-concept experiment detachment profiles will provide signatures of polyanions, which might be related to their intramolecular and intermolecular interaction within flocs, their reactivity with disinfectants or simply their origin. By investigating detachment profiles of immobilized NOM polyanions, the information gained may in future be used for developing innovative NOM removal strategies. In addition, NOM polyanions immobilized on an AFM tip and surface will recreate to a certain extent NOM interactions in situ that are absent in conventional analysis of NOM polyanions.

## 5.2 Contact angle measurements

Figure 5.1 shows measured average contact angles of four probe liquids on immobilized NOM polyanions, polycationic poly-L-lysine (PLL) and uncoated glass.

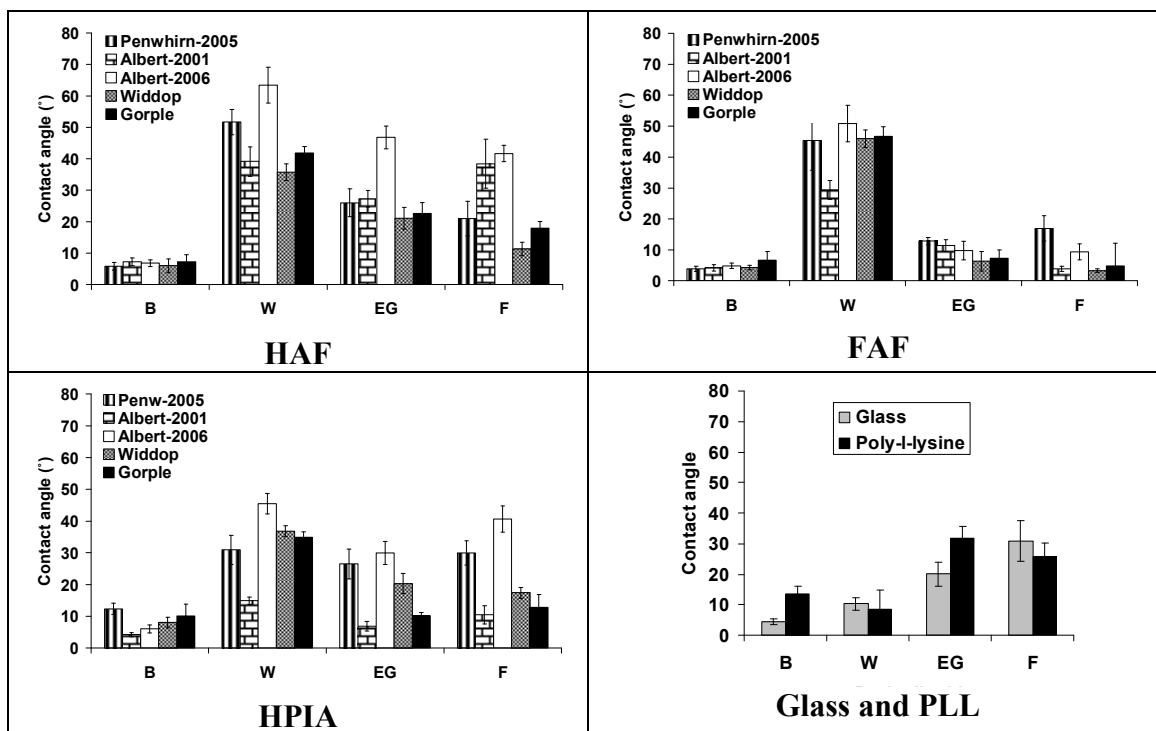


Figure 5.1. Contact angle values of probe liquids on HAF, FAF and HPIA and glass and PLL control surfaces.

Average water contact angles on uncoated glass and PLL were  $10.33 \pm 2.01^\circ$  and  $8.59 \pm 6.16^\circ$ , respectively, which were classed as very hydrophilic (contact angle  $\leq 10^\circ$ ). In

contrast water contact angle on NOM surfaces were much higher. For example, mean water contact angles were  $46.34 \pm 3.8^\circ$ ,  $43.65 \pm 4.9^\circ$  and  $32.59 \pm 2.5^\circ$  on HAF, FAF and HPIA, respectively. The difference between hydrophobic polyanions and HPIA was significant ( $P < 0.001$ ) using the Mann Whitney U test, confirming immobilized HAF/FAF polyanions were less hydrophilic than HPIA (Aiken *et al.*, 1979). The slightly greater hydrophobicity of HAF than FAF is due to humic's greater molecular weight (Yee *et al.*, 2006).

Mean contact angles also varied between sources of the same polyanion and sources collected at different time intervals. For example, the HAF polyanion from Albert water (2006) gave the highest average water contact angle of  $63.39 \pm 5.64^\circ$ , while the 2001 sampling period was only  $39.13 \pm 4.69^\circ$ . This may be caused by seasonal changes in rainfall affecting NOM quantity and composition, which may indicate HAF polyanions were larger. Mean contact angles of other sources were in between the two Albert water sources. Water contact angle of Widdop and Gorple polyanions were similar, which was expected due to their close proximity (2 km).

Contact angles of EG and F on NOM surfaces also gave rise to variation between polyanions. Average EG contact angles were  $28.72 \pm 10.38^\circ$ ,  $9.49 \pm 2.73^\circ$  and  $18.76 \pm 10.02^\circ$  for HAF, FAF and HPIA, respectively. Unlike water contact angles, the mean EG contact angles varied considerably, particularly on HAF and HPIA polyanions. Formamide (F) on NOM surfaces gave smaller contact angles compared to EG, due to the difference in liquid  $\gamma^-/\gamma^+$  ratio.

All polyanions were almost wetted by 1-Bromonaphthalene (B), of which FAF gave the smallest average contact angle of  $4.76 \pm 1.12^\circ$ . Contact angles on HAF were stable at  $6.60 \pm 0.66^\circ$ , while HPIA was dispersed with average contact angles of  $8.15 \pm 3.21^\circ$ . Low CA of 1-bromonaphthalene was due to the high Lifshitz-Van der Waals surface free energy of all hydrophobic polyanions, which is explained in the next section.

### 5.2.1 NOM surface free energy measurements

The dispersive components of the surface free energy ( $\gamma^{LW}$ ) were 44.02 to 44.16 mJ.m<sup>-2</sup> for HAF, 44.05 to 44.30 mJ.m<sup>-2</sup> for FAF and 43.36 to 44.28 mJ.m<sup>-2</sup> for HPIA (Figure 5.2). The difference in  $\gamma^{LW}$  values for HAF and FAF was negligible because the hydrophobic core of both polyanions was centrally located, while polar groups such as COOH, OH and NH<sub>2</sub> are surface-specific.

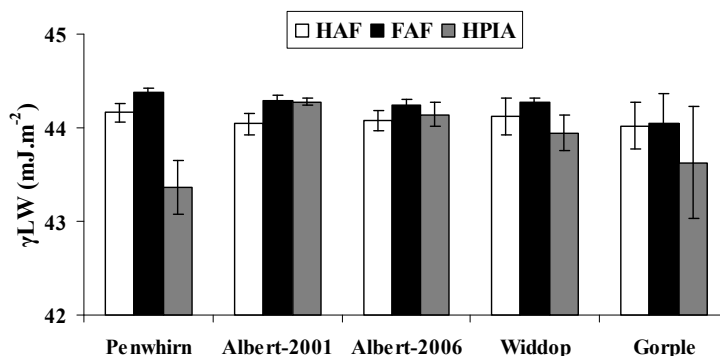
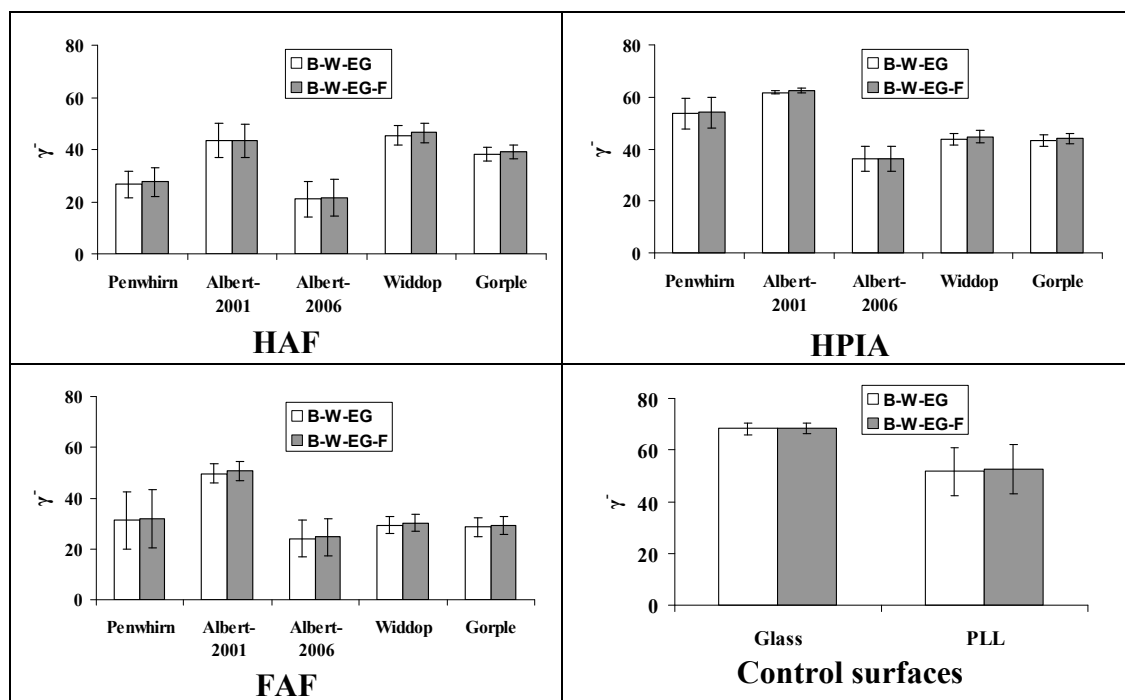


Figure 5.2.  $\gamma^{LW}$  values of HAF, FAF and HPIA polyanions obtained from five water samples.

Such amphiphilic properties of hydrophobic polyanions are of increasing interest, and their micellar conformation has been confirmed with AFM images (Guan *et al.*, 2006). For hydrophobic polyanions, Lower Gorple gave the lowest values of 44.02 mJ.m<sup>-2</sup> (HAF) and 44.05 mJ.m<sup>-2</sup> (FAF). For HPIA, Penwhirn gave the lowest value of 43.36 mJ.m<sup>-2</sup>. Both Albert waters gave similar  $\gamma^{LW}$  values for HAF and FAF, but a relatively large difference of 0.14 mJ.m<sup>-2</sup> was observed for HPIA. Average  $\gamma^{LW}$  values of HAF, FAF and HPIA were 44.02, 44.05 and 43.63 mJ.m<sup>-2</sup> for Lower Gorple compared to 44.13, 44.27 and 43.95 mJ.m<sup>-2</sup> for Widdop.

Figure 5.3 shows the basic ( $\gamma^-$ ) SFE values of immobilized NOM polyanions and glass/PLL controls calculated using the graphical plot method (McCafferty, 2002). PLL and glass gave  $\gamma^-$  values of 52.26 mJ.m<sup>-2</sup> and 68.27 mJ.m<sup>-2</sup>, respectively. Glass's high basicity was due to silanol (SiOH<sup>-</sup>) electron donors, which outnumber deprotonated SiO<sup>2-</sup> groups upon hydration. The  $\gamma^-$  values of NOM polyanions ranged from 21.55 to 46.43 mJ.m<sup>-2</sup>, 23.96 to 50.67 mJ.m<sup>-2</sup> and 36.35 to 62.26 mJ.m<sup>-2</sup> for HAF, FAF and HPIA, respectively.



**Figure 5.3** Histograms showing the  $\gamma$  surface free energy values (in mJ.m<sup>-2</sup>) for the five NOM sources and PLL/glass controls.

All NOM polyanions were strong electron-donors, predominantly due to carboxyl, alkoxyl and alkyl groups (Senesi *et al.*, 1991). HPIA polyanions from Penwhirn and Albert (2001) in particular gave similar  $\gamma$  values to glass, indicating HPIA was a strong electron donor. However, HAF and FAF were mainly aromatic and also comprise of electron-withdrawing (EW) terminals such as carboxyl and carbonyl groups on an aromatic mainframe (Avena and Koopal, 1999; Campitelli *et al.*, 2006 and Kanokkantapong *et al.*, 2006). In the case of HAF, Campitelli *et al.*, (2006) also found they comprise of charged phenolic-OH, carboxylic-COOH and quinone groups due to its large buffering capacity.

The absence of EW groups on HPIA will reduce the polarity of the OH group, thus making it increasingly electron-donating than hydrophobic polyanions (McCormack *et al.*, 2002). The  $\gamma$  values were similar to that obtained by Ramos-Tejada *et al.*, (2006) on adsorbed polyethyleneimine (PEI) films.

The  $\gamma^-$  values of HAF was highest for Albert water (2001) and Widdop because both surfaces were highly oxidised, and was lowest for Albert (2006). On immobilized FAF,  $\gamma^-$  values were also highest for Albert (2001), while Widdop and Gorple gave similar values. For Albert (2001) HPIA polyanions  $\gamma^-$  values were highest again and was very similar to glass, with the Albert (2006) source least electron-donating. Interestingly, all NOM polyanions from Albert (2006) gave the lowest  $\gamma^-$  value, which is thought to be due to fewer electron donors on the surface.

Figure 5.4 gives acidic ( $\gamma^+$ ) SFE values of immobilized NOM polyanions and glass/PLL controls. The  $\gamma^+$  SFE values were 0.04 to 0.30 mJ.m<sup>-2</sup>, 0.18 to 0.81 mJ.m<sup>-2</sup> and 0.03 to 0.26 mJ.m<sup>-2</sup> for HAF, FAF and HPIA, respectively.  $\gamma^+$  values of PLL and glass were 0.29 ± 0.20 mJ.m<sup>-2</sup> and 0.03 ± 0.00 mJ.m<sup>-2</sup>, respectively.

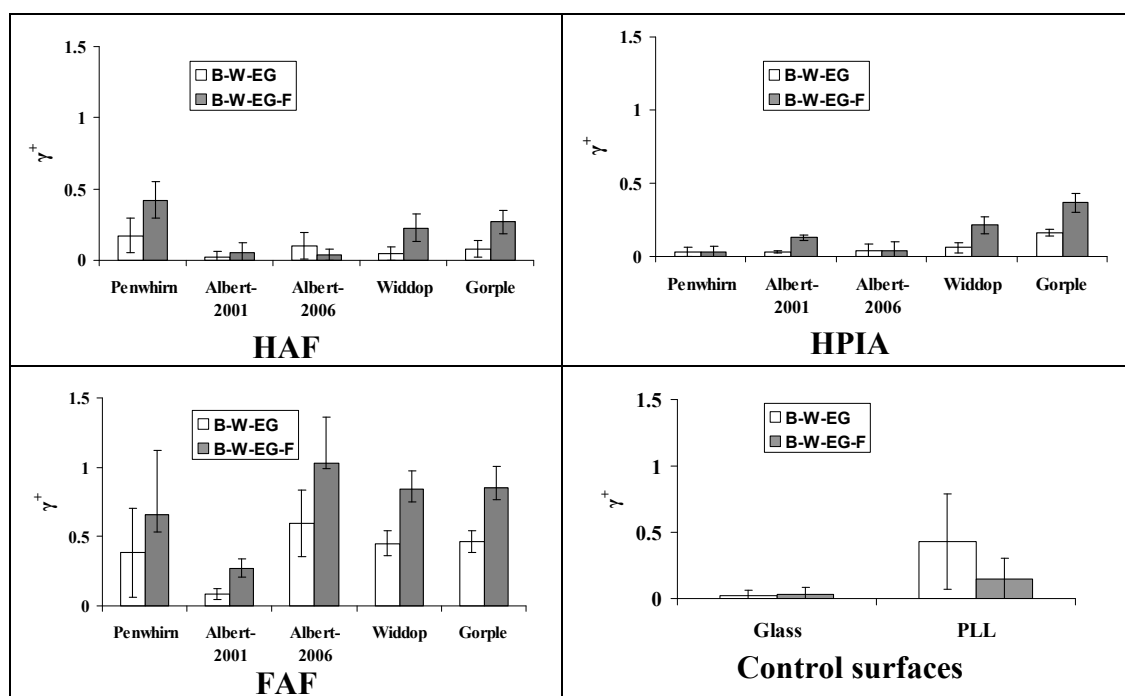


Figure 5.4. Histograms showing the  $\gamma^+$  SFE values (in mJ.m<sup>-2</sup>) for the five sources of HAF, FAF, HPIA and PLL/glass controls.

Acidic component of PLL was twice as much as glass due to the presence of protonated amines (NH<sub>3</sub><sup>+</sup>) that are electron acceptors (Watson *et al.*, 2004). It was clear all NOM polyanions were weak electron acceptors, with few electron-withdrawing terminals. The small  $\gamma^+$  values are not unusual, as Ramos-Tejada *et al.*, (2006) also gave low  $\gamma^+$  values ranging from 0 to 2.5 mJ.m<sup>-2</sup> on adsorbed PEI films. FAF polyanions were most electron-

accepting, which is thought to be due to quinone groups that are electron transporters (Fulton *et al.*, 2004), as well as ketones, aldehydes and amides (Plaza *et al.*, 2007). Quinones are also present on HAF, so  $\gamma^+$  values were expected to be similar to FAF. Albert (2001) gave the lowest  $\gamma^+$  value, which may be linked to fewer quinone moieties or their reduction to hydroquinone groups. The feeders gave high  $\gamma^+$  values for HPIA, which may be caused by an increased density of carboxyl and carbonyl groups on these polyanions.

Due to the size and complexity of NOM polyanions, it was problematic to ascertain whether immobilized polyanions were in the form of spherical (Guan *et al.*, 2006), ring-shaped (Namjesnic-Dejanovic and Maurice, (1998) and Liu *et al.*, (2000)) or linear aggregates, or if they were uniformly adsorbed or dispersed on PLL. Due to the polycationic base, polyanions were expected to adsorb strongly by electrostatic forces (Claesson *et al.*, 2005). Nevertheless, imaging of NOM was very difficult because adsorbed NOM could get displaced and the underlying PLL base be disturbed by the tip. Contact angle measurements gave strong differences in acidic character of adsorbed NOM films, where FAF greater  $\gamma^+$  values than HAF and HPIA, although absolute values were very small compared to the corresponding  $\gamma^-$  values. Furthermore, there was significant variation between NOM sources. For example, the Penwhirn, Albert-2006 and Lower Gorple sources gave the highest  $\gamma^+$  values for HAF, FAF and HPIA polyanions, respectively. However, all NOM polyanions from Albert (2006) gave the lowest  $\gamma^-$  values.

### 5.3 AFM force measurements

Table 5.1 gives a summary of the probes used during force measurements on immobilized NOM, tip characteristics and the rationale behind tip selection.

**Table 5.1** Summary of AFM force measurements performed using both modified and unmodified tips, and the motivation for performing such experiments.

Section in Thesis	Tip modification type	Reason for tip choice	Tip charge	Tip radius ( $\mu\text{m}$ )
5.3.1	Unmodified (silica) tips (SiOH <sup>-</sup> )	Measure differences between (a) NOM polyanions and (b) NOM sources. Compare pull-off lengths to floc strength and coagulation. To use as a standard tip choice.	Negative	0.03
5.3.2	PLL-coated tips (NH <sub>3</sub> <sup>+</sup> ):	Opposite in charge to silica tips so useful to compare	Positive	0.03
5.3.3	NOM-coated tips	Investigate inter-NOM interaction	Negative	0.03
5.3.4	Glycine-coated (NH <sub>2</sub> ) tips:	To compare with silica and PLL-coated tips	Neutral	0.03
5.3.5	XAD4 resin	Used for fractionation – to isolate hydrophilics	None	55
	XAD8 resin:	Used for fractionation – to isolate hydrophobics	None	68
	MIEX® resin:	Used as potential pre-treatment of NOM	None	80
5.3.6	HAF-coated XAD8 resin	To compare results with HAF-coated tips	Negative	55
	FAF-coated XAD8 resin	To compare results with FAF-coated tips	Negative	68
	HPIA-coated XAD4 resin	To compare results with HPIA-coated tips	Negative	80

#### 5.3.1 Silica probe versus NOM surface

Figure 5.5 shows force cycles of a silica tip on NOM surfaces from Penwhirn water and PLL control. Net attractive interactions of varying magnitude were observed on all surfaces, indicated by the presence of ‘jump-to’ events (Figure 5.5, left). Hydrophobic surfaces were least attractive to the hydrophilic silica tip. Sharp *et al.*, (2006) showed at pH 6 hydrophobic polyelectrolytes exhibit a negative zeta potential with high surface charge densities, which may repel the SiOH/SiO<sup>2-</sup> tip via electrostatic repulsion. Deprotonation of COOH and phenolic groups on hydrophobic polyanions are thought to

be caused by the presence of EW groups linking their conjugated aromatic backbone, thus conveying a negative surface charge (Campitelli *et al.*, 2006).

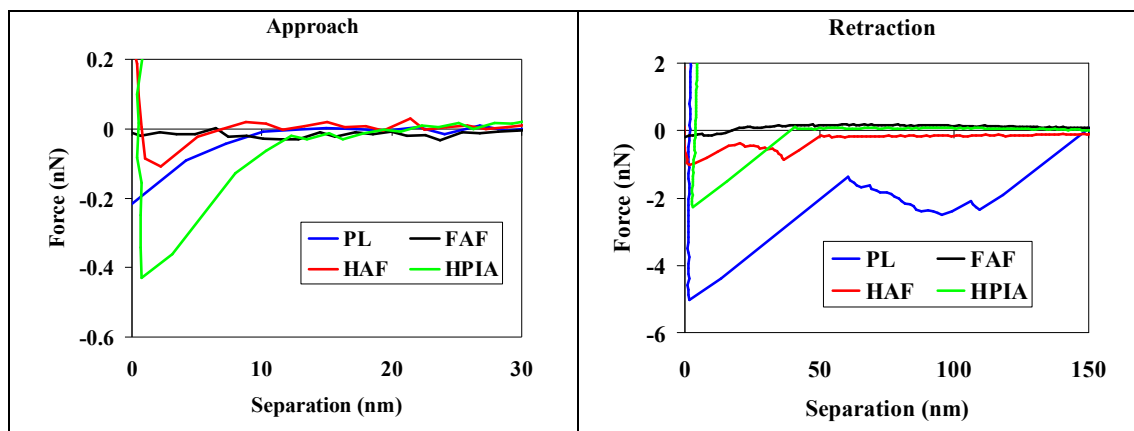


**Figure 5.5** Force vs. separation approach and retraction cycles of a silica tip on HAF, HPIA, FAF polyanions and PLL.

During tip retraction the presence of multiple rupture events meant adhesion forces were taken at the first rupture (or pull-off) event known as peak adhesion force, which intercepted the y-axis (Figure 5.5, right). Subsequent rupture events diminish with increasing length of the pulled polyanion(s), as shown by the reduced force of the second peak event on PLL in Figure 5.5, (right) (Luckham, 2004). In the above example, HAF pull-off length persisted to 50 nm before detachment, followed by HPIA (42 nm) and then FAF (0 to 5 nm).

Figure 5.6a depicts three scenarios during NOM-tip interactions. The schematic shows rupture events were dependant on contact area, which may explain the infrequent pulling events on NOM. Given the heterogeneous nature of NOM polyanions, the tip may interact with NOM ‘tails’, ‘loops’ or compressed micelles, giving different rates of extension of the polyanion (Figure 5.6a). This was because some surface groups on an isolated polyanion will form monomer-surface contacts, while non-adsorbed segments of the polyanion were free to interact with the tip (Haupt *et al.*, 1999 and Claesson *et al.*, 2005). Furthermore, it was impossible to know if detachment events corresponded to a single polyanion or multiple polyanions.



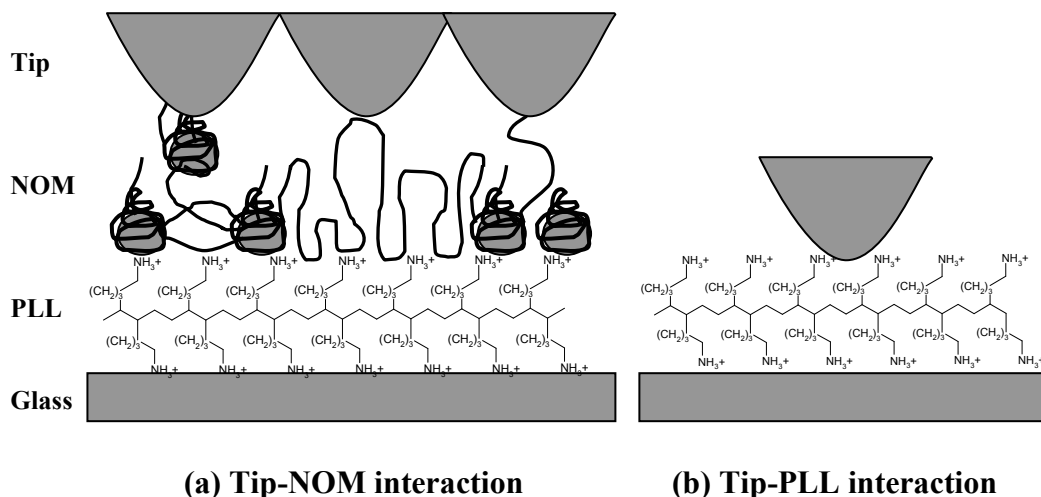


**Figure 5.6** Schematic of three different configurations of polymer-tip interaction during force measurements on NOM (a) and PLL (b).

The polydisperse nature of NOM with multiple functional groups exposed by non-adsorbed monomers also affects adhesion and pulling rates (Vezenov *et al.*, 2005). Of these groups unknown hydrophilic ‘heads’ were orientated to the tip because of the lower interfacial free energy at the hydrophilic group/water interface than the hydrophobic group/water interface (Israelachvili, 1992). Watson *et al.*, (2004) showed immobilized PLL exhibits a brush-like conformation, is less sterically restrained while presenting only cationic  $\text{NH}_3^+$  terminals (Figure 5.6b). As a result, PLL gave distinct pull-off events due to H-bond ( $\text{SiOH}^- \cdots \text{H-NH}_2^+$ ) and predominantly electrostatic ( $\text{SiO}^{2-} \cdots \text{NH}_3^+$ ) interactions (Kwon *et al.*, 2006).

### 5.3.1.1 Attractive forces

Figure 5.7 shows the distribution of attractive forces with one silica tip (U1) on immobilized NOM. There was a clear difference between hydrophobic and hydrophilic polyanions with respect to attractive forces. For instance, HAF/FAF peaked at  $\sim 0.06$  to  $0.1$  nN, apart from Albert 2001 water. HPIA was considerably more attractive to the tip than both hydrophobics with  $\geq 35\%$  of measured forces  $> 0.2$  nN. Of all five samples, Penwhirn and Albert-2001 were most adhesive with most attractive force  $> 0.2$  nN.

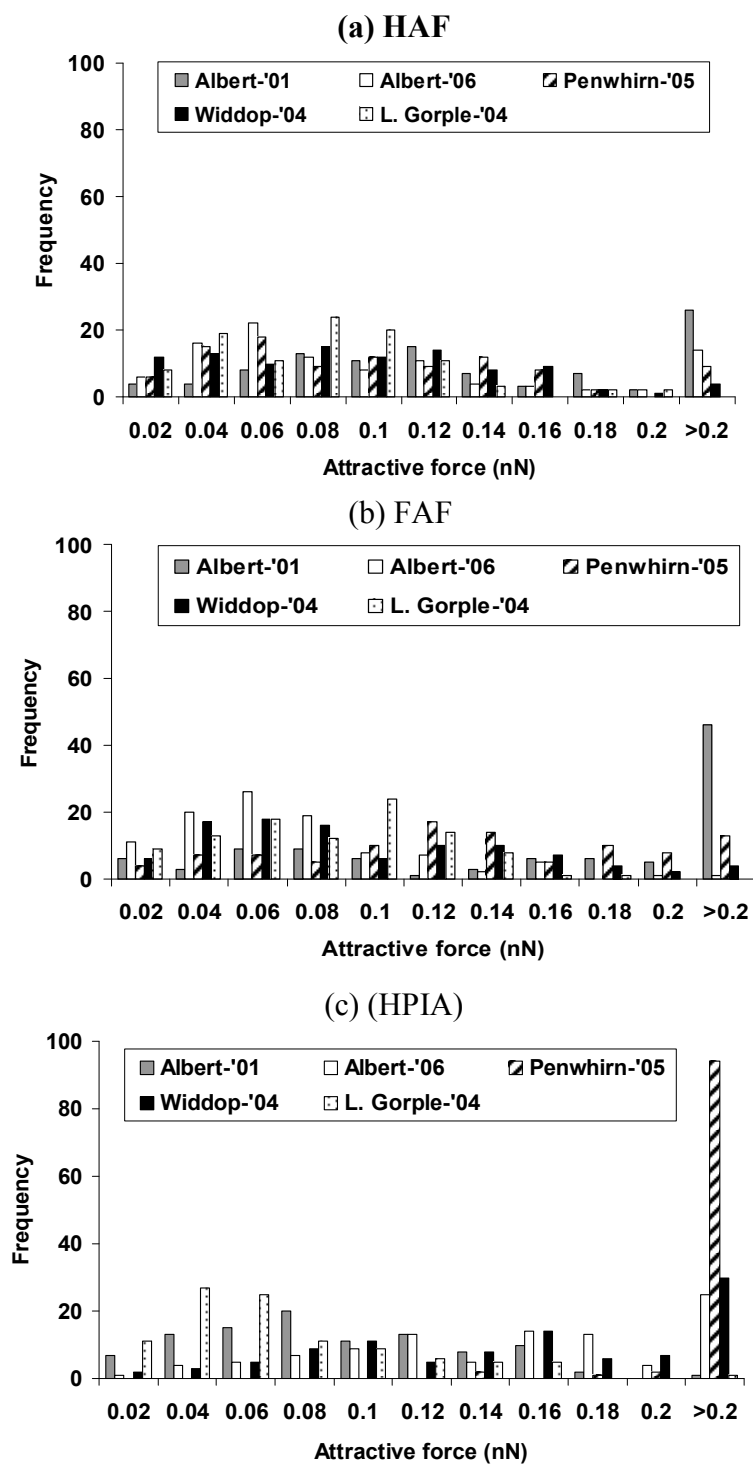


Figure 5.7

Histogram showing the distribution plot of attractive forces with a silica tip (u1) on (a) HAF, (b) FAF and (c) HPIA from all five samples.

### 5.3.1.2 Adhesion forces

Figure 5.8 shows frequency distribution plots of adhesion peaks with one silica tip on NOM surfaces. Immobilized HAF from feed waters were least adhesive, peaking at 0.5 nN, while Albert sources were more adhesive peaking at 1 nN. HAF from Penwhirn was almost twice as adhesive, with data points spread over 1 to 2 nN. With the 2<sup>nd</sup> probe, data points were spread across the force range on Albert 2001, with other HAF samples peaking to 0.5 to 1.5 nN (data not shown).

Immobilized FAF from Penwhirn, Lower Gorple and Albert-2001 peaked at 0.5 nN. Widdop and Albert-2006 samples peaked at 1 nN. This adhesion ranking on all sources was not maintained with the 2<sup>nd</sup> probe, although immobilized FAF from Albert 2001 and Penwhirn still remained least adhesive from all sources.

Immobilized HPIA from Penwhirn gave the strongest adhesion peaks at 3.5 nN and 4.5 nN for probes one and two respectively. Other sources gave much lower adhesion peaks ranging from 0.5 to 2.5 nN with both probes. Analysis of the peak adhesion force with silica tips showed greater variation with hydrophobic polyanions than HPIA. These findings illustrate adhesion peaks on hydrophobic surfaces were complicated by their multiple functionalities and structurally complex backbone, which did not produce reproducible adhesion events. The highly complex nature of hydrophobic surfaces indicates subtle differences in functionality and molecular weight between sources can have a significant affect on adhesion force.

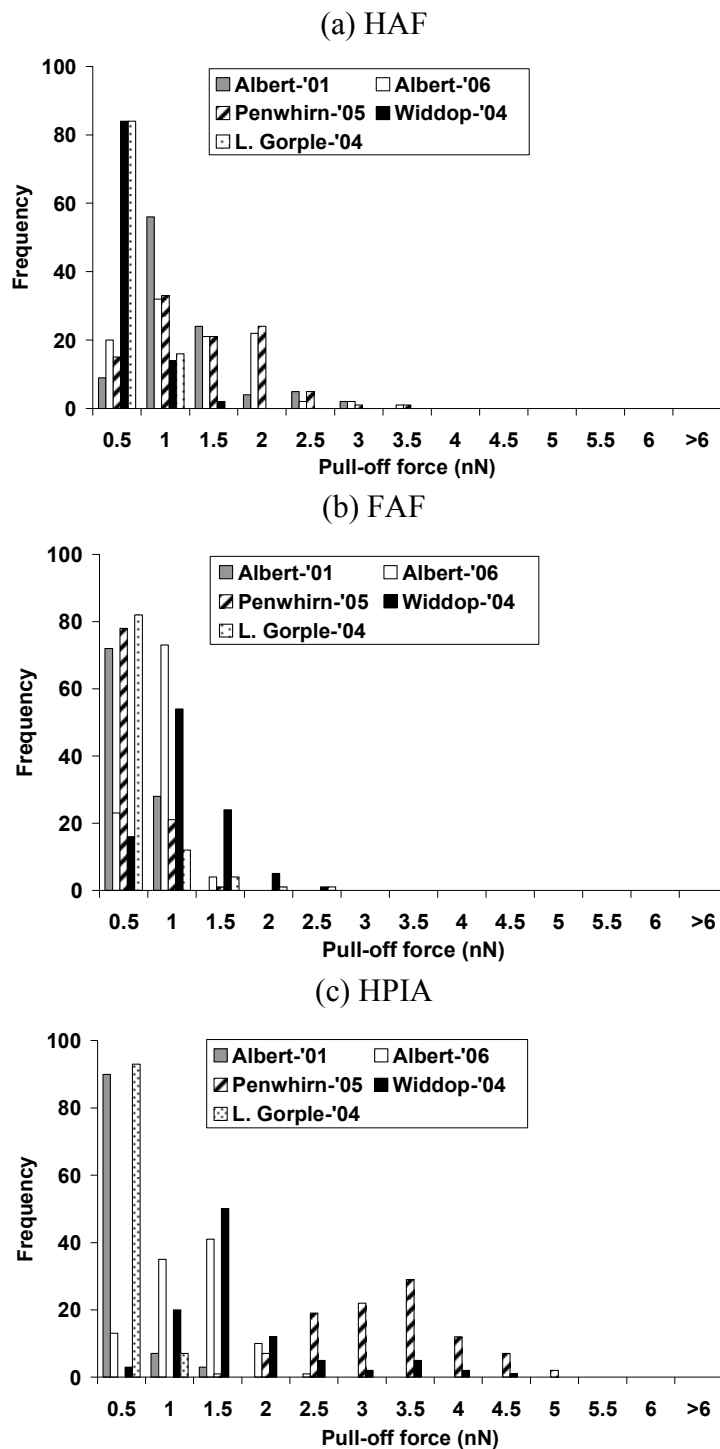


Figure 5.8 Histogram showing the distributions of adhesion peaks with probe U1 on HAF (a), FAF (b) and HPIA (c) from all five samples.

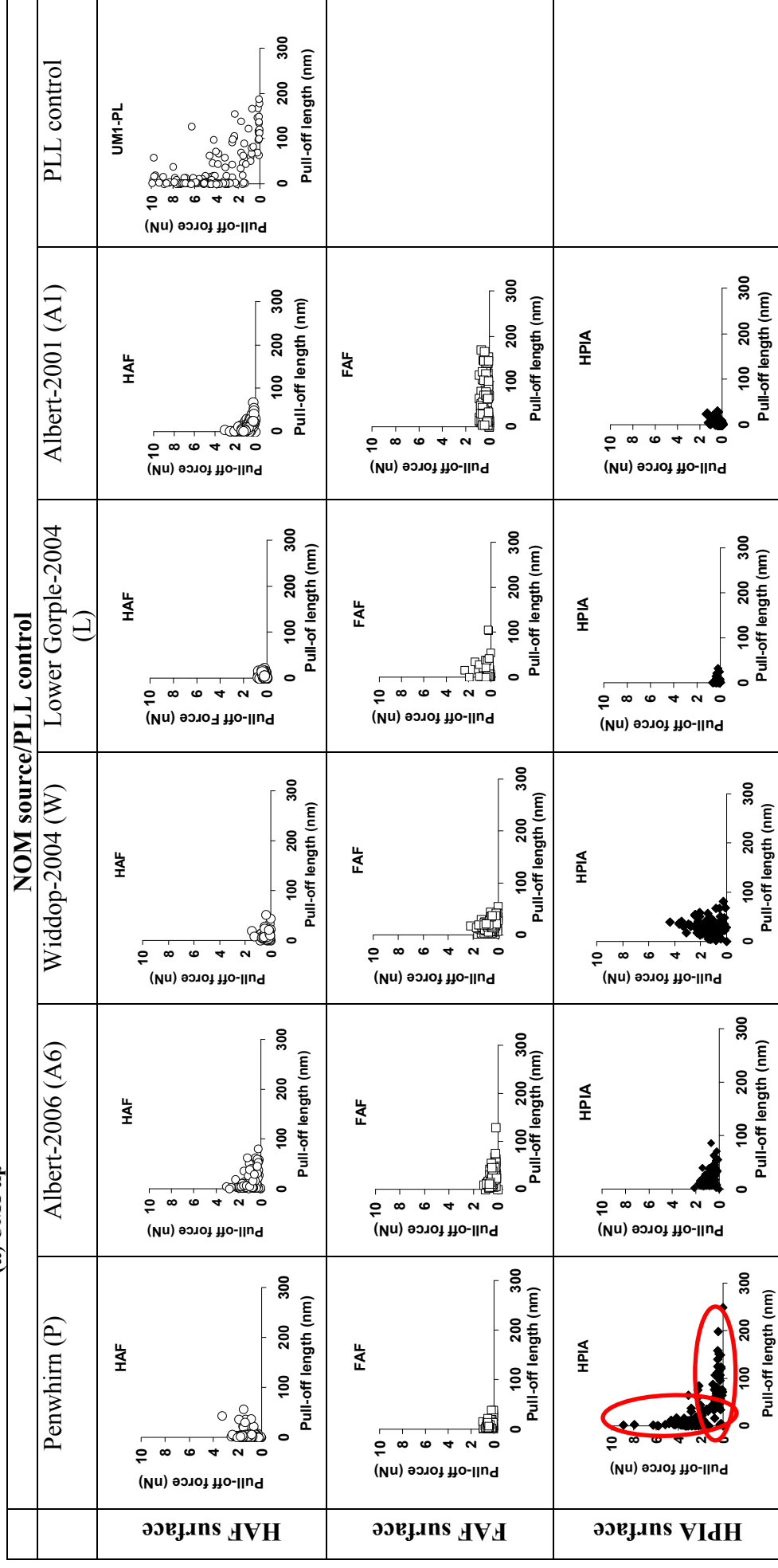
### 5.3.1.3 Pull-off length versus adhesion force

Figure 5.9 (a, b) shows scatter plots of length vs. pull-off force with silica tips on NOM surfaces and PLL controls. Multiple detachment events were observed by the large density of data points on the x-axis, while primary adhesion events along the y-axis were shorter but more adhesive (see Figure 5.9a on HPIA from Penwhirn).

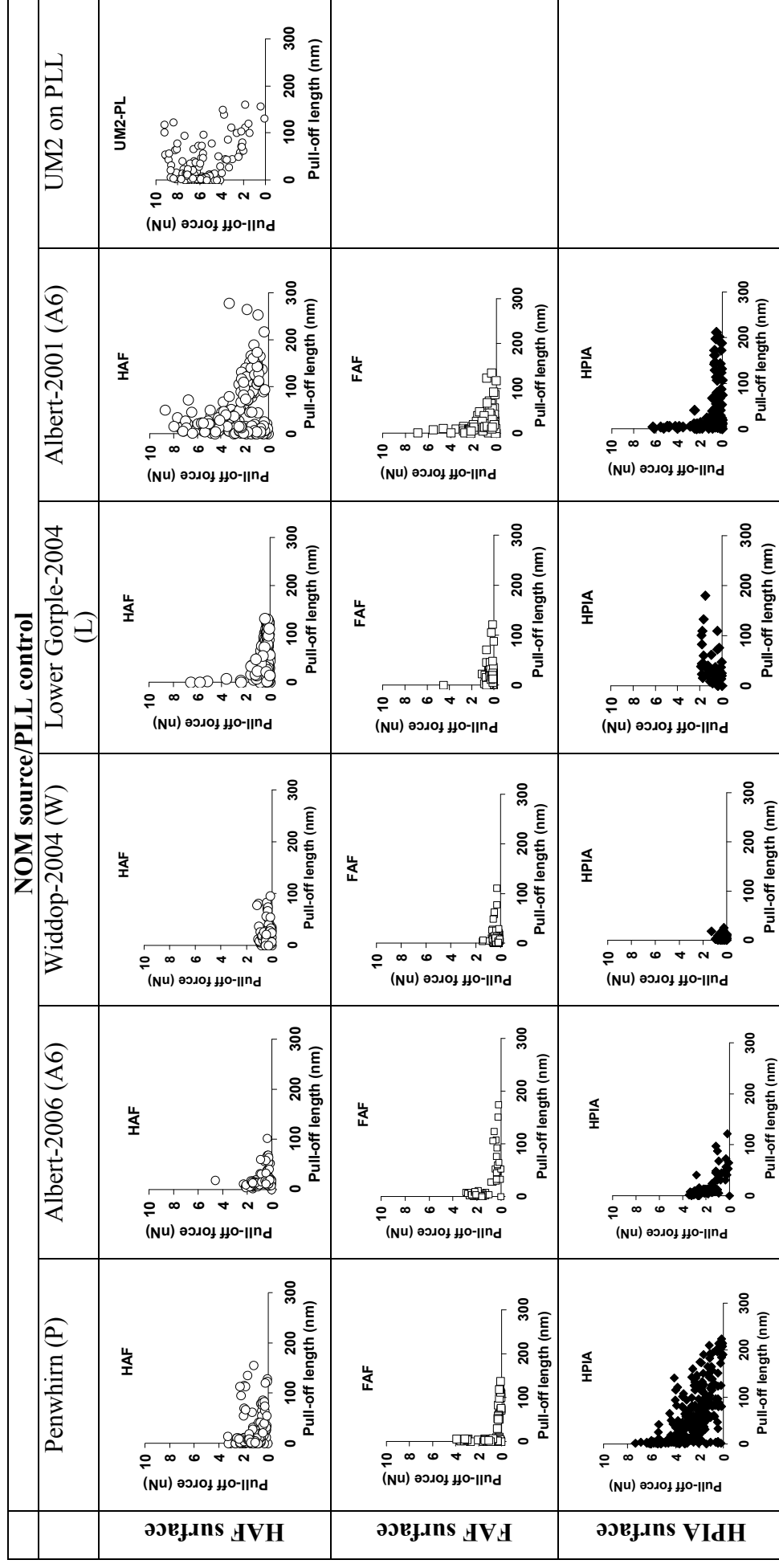
Generally, PLL gave forces an order of magnitude stronger than NOM polyanions. It was thought electrostatic forces were driving adhesion because Watson *et al.*, (2004) found at pH 6 lysine monomers on PLL conveyed protonated  $\text{NH}_3^+$  groups giving an IEP of 10.5, which were attracted electrostatically to  $\text{SiO}^{2-}/\text{SiOH}^-$  groups on the tip (IEP of 2) (McCafferty, 2002). Polycations have also been shown to readily adsorb to negatively charged surfaces in low electrolyte conditions (Claesson *et al.*, 2005). Although adhesion forces on both controls were similar, probe one gave somewhat weaker forces during polymer extension, while probe two gave stronger adhesion. Probe two was less adhesive to PLL relative to NOM polyanions, while pull-off lengths were also longer on NOM than PLL.

The main difference between probe one and two was NOM polyanions from Lower Gorple and Albert (2001) were more adhesive. For instance, on HAF both Albert sources gave lengths reaching ~80 nm with probe one, while probe two gave lengths up to 200 nm on Albert 2001. Both feeders gave pull-off lengths peaking at 40 to 120 nm with considerable variation in their pulled lengths using both probes. HAF from Penwhirn gave maximum length of 45 nm with probe one and just over 120 nm with probe two, with similar density of pull-off length as the feeders. Interestingly, the feeders and Penwhirn HAF also gave similar mean water contact angle values (Figure 5.1), which may be related to their similar detachment signatures.

**Figure 5.9** Scatter plot of pull-off length vs. pull-off force for (a) silica tip 1 and (b) silica tip 2 on NOM surfaces and PLL control.



## (b) UM2 tip



Immobilized FAF from Albert-2006 and 2001 gave peak lengths of 100 to 160 nm with both probes. Both feeders gave peaks of ~80 to 100 nm, which should effectively comprise of the same NOM chemistry and molecular size due to their similar SFE values (Figure 5.1). Pull-off lengths on FAF from Penwhirn were less consistent, giving lengths reaching 50 to 125 nm with both probes. Interestingly, the distribution of adhesion forces was similar on all immobilized FAF polyanions, which may indicate functional groups between sources were similar but varied in density due to variations in molecular weight.

Pull-off lengths on immobilized HPIA from Albert 2006 reached 80 nm with both silica tips. Pull-off lengths from Albert-2001 were less consistent, giving lengths up to 40 nm and 170 nm for tips one and two, respectively. The frequency of pull-off events for both tips was also in sharp contrast to one another. HPIA from the feeders gave detachment lengths of less than 100 nm. Pull-off lengths on Penwhirn HPIA reached 200 nm with both probes, showing a strong preference for this source in particular. Table 5.2 summarises peak adhesion force and pull-off rankings for each source.

**Table 5.2** Summary of pull-off lengths and adhesion forces on NOM sources with silica tips.

Source	Pull-off lengths	Adhesion forces
<b>Albert-2001 (A01)</b>	HAF>FAF=HPIA (U1) HPIA>HAF>FAF (U2)	FAF=HAF>HPIA (U1) HAF>HPIA>FAF (U2)
<b>Albert 2006 (A06)</b>	FAF>HPIA>HAF (U1) FAF>HAF>HPIA (U2)	HAF>HPIA>FAF (U1) HPIA>FAF>HAF (U2)
<b>Penwhirn water (PW)</b>	HPIA>FAF=HAF (U1) HPIA>HAF>FAF(U2)	HPIA>HAF>FAF (U1) HPIA>HAF>FAF (U2)
<b>Widdop (WD)</b>	HPIA>HAF>FAF (U1) HAF>FAF>HPIA (U2)	HPIA>HAF>FAF (U1) FAF>HPIA>HAF (U2)
<b>Lower Gorple (LG)</b>	FAF>HPIA>HAF (U1) HPIA>FAF>HAF (U2)	FAF>HAF>HPIA (U1) HPIA>FAF>HAF (U2)

A comparison between Albert water polyanions indicate FAF and HPIA gave similar adhesive events and pull-off lengths, while HAF was most adhesive. Although the sampling times varied they were expected to have comparable NOM chemistries. Surprisingly, feeder sources did not give the same pull-off lengths and peak forces for all NOM polyanions, indicating there were subtle variations in their surface chemistry. HPIA was shown to dominate pull-off lengths and adhesion force for the majority of



NOM polyanions. A column chart showing adhesion forces at each location on HPIA polyanions is shown in Figure 5.10.

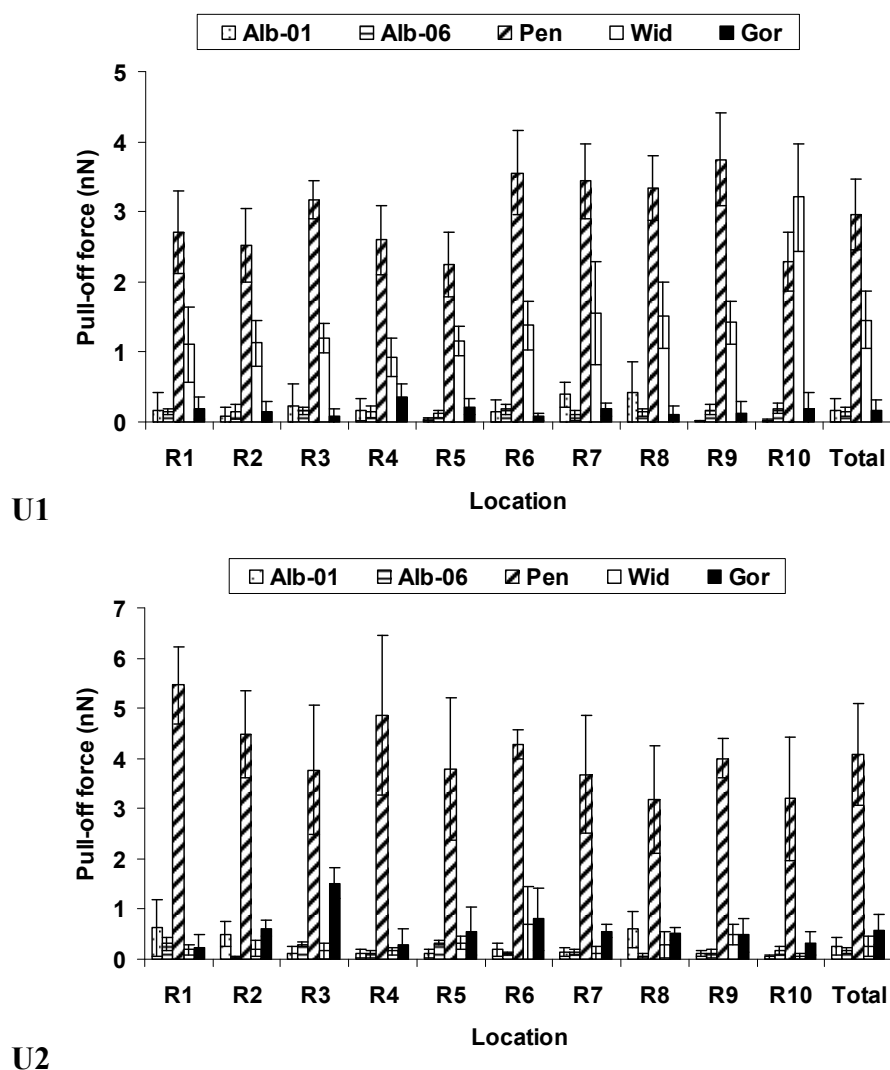


**Figure 5.10.** Column chart showing the distribution of forces at different locations of HPIA polyanions with both unmodified tips (U1 and U2).

The column chart shows HPIA from Penwhirn was consistently more adhesive, and was followed by HPIA from Widdop and Gorple. In a study by Rojas *et al.*, (2002) they suggest polyanion charge density was the driving force of adsorption. The authors observed with reduced polyelectrolyte charge density, adsorbed layer thickness increased, leading to longer detachment lengths. As HPIA has been shown by Sharp *et al.*, (2006) to be less negatively charged than hydrophobic fractions, it appears electrostatic forces were

driving adhesion of HPIA to  $\text{SiO}_3^{2-}$  groups on the tip. However,  $\gamma^+$  values of Penwhirn HPIA were the lowest of the polyanions, so the precise binding mechanism could not be established at present.

### 5.3.2 Silica/PLL probe versus NOM surface

Figure 5.11 shows approach and retract cycles of a PLL-coated tip on immobilized Penwhirn NOM polyanions.

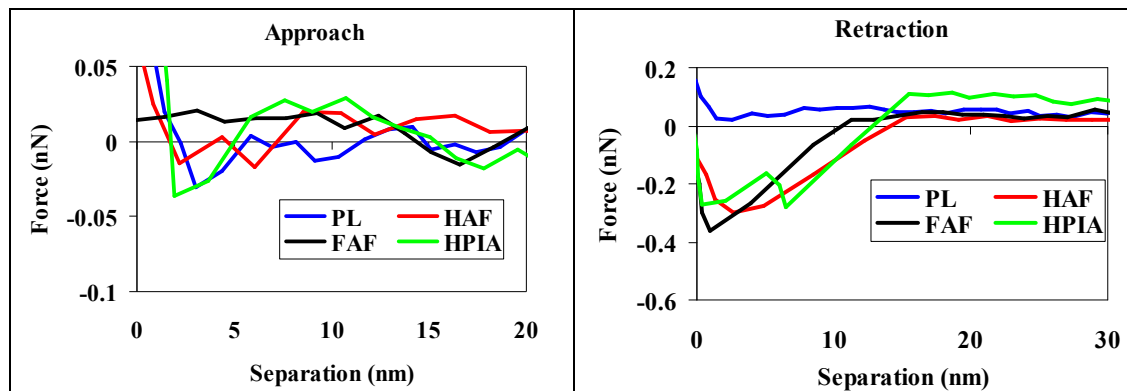


**Figure 5.11** Force vs. separation approach and retraction cycles using one PLL-coated tip on HAF, FAF, HPIA polyanions and PLL control.

Approach cycles did not give sharp jump-to events observed with silica tips due to the reduced density of  $\text{NH}_3^+$  groups on the tip. Instead a net repulsion was observed on all NOM films prior to snap-on at  $\sim 5$  to  $10$  nm. This was because both surfaces were compressible and the polycationic tip exhibited a brush-like conformation (Luckham, 2004). The tip was attracted to NOM polyanions but repulsive to PLL as expected, due to hydrophilic (from its low CA with water) and electrostatic repulsion. When polyelectrolytes overcame long-range steric repulsion,  $\text{NH}_3^+$  groups were expected to adhere strongly to FAF, followed by HAF and then HPIA due to differences in polyanionic charge density (Rojas *et al.*, 2002). During retraction pull-off forces on FAF were strongest, followed by HAF, HPIA, and then PLL (Figure 5.11, right). The origin of FAF's and HAF's high charge density is thought to be due to their aromatic backbone which controls the dissociation constant of COOH, phenolic OH and other functional groups (McCormack *et al.*, 2002).

### 5.3.2.1 Attractive forces

Figure 5.12 shows frequency distributions of attractive forces with one PLL-coated tip. Attractive forces were in the order HPIA>FAF>HAF on all sources except Lower Gorple. For instance, HAF, FAF and HPIA from Penwhirn peaked at 0.02, 0.04 and 0.06 nN, respectively. Similarly, Albert-2006 source peaked at 0.04, 0.06 and 0.14 nN for HAF, FAF and HPIA, respectively. It was unclear whether this trend was due to steric or electrostatic factors, or due to the presence of PLL as the adsorbent. Interestingly, all Penwhirn NOM surfaces gave lower attractive force peaks, and particularly HAF. HAF from Penwhirn gave the highest  $\gamma^+$  values from contact angle data, which indicates electrostatic repulsion may have dominated surface forces. However, FAF and HPIA from Penwhirn were not highly electron-accepting, so their repulsive interactions could not be explained.

### 5.3.2.2 Adhesion forces

Figure 5.13 shows frequency distribution plots of peak adhesion forces using one PLL-coated tip (probe 2). On FAF polyanions, adhesion forces on both Albert sources and Penwhirn water peaked at 0.2 to 0.4 nN. Widdop and Gorple polyanions peaked at 0.6 nN and 0.4 nN, respectively.

On HAF polyanions, Albert-2001 sample peaked at ~0.2 nN, while the 2006 sample was more adhesive, peaking at 0.6 nN. Penwhirn HAF polyanions peaked at 0.4 nN, while Gorple peaked at the much lower force of 0.2 nN. In contrast, the HAF from Widdop was more adhesive, peaking at ~0.2 nN.

On HPIA polyanions, adhesion peaks were ~0.6 to 0.8 nN for all samples except Albert-2006 and Penwhirn samples, which peaked at 0.2 and 0.4 nN, respectively. Albert-2001, Widdop and Lower Gorple polyanions peaked at 1, 1 and 0.6 nN, respectively. Interestingly, both Lower Gorple and Widdop gave similar adhesion peaks, indicating HPIA polyanions had a similar surface chemistry, which was in agreement with their SFE values given in Figures 5.3 and 5.4.

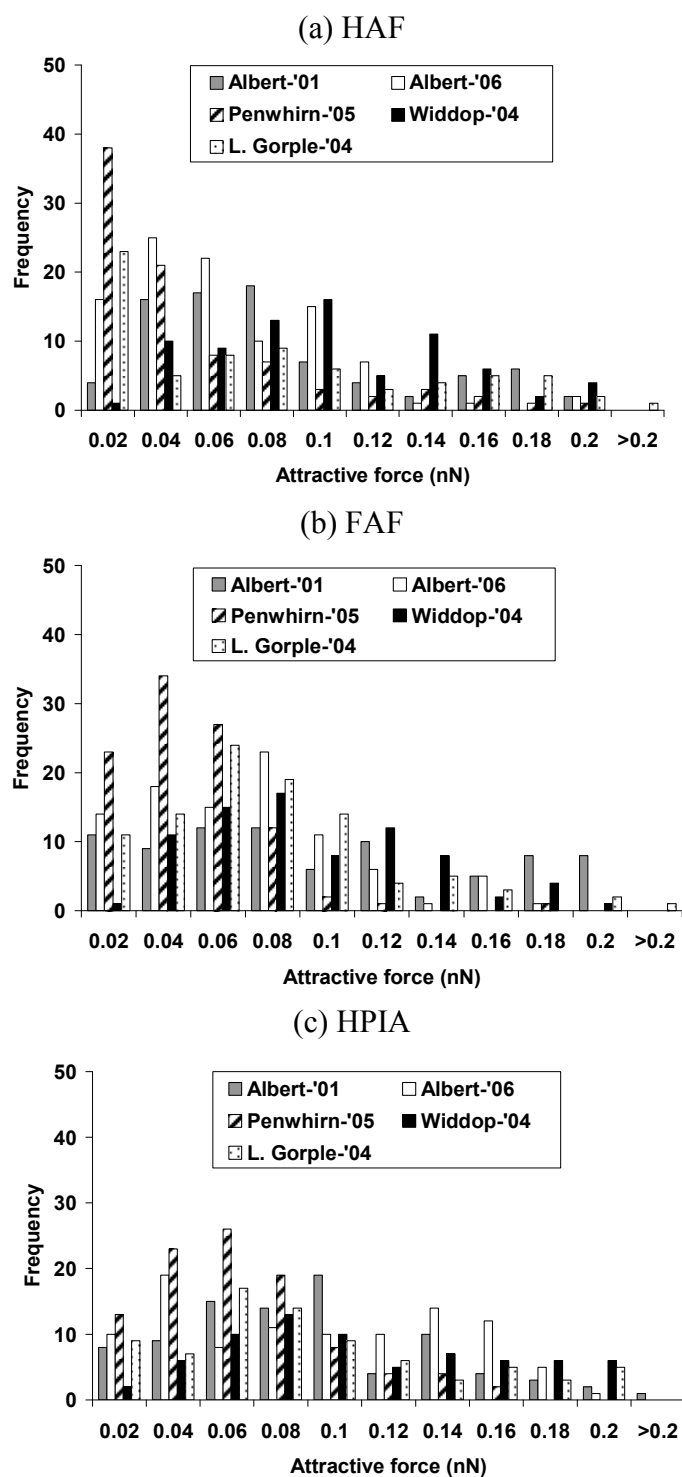


**Figure 5.12** Histogram showing the distribution plot of attractive forces with a PLL coated tip on HAF (a), FAF (b) and HPIA (c) from all five samples.

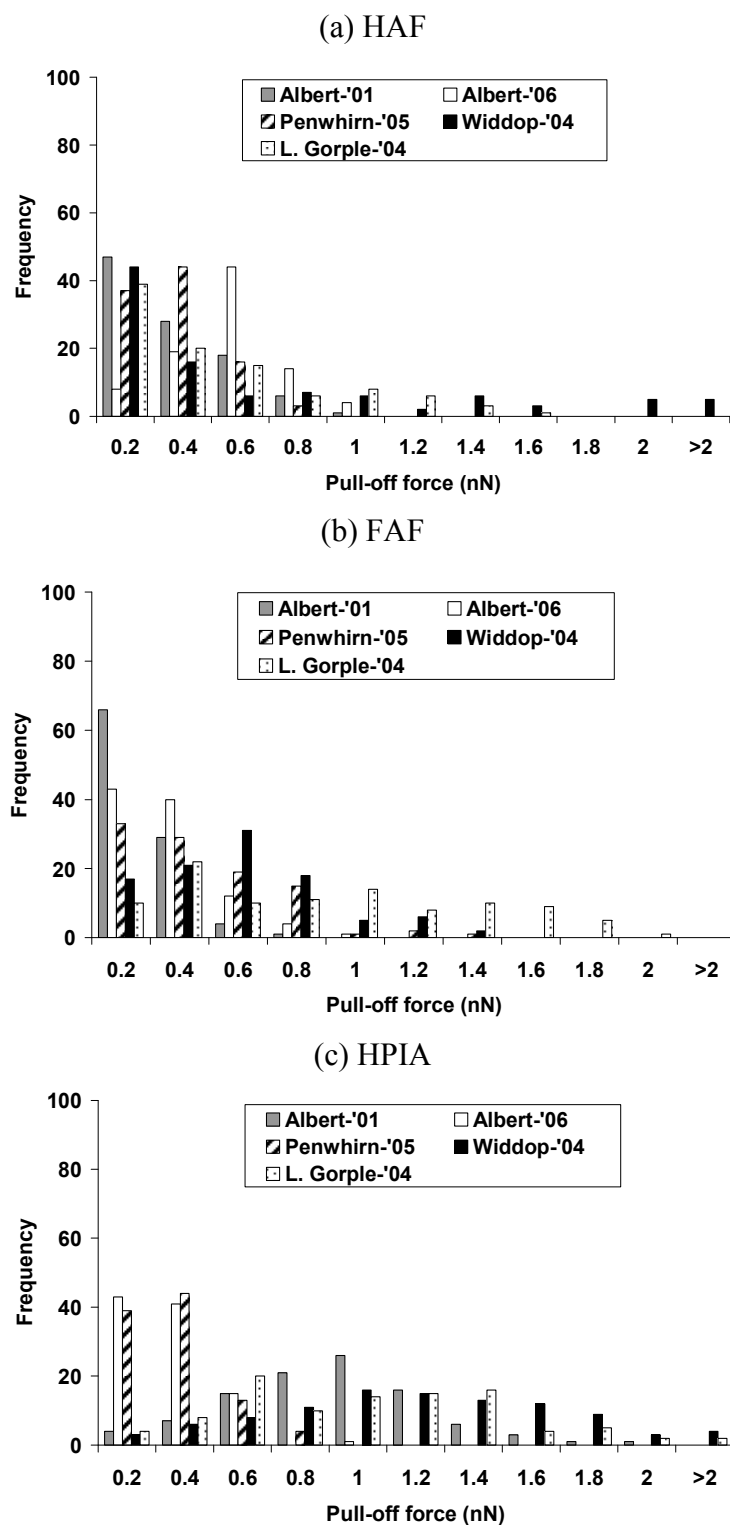


**Figure 5.13** Histogram showing the distribution plot of peak adhesion forces with a PLL coated probe on HAF, FAF and HPIA from all five samples.

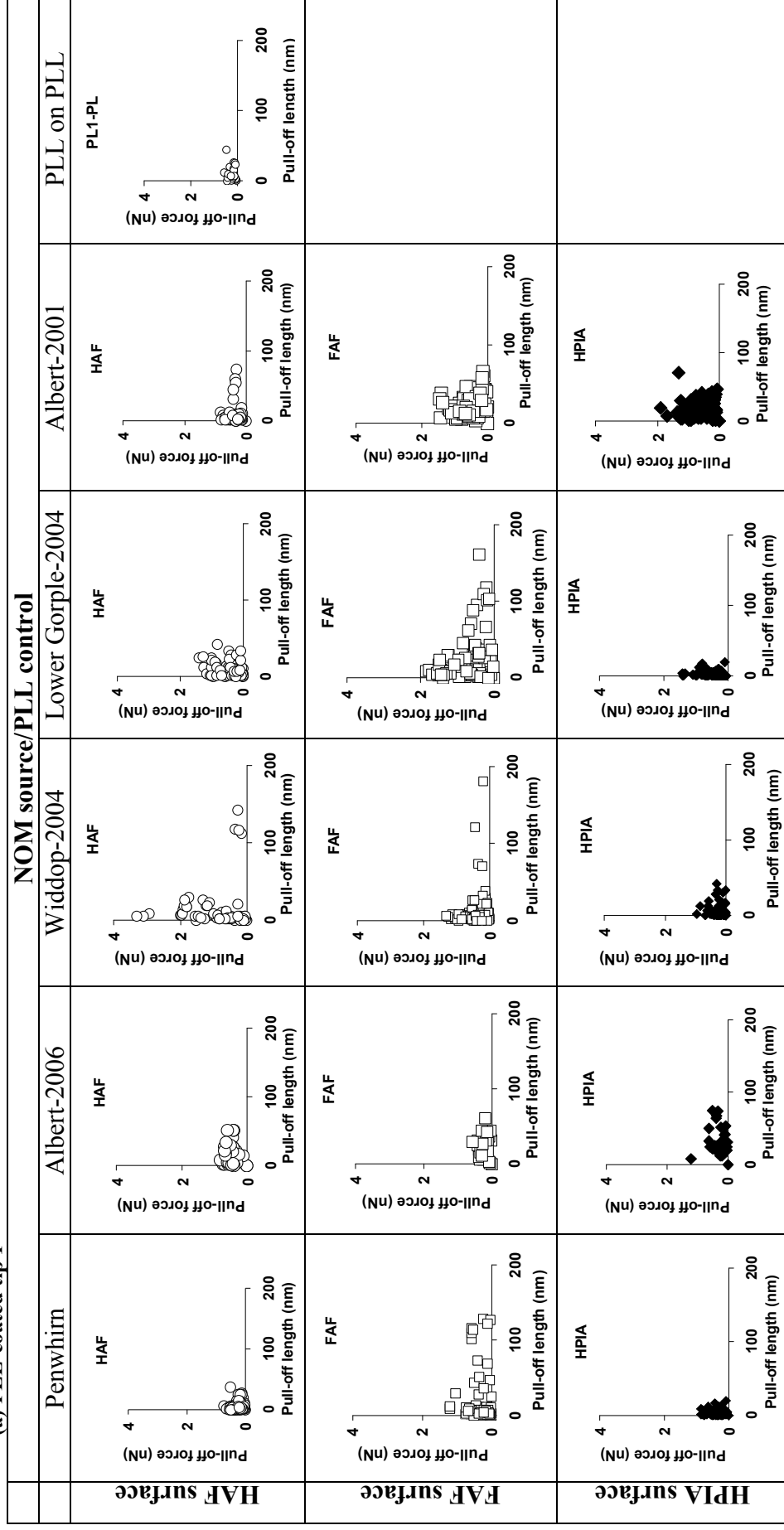
### 5.3.2.3 Pull-off length versus adhesion force

Figure 5.14 (a) and (b) shows pull-off length vs. pull-off force with PLL-coated tips on NOM films and PLL. Both PLL controls gave near identical forces and pull-off lengths, showing the  $\text{NH}_3^+$  groups were stably expressed. PLL tips were more adhesive to NOM polyanions than PLL, where forces reached 1 nN, and lengths peaked to about 40 nm.

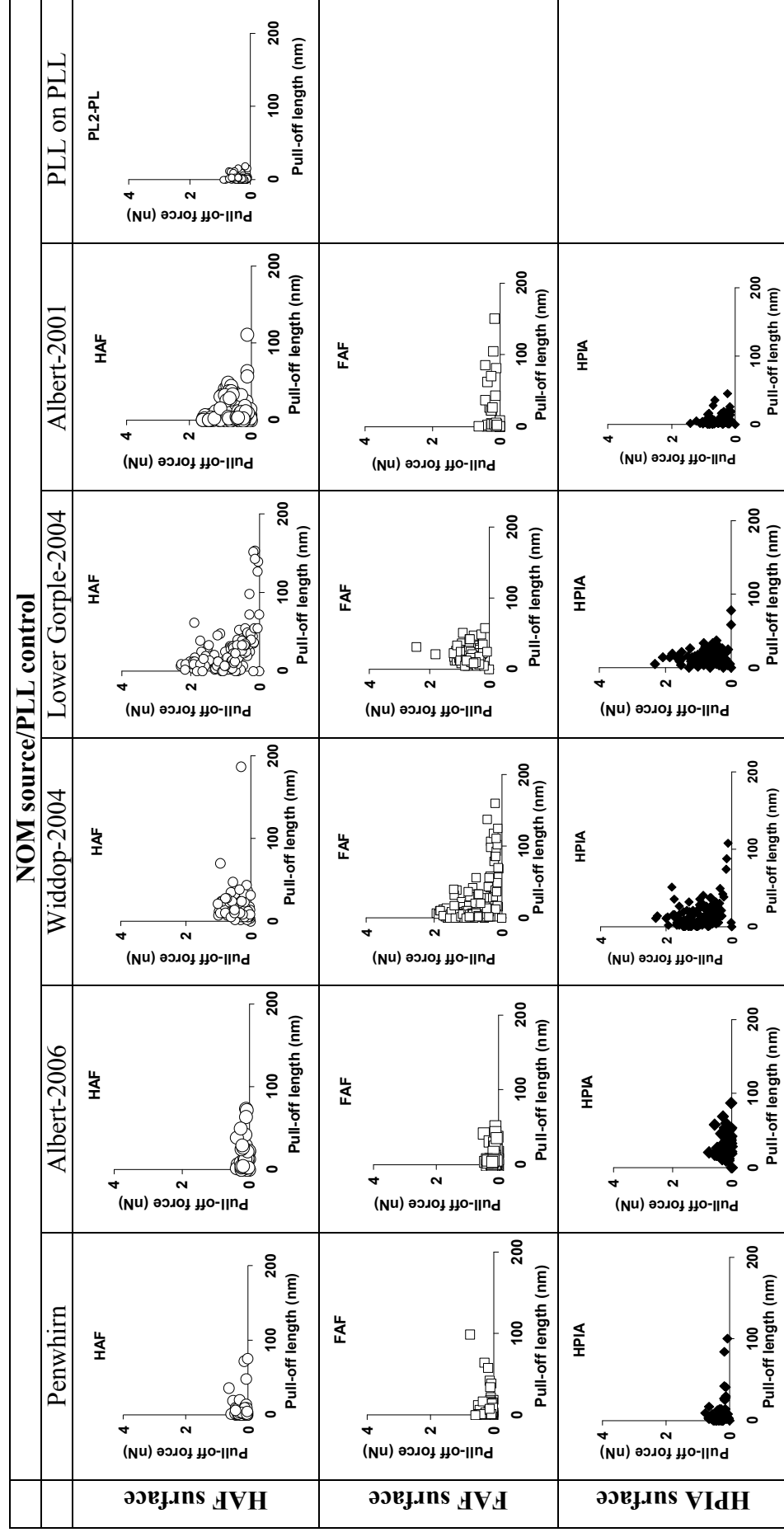
The profile of the scatter plots on HAF and FAF were most dissimilar to PLL controls, which may be due to their anionic surface charge density enhancing electrostatic repulsion between the oppositely charged polyelectrolytes (Rojas *et al.*, 2002). HAF/FAF polyanions were expected to adsorb more strongly to the PLL base with thinner adsorbed layers than HPIA (Rojas *et al.*, 2002). HPIA from Penwhirn in particular gave similar pull-off lengths and forces to PLL, where HPIA is known to have a reduced anionic charge density than hydrophobic polyanions (Sharp *et al.*, 2006). Interestingly, these findings are in agreement with the unmodified tip data, where Penwhirn HPIA was most adhesive to and gave longer detachment lengths than the other sources. HPIA polyanions from both feeder sources were more adhesive, which may be linked to their greater  $\gamma^+$  values from their contact angle measurements (Figure 5.4), Rojas *et al.*, (2002) also showed as the surface charge of polyelectrolytes in highly dilute solutions is reduced the surface becomes increasingly heterogeneous as the interaction gets more complicated.

On HAF polyanions trends were more complex, which may be caused by their different adsorption profile on PLL. For example, HAF from Widdop gave lengths reaching 50 nm and up to 80 nm for Lower Gorple with probe two. Differences were also observed in the adhesion force of both feeder sources, where Lower Gorple was more adhesive with probe two and Widdop dominated using probe one. Overall, both feeders gave a greater density of detachment events than both Albert polyanions. While HAF from Penwhirn gave the narrowest range of pull-off lengths.

**Figure 5.14** Scatter plots of pull-off length vs. pull-off force using PLL-coated tips (a) and (b) on NOM surfaces and PLL control.



(b) PLL coated tip-2





Trends on FAF surfaces were also difficult to identify due to their large variability. For instance, probe two on Penwhirn, Albert-2006 and Albert-2001 polymers gave pull-off lengths up to 80 nm. However, FAF from the feeders gave strong adhesion with mid-range pull-off lengths using probe two. Albert-2001 and the feeders gave peak forces reaching 2 nN, while the Penwhirn source was markedly smaller at 1 to 1.2 nN with probe one. These findings indicate the FAF polymer was difficult to distinguish between sources because both tips did not give consistent interactions. This may be attributed to the orientation of the FAF on PLL, FAF's irregular surface charge or the presence of voids on the immobilized FAF layer (Liu *et al.*, 2000).

Table 5.3 compares the detachment length and adhesion force of NOM polyanions from all five fraction sets. It was clear hydrophobic polyanions dominated adhesion and pull-off length apart from Albert 2006 polyanions. The Albert-2006 gave similar adhesion and pull-off lengths on all NOM surfaces.

**Table 5.3.** Summary of average pull-off lengths and peak adhesion forces on all four sources using PLL tips.

Source	Pull-off lengths	Adhesion forces
<b>Albert 2001</b>	FAF>HAF>HPIA FAF>HAF>HPIA	FAF=HPIA>HAF HAF=HPIA>FAF
<b>Albert 2006</b>	Equal Equal	Equal Equal
<b>Penwhirn water</b>	FAF>HAF>HPIA Equal	FAF>HAF=HPIA Equal
<b>Widdop</b>	Equal FAF>HPIA>HAF	HAF>FAF>HPIA FAF=HPIA>HAF
<b>Lower Gorple</b>	FAF>HAF>HPIA HAF>FAF>HPIA	FAF>HAF=HPIA HAF>HPIA>FAF

### 5.3.3 Silica/PLL/NOM probes versus NOM surface

Silica tips were coated with Penwhirn polyanions immobilised on PLL to observe inter-NOM (NOM on NOM) interactions. Penwhirn water was selected due to the greater quantity of NOM fractions available at the time of the investigation, and because floc size experiments were being conducted with these fractions at the time of these experiments.

### 5.3.3.1 Attractive forces

Figure 5.15 shows frequency distribution plots of attractive forces with NOM-coated tips on NOM polyanions. Attractive forces were in the order  $\text{HPIA} > \text{HAF} > \text{FAF}$ , with forces peaking at 0.2 nN, 0.5 nN and 0.7 nN on FAF, HAF and HPIA, respectively. Apart from FAF-1 and HPIA-1 probes, most probes gave relatively similar attractive forces to HAF. On FAF surfaces attractive forces peaked at lower forces compared to HAF, of which FAF probes were least attractive to FAF polyanions. This may indicate FAF polyanions exhibited long-range electrostatic repulsion due to their charged terminal groups. Interestingly, HPIA probes were more attracted to HPIA polyanions, which may indicate hydrophilic polyanions were less charged and hydrophilic terminal groups enhanced attraction through H-bonding.

### 5.3.3.2 Adhesion forces

Figure 5.16 shows frequency distribution plots of adhesion forces with NOM-coated tips on NOM. Generally, the order of adhesion followed the same trend as the order of attractive forces shown in the previous section, with HPIA most adhesive and FAF least adhesive.

With HAF probes, adhesion was strongest on HAF and HPIA, with most force events peaking at over 2 nN. With HPIA-coated tips, there was strong adhesion to HPIA, followed by HAF then FAF. Analysis of FAF probes gave adhesion in the order,  $\text{HAF} > \text{HPIA} > \text{FAF}$ . Both FAF probes gave maximum adhesion peaks on FAF above 2 nN. However, the FAF-1 probe was most adhesive to HPIA, with adhesion peaking at 3 nN while the second FAF probe gave similar adhesive events to all the polyanions.

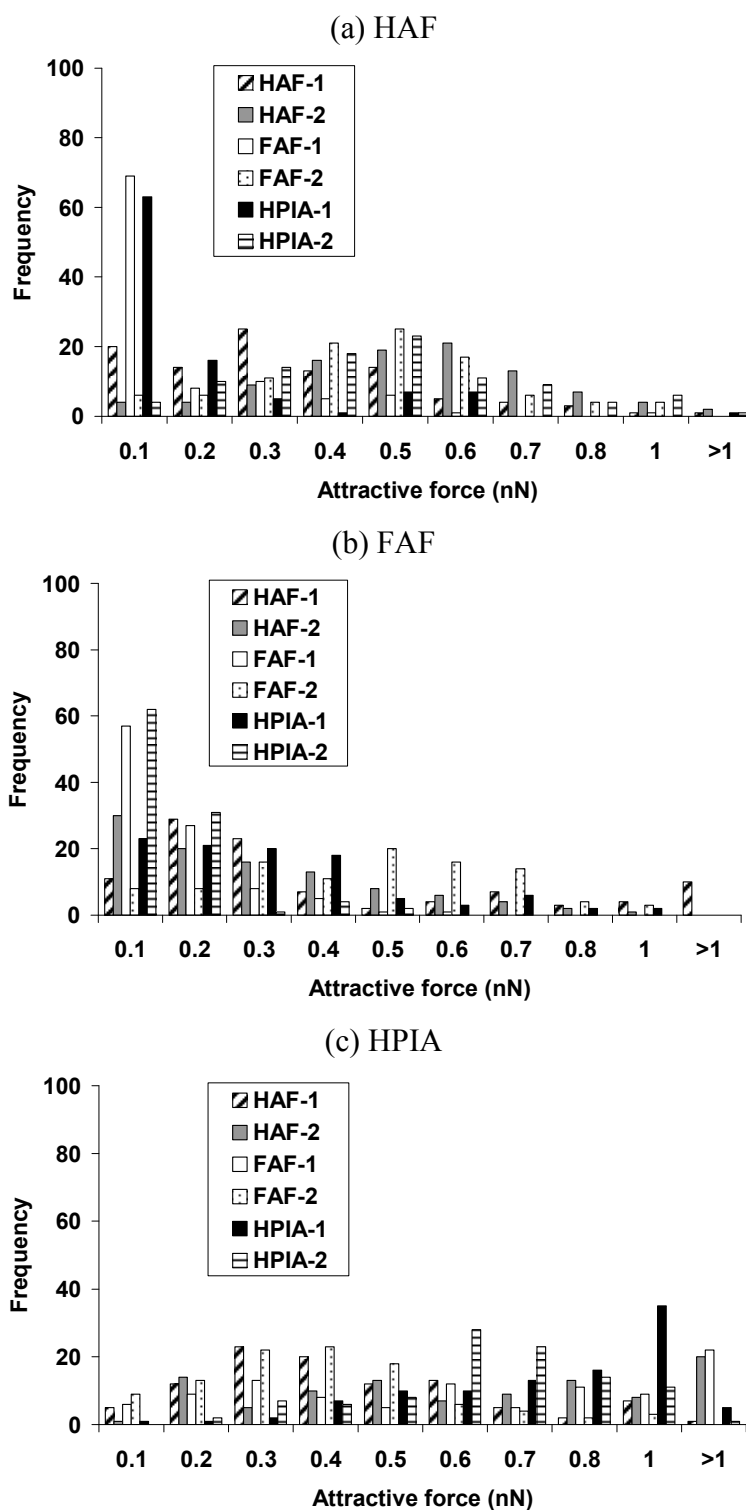


Figure 5.15 Histogram showing the distribution plot of attractive forces with NOM-coated tips on HAF (a), FAF (b) and HPIA (c).

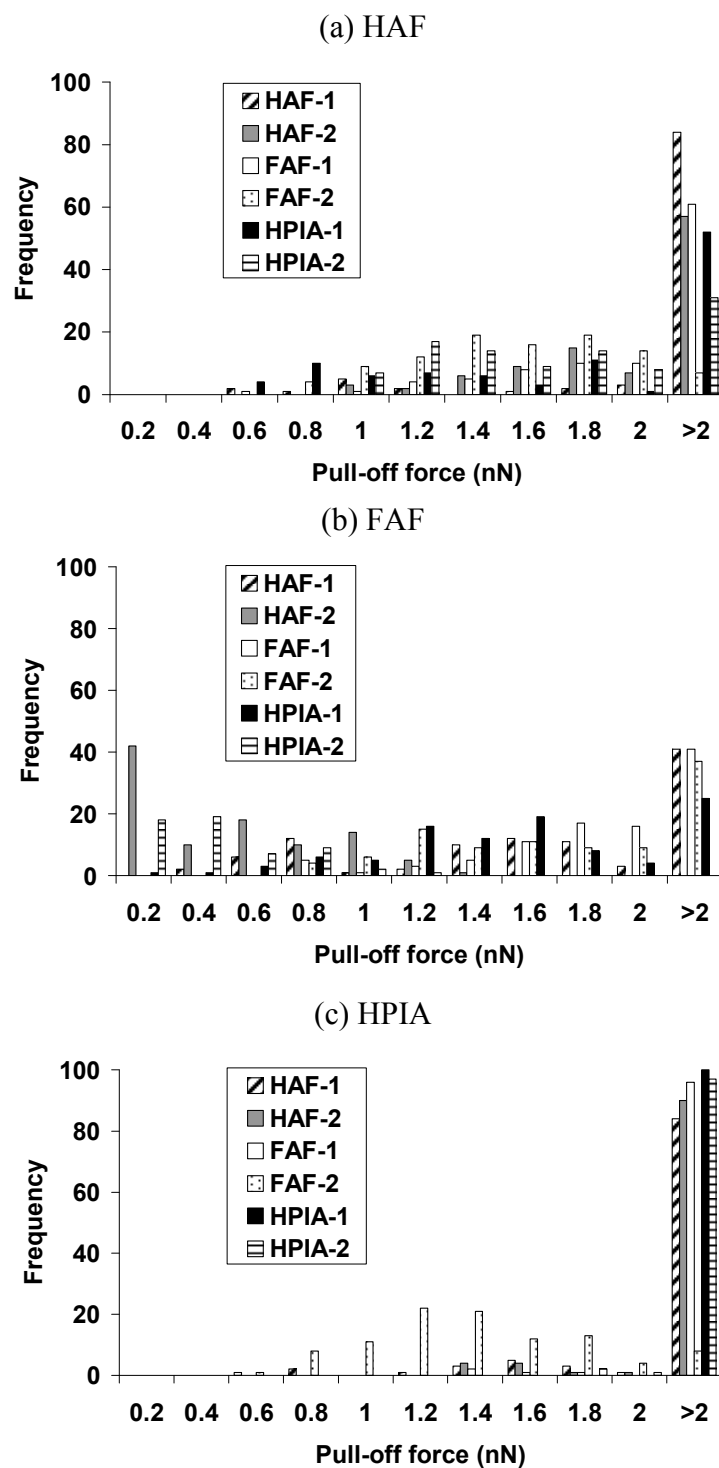


Figure 5.16 Histogram showing distribution plots of adhesion forces with NOM-coated tips on HAF (a), FAF (b) and HPIA (c).

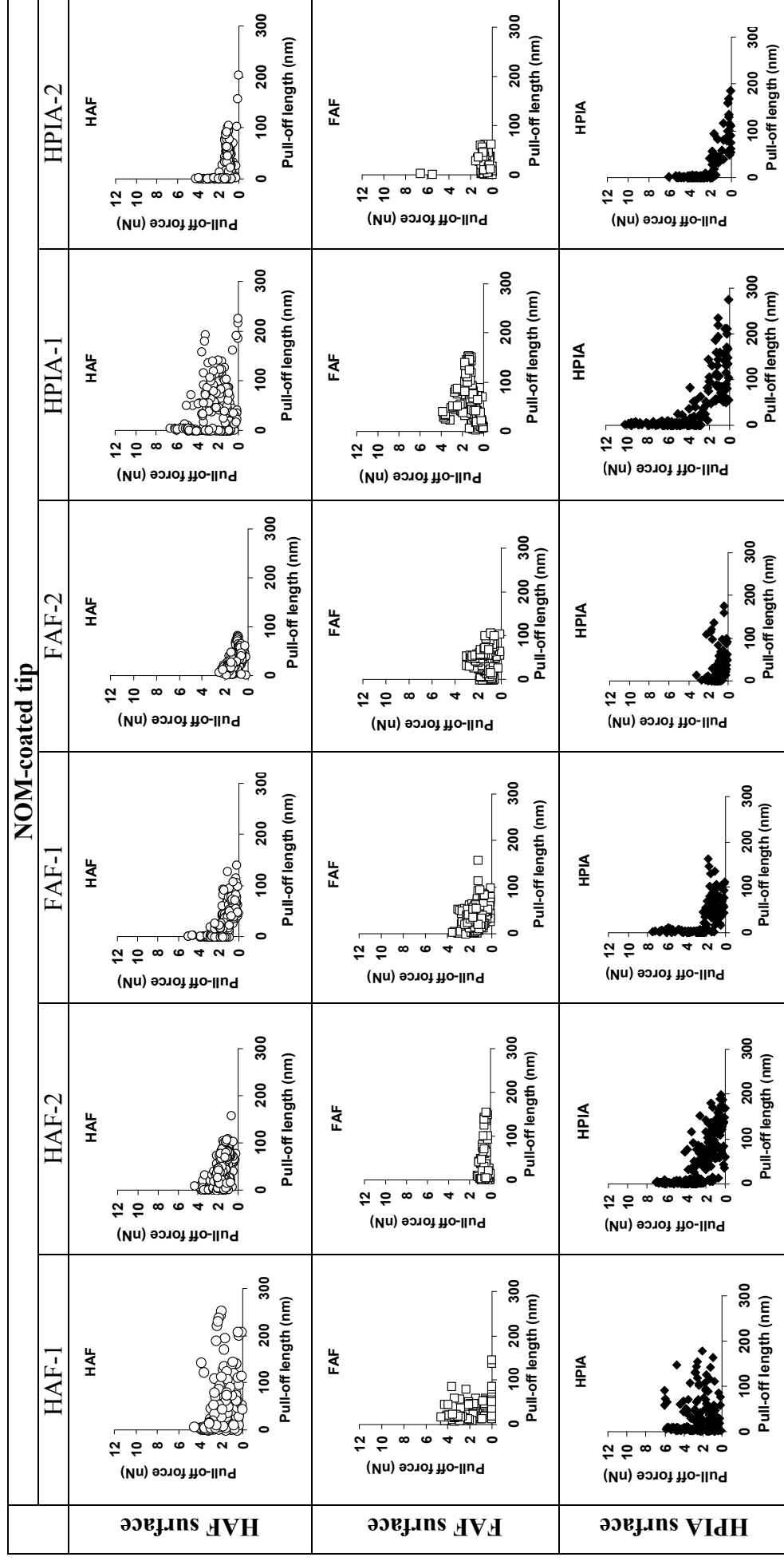
### 5.3.3.3 Pull-off length versus adhesion force

Figure 5.17 shows detachment lengths vs. pull-off force for NOM-coated tips on NOM. HAF-terminated probes adhered strongly to HPIA with lengths reaching 200 nm. Pull-off events on HPIA were also more abrupt shown by the high density of events on the y-axis. This indicates primary detachment events were strongest but also more frequent, although the location of events on polyanions was impossible to establish. Detachment lengths were shortest on FAF, as was the total number of events. Probe HAF-2 on FAF gave longer detachment lengths but weaker forces than the HAF-1 probe. Probe two (HAF-2) gave shorter lengths than probe 1 on HAF polyanions, although actual forces were similar.

With HPIA-coated tips adhesion forces were strongest on HPIA, matched by lengths reaching 200 nm. Pull-off lengths on FAF polyanions at 100 nm were the shortest, indicating there were fewer adhesive interactions with FAF or that FAF polyanions were shorter and more compressed due to their high charge density (Rojas *et al.*, 2002). FAF probes gave similar pull-off lengths on all NOM polyanions, peaking at lengths between 100 to 120 nm. However, the FAF-1 probe did give several strong primary peak adhesion forces on HPIA and HAF polyanions with forces reaching 8 nN, which may have been caused by the PLL base.

Some of the more interesting interactions were observed with symmetrical NOM systems. For instance, the HPIA-HPIA system gave consistent detachment lengths reaching 220 nm. In contrast, FAF-FAF and HAF-HAF systems gave peak events within 150 nm, although HAF gave several lengths up to 250 nm. These results were also found to be significant ( $p < 0.01$ ) using the Mann Whitney U test. Highly charged HAF/FAF polyanions may also adsorb strongly to PLL leading to thinner NOM layers (Rojas *et al.*, 2002). This may show that hydrophobic polyanions were more tightly bound to one another, where binding sites on the surface were limited by the constrained aromatic backbone. When FAF was imaged on a muscovite surface by Namjesnic-Dejanovic *et al.*, (1998), it was shown to adsorb as spherical aggregates ranging from 10-50 nm laterally and 2-10 nm in height. These dimensions seem to be consistent with pull-off lengths of the FAF-FAF system.

**Figure 5.17** Scatter plot of pull-off length vs. pull-off force of NOM-coated tips (columns) on NOM surfaces (rows) from Penwhirn reservoir.



### 5.3.4 Silica/PLL/Glycine probes versus NOM surface

Glycine-coated tips were prepared to functionalize tips with uncharged  $\text{NH}_2$  groups (IEP about 6). Figure 5.18 shows scatter plots of pull-off length vs. adhesion force for two glycine-coated tips on Penwhirn NOM polyanions, PLL and glycine. Also shown are the scatter plots using PLL probes for comparative purposes.

For PLL, glycine, FAF, HAF, and HPIA the average number of detachment events/force cycle was 1.60, 1.55, 1.49, 1.19 and 1.11, respectively. Detachment lengths reached 200 nm on PLL, which implies PLL exhibited a coiled/compressed configuration because Sawant and Nicolau, (2006) found the height of a PLL monolayer was  $\sim 12$  nm. The scatter plots show adhesion forces and detachment lengths were stronger in the glycine-PLL system than the PLL-PLL system. This indicates glycine tips comprised of uncharged  $\text{NH}_2$  terminals, because charged  $\text{NH}_3^+$  groups are normally repelled by the PLL surface. As the monolayer of glycine-terminated PLL- tip and the PLL surface varied, their charge densities were not necessarily the same (Giesbers *et al.*, 2002). This difference may have enhanced adhesion via electrostatic forces.

The strong glycine-glycine interaction was puzzling because their charge density was expected to be similar, although the thickness of the PLL base on both surfaces could not be established. However, Giesbers *et al.*, (2002) also found strong adhesion between amine-terminated silica surfaces at pH 6 in low electrolyte solutions, and proposed this was due to H-bonding between  $\text{NH}_2$  and  $\text{NH}_3^+$  terminals. This was because at pH 6, glycine was expected to comprise of predominantly  $\text{NH}_2$  groups with residual  $\text{NH}_3^+$  groups. Glycine also gave detachment lengths reaching 100 nm, although it was clearly the smallest molecule. This may be caused by pulling of the PLL base from the tip and/or surface during the retraction cycle. Pull-off lengths on NOM polyanions were in the order  $\text{FAF} > \text{HAF} > \text{HPIA}$  and forces in the order  $\text{HAF} > \text{FAF} = \text{HPIA}$ . Both glycine and FAF gave similar peak detachment lengths, although glycine was twice as adhesive with a force of  $1.20 \pm 0.61$  nN.

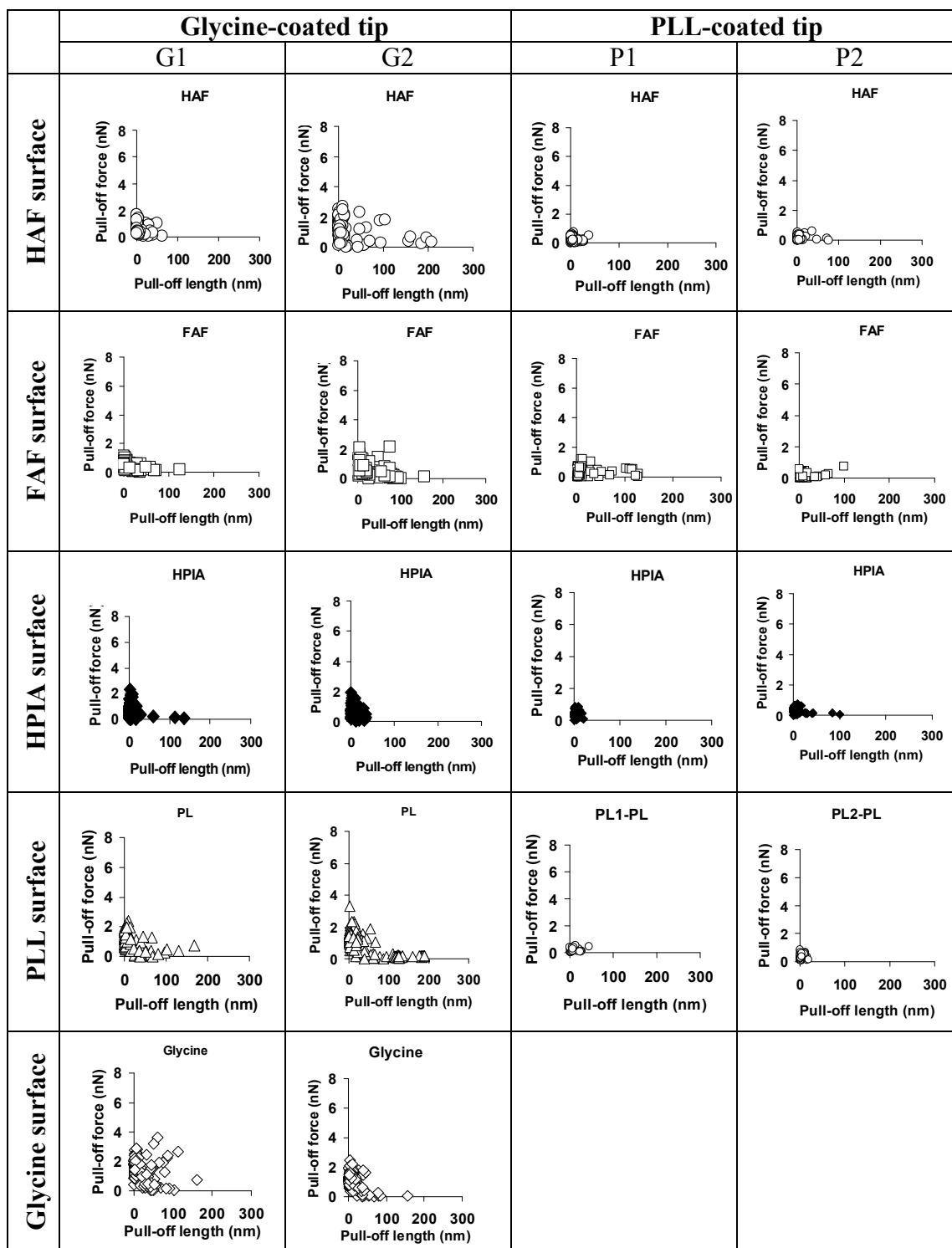


Figure 5.18 Scatter plot of force vs. pull-off length for glycine-coated (left) and PLL (right) tips on polyanions from Penwhirn reservoir.



It is thought the origin of glycine's adhesion to FAF and HAF was due to a combination of electrostatic and H-bonding forces. This was because residual  $\text{NH}_3^+$  groups may adhere to  $\text{COO}^-$  and phenolic- $\text{O}^-$  groups on FAF and HAF terminals. Giesbers *et al.*, (2002) observed adhesion was strongest with the  $\text{COOH-NH}_2$  system at pH 7 using chemical force microscopy, when both surfaces were oppositely charged. The mainly uncharged  $\text{NH}_2$  groups on glycine may contribute to glycine's adhesion to FAF, HAF and HPIA via H-bonding because average forces between NOM polyanions were similar with both glycine probes. Although the total number of interactions varied between PLL and NOM polyanions, there were no significant differences between adhesion and detachment length.

### 5.3.5 XAD4/XAD8/MIEX® probes versus NOM surface

XAD4, XAD8 and MIEX® resins were used to modify AFM tips and analyze the detachment signatures with Penwhirn NOM polyanions. Two probes for each resin were prepared and Figure 5.19 shows optical images of three of the six resin-modified probes used in this section.

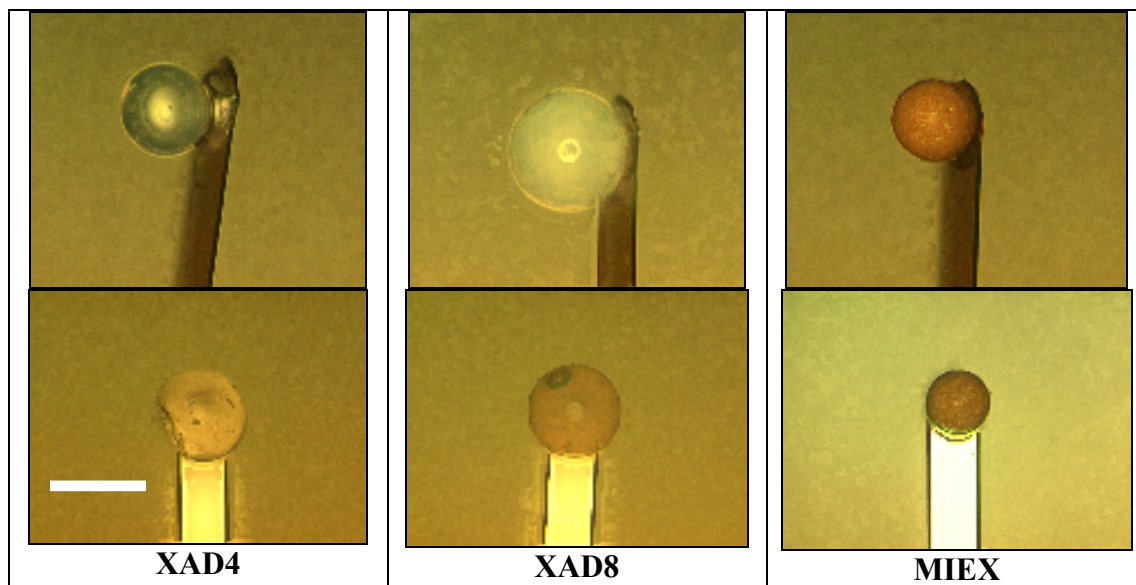


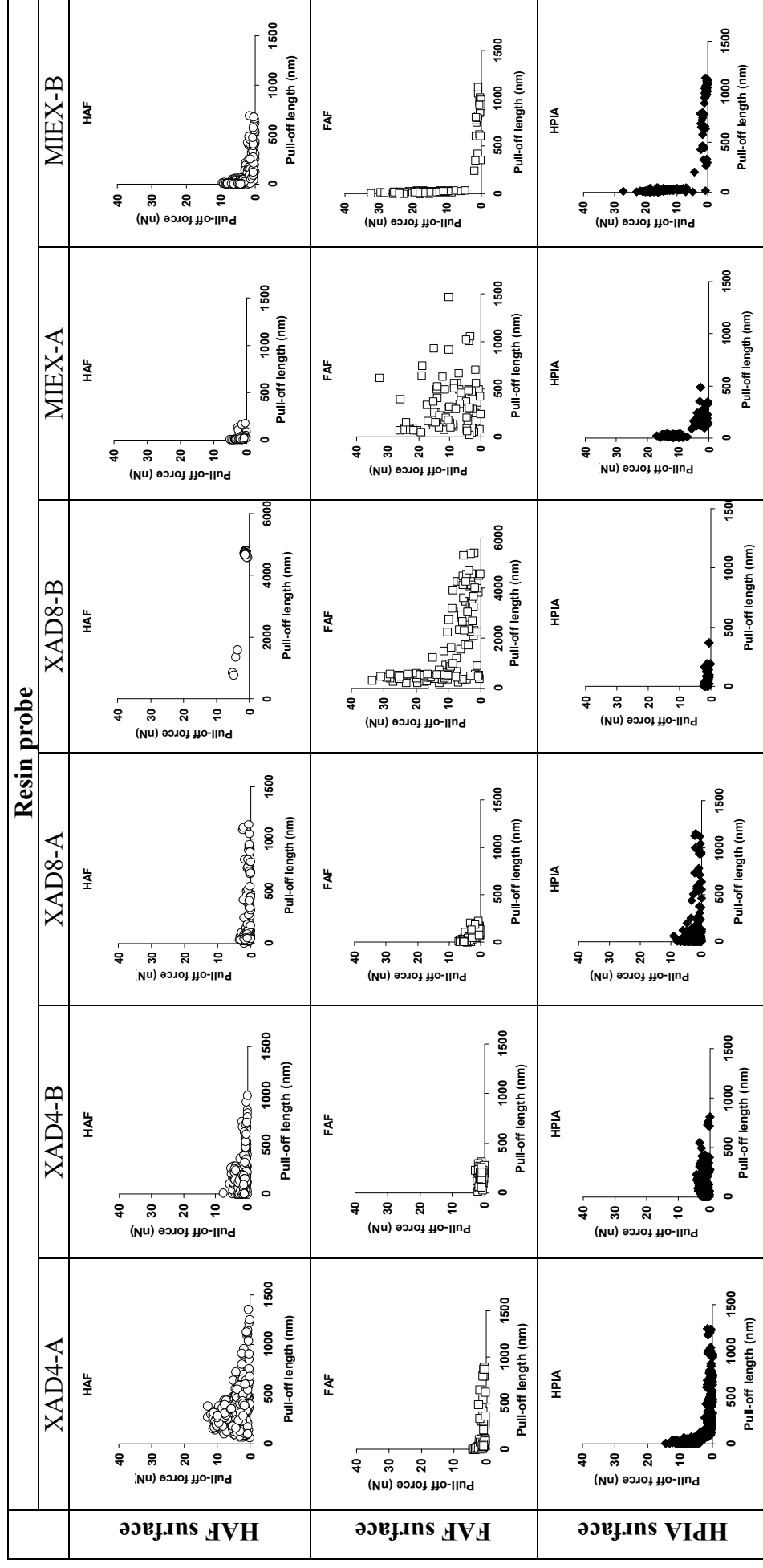
**Figure 5.19** Optical microscope images (x40) of AFM tips modified with XAD4, XAD8 and MIEX® resins showing side (top) and birds-eye views (bottom). Each image was a montage produced from images taken at different focal lengths. Scale bar 60  $\mu\text{m}$ . Software used to generate image was Auto-Montage (Synoptics Ltd, version 3.02.005).

The XAD8 resin was much larger than XAD4 and MIEX® resins. Pull-off lengths with both XAD4 probes were ranked HAF>HPIA>FAF, corresponding to 1.4µm, 1 µm and 0.9 µm, respectively (Figure 5.20). Pull-off forces followed the same trend. Detachment lengths were almost an order of magnitude larger than when unmodified tips were used (Figure 5.9a, b). The larger XAD8 resin shown in Figure 5.19 contributed to the unstable force profiles given in Figure 5.20. For instance, the XAD8-A gave pull-off lengths of 1.2µm, 1.2 µm and 0.3 µm for HAF, HPIA and FAF, respectively. The corresponding adhesion force was in the order HPIA>FAF>HAF. The second probe gave detachment lengths reaching 5.5 µm, 1.8 µm and 0.2 µm for FAF, HAF and HPIA, respectively.

Adhesion force rankings did not follow the same trend as the fractionation process where XAD8 normally has a preference for hydrophobic polyanions. This was because the conditions used for force measurements differ considerably from those during fractionation. During the fractionation of hydrophobic (HPOA) fractions, the solution is acidified to pH 2, thus reducing the surface charge of HAF/FAF polyanions. Although the hydrophobics remained soluble during adsorption to XAD8, their surface charge was effectively modified, while force measurements were performed at pH 6. At pH 6, all polyanions exhibited a negative surface charge (Droppo *et al.*, 2005), so their adsorption to the uncharged XAD8 resin was not expected to differ by much. In fact the ranking of pull-off forces and detachment lengths with both XAD-8 probes fluctuated. Although HAF/FAF polyanions did give longer detachment lengths this was effectively due to their greater molecular weight. The greater surface area of XAD8 compared to XAD4 resins also permits greater contact area with NOM polyanions.

With the MIEX® probe ranking of pull-off length was FAF>HPIA>HAF with values of 1.2 µm, 1.2 µm and 0.75 µm, respectively. Pull-off forces followed the same order with values of  $11.65 \pm 0.17$  nN,  $9.43 \pm 1.71$  nN and  $2.63 \pm 0.92$  nN for FAF, HPIA and HAF, respectively. MIEX® pore size at ~45 nm was twice as large as XAD8, but this was unlikely to have played the only role.

Figure 5.20. Scatter plot of force vs. pull-off length for three resin-attached probes (column) on three NOM polyanions (rows).



These findings correlated with macroscale fraction removal studies by Fearing *et al.*, (2004), where 90% of FAF, 90% of HAF and 75% of HPIA was removed using Albert reservoir water. However, quantitative analysis of pull-off events indicated HPIA/HAF dominated with 1.54 events/curve with FAF giving only 1.15 events/curve. Like XAD resins, the precise cause of this difference was yet to be established.

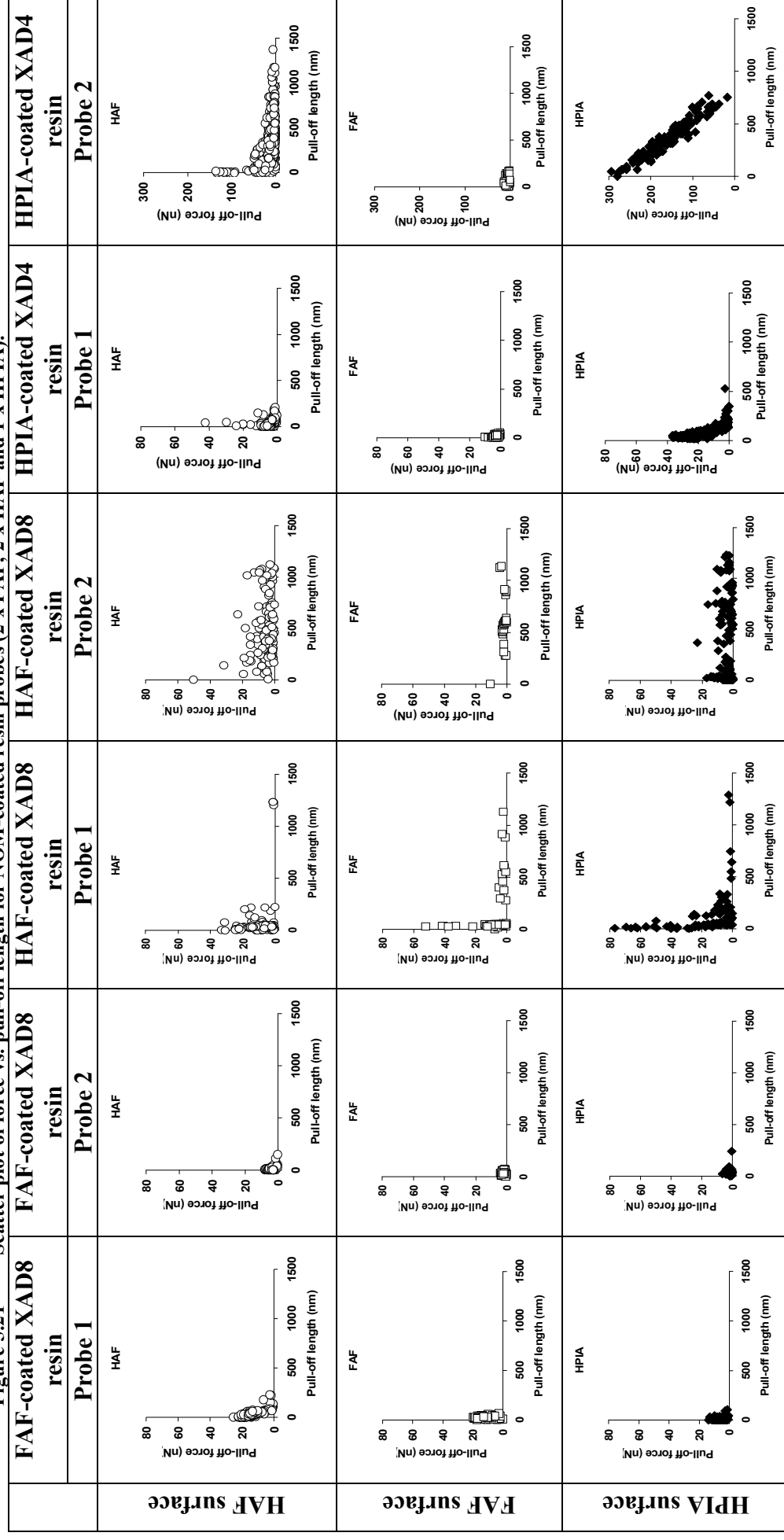
### 5.3.6 Resin/NOM probes versus NOM surface

Resins used in section 5.3.5 were coated with NOM polyanions from Penwhirn reservoir, to compare datasets with NOM-coated tips. The procedure used to attach resins to the tip was used, but NOM polyanions were adsorbed to the resin after attachment to the cantilever. Figure 5.21 shows scatter plots of six NOM-coated resin probes on immobilized NOM.

With FAF-coated probes pull-off lengths were in the order HAF>FAF>HPIA, with lengths reaching 200 nm, 100 nm and 150 nm for HAF, FAF and HPIA, respectively. Variation in pull-off length between polyanions was relatively small, although HAF was most adhesive, peaking at 27 nN. FAF and HPIA gave similar forces, which was consistent with both probes. When compared to FAF-coated tips in section 5.3.3, they also showed little variation between FAF-coated tips. These findings indicate both techniques of FAF polyanion termination were in agreement, confirming FAF's indiscriminate interaction with all NOM polyanions. These findings appear to substantiate FAF's important role in NOM surface interactions and floc formation (Sharp *et al.*, 2006).

For HAF-coated probes, pull-off lengths were in the order HPIA>HAF>FAF with lengths reaching 1.3  $\mu\text{m}$ , 1.2  $\mu\text{m}$  and 1  $\mu\text{m}$ , respectively. Adhesion forces also gave an identical ranking order. There were considerably fewer adhesive events with FAF compared to HAF and HPIA. These result also linked with HAF-coated tips, where the same pull-off length and adhesion force ranking was obtained. HAF-coated-resins appeared to behave consistently, and adhesion ranking was reproducible with both probes.

Figure 5.21 Scatter plot of force vs. pull-off length for NOM-coated resin probes (2 x FAF, 2 x HAF and 1 x HPIA).



HPIA-coated probes gave pulling lengths in the order HPIA>HAF>FAF with probe one and HAF>HPIA>FAF with probe two. Probe two gave longer pulling lengths on HPIA prior to the first adhesion peak, which was shown by the large number of data points diagonally between the axes. This was because the HPIA polyanion was elongated prior to detachment. The adhesion forces were considerably stronger for HPIA followed by HAF, and this ranking was similar to that obtained with HPIA-coated tips, confirming strong interaction between HPIA-HPIA polyanions.

### 5.3.7 Interpretation of detachment signatures with AFM tips

There were two reasons for using silica and PLL tips. One was to compare measured adhesion forces and pull-off lengths, and the other was to test PLL as a model of synthetic bridging flocculants. Table 5.4 gives a summary of polyanion dominance obtained with silica and PLL-coated tips.

**Table 5.4.** A summary comparing dominant polyanions using silica and PLL-coated tips.

	Silica tip (-ve)		PLL tip (+ve)	
	Adhesion	Length	Adhesion	Length
<b>Dominant fraction</b>				
<b>Albert-01</b>	HAF/HPIA	HAF	FAF/HAF	FAF
<b>Albert-06</b>	FAF	HAF/HPIA	Equal	Equal
<b>Penwhirn</b>	<b>HPIA</b>	<b>HPIA</b>	FAF	FAF
<b>Lower Gorple</b>	FAF/HPIA	FAF/HPIA	HAF/FAF	FAF/HAF
<b>Widdop</b>	HPIA/FAF	HPIA/FAF	HAF/FAF	FAF/HAF

Silica tips were more adhesive to HPIA polyanions from Penwhirn and both feeders, while both Albert samples were adhesive to hydrophobic polyanions. HPIA polyanions from Penwhirn were also more hydrophilic (Figure 5,1), making terminal groups more accessible, although specific functional groups were not known.

Generally, FAF from hydrophobic polymers gave fewer adhesion events, which indicates they were less adhesive to the negatively-charged tip. This is thought to be due to the charged anionic terminals on FAF, which may extend farther into the bulk solution, resulting in net electrostatic repulsion (Claesson *et al.*, 2005). Moreover, the affinity of water molecules to the tip's residual SiOH<sup>-</sup> groups has been shown to be much stronger

than hydrophobic polyanions (Nalaskowski *et al.*, 2003). The data suggests silica tips can be used to probe adhesion forces between HPIA polyanions from different sources, but tips were less sensitive to hydrophobic polyanions because they were effectively unable to ‘grab’ the polymers. The inability to adhere to hydrophobic polyanions suggests adhesion was primarily electrostatic in origin, because surface charge was one of the main differences between HPIA and hydrophobic polyanions.

In general, PLL-coated tips were more adhesive to FAF and HAF polyanions from all sources, giving longer detachment lengths. This was although attractive forces were smaller in magnitude and repulsive to NOM polyanions compared to silica tips. Reduced attractive forces were primarily due to the unfavourable entropy associated with compressing polymer chains of two modified surfaces (Israelachvili, 1992). Abraham *et al.*, (2000) suggested repulsive attractive forces between polyelectrolyte brushes are predominantly steric and not electrostatic in origin. Penwhirn polyanions gave the smallest mean attractive force, indicating polyanionic length was a contributing factor, although their surface charge was not known. HAF and FAF polyanions from Widdop gave the strongest mean attractive force. This was also matched by pull-off lengths, where hydrophobic Penwhirn polyanions were generally shorter and less adhesive to PLL-terminated probes. This difference in adhesion is thought to be related to fraction molecular weight and surface chemistry, which varies according to their source (Goslan *et al.*, 2003). Consequently, shorter polyanions would not extend as far into the bulk solution, thus reducing contact area, which is illustrated in Figure 5.22.

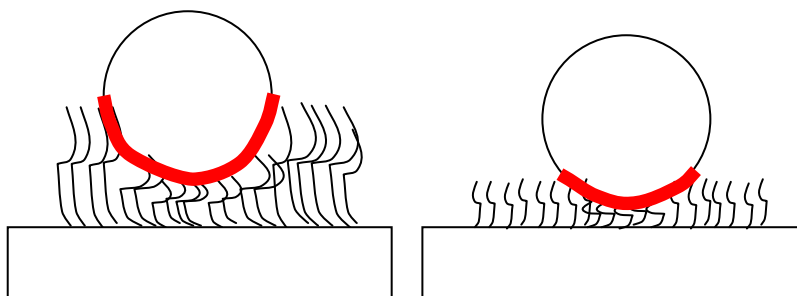


**Figure 5.22.** Comparison of high MW (left) and low MW NOM polyanions showing increased contact area and interaction (highlighted) is prevalent with the high MW polyanions from Widdop and Gorple reservoirs. Diagram not to scale.

In a study by Yamamoto *et al.*, (2000) they suggested polymer brush density was also a probable cause, although the density of NOM polyanions used during this study was not known. Generally feeder sources provided more consistent data because they both showed FAF polyanions to be longer and/or more adhesive. It was not known whether this was due to its surface chemistry or molecular weight. Hence, the binding mechanism of PLL to FAF remained unclear although electrostatic forces between deprotonated  $\text{COO}^-$ /phenolic  $\text{O}^-$  anionic sites with  $\text{NH}_3^+$  was likely mechanism (Kollist-Siigur *et al.*, 2001; Reemtsma and These, 2005). The reduced hydrophobicity of FAF relative to HAF from contact angle measurements (Figure 5.1), also suggests there were more hydrophilic groups on FAF that were accessible to  $\text{NH}_3^+$  terminals on the PLL tip (Yee *et al.*, 2006). Consequently, the hydrophilicity of FAF and HAF polyanions was subject to change as water was increasingly displaced during approach cycles.

### 5.3.8 Interpretation of detachment signatures in NOM-NOM systems

While silica, PLL- and glycine-coated tips gave some control over the specificity of one surface, NOM-coated tips increased the complexity. However, this was a very important part of the study because detachment signatures may be linked to their floc size and subsequent coagulation performance. A schematic of symmetrical NOM interactions is illustrated in Figure 5.23.

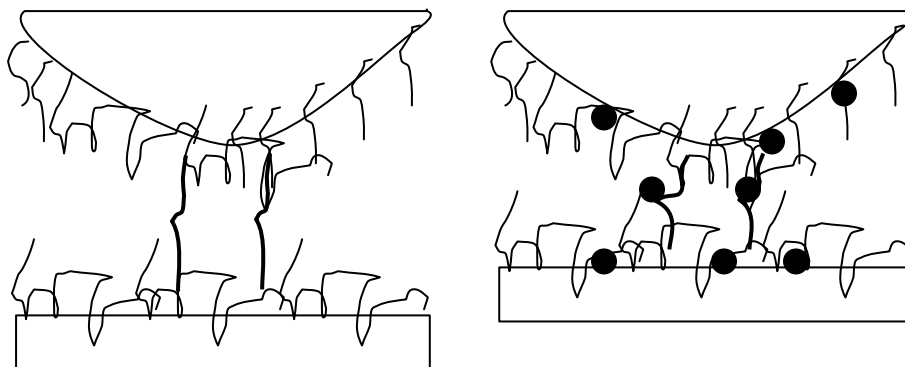


**Figure 5.23** Schematic of pull-off interaction between HPIA-HPIA (left) and HAF-HAF/FAF-FAF systems showing longer lengths for HPIA than hydrophobics. Balls (right) indicate micellar structure of hydrophobic polyanions. Micelles are for illustrative purposes only.

Based on polymer hydrophobicity, HAF-HAF interactions were similar to FAF-FAF although rupture events were less tightly bound due to HAF's greater molecular weight.



The hydrophilicity of HPIA may have promoted a branched configuration because terminal groups had a greater affinity for water according to contact angle measurements (Figure 5.1), enabling polyanions to interact with hydrophilic groups. Furthermore, data from unmodified and PLL tips showed Penwhirn HPIA was potentially longer and had a less negative surface charge than the other sources. As such, HPIA may be more open in contrast to HAF/FAF at the intermolecular level, and the availability of binding sites was high, given by L-shaped scatter plots. Polyanions that gave L-shaped scatter plots indicate they unwind more easily, while a high density of interactions indicate their binding sites are readily available and potentially less compressed. The potentially more open structure of HPIA provides aliphatic (predominantly COOH) groups that can bind to hydrophilic terminals on HAF/FAF, by hydrogen bonding. This interaction was most likely due to the shielding of hydrophobic segments from water.

In non-symmetric systems adhesion between FAF-NOM was indiscriminate, compared to HAF and HPIA polyanions. Although studies by Sharp *et al.*, (2006) and Jefferson *et al.*, (2004) have indicated the zeta potential and charge density of FAF flocs was most negative, it is not known how surface charge was distributed around a single polyanion, and whether the polyanion was in a compressed or open configuration on PLL. A clue may be provided with approach cycles because FAF was least attractive to NOM polyanions. For instance, it was likely FAF polyanions were highly compressed due to electrostatic and steric repulsion. This was because Rojas *et al.*, (2002) found with increasing charged density of the cationic polyelectrolyte acrylamide-[3-(2-methylpropionamido)propyl] trimethylammonium chloride (AM-MAPTAC-X) on negatively-charged mica, adsorbed polyelectrolyte layer thickness decreased. HAF polyanions also gave shorter detachment lengths than HPIA, where HAF also exhibits greater anionic surface charge density than HPIA (Sharp *et al.*, 2006). Approach cycles on hydrophobic polyanions may also induce a change in the conformation of FAF terminals, so as water was displaced polyanions rearrange to expose hydrophobic segments, resulting in hydrophobic attraction. These findings suggest FAF polyanions were most likely to control coagulation performance during NOM removal, because of its

inherent ability to attach to both hydrophilic and hydrophobic terminals. Furthermore, Guo and Ma, (2006) found the size of FAF polyanions were highly dependent on solution chemistry and adsorbent surface.

### **5.3.9 Comparison of tip-modification methods-NOM-coated tips vs. NOM-coated resins**

The results obtained with NOM-coated resin showed FAF-coated tips did not discriminate between NOM polyanions as well as HAF- and HPIA-coated tips. HAF and HPIA-coated tips however, gave similarities in the adhesion and pull-off length rankings with NOM-coated tips. Furthermore, the HPIA-HAF interaction appeared to be stronger than the HPIA-FAF interaction, which also drew a strong parallel with the NOM coated tips.

The NOM-coated resins and NOM-coated tip gave comparable adhesion rankings. However, the surface area of resin-modified tips was much greater than silica tips, so the high density of rupture events were caused by the pulling of multiple polyanions. Considering the length of pulling events, both NOM and PLL polymers were pulled, and subsequent events were dependent on which polyanion (NOM or PLL) was the shortest during retraction. This level of uncertainty made resin-modified probes unlikely to provide information that will be of use in an operational perspective. Nevertheless, in order to obtain more consistent force data, it will be interesting to compare this data to results obtained from using much smaller resin-modified probes.

### **5.3.10 Potential application of detachment signatures to NOM removal performance**

As the experiments performed in this investigation were a proof-of-concept study, any potential link to macroscale studies was very important, as it would form the basis of further studies. The water characteristics that were studied included floc size, floc strength and MIEX® data. Floc size and strength data was specific to fractionated water from Albert WTW during April-2002-October 2004, January 2006 and from Penwhirn WTW in August 2005. MIEX® data was obtained from Maxime Mergen, and involved

the study of raw waters from Penwhirn and Albert water reservoirs. Table 5.5 gives floc size data and MIEX® data obtained from the specified sources.

**Table 5.5. Summary of parameters used to compare to AFM pull-off forces and pull-off lengths.**

	Albert WTW			Penwhirn WTW
<b>Sampling period</b>	April-02-October-04	Unknown	January 2006	November 2005
<b>Reference/source</b>	Sharp <i>et al.</i> , (2006)	Jefferson <i>et al.</i> , (2004)	Maxime Mergen	Maxime Mergen
<b>Floc size (<math>\mu\text{m}</math>)</b>				
HAF	723	932		
FAF	532	818		
HPIA	759	949		
<b>Raw (<math>d_{50}</math>)</b>			577.69	478.12
<b>Settling rate (<math>\mu\text{m s}^{-1}</math>)</b>				
HAF/FAF/HPIA	1497/710/1492	1.3/1.8/2.5		
<b>Floc strength</b>				
HAF	-0.75 (weak)			
FAF	-0.64 (strong)			
HPIA	-0.74			
<b>Raw</b>	-0.52		0.58	0.43

### 5.3.10.1 Linking symmetric NOM interactions with floc properties

It was anticipated floc size can be linked to detachment events from symmetric NOM interactions. To date, Sharp *et al.*, (2006) provided the only available data looking at the size of fractionated flocs. Floc size, given in Table 5.5 was ranked in the order HPIA>HAF>FAF from the Albert WTW. Figure 5.24 shows scatter plots of symmetric NOM systems obtained from two NOM-coated tips were in the order HPIA>HAF>FAF, which was linked to their apparent floc size, and also the floc breakage rates.

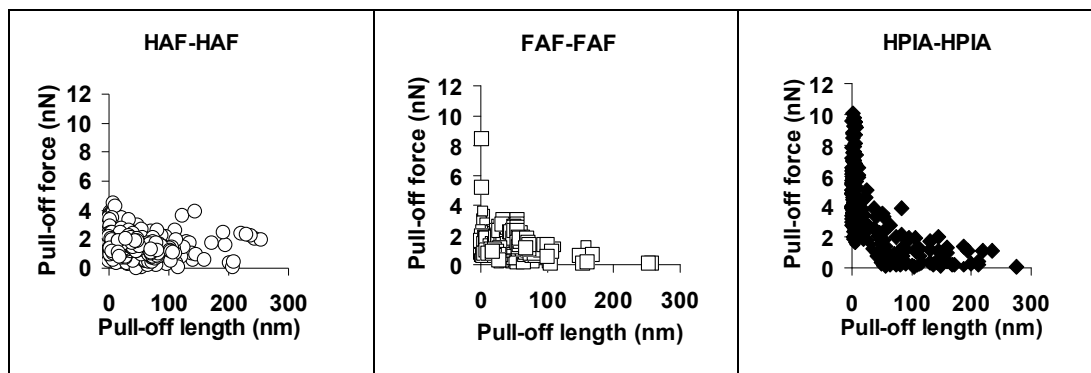


**Figure 5.24** Scatter plots showing force vs. pull-off length of symmetric NOM systems.

The scatter plot of HPIA was L-shaped, indicating polyanions gave strong and weak pull-off forces during long and short pull-off lengths respectively. Furthermore, HPIA chains were highly branched, demonstrated by the high density of events during polymer extension, which were nearly twice as long as the adhesive core of hydrophobic polyanions. These nano-scale surface-specific interactions may also transfer to the macroscale where Jefferson *et al.*, (2004) observed the larger HPIA flocs were fractal-like, while FAF/HAF was compact. The greater number of holes observed on HPIA flocs by Jefferson *et al.*, (2004) may be caused by the greater density of hydrophilic groups that have a preference for water. This may also explain when HPIA flocs undergo shear, they readily re-combine due to the large number of binding sites on HPIA terminals. The more compact FAF flocs were caused by hydrophobic attractive forces between FAF polyanions, with charged terminals predominantly orientated to the bulk.

Given how surface-specific interactions can be linked to floc size experiments, it would be interesting to investigate a link between the AFM data and raw water floc sizes, which comprise of non-fractionated NOM. Raw water floc size experiments using Penwhirn water (2005) and Albert water (2006) were performed by Maxime Mergen (Cranfield University). Sharp *et al.*, (2006) found raw water floc size was dominated by FAF, so pull-off length and adhesion forces are given in reference to FAF using PLL-coated tips. Floc sizes ( $d_{50}$  values) were 478.12  $\mu\text{m}$  and 577.69  $\mu\text{m}$  for Penwhirn water and Albert water 2006, respectively. However, FAF polyanions from Penwhirn were longer than Albert 2006 when PLL tips were used, the cause of which has been explained in section 5.3.7. Strength factors were 0.58 and 0.43 for Albert-2006 and Penwhirn waters, respectively, where 1 is the maximum. Interestingly, peak adhesion forces of FAF polyanions from Albert (2006) were considerably stronger, as shown in Figure 5.8b, indicating Penwhirn FAF polyanions were either less charged or smaller in size. These findings show that adhesion force data on FAF polyanions using PLL-tips may be used as an indicator of raw water floc strength.

Flocs, in general do not only comprise of organic matter, but also consist of the coagulant, which in the examples given above are iron-based  $\text{Fe}(\text{OH})_3$  coagulants. For FAF polyanions, their restricted floc size may be caused by complete charge neutralization of  $\text{Fe}^{3+}$ , where densely packed FAF polyanions cause charge reversal, resulting in electrostatic repulsion between subsequent FAF flocs. AFM images of FAF polyanions have shown it to deposit as micellar structures that are dispersed over the surface, but the structure has been shown to change with increasing concentration and solution conditions (Namjesnik-Dejanovic and Maurice, 1998). Consequently, FAF floc structure also appears to be dependent on the solution conditions, and additional investigation is required in order to measure the FAF pull-off lengths and adhesion forces in different ionic strengths.

## Chapter 6

## Overview Discussion

### 6.1 Application of unmodified tips to water treatment systems

One of the main objectives of this project was to assess the usefulness of AFM force measurements using unmodified AFM tips with application to water treatment systems. Unmodified tips are seldom used for probing interfacial interactions with application to water treatment because particles of more relevance to the interacting bodies are preferred. The significance of using unmodified tips was to assess how relevant this was to real-life conditions, and whether the tip must be modified in order to screen materials at a very small level for their propensity to scale.

In the calcite section of this study, force measurements were performed in synthetic hard water to make the solution more relevant to process-specific environments. Measurements were also performed in natural hard water to replicate these conditions, but due to contamination of the tip, cantilever and sample, data from the experiments was not used. Contamination was unavoidable because natural hard water contained inorganic as well as organic material, which deposited on surfaces during force measurements. Although samples were cleaned prior to use, they were neither chemically nor mechanically modified. When results in synthetic hard water were compared to the macroscale scaling rate experiments, they showed there were limitations posed by the use of unmodified tips. The small tip dimensions relative to asperity size on many of the samples meant contact area was driving adhesion forces at the interface. This was not to say contact area was unimportant, but it was found that for RF steel, SB steel, used copper, 'k. coating' and TiN this seemed to be the main factor driving adhesion. On the other hand surface forces and particularly hydrophilic and hydrophobic forces dominated interfacial interactions on materials that gave low  $R_a$  values. Importantly, force measurements with unmodified tips were able to show why amorphous carbon coatings were least adhesive, and increasing surface roughness will undoubtedly have a

detrimental effect on scaling rate. Therefore, it can be said that the value of unmodified tips in probing interfacial interactions that are relevant to applied systems in water treatment was limited by the samples' surface topography. Contact angle measurements complemented the AFM data, indicating hydrophilic repulsion due to high electron donor ( $\gamma^-$ ) values was preventing adhesion to SiO<sub>2</sub> tips.

In the NOM chapter of this project, unmodified tips provided a controlled negatively-charged surface. The highly complex NOM polyanions used in this study were also negatively-charged, so their interaction with silica tips was interesting to observe. As NOM polyanions were heterogeneous, flexible and with no well-defined surface structure, a greater range of interactions was observed. Ultrapure water was used in these experiments to reduce the number of outside influences on the complex interface. The findings indicated that there were noticeable differences between NOM polyanions when unmodified tips were used. For instance, the extent of polyanion stretching had a pronounced affect on pull-off force and detachment length. For instance, detachment lengths were longest for HPIA polyanions, which was in agreement with a study by Rojas *et al.*, (2002) where they used polycations. Adhesion and detachment lengths on HPIA were most similar to the PLL control, with FAF most dissimilar to the control. Differences were also observed between HPIA polyanions from different sources, with Penwhirn HPIA more adhesive and giving longer detachment lengths. Considering polyanion surface charge density controlled adhesion, force measurements on immobilized NOM polycations may be used as an indicator of polyanion size, as well as surface charge density. Both these properties may be of crucial importance in understanding the makeup of the polyelectrolytic proportion of flocs and their influence on coagulation performance.

Although unmodified silica tips are unlikely to represent one of the surfaces of interest when investigating interfacial interactions in water treatment systems, it has been shown that they can be used to screen materials with an  $R_a < 50$  nm effectively based on their adhesion profile. Also, due to their negative charge, well defined contact area and general

robustness, they can also be used to screen polyelectrolytes and other charged surfaces in different liquid.

## 6.2 Application of modified tips to water treatment

Nearly all tip modification methods with application to water treatment have focussed on optimizing ultrafiltration and nanofiltration membrane performance (Lee and Elimelech, 2006; Brant *et al.*, 2006 and Li and Elimelech, 2004). Furthermore, tips are normally modified with colloids of well defined size and topography. When poorly defined or non-spherical foulants such as calcium carbonate and gypsum crystals are attached to the cantilever, there must be a balance between making experimental conditions relevant to fouling, and understanding the limitation of the technique due to contact area. For instance, in the calcite section of this project, tips were modified with calcite crystals by growing crystals on the tip and by attaching them to the cantilever. Both methods were seemingly more relevant to scaling compared to unmodified tips. And although calcite surfaces themselves are homogeneous, their orientation on the cantilever was not always easy to control, while their surface topography was not always uniform, leading to differences in contact area on different substrates. Furthermore, the  $R_a$  of substrate materials ranged from 10 to 280 nm, which exacerbated problems with regard to contact area.

There were also fundamental differences between the rapid scaling experiments and force measurements, which have already been discussed in detail. For these reasons, force measurements with calcite-modified tips did not give the expected linear correspondence with scaling rate experiments, because some materials were more sensitive to surface forces than others. Therefore, materials had to be grouped into their  $R_a$  values. For instance, from the force-sensitive (low  $R_a$ ) materials, Graphit-iC and Dymon-iC were least adhesive whilst PTFE and copper were most adhesive to calcite probes. Unsurprisingly, high  $R_a$  substrates such as RF steel, SB steel and used copper gave greater scaling rates, although force measurements with calcite tips did not necessarily show them as highly adhesive. This was effectively because contact area with calcite



probes did not recreate many of the interlocking effects that are present when rough surfaces scale during the induction period (Keysar *et al.*, 1994). Other reasons may be because the calcite crystal size in asperities of scaled substrates may be different to those used on calcite probes.

In the NOM chapter of this project, chemically-adsorbed probes were used to study interactions between charged and uncharged surfaces with adsorbed NOM polyanions. This was central to understanding the interactions between NOM polyanions, differences between NOM sources, and how this may be used to optimize coagulation performance during NOM removal. These probes were more analogous to unmodified tips by virtue of their contact area but exhibited a different surface charge and surface chemistry. As PLL was opposite in sign to NOM polyanions, electrostatic forces dominated adhesion to NOM polyanions, with PLL having a preference for HAF and FAF. This was in contrast to unmodified tips, which gave a preference for HPIA polyanions. The cationic charge on the tip was maintained because the tips were repulsive to PLL surfaces in ultrapure water. Force measurements with PLL tips were not performed on PLL in between sample changes which may give a better indication of the robustness of the PLL layer. The quality of the PLL layer and its preference for FAF which have been shown to impart the negative surface charge, also means PLL or similar polycations may in future be used as a bridging flocculant for the removal of FAF from drinking water (Fellows and Doherty, 2006).

Because not all fouling particles in water treatment systems, whether crystalline or heterogeneous, are of well-defined geometry, topography and/or surface chemistry, AFM tips modified with such particles can still be shown to be of great value. This has been demonstrated both in the literature (Finot *et al.*, 2001 and Plaschke *et al.*, 2000), and in the present study. In this study tips modified with calcite and polymers such as organic matter or other polyelectrolyte, gave contrasting force profiles that were unique to their colloidal size and surface chemistry. Although the scale of their interactions were different, both methods of modification were shown to be effective in screening host

materials with varying surface chemistry, and can successfully be applied in numerous diagnostic or screening applications. NOM-coated or polymer-coated tips in particular were shown to be highly specific due to the intermolecular pulling events, and have been shown to recreate some of the colloidal interactions that take place in NOM coagulation processes. As a result, there is no doubt tips modified with heterogeneous particles can be used as a platform to understand adhesion phenomena that will enhance the ability to predict the behaviour of foulants in the environment.

## Chapter 7

## Conclusions

The main conclusions drawn from the work presented here are:

1. **Fundamental differences between bench-scale scaling experiments and AFM force measurements dictate whether the induction period and/or fouling period of the scaling process can be assessed.** The surface-sensitive AFM was applicable primarily to the induction period of scaling, where surface properties control the rate of nucleation and growth of the deposit. This enables the screening of materials by assessing the induction period of inorganic scaling, by measuring the adhesion strength of foulants to a range of surfaces. In contrast, conventional scaling experiments observe the scaling process as a whole, due to difficulties in knowing when the induction period ends and the fouling period commences.
2. **A noticeable correlation between the theoretical work of adhesion ( $W_{132}$ ) from sextet and triplet methods and macroscale scaling rate experiments was obtained with materials giving an  $R_a$  below 50 nm and a scaling rate of less than  $10 \text{ g CaCO}_3 \text{ m}^{-2} \cdot \text{h}^{-1}$ .** It was deduced that materials that have a  $R_a$  of above 50 nm were likely to scale at a greater rate due to surface asperities, whereas surface force effects will dominate with materials with a  $R_a$  below 50 nm. Hence, for materials that gave a scaling rate above  $10 \text{ g CaCO}_3 \text{ m}^{-2} \cdot \text{h}^{-1}$ , surface roughness was the driving force enhancing calcite adhesion.
3. **Calcite-probe modification did not correlate with macroscale scaling rate experiments but unmodified tips showed some correlation for group II materials (amorphous carbon coatings, TiN, aluminium, PTFE and ‘k. coating’) only.** The material ranking of adhesion force was modified when the

quality of the calcite probe was systematically changed. For instance, rough calcite probes were adhesive to RF steel and atomically-flat calcite probes were less adhesive to rough substrate materials. However, the unmodified tips proved more effective but were limited to group II materials only. However, contact angles and  $W_{132}$  remain the most appropriate method.

4. **Theoretical adhesion calculations with the roughness model (Rabinovich *et al.*, 2000a, b) underestimated force measurements to group I (MF steel, RF steel, SB steel, both gold samples and both copper samples) materials but showed excellent agreement to group II (amorphous carbon coatings, TiN, aluminium, PTFE and ‘k. coating’) materials using silicon as the adhesive.** The magnitude of adhesion force was accurate to the nearest 0.1 nN for group II materials but estimated smaller forces for the group I materials by at least an order of magnitude. Furthermore, the roughness model did not calculate an increase in adhesion force with increased surface roughness, indicating the model can be applied where the interacting system is a sphere-flat surface with nanoscale roughness. Therefore, the roughness model could not be applied to a tip-asperity interaction, where the asperity is either a peak or a valley.
  
5. **The origin of repulsive forces on Dymon-iC and Graphit-iC materials was due to hydrophilic repulsion while enhanced adhesion was caused by hydrophobic attraction.** Adhesion forces were significantly reduced on Dymon-iC and Graphit-iC with modified and unmodified tips and both materials were the most hydrophilic from water contact angle measurements. The ratio of  $\gamma^-/\gamma^+$  of both amorphous carbon coatings materials and calcite was similar, resulting in electrostatic repulsion. PTFE and copper, both of which gave  $R_a$  values below 50 nm, gave water contact angles  $> 70^\circ$ . Acidic sites on PTFE and copper were also found to enhance adhesion because calcite was basic.

In the second part of study, the following conclusions can be drawn:

6. NOM characterization with unmodified tips provided the following information:
  - a. **Detachment events with silica tips were longer on HPIA polyanions from Penwhirn and both feeders, while both Albert samples were adhesive to hydrophobic polyanions.** HPIA polyanions from Penwhirn were also more hydrophilic. Generally, FAF from hydrophobic polymers gave fewer adhesion events, which indicates they were less adhesive to the predominantly  $\text{SiO}^{2-}$  charged tip, and electrostatic forces dominated.
7. NOM characterization with modified tips provided the following information.
  - a. **Using PLL-coated tips, electrostatic forces also dominated interactions with NOM polyanions, with PLL having a preference for HAF and FAF.** This was in contrast to unmodified tips, which gave a preference for HPIA polyanions. The cationic charge on the tip was maintained because the tips were repulsive to PLL surfaces in ultrapure water. PLL tips also gave distinct attractive forces that varied between sources. This approach could be used for identifying molecular size of all polyanions, as the poly-l-lysine tips were able to distinguish between HAF and FAF polyanions from Widdop and Penwhirn water reservoirs.
  - b. **In symmetric NOM-NOM systems, HPIA-HPIA dominated both adhesion and detachment lengths, while FAF-FAF and HAF-HAF gave similar adhesion profiles.** The hydrophilicity of HPIA may have promoted a branched configuration because terminal groups had a greater affinity for water according to contact angle measurements. It is thought these intermolecular interactions can be transferred to floc size experiments, where HPIA flocs were biggest and FAF flocs were smallest. In non-symmetric systems adhesion between FAF-NOM was

indiscriminate, compared to HAF and HPIA polyanions. These findings suggest FAF polyanions were most likely to control coagulation performance during NOM removal, because of its inherent ability to attach to both hydrophilic and hydrophobic groups.

- c. **Glycine-coated tips did not show any significant difference between interactions with NOM polyanions, and so are poor quality model compounds.** The uncharged  $\text{NH}_2$  terminals also gave similar adhesive and polymer-pulling interactions with PLL, indicating the probe gave no overall preference for polyanionic or polycationic surfaces.
- d. **Like glycine-coated tips, the uncharged XAD resins also gave no overall preference for NOM polyanions.** Of the resin-modified probes the MIEX® resins provided the most robust data set having a preference for FAF, and correlated with macroscale NOM removal experiments. Adhesion forces were less specific and the reproducibility was poor with significant fluctuation between successive probes. As a result, NOM-coated AFM tips provide the most detailed information regarding a fraction's surface character and potential reactivity with other surfaces. However, FAF-coated resins did confirm the reactivity of the FAF fraction demonstrating equal adhesion to all the fractions, while HAF and HPIA showed preference for themselves.

## Chapter 8

## Future Work

During this research project, it was not always feasible to investigate all ideas or options thoroughly, and so a number of suggestions for further research are made:

1. Further investigation on the size of calcite crystals deposited on high and low  $R_a$  substrates during scaling experiments, so that any difference in crystal size can be transferred to force measurements.
2. Use the contact angle hysteresis approach on substrate materials so that the surface free energy values can be compared to those obtained in this project.
3. Perform force measurements using calcite-modified tips on substrates at elevated temperatures, so that these findings may be compared to scaling experiments.
4. Develop a method of preparing calcite probes so that a monolayer of calcite is grown on the AFM tip. These results can provide direct comparison to unmodified tips due to similar contact areas.
5. Perform zeta potential measurements of individual NOM fractions so that differences in adhesion and pull-off length can be related to surface charge of polyanions.
6. Perform force measurements on NOM polyanions in the presence of electrolyte, and optionally in the presence of coagulants.
7. Perform imaging of immobilized NOM polyanions using AFM tapping mode, so that adsorbed polyanions can be compared to the literature and possibly perform force measurements on known locations of the polyanion.

## Chapter 9

## References

- Abraham, T., Giasson, S., Gohy, J.F. and Jerome, R. (2000) Direct measurements of interactions between hydrophobically anchored strongly charged polyelectrolyte brushes. *Langmuir*, **16**, 4286-4292.
- Adler, J.J., Rabinovich, Y.I. and Moudgil, B.M. (2001) Origins of the Non-DLVO force between glass surfaces in aqueous solution. *Journal of Colloid & Interface Science*, **237**, 249-258.
- Aiken, G.R., Thurman, E.M., Malcolm, R.L. and Walton, H.F. (1979) Comparison of XAD macroporous resins for the concentration of fulvic-acid from aqueous-solution. *Analytical Chemistry*, **51**, 1799-1803.
- Alvarez-Puebla, R.A., Garrido, J.J. and Aroca, R.F. (2004) Surface-enhanced vibrational microspectroscopy of fulvic acid micelles. *Analytical Chemistry*, **76**, 7118-7125.
- Avena, M.J. and Koopal, L.K. (1999) Kinetics of humic acid adsorption at solid-water interfaces. *Environmental Science & Technology*, **33**, 2739-2744.
- Balnois, E., Wilkinson, K.J., Lead, J.R. and Buffle, J. (1999) Atomic force microscopy of humic substances: effects of pH and ionic strength. *Environmental Science & Technology*, **33**, 3911-3917.
- Barthez-Labrousse, M.G. (2002) Acid-base characterisation of flat oxide-covered metal surfaces. *Vacuum*, **67**, 385-392.
- Beach, E.R., Tormoen, G.W. and Drelich, J. (2002) Pull-off forces measured between hexadecanethiol self-assembled monolayers in air using an atomic force microscope: Analysis of surface free energy. *Journal of Adhesion Science & Technology*, **16**, 845-868.
- Beyer, M.K. and Clausen-Schaumann, H. (2005) Mechanochemistry: The mechanical activation of covalent bonds. *Chemical Reviews*, **105**, 2921-2948.
- Black, B. D., Harrington, G. W. and Singer, P. C. (1996) Impact of organic carbon removal on cancer risks posed by drinking water chlorination. *Journal American Water Works Association*, **88** (12), 40.
- Bornhorst, A., Muller-Steinhagen, H. and Zhao, Q. (1999) Reduction formation under pool boiling conditions by ion implantation and magnetron sputtering on heat transfer surfaces. *Heat Transfer Engineering*, **20**, 6-14.



- Bowen, W.R. and Doneva, T.A. (2000) Atomic force microscopy studies of membranes: effect of surface roughness on double-layer interactions and particle adhesion. *Journal of Colloid & Interface Science*, **229**, 544-549.
- Boyer, T.H. and Singer, P.C. (2006) A pilot-scale evaluation of magnetic ion exchange treatment for removal of natural organic material and inorganic anions. *Water Research*, **40**, 2865-2876.
- Brant, J.A., Johnson, K.M. and Childress, A.E. (2006) Examining the electrochemical properties of a nanofiltration membrane with atomic force microscopy. *Journal of Membrane Science*, **276**, 286-294.
- Burks, G.A., Velegol, S.B., Paramonova, E., Lindenmuth, B.E., Feick, J.D. and Logan, B.E. (2003) Macroscopic and nanoscale measurements of the adhesion of bacteria with varying outer layer surface composition. *Langmuir*, **19**, 2366-2371.
- Burnham, N.A. and Colton, R.J. (1989) Measuring the nanomechanical properties and surface forces of materials using an atomic force microscope. *Journal of Vacuum Science & Technology A-Vacuum Surfaces & Films*, **7** (4), 2906-2913.
- Butt, H.J. (1994) A technique for measuring the force between a colloidal particle in water and a bubble. *Journal of Colloid & Interface Science*, **166**, 109-117.
- Butt, H.J., Jaschke, M. and Ducker, W. (1995) Measuring surface forces in aqueous-electrolyte solution with the atomic-force microscope. *Bioelectrochemistry & Bioenergetics*, **38**, 191-201.
- Butt, H.J., Cappella, B. and Kappl, M. (2005) Force measurements with the atomic force microscope: technique, interpretation and applications. *Surface Science Reports*, **59**, 1-152.
- Callow, J.A., Crawford, S.A., Higgins, M.J., Mulvaney, P. and Wetherbee, R. (2000) The application of atomic force microscopy to topographical studies and force measurements on the secreted adhesive of the green alga enteromorpha. *Planta*, **211**, 641-647.
- Callow, M.E. and Callow, J.A. (2002) Marine biofouling: a sticky problem. *Biologist*, **49** (1), 1-5.
- Campitelli, P.A., Velasco, M.I. and Ceppi, S.B. (2006) Chemical and physicochemical characteristics of humic acids extracted from compost, soil and amended soil. *Talanta*, **69**, 1234-1239.
- Cappella, B. and Dietler, G. (1999) Force distance curves by atomic force microscopy. *Surface Science Reports*, **34**, 1-104.

- Cavalier, K. and Larche, F. (2002) Effects of water on the rheological properties of calcite suspensions in dioctylphthalate. *Colloids & Surfaces A: Physicochemical & Engineering Aspects*, **197** (1-3), 173-181.
- Christl, I., Knicker, H., Kogel-Knabner, I. and Kretzschmar, R. (2000) Chemical heterogeneity of humic substances: characterization of size fractions obtained by hollow-fibre ultrafiltration *European Journal of Soil Science*, **51** (4), 617-625.
- Christy, A.A. and Egeberg, P.K. (2000) Characterisation of natural organic matter from the nordic typing project water samples by chemometric analysis of their near infrared spectral profiles. *Chemometrics & Intelligent Laboratory Systems*, **50**, 225-234.
- Churchill, H., Teng, H. and Hazen, R.M. (2004) Correlation of pH-dependent surface interaction forces to amino acid adsorption: implications for the origin of life. *American Mineralogist*, **89**, 1048-1055.
- Claesson, P.M., Poptoshev, E., Blomberg, E. and Dedinaite, A. (2005) Polyelectrolyte-mediated surface interactions. *Advances in Colloid & Interface Science*, **114**, 173-187.
- Cleveland, J.P., Manne, S., Bocek, D. and Hansma, P.K. (1993) A non-destructive method for determining the spring constant of cantilevers for scanning force microscopy. *Review of Scientific Instruments*, **64**, 403-405.
- Colton, R. J., Engel, A., Frommer, J.E., Gaub, H.E., Gewirth, A.A., Guckenberger, R., Heckl, W.M., Parkinson, B. and Rabe, J. (2001) *Procedures in scanning probe microscopes*. John Wiley and Sons Ltd, New York, NY, USA.
- Considine, R.F., Dixon, D.R. and Drummond, C.J. (2002) Oocysts of cryptosporidium parvum and model sand surfaces in aqueous solutions: an atomic force microscope (AFM) Study. *Water Research*, **36**, 3421-3428.
- Cosslett, C. (2001) *The effects of magnetic water treatment on limescale formation*. MSc Thesis, Cranfield University Press, Cranfield University.
- Della Volpe, C. and Siboni, S. (2000) Acid-Base surface free energies of solids and the definition of scales in the Good-van Oss-Chaudhury theory. *Journal of Adhesion Science & Technology*, **14**, 235-272.
- Doyle, J.D., Oldring, K., Churchley, J. and Parsons, S.A. (2002) Struvite formation and the fouling propensity of different materials. *Water Research*, **36**, 3971-3978.
- Drechsler, A., Petong, N., Zhang, J.F., Kwok, D.Y. and Grundke, K. (2004) Force measurements between teflon AF and colloidal silica particles in electrolyte solutions. *Colloids & Surfaces a-Physicochemical & Engineering Aspects*, **250**, 357-366.

- Drelich, J., Tormoen, G.W. and Beach, E.R. (2004) Determination of solid surface tension from particle-substrate pull-off forces measured with the atomic force microscope. *Journal of Colloid & Interface Science*, **280**, 484-497.
- Droppo, I. J., Leppard, G. G., Liss, S. N., and Milligan, T. G. (2005) *Flocculation in natural & engineered environmental systems*. Boca Raton/London/New York/Washington, D.C, CRC Press.
- Ducker, W.A., Senden, T.J. and Pashley, R.M. (1991) Direct measurement of colloidal forces using an atomic force microscope. *Nature*, **353**, 239-241.
- Dunn, S., Impey, S., Kimpton, C., Parsons, S.A., Doyle, J. and Jefferson, B. (2004) Surface diagnostics for scale analysis. *Water Science & Technology*, **49**, 183-190.
- Fa, K.Q., Tao, J.A., Nalaskowski, J. and Miller, J.D. (2003) Interaction forces between a calcium diolate sphere and calcite/fluorite surfaces and their significance in flotation. *Langmuir*, **19**, 10523-10530.
- Fearing, D.A., Banks, J., Guyetand, S., Eroles, C.M., Jefferson, B., Wilson, D., Hillis, P., Campbell, A.T. and Parsons, S.A. (2004) Combination of Ferric and Miex (R) for the treatment of a humic rich water. *Water Research*, **38**, 2551-2558.
- Fellows, C. M. and Doherty, W. O. S. (2006) Insights into bridging flocculation. *Macromolecules Symposium*, **231**, 1-10.
- Feng, X.J., Simpson, A.J. and Simpson M.J. (2005) Chemical and mineralogical controls on humic acid sorption to clay mineral surfaces. *Organic Geochemistry*, **36**, 1553-1566.
- Ferris, F.G., Phoenix, V., Fujita, Y. and Smith, R.W. (2004) Kinetics of calcite precipitation induced by ureolytic bacteria at 10 to 20° c in artificial groundwater. *Geochimica Et Cosmochimica Acta*, **68**, 1701-1710.
- Field, S.K., Jarratt, M. and Teer, D.G. (2004) Tribological properties of graphite-like and diamond-like carbon coatings. *Tribology Int*, **37**, 949-956.
- Fielden, M.L., Hayes, R.A. and Ralston, J. (1996) Surface and capillary forces affecting air bubble-particle interactions in aqueous electrolyte. *Langmuir*, **12**, 3721-3727.
- Filip, D., Uricanu, V.I., Duits, M.H.G., Agterof, W.G.M. and Mellema, J. (2005) Influence of bulk elasticity and interfacial tension on the deformation of gelled water-in-oil emulsion droplets: an AFM study. *Langmuir*, **21**, 115-126.
- Finot, E., Lesniewska, E., Mutin, J.C. and Goudonnet, J.P. (1999) Investigations of surface forces between gypsum crystals in electrolytic solutions using microcantilevers. *Journal of Chemical Physics*, **111**, 6590-6598.

- Finot, E., Lesniewska, E., Goudonnet, J.P., Mutin, J.C., Domenech, M. and Kadi, A.A. (2001) Correlating surface forces with surface reactivity of gypsum crystals by atomic force microscopy. comparison with theological properties of plaster. *Solid State Ionics*, **141**, 39-46.
- Förster, M. and Bohnet, M. (1999) Influence of the interfacial free energy crystal/heat transfer surface on the induction period during fouling. *International Journal of Thermal Sciences*. **38**, 944-954.
- Förster, M., Augustin, W. and Bohnet, M. (1999) Reduction of fouling on heat transfer surfaces. *Chemie Ingenieur Technik*, **71**, 1391-1395.
- Förster, M. and Bohnet, M. (2000) Modification of molecular interactions at the interface crystal/heat transfer surface to minimize heat exchanger fouling. *International Journal of Thermal Sciences*, **39**, 697-708.
- Frank, B.P. and Belfort, G. (2002) Adhesion of mytilus edulis foot protein 1 on silica: ionic effects on bifouling. *Biotechnology Progress*, **18**, 580-586.
- Freitas, A.M. and Sharma, M.M. (2001) Detachment of particles from surfaces: an AFM study. *Journal of Colloid & Interface Science*, **233**, 73-82.
- Friedsam, C., Becares, A.D., Jonas, U., Seitz, M. and Gaub, H.E. (2004) Adsorption of polyacrylic acid on self-assembled monolayers investigated by single-molecule force spectroscopy. *New Journal of Physics*, **6**.
- Fulton, J.R., Mcknight, D.M., Foreman, C.M., Cory, R.M., Stedmon, C. and Blunt, E. (2004) Changes in fulvic acid redox state through the oxycline of a permanently ice-covered antarctic lake. *Aquatic Sciences*, **66**, 27-46.
- Gibson, C.T., Watson, G.S. and Myhra, S. (1996) Determination of the spring constants of probes for force microscopy/spectroscopy. *Nanotechnology*, **7**, 259-262.
- Gibson, C.T., Smith, D.A. and Roberts, C.J. (2005) Calibration of silicon atomic force microscope cantilevers. *Nanotechnology*, **16**, 234-238.
- Giesbers, M., Kleijn, J.M. and Stuart, M.A.C. (2002) Interactions between acid- and base-functionalized surfaces. *Journal of Colloid & Interface Science*, **252**, 138-148.
- Good, R.J. (1992) Contact-angle, wetting, and adhesion - a critical-review. *Journal of Adhesion Science & Technology*, **6**, 1269-1302.
- Goodman, F.O. and Garcia, N. (1991) Roles of the attractive and repulsive forces in atomic-force microscopy. *Physical Review B*, **43**, 4728-4731.

- Gordeliy, V.I., Kiselev, M.A., Lesieur, P., Pole, A.V. and Teixeira, J. (1998) Lipid membrane structure and interactions in dimethyl sulfoxide/water mixtures. *Biophysical Journal*, **75**, 2343-2351.
- Goslan, E. (2003) *Natural organic matter character & reactivity*. PhD Thesis, Cranfield University Press, Cranfield University.
- Grasso, D., Subramaniam, K., Butkus, M., Strevett, K. and Bergendahl, K. (2002) A review of non-DLVO interactions in environmental colloidal systems. *Reviews in Environmental Science and Biotechnology*, **1**, 17-38.
- Green, C.P., Lioe, H., Cleveland, J.P., Proksch, R., Mulvaney, P. and Sader, J.E. (2004) Normal and torsional spring constants of atomic force microscope cantilevers. *Review of Scientific Instruments*, **75**, 1988-1996.
- Guan, X.H., Shang, C. and Chen, G.H. (2006) Competitive adsorption of organic matter with phosphate on aluminum hydroxide. *Journal of Colloid & Interface Science*, **296**, 51-58.
- Guo, J. and Ma, J. (2006) AFM study on sorbed NOM and its fractions isolated from river songhua. *Water Research*, **40**, 1975-1984.
- Hasson, D., Drak, A. and Semiat, R. (2003) Induction times induced in an ro system by antiscalants delaying  $\text{CaSO}_4$  precipitation. *Desalination*, **157**, 193-207.
- Haupt, B.J., Ennis, J. and Sevick, E.M. (1999) The detachment of a polymer chain from a weakly adsorbing surface using an AFM tip. *Langmuir*, **15** (11), 3886-3892.
- He, B., Lee, J. and Patankar, N. A. (2004) Contact angle hysteresis on rough hydrophobic surfaces. *Colloids & Surfaces A: Physicochemical & Engineering Aspects*, **248** (1-3), 101-104.
- Heim, L.O., Ecke, S., Preuss, M. and Butt, H.J. (2002) Adhesion forces between gold and polystyrene particles. *Journal of Adhesion Science & Technology*, **16**, 829-843.
- Heinz, W.F. and Hoh, J.H. (1999) Spatially resolved force spectroscopy of biological surfaces using the atomic force microscope. *Trends in Biotechnology*, **17**, 143-150.
- Henderson, E. (1994) Imaging of living cells by atomic force microscopy. *Progress in Surface Science*, **46** (1), 39-60.
- Hodges, C.S., Cleaver, J.A.S., Ghadiri, M., Jones, R. and Pollock, H.M. (2002) Forces between polystyrene particles in water using the afm: pull-off force vs particle size. *Langmuir*, **18**, 5741-5748.

- Holysz, L. and Chibowski, E. (1994) Surface Free-Energy Components of Calcium-Carbonate and Their Changes Due to Radiofrequency Electric-Field Treatment. *Journal of Colloid & Interface Science*, **164** (1), 245-251.
- Holysz, L. (2000) Investigation of the effect of substrata on the surface free energy components of silica gel determined by thin layer wicking method. *Journal of Materials Science*, **35**, 6081-6091.
- Hooton, J.C., German, C.S., Roberts, C.J., Allen, S., Davies, M.C., Tendler, S.J.B. and Williams, P.M. (2003) Estimation of inter-particulate contact area and geometry between individual particles in pharmaceutical aerosols. *Abstracts of Papers of the American Chemical Society*, **226**, U369 Part 1.
- Hutter, J.L. and Bechhoefer, J. (1993) Calibration of atomic-force microscope tips. *Review of Scientific Instruments*, **64**, 1868-1873.
- Israelachvili, J. (1992) *Intermolecular & surface forces*. 2<sup>nd</sup> edition, Academic Press, California, USA.
- Jacquot, C. and Takadoum, J. (2001) A study of adhesion forces by atomic force microscopy. *Journal of Adhesion Science & Technology*, **15**, 681-687.
- Jada, A., Ait Akbour, R. and Douch, J. (2006) Surface charge and adsorption from water onto quartz sand of humic acid. *Chemosphere*, **64**, 1287-1295.
- Jefferson, B., Jarvis, P., Sharp, E., Wilson, S. and Parsons, S.A. (2004) Floes through the looking glass. *Water Science & Technology*, **50**, 47-54.
- Kanokkantapong, V., Marhaba, T.F., Wattanachira, S., Panyapinyophol, B. and Pavasant, P. (2006) Interaction between organic species in the formation of haloacetic acids following disinfection. *Journal of Environmental Science & Health Part a-Toxic/Hazardous Substances & Environmental Engineering*, **41**, 1233-1248.
- Kappl, M. and Butt, H.J. (2002) The colloidal probe technique and its application to adhesion force measurements. *Particle & Particle Systems Characterization*, **19**, 129-143.
- Karabelas, A.J. (2002) Scale formation in tubular heat exchangers - research priorities. *International Journal of Thermal Sciences*, **41**, 682-692.
- Keller, D., Rozlosnik, N. and Mouritsen, O.G. (2003) Investigation of free phospholipid model membranes and natural membranes by AFM. *Biophysical Journal* **84**, 48A-48A Part 2 Suppl. S.
- Keysar, S., Semiat, R., Hasson, D. and Yahalom, J. (1994) Effect of surface-roughness on the morphology of calcite crystallizing on mild-steel. *Journal of Colloid & Interface Science*, **162**, 311-319.

- Klapper, L., Mcknight, D.M., Fulton, J.R., Blunt-Harris, E.L., Nevin, K.P., Lovley, D.R. and Hatcher, P.G. (2002) Fulvic acid oxidation state detection using fluorescence spectroscopy. *Environmental Science & Technology*, **36**, 3170-3175.
- Kokkoli, E. and Zukoski, C.F. (2000) Surface Forces Between Hydrophilic Self-Assembled Monolayers in Aqueous Electrolytes. *Langmuir* **16**, 6029-6036.
- Kollist-Siigur, K., Nielsen, T., Gron, C., Hansen, P. E., Helweg, C., Jonassen, K. E. N., Jorgensen, O. and Kirso, U. (2001) Sorption of polycyclic aromatic compounds to humic and fulvic acid HPLC column materials. *Journal of Environmental Quality*, **30**, 526-537.
- Krasner, S.W., McGuire, M. J., Jacangelo, J. G., Patania, N. L., Reagan, K. M. and Aieta, E. M. (1989) The occurrence of disinfection by-products in united-states drinking-water. *Journal American Water Works Association*, **81**, 41-53.
- Kvasnica, S., Schalko, J., Eisenmenger-Sittner, C., Benardi, J., Vorlaufer, G., Pauschitz, A. and Roy, M. (2006) Nanotribological study of PECVD DLC and reactively sputtered Ti containing carbon films. *Diamond & Related Materials*, **15** (10), 1743-1752.
- Kwon, K. D., Vadillo-Rodriguez, V., Logan, B. E. and Kubicki, J.D. (2006) Interactions of biopolymers with silica surfaces: force measurements and electronic structure calculation studies. *Geochimica et Cosmochimica Acta*, **70**, 3803-3819.
- Lee, S. and Elimelech, M. (2006) Relating organic fouling of reverse osmosis membranes to intermolecular adhesion forces. *Environmental Science & Technology*, **40**, 980-987.
- Leite, F.L. and Herrmann, P.S.P. (2005) Application of atomic force spectroscopy (AFS) to studies of adhesion phenomena: A review. *Journal of Adhesion Science & Technology*, **19**, 365-405.
- Li, Y.Q., Tao, N.J., Pan, J., Garcia, A.A. and Lindsay, S.M. (1993) Direct measurement of interaction forces between colloidal particles using the scanning force microscope. *Langmuir*, **9**, 637-641.
- Li, B.K. and Logan, B.E. (2004) Bacterial adhesion to glass and metal-oxide surfaces. *Colloids & Surfaces B-Biointerfaces*, **36**, 81-90.
- Li, Q.L. and Elimelech, M. (2004). Organic fouling and chemical cleaning of nanofiltration membranes: measurements and mechanisms. *Environmental Science & Technology*, **38**, 4683-4693.
- Liu, A.G., Wu, R.C., Eschenazi, E. and Papadopoulos, K. (2000) AFM on humic acid adsorption on mica. *Colloids & Surfaces a-Physicochemical & Engineering Aspects*, **174**, 245-252.

- Liu, J.J., Xu, Z.H. and Masliyah, J. (2005) Colloidal forces between bitumen surfaces in aqueous solutions measured with atomic force microscope. *Colloids & Surfaces a-Physicochemical & Engineering Aspects*, **260**, 217-228.
- Lower, S.K., Tadanier, C.J. and Hochella, M.F. (2000) Measuring interfacial and adhesion forces between bacteria and mineral surfaces with biological force microscopy. *Geochimica Et Cosmochimica Acta*, **64**, 3133-3139.
- Luckham, P.F. (2004) Manipulating forces between surfaces: applications in colloid science and biophysics. *Advances in Colloid & Interface Science*, **111**, 29-47.
- MacAdam, J. (2005) *Calcium carbonate scale formation & control*. PhD Thesis, Cranfield University Press, Cranfield University.
- Mantel, M., Rabinovich, Y.I., Wightman, J.P. and Yoon, R.H. (1995) A study of hydrophobic interactions between stainless-steel and silanated glass-surface using atomic-force microscopy. *Journal of Colloid & Interface Science*, **170** (1), 203-214.
- Mao, J.D., Xing, B. and Schmidt-Rohr, K. (2001) New structural information on a humic acid from two-dimensional h-1-c-13 correlation solid-state nuclear magnetic resonance. *Environmental Science & Technology*, **35**, 1928-1934.
- Maurice, P.A. and Namjesnik-Dejanovic, K. (1999) Aggregate structures of sorbed humic substances observed in aqueous solution. *Environmental Science & Technology*, **33**, 1538-1541.
- McCafferty, E. (2002) Acid-base effects in polymer adhesion at metal surfaces. *Journal of Adhesion Science & Technology*, **16**, 239-255.
- McCormack, A.C., McDonnell, C.M., O'Ferrall, R.A.M., O'Donoghue, A.C. and Rao, S.N. (2002) Protonated benzofuran, anthracene, naphthalene, benzene, ethene, and ethyne: Measurements and estimates of pK(a) and pK(R). *Journal of the American Chemical Society*, **124**, 8575-8583.
- McGuire, M. J., Addai-Mensah, J. and Bremmell, K.E. (2006) The effect of polymer structure type, pH, and shear on the interfacial chemistry, rheology and dewaterability of model iron oxide dispersions. *Colloids and Surfaces A: Physicochem. Eng. Aspects*, **275**, 153-160.
- McMurray, J. (1995) *Organic Chemistry*, 4<sup>th</sup> edition, pp 28, Brooks/Cole Publishing Co., California.
- Mcnamee, C.E., Tsujii, Y., Ohshima, H. and Matsumoto, M. (2004) Interaction forces between two hard surfaces in particle-containing aqueous systems. *Langmuir*, **20**, 1953-1962.



- Mertig, M., Klemm, D., Pompe, W., Zanker, H. and Bottger, M. (1999) Scanning force microscopy of spin-coated humic acid. *Surface & Interface Analysis*, **27**, 426-432.
- Morales-Cruz, A.L., Tremont, R., Martinez, R., Romanach, R. and Cabrera, C.R. (2005) Atomic force measurements of 16-mercaptohexadecanoic acid and its salt with  $\text{CH}_3$ ,  $\text{OH}$ , And  $\text{CONHCH}_3$  functionalized self-assembled monolayers. *Applied Surface Science*, **241**, 371-383.
- Mosley, L.M., Hunter, K.A. and Ducker, W.A. (2003) Forces between colloid particles in natural waters. *Environmental Science & Technology*, **37**, 3303-3308.
- Muller-Steinhagen, H., Zhao, Q., Helali-Zadeh, A. and Ren, X.G. (2000) The effect of surface properties on  $\text{CaSO}_4$  scale formation during convective heat transfer and subcooled flow boiling. *Canadian Journal of Chemical Engineering*, **78**, 12-20.
- Murray C A. (2005) *Novel treatment options for coagulant & potable sludge*. PhD Thesis, Cranfield University Press, Cranfield University.
- Nalaskowski, J., Drelich, J., Hupka, J. and Miller, J.D. (2003) Adhesion between hydrocarbon particles and silica surfaces with different degrees of hydration as determined by the AFM colloidal probe technique. *Langmuir*, **19**, 5311-5317.
- Namjesnik-Dejanovic, K. and Maurice, P.A. (1998) Conformations of fulvic acids determined by atomic force microscopy. *Abstracts of Papers of the American Chemical Society*, **216**, U808.
- Namjesnik-Dejanovic, K. and Maurice, P.A. (2001) Conformations and aggregate structures of sorbed natural organic matter on muscovite and hematite. *Geochimica Et Cosmochimica Acta*, **65**, 1047-1057.
- Ohler, B. (2007) Cantilever spring constant calibration using laser Doppler virometry. *Review of Scientific Instruments*, **78**, 063701-1 to 063701-5.
- Ong, Y.L., Razatos, A., Georgiou, G. and Sharma, M.M. (1999) Adhesion forces between e-coli bacteria and biomaterial surfaces. *Langmuir*, **15**, 2719-2725.
- Ostrovskaya, L.Y. (2003) Studies of diamond and diamond-like film surfaces using xaes, afm and wetting. *Vacuum* **68**, 219-238.
- Owen, D.M., Amy, G.J., Chowdhury, Z.K., Paode, R., McCoy, G. and Viscosil, K. (1995) NOM-characterization and treatability. *Journal American Water Works Association*, **87**, 46-63.
- Panorchan, P., Thompson, M.S., Davis, K.J., Tseng, Y., Konstantopoulos, K. and Wirtz, D. (2006) Single-molecule analysis of cadherin-mediated cell-cell adhesion. *Journal of Cell Science*, **119**, 66-74.

- Panyapinyopol, B., Marhaba, T.F., Kanokkantapong, V. and Pavasant, P. (2005) Characterization of precursors to trihalomethanes formation in Bangkok source water. *Journal of Hazardous Materials*, **120**, 229-236.
- Pasche, S., Textor, M., Meagher, L., Spencer, N.D. and Griesser, H.J. (2005) Relationship between interfacial forces measured by colloid-probe atomic force microscopy and protein resistance of poly(ethylene glycol)-grafted poly(L-lysine) adlayers on niobia surfaces. *Langmuir*, **21**, 6508-6520.
- Perry, A.J., Manory, R.R., Ward, L.P. and Kavuri, P.P. (2000) The effects of metal ion post-implantation on the near surface properties of tin deposited by CVD. *Surface & Coatings Technology*, **133**, 203-207.
- Plaschke, M., Romer, J., Klenze, R. and Kim, J.I. (2000) Influence of Europium(III) on the adsorption of humic acid onto mica studied by AFM. *Surface & Interface Analysis*, **30**, 297-300.
- Plaza, C., Senesi, N., Brunetti, G. and Mondelli, D. (2007) Evolution of the fulvic acid fractions during co-composting of olive oil mill wastewater sludge and tree cuttings. *Bioresource Technology*, **98** (10), 1964-1971.
- Qin, J. J., Oo, M. H., Kekre, K. A., Knops, F. and Miller, P. (2006) Impact of coagulation pH on enhanced removal of natural organic matter in treatment of reservoir water. *Separation & Purification Technology*, **49**, 295-298.
- Rabinovich, Y.I., Adler, J.J., Ata, A., Singh, R.K. and Moudgil, B.M. (2000a) Adhesion between nanoscale rough surfaces - I. role of asperity geometry. *Journal of Colloid & Interface Science*, **232**, 10-16.
- Rabinovich, Y.I., Adler, J.J., Ata, A., Singh, R.K. and Moudgil, B.M. (2000b) Adhesion between nanoscale rough surfaces - II. Measurement and comparison with theory. *Journal of Colloid & Interface Science*, **232**, 17-24.
- Radelczuk, H., Holysz, L. and Chibowski, E. (2002) Comparison of the Lifshitz-Van Der Waals/Acid-Base and contact angle hysteresis approaches for determination of solid surface free energy. *Journal of Adhesion Science & Technology*, **16**, 1547-1568.
- Reemtsma, T. and These, A. (2005) Comparative investigation of low-molecular-weight fulvic acids of different origin by Sec-Q-Tof-Ms: new insights into structure and formation. *Environmental Science & Technology*, **39**, 3507-3512.
- Ramos-Tejada, M. M., Ontiveros-Ortega, A., Gimenez-Martin, E., Espinosa-Jimenez, M. and Diaz, A. M. (2006) Effect of polyethyleneimine ion on the sorption of a reactive dye onto Leacril fabric: Electrokinetic properties and surface free energy of the system. *Journal of Colloid & Interface Science*, **297** (1), 317-321.

- Rojas, O. J., Ernstsson, M., Neumann, R. D. and Claesson, P. M. (2002) Effect of polyelectrolyte charge density on the adsorption and desorption behaviour on mica. *Langmuir*, **18** (5), 1604-1612.
- Sader, J.E., Chon, J.W.M. and Mulvaney, P. (1999) Calibration of rectangular atomic force microscope cantilevers. *Review of Scientific Instruments*, **70**, 3967-3969.
- Sander, S., Mosley, L.M. and Hunter, K.A. (2004) Investigation of interparticle forces in natural waters: effects of adsorbed humic acids on iron oxide and alumina surface properties. *Environmental Science & Technology*, **38**, 4791-4796.
- Santos, O., Nylander, T., Rosmaninho, R., Rizzo, G., Yiantsios, S., Andritsos, N., Karabelas, A., Muller-Steinhagen, H., Melo, L., Boulange- Petermann, L., Gabet, C., Braem, A., Tragardh, C. and Paulsson, M. (2004) Modified stainless steel surfaces targeted to reduce fouling - surface characterization. *Journal of Food Engineering*, **64**, 63-79.
- Sawant, P. D. and Nicolau, D. V. (2006) Hierarchy of DNA immobilization and hybridization on poly-L-lysine: an atomic force microscopy study. *Smart Materials & Structures*, **15**, S99-S103.
- Senden, T.J. and Ducker, W.A. (1994) Experimental-determination of spring constants in atomic-force microscopy. *Langmuir*, **10**, 1003-1004.
- Senesi, N., Miano, T. M., Provenzano, M. R. and Brunetti, G. (1991) Characterization, differentiation, and classification of humic substances by fluorescence spectroscopy. *Soil Science*, **152**, 259-271.
- Sharp, E.L., Parson, S.A. and Jefferson, B. (2004) The effects of changing NOM composition and characteristics on coagulation performance, optimisation and control. *Water Science & Technology*, **4**, 95-102.
- Sharp, E.L., Parson, S.A. and Jefferson, B. (2006) Coagulation of NOM: Linking character to treatment. *Water Science & Technology*, **53**, 67-76.
- Shi, X.H. and Zhao, Y.P. (2004) Comparison of various adhesion contact theories and the influence of dimensionless load parameter. *Journal of Adhesion Science & Technology* **18**, 55-68.
- Singer, P. C. (1999) Humic substances as precursor for potentially harmful disinfection by-products, *Water Science Technology*, **40** (9), 25-30.
- Singer, P. C. and Bilky, K. (2002) Enhanced coagulation using a magnetic ion exchange resin, *Water Research*, **36**, 4009-4022.
- Stefanescu, D.M. (1990) *ASM Handbook Volume 15: Casting*. ASM International, Ohio, OH, USA.

- Taboada-Serrano, P., Vithayaveroj, V., Yiacoumi, S. and Tsouris, C. (2005) Surface charge heterogeneities measured by atomic force microscopy. *Environmental Science & Technology*, **39**, 6352-6360.
- Tabor, D. (1977) Surface forces and surface Interactions. *Journal of Colloid & Interface Science*, **58**, 2-13.
- Tanaka, M., Asahi, Y. and Masuda, S. (1994) Interaction between drugs and water-soluble polymers .5. binding position of indomethacin and its related-compounds to bovine serum-albumin. *Polymer*, **35** (7), 1512-1517.
- Thurman, P.C. (1985) Waste-water treatment plants. *Landscape Architecture*, **75**, 52-54.
- Turq, V., Ohmae, N., Martin, J.M., Fontaine, J., Kinoshita, H. and Loubet, J. (2005) Influence of humidity on microtribology of vertically aligned carbon nanotube film. *Tribology Letters*, **19**, 23-28.
- Vadillo-Rodriguez, V., Busscher, H.J., Van Der Mei, H.C., De Vries, J. and Norde, W. (2005) Role of lactobacillus cell surface hydrophobicity as probed by afm in adhesion to surfaces at low and high ionic strength. *Colloids & Surfaces B-Biointerfaces*, **41**, 33-41.
- Van Oss, C.J., Good, R.J. and Chaudhury, M.K. (1986) The role of van-der Waals forces and hydrogen-bonds in hydrophobic interactions between bio-polymers and low-energy surfaces. *Journal of Colloid & Interface Science*, **111**, 378-390.
- Van Oss, C.J. (2002) Use of the combined Lifshitz-van der Waals and Lewis acid-base approaches in determining the apolar and polar contributions to surface and interfacial tensions and free energies. *Journal of Adhesion Science & Technology*, **16**, 669-677.
- Van Oss, C.J. (2003) Long-range and sort range mechanisms of hydrophobic attraction and hydrophilic repulsion in specific and aspecific interactions. *Journal of Molecular Recognition*, **16**, 177-190.
- Vezenov, D.V., Noy, A. and Ashby, P. (2005) Chemical force microscopy: probing chemical origin of interfacial forces and adhesion. *Journal of Adhesion Science & Technology*, **19**, 313-364.
- Wang, M.S., Palmer, L.B., Schwartz, J.D. and Razatos, A. (2004) Evaluating protein attraction and adhesion to biomaterials with the atomic force microscope. *Langmuir*, **20**, 7753-7759.
- Watson, G.S., Blach, J.A., Cahill, C., Nicolau, D.V., Pham, D.K., Wright, J. and Myhra, S. (2004) Interactions of poly(amino acids) in aqueous solution with charged model surface - analysis by colloidal probe. *Biosensors & Bioelectronics*, **19**, 1355-1362.

- Weidenhammer, P. and Jacobasch, H.J. (1996) Investigation of adhesion properties of polymer materials by atomic force microscopy and zeta potential measurements. *Journal of Colloid & Interface Science*, **180** (1), 232-236.
- Wilkinson, K.J., Balnois, E., Leppard, G.G. and Buffle, J. (1999) Characteristic features of the major components of freshwater colloidal organic matter revealed by transmission electron and atomic force microscopy. *Colloids & Surfaces a-Physicochemical & Engineering Aspects*, **155**, 287-310.
- Wu, W., Giese, R.F. and Vanoss, C.J. (1996) Change in surface properties of solids caused by grinding. *Powder Technology*, **89**, 129-132.
- Xu, L.C. and Logan, B.E. (2006) Interaction forces measured using AFM between colloids and surfaces coated with both dextran and protein. *Langmuir*, **22**, 4720-4727.
- Yamamoto, S., Ejaz, M., Tsujii, Y. and Fukuda, T. (2000) Surface interaction forces of well-defined, high-density polymer brushes studied by atomic force microscopy. 2. Effect of graft density. *Macromolecules*, **33**, 5608-5612.
- Yang, Q.F., Liu, Y.Q., Gu, A.Z., Ding, J. and Shen, Z.Q. (2002) Investigation of induction period and morphology of CaCO<sub>3</sub> fouling on heated surface. *Chemical Engineering Science*, **57** (6), 921-931.
- Yee, M. M., Miyajima, T. and Takisawa, N. (2006) Evaluation of ampiphilic properties of fulvic acid and humic acid by alkylpyridinium binding activity. *Colloid & Surfaces A: Physicochemical Eng. Aspects*, **262**, 182-188.
- Zbytniewski, R. and Buszewski, B. (2005) Characterization of natural organic matter (NOM) derived from sewage sludge compost. Part 1: Chemical and spectroscopic properties. *Bioresource Technology*, **96**, 471-478.
- Zhang, R., Vigneswaran, S., Ngo, H. H. and Nguyen, H. (2006) Magnetic ion exchange (MIEX (R)) resin as a pre-treatment to a submerged membrane system in the treatment of biologically treated wastewater. *Desalination*, **192**, 296-302.
- Zhao, Q., Liu, Y. and Abel, E.W. (2005) Surface free energies of electroless Ni-P based composite coatings. *Applied Surface Science*, **240** (1-4), 441-451.
- Zhao, Q., Liu, Y. and Wang, C. (2005b) Development and evaluation of electroless Ag-PTFE composite coatings with anti-microbial and anti-corrosion properties. *Applied Surface Science*, **252**, 1620-1627.

## Chapter 10

## Appendices

### Appendix A

\*Force file list \Version: 0x04420004 \Date: 09:38:45 PM Sun Mar 05 2006 \Start context: FOL \Data length: 20480 \Text: \History: \Navigator note: \*Equipment list \Description: Extended D3000 \Controller: IIIA \Microscope: D3000 \Extender: Basic \Serial stage: Yes \Vision: None \Scanner file: xydmmsg1.scn \Profile name: tapping \Motor sensitivity: 400 \Analog 2: User defined \*Scanner list \Scanner type: Dimension \Piezo size: G \File name: xydmmsg1.scn \Motor direction: Reverse \Allow rotation: Allow \Piezo cal: 440 \X sensitivity: 151.906 \X derate: 0.258557 \X mag: 1.5 \X mag1: 0.8 \X arg: 3.5 \X round: 0 \Y sensitivity: 166.673 \Y derate: 0.338919 \Y mag: 1.6 \Y mag1: 1 \Y arg: 3.5 \X slow sensitivity: 172.976 \X slow derate: 0.298243 \Y fast sensitivity: 152.53 \Y fast derate: 0.254392 \X slow-fast coupling: 0.63592 \X slow-fast coupling derating: 0.000677825 \Y slow-fast coupling: 0.661592 \Y slow-fast coupling derating: 0.000732552	\Fast cal freq: 0.500288 \Slow cal freq: 0.488563 \Xs-Yf coupling: 0.131619 \Xs-Yf coupling derating: 0.000162896 \Ys-Xf coupling: 0.144045 \Ys-Xf coupling derating: 0.000201102 \X offset sens: 280 \Y offset sens: 280 \Bias derate: 0 \@Sens. Zscan: V 15.00000 nm/V \@Sens. Current: V 10.00000 nA/V \*Ciao scan list \Parameter select: Main \Operating mode: Force \Tip serial number: \Scan size: 0 nm \X offset: 0 nm \Y offset: 0 nm \Rotate Ang.: 0 \Samps/line: 512 \Lines: 512 \Y disable: Enabled \Aspect ratio: 1:1 \Bidirectional scan: Disabled \Scan line shift: 0 \Scan rate: 1.00058 \Tip velocity: 0 \Minimum scan rate: 0.02 \Lift rate: 4 \X drift: 0 \Y drift: 0 \Step XY size: 300 \Cycles: 10 \Step XY period: 0.005 \Step size: 3 \Units: Metric \Color table: 12 \Scope dualtrace: Dual \Auto X Sep: 0 \Auto Y Sep: 0 \Auto pattern: Linear \Auto number: 2 \Capture direction: Up \Capture prelines: 50 \Engage Setpoint: 1
--	--

\Drive feedback: Disabled	\@1:DeflectionLimit: V (20.00000 V/LSB)
\Drive time: 5	2.500000 V
\Drive setpoint: 2	\@1:FM igain: V (1.000000 1/LSB) 0
\Drive gain: 3.82821	\@1:FM pgain: V (1.000000 1/LSB) 0
\Profiler profiling: Disabled	\@1:AmplitudeLimit: V (20.00000 V/LSB)
\Profiler length goal: 500	2.500000 V
\Profiler length actual: 0.001	\@Lift start height: V [Sens. Zscan] (0.0008136220
\Profiler speed: 1	V/LSB) 0.09248047 V
\Profiler scan time: 0.001	\@Lift scan height: V [Sens. Zscan] (0.0008136220
\Profiler resolution: 0.001	V/LSB) 1.330190 V
\Profiler x position: 0	\@Drive height: V [Sens. Zscan] (0.0008136220
\Profiler y position: 0	V/LSB) 0 V
\Profiler profiler position: 0	\@2:AFMSetDeflection: V (0.0003051758 V/LSB)
\Profiler direction: Forward	-0.05000000 V
\Profiler axis: Aux	\@3:AFMSetDeflection: V (0.0003051758 V/LSB)
\Profiler ramp-up ideal-distance multiplier: 25	1.000000 V linked
\Profiler ramp-up total-distance minimum: 2	\@2:TMSetAmplitude: V (0.0003051758 V/LSB)
\Profiler ramp-up total-distance goal: 10	2.100695 V
\Profiler backlash-removal distance: 10	\@3:TMSetAmplitude: V (0.0003051758 V/LSB)
\Profiler backlash-removal speed: 33	2.000000 V linked
\Gain start: 32	\@2:TMSetDeflection: V (0.0003051758 V/LSB)
\Gain end: 440	0 V
\Gain incr: 1.6	\@3:TMSetDeflection: V (0.0003051758 V/LSB)
\Pro. Gain factor: 1.5	1.000000 V linked
\Max shift: 0.02	\@2:TMSetPhase: V (0.005493164 deg/LSB) -
\Lines/gain: 8	0.4445068 deg
\Gain offset: 0.95	\@3:TMSetPhase: V (0.005493164 deg/LSB) 0
\Auto Gain: Disabled	deg
\@InterleaveList: S [InterleaveOffMode]	\@2:STMSetCurrent: V [Sens. Current]
"Disabled"	(0.0003051758 V/LSB) 0.5000000 V
\@LinearizeList: S [LinearizeOffMode]	\@3:STMSetCurrent: V [Sens. Current]
"modeLinearizeOff"	(0.0003051758 V/LSB) 10.00000 V
\@OxideList: S [OxideOffMode] "Open"	\@2:cnZmod: V (0.0000152588 1/LSB) 0
\@MicroscopeList: S [AFMMode] "Contact"	\@3:cnZmod: V (0.0000152588 1/LSB) 0
\@4:SPMFeedbackList: S [SPMFb] "Deflection"	linked
\@3:SPMFeedbackList: S [SPMFb] "Deflection"	\@2:SPMFbIgain: V (0.03125000 1/LSB) 3.250000
linked	\@3:SPMFbIgain: V (0.03125000 1/LSB) 2.000000
\@2:Input feedback: S [] ""	linked
\@3:Input feedback: S [] ""	\@2:SPMFbPgain: V (0.03125000 1/LSB)
\@Sens. Deflection: V 254.2875 nm/V	3.750000
\@Sens. Friction: V 1.000000	\@3:SPMFbPgain: V (0.03125000 1/LSB)
\@Sens. Amplitude: V 1.000000	4.000000 linked
\@Sens. Phase: V 1.000000	\@2:SPMFbSgain: V (0.0000305176 1/LSB) 0
\@Sens. Frequency: V 1.000000	\@3:SPMFbSgain: V (0.0000305176 1/LSB) 0
\@Sens. Potential: V 1.000000	linked
\@Sens. dC/dV: V 1.000000	\@2:Drive frequency: V (0.0000058208 kHz/LSB)
\@Sens. Fdback bias: V 1.000000	284.5195 kHz
\@Sens. In 0: V 1.000000	\@3:Drive frequency: V (0.0000058208 kHz/LSB)
\@Sens. Thermal: V 1.000000	74.43070 kHz
\@Sample period: V (0.1000000 us/LSB) 16.00000	\@2:Drive phase: V (0.005493164 deg/LSB) -
us	32.89856 deg
\@1:Z limit: V [Sens. Zscan] (0.006713867 V/LSB)	\@3:Drive phase: V (0.005493164 deg/LSB) 0
200.0000 V	deg

\@2:Lock-in phase: V (0.005493164 deg/LSB) 90.00000 deg	\Scratch angle: 0
\@3:Lock-in phase: V (0.005493164 deg/LSB) 90.00000 deg	\Size linked: Off
\@2:Drive amplitude: V (0.6103516 mV/LSB) 561.1986 mV	\Lift height: 100
\@3:Drive amplitude: V (0.6103516 mV/LSB) 988.1962 mV	\Columns: 1
\@2:Stray cap adj: V (0.0003051758 V/LSB) 0 V	\Rows: 1
\@3:Stray cap adj: V (0.0003051758 V/LSB) 0 V	\Column step: 0
\@2:AC bias ampl: V (0.0003051758 V/LSB) 0 V	\Row step: 0
\@3:AC bias ampl: V (0.0003051758 V/LSB) 0 V	\Capture: Enabled
\@2:Fdback bias setpt: V (0.0003051758 V/LSB) 0 V	\Tip factor: 0
\@3:Fdback bias setpt: V (0.0003051758 V/LSB) 0 V	\True resonance: 286.471
\@2:Bias Frequency: V (0.0000058208 kHz/LSB) 0 kHz	\Tip type: User 1
\@3:Bias Frequency: V (0.0000058208 kHz/LSB) 0 kHz	\Feedback type: None
\@2:DC bias: V (0.0003662109 V/LSB) 0 V	\Feedback counts: 0
\@3:DC bias: V (0.0003662109 V/LSB) 0 V	\@Z scan start: V [Sens. Zscan] (0.006713867 V/LSB) -26.23724 V
\@2:Bias: V (0.3051758 mV/LSB) 500.0000 mV	\@Z scan size: V [Sens. Zscan] (0.006713867 V/LSB) 15.03758 V
\@3:Bias: V (0.3051758 mV/LSB) 0 mV	\@Z step size: V [Sens. Zscan] (0.006713867 V/LSB) 0.01000000 V
\@2:Analog 1: V (0.0003051758 V/LSB) 0 V	\@Sample period: V (0.1000000 us/LSB) 35.00000 us
\@3:Analog 1: V (0.0003051758 V/LSB) 0 V	\@4:Image Data: S [Deflection] "Deflection"
\@2:Analog 2: V (0.0003662109 V/LSB) 0 V	\@4:Trig threshold Deflection: V [Sens. Deflection] (0.0000381470 V/LSB) 0 V
\@3:Analog 2: V (0.0003662109 V/LSB) 0 V	\@4:Threshold step Deflection: V [Sens. Deflection] (0.0000381470 V/LSB) 0 V
\*Ciao force list	\@4:Ramp channel: S [Zsweep] "Z"
\Scan rate: 1.99298	\@4:Ramp size Zsweep: V [Sens. Zscan] (0.0008136220 V/LSB) 26.66667 V
\Reverse rate: 1.99298	\@4:Ramp offset Zsweep: V [Sens. Zscan] (0.0008136220 V/LSB) -4.350245 V
\Samps/line: 256 194	\@4:Feedback value Zsweep: V [Sens. Zscan] (0.0008136220 V/LSB) 0 V
\Ave lines: 1	\*Ciao force image list
\Display mode: Both	\Data offset: 20480
\Trigger mode: Absolute	\Data length: 1024
\Trig slope: Positive	\Bytes/pixel: 2
\Plot start: 0	\Start context: FOL
\Plot end: 1	\Data type: FORCE
\Auto start: Enable	\Do zoffder: 0
\Auto offset: Enabled	\Note:
\Start mode: Calibrate	\Plane fit: 0 0 0 0
\End mode: Retracted	\Frame direction: Up
\Ramp delay: 0	\Stage X: 0
\Reverse delay: 0	\Stage Y: 0
\Indent setpoint: -1	\Stage type: N/A
\X Rotate: 0.8	\Profile length: 0
\Scratch length: 100 nm	\Profile speed [um/s]: 0
\Scratch rate: 1	\Samps/line: 256 194
	\Scan line: Main
	\Realtime plane fit: Line
	\Offline plane fit: Full



\Force display mode: Normal \Spring constant: 0 \Separation Scale: 0 \Force offset: 0 \Z magnew force: 1 \Scope coupling: DC \Smoothing filter: 0 \Graph function: i \STS I range: 15000 \STS DLI/DLV range: 10 \STS DLI/DV range: 10 \STS DI/DV range: 10 \STS Log(i) range: 10 \@4:Image Data: S [Deflection] "Deflection" \@Z magnify: C [4:Z scale] 1.000000 \@4:Z scale: V [Sens. Deflection] (0.0000381470 V/LSB) 0.1949472 V \@4:Z offset: V [Sens. Deflection] (0.0000381470 V/LSB) -0.4648680 V \@Z scan size: V [Sens. Zscan] (0.006713867 V/LSB) 15.03758 V \@4:Ramp size: V [Sens. Zscan] (0.0008136220 V/LSB) 26.66667 V \@4:Ramp offset: V [Sens. Zscan] (0.0008136220 V/LSB) -4.350245 V \*File list end →	
---	--

## Appendix B

```
% A program to read multiple AFM di Force versus distance curves for
% analysis of adhesion force - for use with the Cranfield D3000 instrument.

% Load in multiple file names

clear all
close all

[FileNames,Path] = uigetfiles('*.','Any text');

% then get number of files loaded

Diment = size(FileNames);

%input spring constant of cantilever
k=input ('Enter spring constant of cantilever in (N/m): ');

%setup zero array for force

force_data = zeros(Diment(1,2),1);
force_peak_total = 0;
length_peak_total = 0;
total_count_total = 0;

for run = 1:Diment(1,2)

total_counts = 0

Filename = char(FileNames(1,run));

file = [Path,Filename]

fid=fopen(file,'r');
A=fread(fid,'int16');

%version = input ('specify version of Nanoscope file: (1: ICAL as of feb. 2003, 0: older): ')
%          above line is an optional variation of the program
%switch version      optional variation
%case 1              optional variation

frewind(fid);
for i=1:55
% goes to \@Sens. Zscan in line 56. Note: 5870/440=13.34== Sens. Zscan
% 5870 nm is the Max displacement of piezo J, thus this factor converts
% the piezo displacement from volts to nm
    line=fgetl(fid);

end

j=findstr(':',line);
```

```

    Sens_ZScan=str2num(line(j+4:j+11));

frewind(fid);
for i=1:191
% goes to \Samps/line (i.e. number of points in force curve) in line 338.

    line=fgetl(fid);

end

j=findstr(':',line);
N_points=str2num(line(j+2:j+4));

frewind(fid);
for i=1:229
    line=fgetl(fid);

end

j=findstr(' ',line);
V_Ramp_size=str2num(line(j+1:j+8));

Zmax=V_Ramp_size*Sens_ZScan;

N=N_points-1;

x=0:Zmax/N:Zmax;

y1=A(10240:10240+N);
y2=A(10241+N_points:10240+2*N_points);

frewind(fid);
for i=1:266

% goes to line 266, where digital to analog conversion factor ('sensitivity') is given
% This factor converts the photodiode signal from [LSB units] to [V].

    line=fgetl(fid);

end

j=findstr('(',line);
Sens_Deflection_AD=str2num(line(j+1:j+12));

frewind(fid);
for i=1:127

% Line above is the V to nm conversion factor ('sensitivity') of photodiode signal
% It uses the sens. Deflection number given in the graph window of the DI-software.

```

```

    line=fgetl(fid);

end

j=findstr(':',line);
Sens_Deflection=str2num(line(j+4:j+12));

Def_ext=y1*Sens_Deflection_AD*Sens_Deflection;    %Deflection extend
Def_ret=y2*Sens_Deflection_AD*Sens_Deflection;    %Deflection retract

Def_ext=Def_ext - Def_ext(N_points); %Def_ext offset to have zero def at start of curve
Def_ret = Def_ret - Def_ret(N_points); %Def_ret offset to have zero def at start of curve

%removing slope from Def_ext and Def_ret
array = (1:N_points);
x_re = reshape(x,N_points,1);
x_re_sl = (N_points-70:N_points);
x_re_sl = reshape(x_re_sl,71,1);

Def_ret_sl = Def_ret(N_points-70:N_points);
ret_slope = polyfit(x_re_sl,Def_ret_sl,1);

ret_slope_fit = ret_slope(1,2) + ret_slope(1,1)*array;
ret_slope_fit_b = reshape(ret_slope_fit,N_points,1);

Def_ret_new = Def_ret - ret_slope_fit_b;
Def_ext_new = Def_ext - ret_slope_fit_b;

F_ext=k*Def_ext_new*1000;
F_ret=k*Def_ret_new*1000;

F_ret_min = min(F_ret);
F_ext_min = min(F_ext);

force_data_ret(run,1)=F_ret_min;
force_date_ext(run,1)=F_ext_min;

% Add peak indentification

% First identify noise level from the last 50 data points on the retract
% curve.

noise_level = 2*(max(F_ret(N_points-50:N_points)) - min(F_ret(N_points-50:N_points)));
% Find jump points
posit = 0

for i=1:N_points-1
    if F_ret(i+1,1)-F_ret(i,1) > noise_level
        total_counts = total_counts+1
        posit(total_counts,1) = i
    end
end

```

```

        if total_counts > 1
            if posit(total_counts,1) - posit(total_counts-1,1) < 4
                total_counts = total_counts-1
            end
        end
    end
end
end

if total_counts>1

if posit(end,1)-posit(end-1,1) < 4
    posit(end,1) = NaN
end
end

no_of_peaks(run,1) = total_counts

% determining ideal curve

array = (1:N_points);
zero_point = find(F_ret<0);
ideal_curve_data_y = F_ret(1:30);
ideal_curve_data_x = (1:30);
ideal_curve_data_x = reshape(ideal_curve_data_x,30,1);

ideal_curve_parameters = polyfit(ideal_curve_data_x,ideal_curve_data_y,1);

ideal_curve = ideal_curve_parameters(1,2) + ideal_curve_parameters(1,1)*array;

figure

plot(x,F_ext,'-b',x,F_ret,'-r',x,F_ret_min,'-g',x,F_ext_min,'-m',x,ideal_curve,'-g','LineWidth',2);

hold on
force_peak = 0;
length_peak = 0;

if total_counts > 0

for j = 1:total_counts
    x_j = x(posit(j,1));
    F_ret_j = F_ret(posit(j,1));
    plot(x_j,F_ret_j,'ko')
    %measuring force
    force_peak(j,1) = F_ret_j;
    %measuring length
    length_ideal = find(ideal_curve<F_ret_j);
    length_peak(j,1) = x_j-x(length_ideal(1,1));
end
end

hold off

grid on

```

```

xlabel('PIEZO DISPLACEMENT (nm)');

ylabel('FORCE (pN)');

x_corr = (0.25*max(x)/2);
y_corr = (max(F_ret));
y_corr_2 = 0.8*y_corr;

text(x_corr,y_corr,['Adhesion Force (pN) =', num2str(F_ret_min)]);
text(x_corr,y_corr_2,['filename ', Filename]);

if total_counts > 0
force_peak_total = [force_peak_total;force_peak];
length_peak_total = [length_peak_total;length_peak];
total_count_total = [total_count_total;total_counts];
end
end

no_of_bars_force = ceil((max(-1*force_peak_total))/200);
no_of_bars_length = ceil((max(length_peak_total))/20);
no_of_bars_count = max(total_count_total)+1;

force_hist_raw = hist(force_peak_total,no_of_bars_force);
length_hist_raw = hist(length_peak_total,no_of_bars_length);
counts_hist_raw = hist(total_count_total,no_of_bars_count);

figure

subplot(2,2,1), plot(length_peak_total,force_peak_total,'ro')
xlabel('length / nm')
ylabel('force / pN')

subplot(2,2,2), hist(force_peak_total,no_of_bars_force)
xlabel('force / pN')
ylabel('no of events')

subplot(2,2,3), hist(length_peak_total,no_of_bars_length)
xlabel('length / nm')
ylabel('no of events')

subplot(2,2,4), hist(total_count_total,no_of_bars_count)
xlabel('events per curve')

length_peak_sort = sort(length_peak_total);
total_count_sort = sort(total_count_total);

```

**Appendix C**